INVESTIGATION OF ROCKFALL AND SLOPE INSTABILITY WITH ADVANCED GEOTECHNICAL METHODS AND ASTER IMAGES

by

FHATUWANI SENGANI

submitted in accordance with the requirements for
the degree of

DOCTOR OF PHILOSOPHY

in the subject

MINING ENGINEERING (ROCK ENGINEERING)

at the

UNIVERSITY OF SOUTH AFRICA

SUPERVISOR: PROF F. MULENGA

(March 2021)

DECLARATION

Name: Fhatuwani Sengani

Student number: 67137180

Degree: Doctor of Philosophy

Investigation of Rockfall and Slope Instability with Advanced Geotechnical Methods and Aster Images

I declare that the above thesis is my own work and that all the sources that I have used or quoted have been indicated and acknowledged by means of complete references.

I further declare that I submitted the thesis to originality checking software and that it falls within the accepted requirements for originality.

I further declare that I have not previously submitted this work, or part of it, for examination at Unisa for another qualification or at any other higher education institution.

_____   __04 March 2021
SIGNATURE   DATE

Abstract

The objective of this thesis was to identify the mechanisms associated with the recurrence of rock-slope instability along the R518 and R523 roads in Limpopo. Advanced geotechnical methods and ASTER imagery were used for the purpose while a predictive rockfall hazard rating matrix chart and rock slope stability charts for unsaturated sensitive clay soil and rock slopes were to be developed. The influence of extreme rainfall on the slope stability of the sensitive clay soil was also evaluated.

To achieve the above, field observations, geological mapping, kinematic analysis, and limit equilibrium were performed. The latter involved toppling, transitional and rotational analyses. Numerical simulation was finally resorted to. The following software packages were employed: SWEDGE, SLIDE, RocData, RocFall, DIPS, RocPlane, and Phase 2. The simulation outputs were analyzed in conjunction with ASTER images. The advanced remote sensing data paved the way for landslide susceptibility analysis.

From all the above, rockfall hazard prediction charts and slope stability prediction charts were developed. Several factors were also shown by numerical simulation to influence slope instability in the area of study, i.e. sites along the R518 and R523 roads in the Thulamela Municipality. The most important factors are extreme rainfall, steep slopes, geological features and water streams in the region, and improper road construction. Owing to the complexity of the failure mechanisms in the study area, it was concluded that both slope stability prediction charts and rock hazard matrix charts are very useful. They indeed enable one to characterize slope instability in sensitive clay soils as well as rockfall hazards in the study area. It is however recommended that future work is undertaken to explore the use of sophisticated and scientific methods. This is instrumental in the development of predictive tools for rock deformation and displacement in landslide events.

KEY TERMS: Rockfall, Slope stability, Limit Equilibrium, Finite Element Method, ASTER images, Particle Finite Element Methods, Numerical Modeling

List of publications

The articles below have been published or submitted to peer-reviewed journals in fulfillment of the requirements for the degree of Doctor of Philosophy.

Sengani, F., Mulenga, F., 2020. A review on the application of Particle Finite Element Methods (PFEM) to cases of slope instability (landslide). International Journal of Geotechnical Engineering. https://doi.org/10.1080/19386362.2020.1814027.

Sengani, F.; Mulenga, F. Application of Limit Equilibrium Analysis and Numerical Modeling in a Case of Slope Instability. Sustainability 2020, 12, 8870. https://doi.org/10.3390/su12218870

Sengani, F.; Mulenga, F. Influence of Rainfall Intensity on the Stability of Unsaturated Soil Slope: Case Study of R523 Road in Thulamela Municipality, Limpopo Province, South Africa. Appl. Sci. 2020, 10(24), 8824; https://doi.org/10.3390/app10248824

Sengani, F., Muavhi, N., Mulenga, F., 2021. Advanced Analysis of Road-Slope Stability in a Brittle and Faulted Rockmass Terrain by Several Techniques, Transportation Geotechnics (2021), https://doi.org/10.1016/j.trgeo.2021.100545

Sengani, F., Muavhi, N., Mulenga, F. 2021. Development of slope stability hazard assessment and prediction of recurrence chart: ASTER images and FEM-based approaches. Journal of African Earth Sciences (Journal). *Accepted*.

Sengani F., Zvarivadza T. (2019) Evaluation of Factors Influencing Slope Instability: Case Study of the R523 Road Between Thathe Vondo and Khalvha Area in South Africa. In: Widzyk-Capehart E., Hekmat A., Singhal R. (eds) Proceedings of the 18th Symposium on Environmental Issues and Waste Management in Energy and Mineral Production. SWEMP 2018. Springer, Cham. https://doi.org/10.1007/978-3-319-99903-6_7

Sengani, F., Mulenga, F. New hazard assessment for rock falls in near-vertical blocky rock environments. Environmental Earth Sciences (Journal). *Under revision*

Sengani, F., Mulenga, F . Sensitivity Analysis and Flow Evolution of the Slope Instability Occurred in R518 and R523 regional Roads in the Northern Part of South Africa. Geomechanik und Tunnelbau - Geomechanics and Tunnelling (Journal). *Under review*

Sengani, F., Mulenga, F., Nkanyane, F., and Baiyegunhi, C., Rock-slope Instability Assessment and Prediction Methods for Surface Excavations in Mountainous Terrain: A state-of-the-art review. (Journal). *In Preparation*

Sengani, F., Mulenga, F. Comparison Between Latin HyperCube and Monte Carlo Simulation in Assessing the Safety Factor (FoS) of the Soil Slope under Mechanical Blasting Conditions. Engineering with Computers (Journal). *In Preparation*

Dedication

Khakhamela, Vele, Silwane, Lutiti lu ambara dzhasi, tshau fuka na tshau adza, tshitaka tshitwu, marunga dzindevhelaho, dambatshekwa lina segere, tshiulu tshamandini. Avha a tshi sendela Sengani, mudulu wa Mmbulaheni, Radukununu, Nyamulambilu wa ha Nethathe na vhanwe, ene ene wa ha Nefundudzi, nya nkodolela wa sa kodolela u do wela, hayani havho nwali. Ha pfala kwatha itshi tavha mukosi u fhandula ho mbilu, mukosi wa u luvha vho Nwali na Nwali muhulu ene Ragole. Dungudzi u rotisa mutodzi, mutodzi wa tshilolo, a tshi vhidzelela vho Nwali na Ragoli ari "vho Nwali na Ragolo, vho Nwali na Ragolo, Vho Nwali na Ragolo, vho na ni ha mudi Mulilangoma ngei pfamoni ya manwalo, vhadziya tshingwindingwindi nda vheka vho difha maanda vha tshilingedza ukweta Tombo la vho Nwali na Ragolo uri li lile madi nga u viela lofha la vho Nwali na Ragolo Bakoni vhana vha edza Pfuko vha Musuku, vha tshiri Mahunguvhu hanga ivhoni". Dungudzi ahuwelela vho Nwali and Ragolo ari zwila zwithu zwo iteya, hari hwiiiiii, mifhululu yee ngindi ngindi, vhari na ngoho hutungula Pfene ha vho-Ravhembalani fhasi ha dzaula la muvhula, Dungudzi ari vho Nwali na vho Nwali vha Thavhani dzaha Molepo na Mamabolo na Ragolo, murorwane a u tungulwe ri divhe uri ri sendama nga lufhio lurumbu. He duuuu a khunyeledza nga uri "zwila zwithu zwo iteya". Ambo lavhelese vhudzula vho Nwali and Ragolo, ndi hone a tshi kuda Magota na u vusa vhane vha zwi Ingamo nga Thakula, ha pfala muungo u tshi vhidza vho the vhala vha daka la Ha-Nethathe na Nefundudzi, vhazwala na ma Khotsi-muhulu. Vha swika vho Nwali and Ragole vhari ngwana ya vhakololo ene ene mukololo "tshi kwilikwili tshi tula tshi nau nau" vhari vhalitshe fhedzi "Dzhiedzhie lola mutanga mutanga wa li la vho" vho Nwali na Ragolo vhari mahunguvhu ayo o vheya lwayo kha vhuredzi ha Zwifhoni husa vheiwi lwalo, vho Nwali na Ragolo vhe mirumba khai tambale tshanga rido tanga migadoni hune Ragole a thuka hone. Ha unga mukosi wa tshitameye tshi tshi vhidzelela mavhudzi a vho kwashaho khali ya vho Nwali and Ragolo, ha pfala khuwa ya zwililo. Wa salipfa uvhuzwani u doli pfela vhulaloni, ya lila Ngomalungundu yone yone ya vho Nwali na Ragolo, Khakhamela, Silwane, iwe mula Mundandane, Ndaa.

Acknowledgments

In the memory of my late grandfather, grandmother, uncle, and aunt

Chief Vho-Mmbulaheni Sengani, Vho-Mukumela Nekokwane, Vho-Simon Mmbulaheni Mudalahothe and Vho-Julia Ntshengedzeni Mudalahothe (vha edele nga mulalo ndaa!!!)

Table of contents

List of Figures

xix

List of Tables

List of Abbreviations

ALE	Arbitrary Lagrangian-Eulerian
ASTER	Advanced Space-borne Thermal Emission and Reflection Radiometer
DEMs	Digital Elevation Models
ERHA	Evolving Rockfall Hazard Assessment
EROS	Earth Resources Observation and Science
FE	Finite Element
FEM	Finite Element Method
FoS	Factor of Safety
FPL	Fluid Pressure Laplacian technique
FR	Frequency Ratio
FSSI	Fluid Solid Structure Interaction
G-PFEM	Geotechnical Particle Finite Element Method
GPS	Global Positioning System
IDA	Inverse Distance Algorithm
ISRM	International Society for Rock Mechanics
JA	Joint Aperture
JI	Joint Infilling
JP	Joint Persistence
JRC	Joint Roughness Coefficient
Jn	Joint Set

JS	Joint Spacing
JW	Joint Weathering
LE	Limit Equilibrium
LEM	Limit Equilibrium Method
LL	Liquid Limit
LPDAAC	Land Process Distributed Active Archive Center
LSM	Landslide Susceptibility Mapping
NDVI	Normalized Difference Vegetation Index
PALSAR	Phased Array type L-band Synthetic Aperture Radar
PFEM	Particle Finite Element Method
PI	Plastic index
PL	Plastic Limit
PPP	Polynomial Pressure Projection
QRA	Quantitative Risk Analysis
RITSS	Remeshing and Interpolation Technique with Small Strain
RMR	Rock Mass Rating
ROIs	Regions of Interest
RQD	Rock Quality Designation
S	Sites
SAWS	South African Weather Service
SWIR	Shortwave Infrared
SPFEM	Smooth Particle Finite Element Method

SWEDGE	Surface Wedge Analysis for Slopes
TIR	Thermal Infrared
UEM	Unique Element Method
USCS	Unified Soil Classification System
UCS	Uniaxial Compressive Strength
VNIR	Visible and Near-Infrared
WoE	Weight of Evidence

List of Symbols

a	Measure of the level of landslide activity
A	Number of cells
Ac_i	Number of cells of the category (i)
Al	Total number of landslides cells
Al_i	Number of landslides cells of the category (i)
Ao	Number of cells outside the landslides
b	Gradient of the relation
b^e	Elastic left Cauchy Green tensor
C	Cohesion of slope
C	Value of the element at risk
${}^nC$	Cloud
c	Constant parameter
C_C	Curvature
C_u	Coefficient of uniformity
D_{10}, D_{30}, and D_{60}	Grain size corresponding to 10%, 30%, and 60% passing
d_i	Distance between the i-th neighboring Gauss point
E	Interslice forces
E, T & W	Forces
FR_j	FR value for the chosen class of factor j
F	Yield function
$f(x)$	Interslice force function

$f(\tau, q)$	Yield surface
F_f	Factor of Safety
F^e	Pure elastic loading
F^p	Plastic deformation
g	Plastic potential
g_t	Tangential gap
g_t^e	Elastic decomposition
g_t^s	Plastic part
g_n^-	Penetration function
h	Hardening parameters
J_2	Second invariant
LS	Landslide Susceptibility
l^p	Plastic velocity gradient
$L_v t$	Plastic part
m_v	Compressibility
n	Number of variables
n	Outwards
N	Cumulative number of landslides greater than magnitude
P	Probability
p	Cauchy mean pressure
$P(M_i)$	Probability of occurrence of a rockfall of magnitude M_i
$P(T|X_j)$	Probability of the element being at the point X

R	Risk due to the occurrence of a rockfall of magnitude M_i
S	Boundary
S_t	Soil Sensitivity
S_u	Undrained shear strength
t	Time
t	Tractions
t	Tangential contact stress
T	Factor of Safety
W	Stored energy function
W_n	Moisture content
w_i	Weighting function
X_{ij}	Vulnerability *of the element impacted by a rockfall*
$Z_1\ to\ Z_9$	Altitude values in 3×3 cellular networks
α	Intercept of the model
β	Beta values associated with each of the independent variables
β	Slope gradient
$\mathbb{C}$	Elastic compliance modulus
ϵ	Penalty parameter
θ	Lodes Angle of the Kirchhoff stress
Φ	Cumulative normal distribution function
ϕ	Angle of internal friction of slope
ρ	Density
σ	Stress

σ_n	Normal total contact stresses
σ_i	Stresses at the i-th neighboring Gauss point
σ^d	Deviatoric part of the Cauchy stress tensor
u	Solid displacement
μ	Initial boundary conditions
τ	Kirchhoff stress tensor related to the Cauchy stress
λ	Scale factor of the assumed function
$\dot{\lambda}$	Plastic multiplier
$\dot{\gamma}$	Plastic multiplier
γ	Unit Weight
Γ_c	Boundary in contact
∇	Linear strain-displacement
Δ_s	The cell size.

Chapter 1   Introduction

1.1   Context of the research

Geotechnical problems are usually described by means of a combination of algebraic, differential, and integral equations. This is because geotechnical engineering or more accurately geomechanics is a subset of solid mechanics. As such, associated problems are too complex that empirical methods fall short in the scope of their applicability. Indeed, concepts like rock mass classification, kinematic analysis, and stability charts have shown their limitation although commonly used in the analysis of slope stability (De Borst and Vernmeer, 1984; Yu and Mitchell, 1998; Zhang, 2014; Monforte et al., 2017 & 2018). That is why numerical modeling techniques are increasingly preferred over empirical techniques.

Numerical methods are known to rely on computer algorithms capable of producing approximate yet practical and meaningful solutions to engineering problems. The traditional Lagrangian Finite Element Method (FEM) has been considered to be the most appropriate numerical technique for the analysis of nonlinear problems of solid mechanics (Onate and Garcia, 2001; Onate et al., 2004; Larese et al., 2008; Lohner, 2008; Baiges and Codina, 2010; Bazilevs et al., 2010; Takizawa and Tezduyar, 2011). However, FEM becomes of little use when large strains emerge with the potential of resulting in limit loads that can trigger failure.

Most applications of the traditional Lagrangian FEM to slope stability analysis represent failure as a specific time point during the deformation process (e.g. Khoa and Jostad, 2010; Baba et al., 2012; Ishii et al., 2012; Conte et al., 2014; Fawaz et al., 2014; Wang et al., 2014; Maji, 2017). This approach cannot be used to predict the internal behavior of a solid continuum. In landslides, for instance, soil behavior transitions from solid-like to liquid-like and then back to a solid-like phase. In such a problem, the key concern is to understand the mechanism triggering the unstable

behavior to predict future sliding occurrences. A better understanding of the internal behavior of the sliding continuum cannot be gained with the traditional Lagrangian FEM. Two reasons are ascribed to this: first, the severe mesh distortion and boundary evolution that results from large changes in geometry, and second, the difficulty in solving efficiently and robustly the highly nonlinear and non-smooth discrete governing equations (Zhang, 2014).

Particle Finite Element Method (PFEM) can be regarded as a viable option in the search for solutions to nonlinear problems. They are suitable for the analysis of geotechnical problems (Monforte et al., 2018). Nevertheless, the underlying models have been noted to experience volumetric locking around the framework used for finite element discretization. This usually leads to numerical instability and stiffening as well as spurious high spatial variability in the solution (Babuska, 1971; Brezzi, 1974; Bathe, 2010). Analysis techniques such as Fluid Pressure Laplacian (FPL) and Polynomial Pressure Projection (PPP) have been used to improve the PFEM (Raviart and Thomas, 1977; Perez-Foguet and Armero, 2002; Onate et al., 2004; Preising and Prevost, 2011). Although encouraging results have been produced since PFEM as a numerical analysis tool still has a long way notably in terms of the level of accuracy of simulation outputs. In this thesis, FEM in conjunction with the Advanced Space-borne Thermal Emission and Reflection Radiometer (ASTER) is explored in the analysis of rockfalls and slope instability. The latter is to supplement FEM with actual data and enhance the understanding and prediction of the mechanism and recurrence of rock-slope instability. Two Thulamela Municipality roads in the Limpopo province of the Republic of South Africa have been identified as the case study for this doctoral research. The data collected and subsequent analysis are expected to produce meaningful insights into rockfalls, slope stability, and landslides.

1.2 Statement of the problem

The instability of rock slopes is continually reported as a worldwide problem (Göktepe and Keskin, 2018). Experts in the field of rock and geotechnical engineering are constantly called upon to analyze and predict the stability of a given slope. They are also required to assess the risks associated with unsafe areas, their potential failure mechanism, and the possible remedial measures (Eberhardt, 2003). The underlying simulation analysis is mainly centered on the Lagrangian FEM or PFEM which in turn provides insights on rock stability and toppling. The problem is that PFEM is better suited for simple slope geometries and basic loading conditions that cannot be used to describe the complex behavior of actual sites. PFEM also provides little information on the slope failure mechanism; and therefore, is inadequate in real-life situations (Eberhardt, 2003). Due to the nature of the rock mass, PFEMs are found to be useful but require further refinements.

To this end, the FEM framework is coupled with remote sensing techniques in an attempt to fill the gap inherent to rock slope instability. The aim is to indeed enrich the geotechnical analysis and update the underlying simulation models. The mechanisms associated with the occurrence of rock slope instability are expected to be clarified. Here, the Thulamela Municipality in Limpopo was used as a case study for the development of new realistic stability charts and hazard maps.

1.3 Research objectives

Dow (2015) has argued that solutions to real-world solid mechanics problems are impossible to find. This is because key input parameters are often too complex to be captured well. The geometry, boundary, and loading conditions of the rock mass epitomize well this complexity. To circumvent the problem, approximate solutions are recommended for so long as they provide meaningful insight into the behavior of the rock mass. Remote

sensing techniques are used as a complement to bridge the gap between approximation and reality.

It is in line with the above that the following research objectives are set out as part of the scope of the study:

- Apply the FEM together with remote sensing techniques in investigating the mechanisms behind slope instability along the R518 and R523 roads in Limpopo
- Develop a predictive rockfall hazard rating matrix chart for the R518 and R523 roads
- Develop a slope stability chart and criterion for unsaturated sensitive clay soil in mountainous areas.

ASTER is selected as the remote sensing technique. It is anticipated that cases of rockfalls and slope stability may be analyzed in the future based on the FEM-ASTER paradigm proposed in this research thesis. This may potentially enable one to deal with the problems of predicting rockfalls and slope stability more effectively.

1.4　Formulation of the research hypothesis

The point of departure of this research is to argue that the combined use of numerical tools and remote sensing techniques may have scientific benefits. From a geotechnical point of view, this has the potential to provide greater insights into slope instability, their failure mechanism, and deposition. The understanding is that remote sensing data may improve the numerical rendering of rock slope behavior.

The analysis of the stability of rock slopes is performed primarily to assess their safety (Rabie, 2013; Ansari et al., 2014; Rubio, 2016; Göktepe and Keskin, 2018). However, the selection of the analysis tool depends on the conditions of the site and its expected mode of failure (Duncan, 1996; Eberhardt, 2003; Rubio, 2016). The challenge has been in finding adequate

tools that can describe failure as a nonlinear phenomenon involving solid-like and liquid-like behaviors. The latter known as Fluid-Solid-Structure Interaction (FSSI) cannot be solved using, for example, the classical Arbitrary Lagrangian-Eulerian (ALE) formulation of the FEM framework (Peric et al., 1996; Oliver et al., 2007; Wang et al., 2015).

Over the last two decades, a framework known as the Particle Finite Element Method (or PFEM) has been explored in the field of geotechnical engineering. The numerical modeling paradigm is a combination of finite element and meshless finite element methods. It revolves around the numerical resolution of the Lagrangian formulation of particulate systems. The technique has gained popularity thanks to pioneering work by Aubry et al. (2005), Idelsohn et al. (2003 & 2004), Onate et al. (2004 & 2008), and Larese et al. (2008). Originally, the PFEM was intended to solve solid particulate systems interacting with fluid (Zhang, 2014). It is widely used in fluid mechanics because it allows for mesh distortion while following the evolution of free surfaces (Zhang et al., 2014 – 2019).

PFEM is now being contemplated for the analysis of slope stability in areas of high rainfall. In light of this, it is hypothesized that by coupling the FEM framework and the ASTER images, a better description of such slope instability settings may ensue. The conjecture is tested along the R518 and R523 roads of the Thulamela Municipality where extreme rainfalls and recurring rockfalls are always experienced.

1.5   Contribution to the body of knowledge

The doctoral study is anticipated to contribute to a better description of the mechanism associated with rockfalls and landslides. The R518 and R523 roads were used as case studies while the empirical data collected on-site helped validate the simulation model constructed for the purpose.

It is crucial to indicate that the combination of ASTER and FEM is not in wide use in the field of rock mechanics. As such, there is room enough to

explore the technique and attempt to provide a better description of the slope stability problems. The added value of the endeavour may lie in the development of rockfall hazard prediction charts. Indeed, the hazard matrix chart proposed by Lateltin et al. (2005) and Ferrari et al. (2017) rate hazard based on the kinetic energy of the rock mass. However, the chart itself does not consider for example the effect of rainfall when rating slope hazard. This thesis attempts to bridge this gap. Furthermore, previous studies on the recurrence of slope stability along Thulamela roads were based on visual observation and field measurement. And to the best of my knowledge, no detailed study into the mechanisms associated with recurrent slope instability in the municipality is available. The joint use of FEM and ASTER images is a step towards a theoretical description of the mountainous regions of the Thulamela Municipality. Lastly, PFEM has not been reported to predict the re-occurrence of the slope instability and the final deposition of sliding or rolling material. ASTER images are used to contribute with initial data for validation and calibration of FEM simulation models.

1.6   Location of the study area

The scope of the study is limited to two national roads located in the Thulamela Municipality: the R518 and the R523.

The Thulamela Municipality is a Category B (categories are based on population people and size of the municipality based in distance or area coverage) municipality situated within the Vhembe District in the far north of the Limpopo province as shown in Figure 1.1. The Kruger National Park forms its eastern boundary while the southern and south-western side is bordered by the Makhado Municipality.
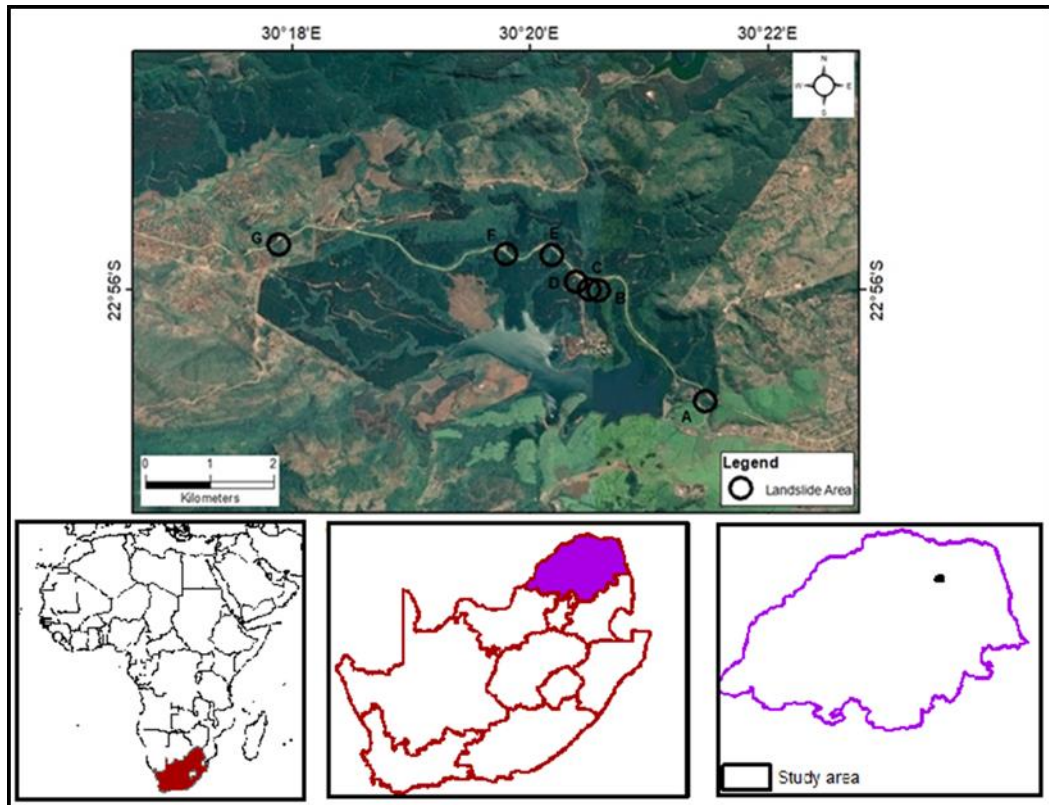
Figure 1.1 Locality map of the study area

As the smallest of the four municipalities in the district, Thulamela is spread over about 2 642 km². It is, however, the largest in the province in terms of population size (Thulamela Municipality, 2019).

The R518 and R523 roads identified for this research are situated in the rugged topography of the Southpansberg Group. This geological group is partially buried beneath sedimentary and volcanic rocks of different thicknesses. The group is dominated by large faults and joints thereby creating a discrete and blocky rock mass especially in Thulamela (Barker, 1979; Barker et al., 2006; Brandl, 1981 & 1986). Furthermore, a conjugate fault and joint set have been evidenced in the northwest-southeast and northeast-southwest directions with quartz veins filling the brecciated joints and faults (see Figure 1.2). It is these geological features that have led to high rockfalls and slope stability problems on the roadside. An attempt is made to understand these phenomena with the help of computer-based simulation tools built around the FEM framework and ASTER images.
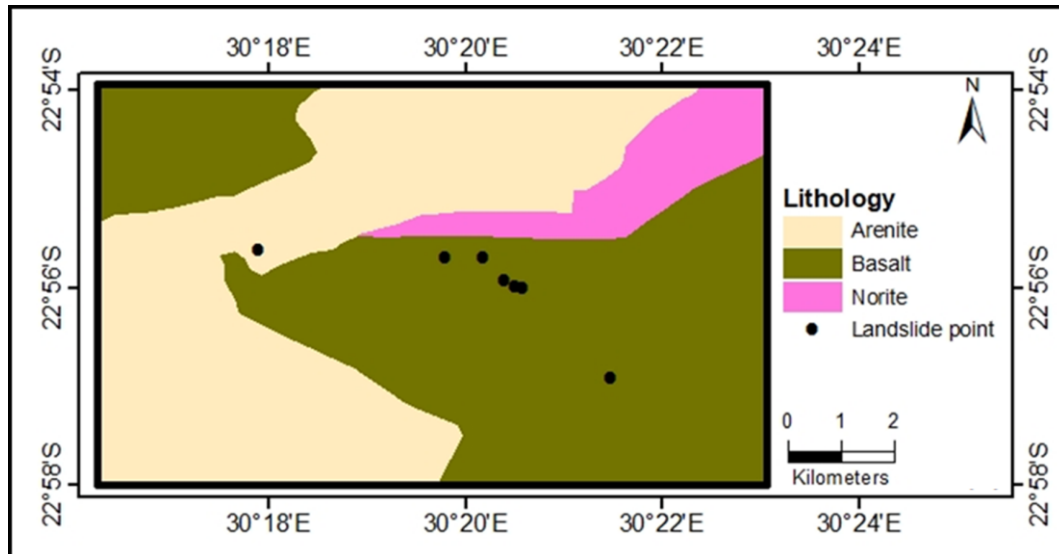
Figure 1.2 Geological map of the study area

These roads are the bloodline between villages and surrounding townships. Safety is therefore critical when one considers the fact that they were excavated by the blasting of very sloppy and unstable terrain (Sengani and Zvarivadza, 2019). The two roads also pass through several rivers (Mutanamba, 2013). Intensive summer rainfall and human activities in the study area also make roads susceptible to frequent slope failure.

Several remedial measures have been suggested and implemented but rockfalls and slope instability are still reported at an alarming rate. For example, Mutanamba (2013) analyzed the stability of the cut-slope along the R523 road between Thathe Vondo and Khalavha. First, geological structures, properties of the soil, and groundwater regime were surveyed. Then, conventional analytical methods were used to classify the type of soil and produce slope stability charts. Finally, two types of failures occurring close to the road were identified from the findings: rotational slump failure and rockfall in the form of toppling. The qualitative findings, however, could not be used to comprehensively describe the underlying mechanism of landslide, occurrence, and deposition. That is what the present research is attempting to explore.

1.7 Layout of the thesis

Besides the introductory chapter, a detailed literature review on rock-slope stability is discussed in chapter two. The chapter commences with an overview of rock-slope stability and the common terms used are outlined. Analysis methods for rock-slope stability such as conventional method, limit equilibrium, and kinematic analysis are then discussed. A great deal of reviewing the literature on Finite Element Methods is documented while their shortcomings in geotechnical applications are identified. This is followed by a review of remote sensing techniques and ASTER images as well as their use in investigating geotechnical problems. Next, previous studies of slope stability problems along the Thulamela municipality roads are reviewed. Finally, the chapter concludes by identifying the knowledge gap being the object of this doctoral research. The gap is summarised as the lack of a theoretical framework descriptive of rock slope stability in extremely rainy areas.

Chapter three outlines the research methodologies followed in this thesis. Field observation and measurement are done are presented. Laboratory tests of soil and rock samples collected on-site are also discussed. A detailed description of the methodology followed in collecting remote sensing data for the production of ASTER images is then made. Subsequent to this, numerical experiments are presented to generate data for kinematic and limit equilibrium analysis. The simulation models were set to simulate the behavior of the slopes under investigation.

Chapter four commences with an analysis of data collected during field observations, field measurement, and laboratory analysis. Soil grading, soil classification, Atterberg's limit, mechanical properties of soil, geological mapping, and cross-section of the study area were produced as a result of the analysis.

Chapter five explores the application of kinematic analysis and limit equilibrium methods to the case study areas. Detailed kinematic analysis of slope stability is made using wedge failure analysis (wedge failure was

selected because it was the most pronounced failure in the study area). Limit equilibrium is finally used to explore the behavior of the slope through transitional analysis, toppling analysis, rotational analysis. The above analyses are supplemented with numerical tools such as SWEDGE, RocPlane, DIPs, SLIDEs, and Phase 2 for a comprehensive sense-making of the results.

The application of the remote sensing technique, the development of the FEM model, and its subsequent validation are discussed in chapter six. The software package Phase 2 is also used here to gain a better understanding of the mechanism behind slope instability. Slope stability prediction hazard charts are finally proposed for unsaturated soil slopes.

Chapter seven covers a detailed discussion of rockfall supported with DIPs simulation results to mimic field observation. Rockfall trajectory analysis is also performed using the Rockfall software. This then enabled the production of a rockfall hazard prediction chart further validated against published secondary data. Last, a statistical analysis of the historical rainfall records of the area was established to denote the duration where extreme rainfall is experienced. This was used to perform numerical simulations on the slope subjected to rainfall (see Chapter 8). The idea was to explore the effect of rainfall intensity on the slope stability of unsaturated soil. Upon, providing elements of answers to the rainfall effects, the thesis was concluded in chapter nine with the key research findings as well as the recommendations for future work.

Chapter 2   Literature review

The basics of the Particle Finite Element Method (PFEM) and its application to cases of rockfall and slope stability are reviewed in this chapter. This entails the formulation underpinning the PFEM in a Lagrangian continuum. The formulation specifically covers the governing equations, the local integration, and the mesh mapping. Cases of successful application of the method to geotechnical problems are also discussed. Although several encouraging studies exist, the development of the PFEM framework still has a long way. This is captured by highlighting the benefits and shortcomings of the PFEM framework in the study of rock slope stability.

In terms of rock slope stability, past work is reviewed to highlight some cardinal points of rock instability as well as the types of landslides. Kinematic analysis and limit equilibrium analysis are discussed as the central conventional analysis methods for slope stability. A brief on rockfall prediction methods are also outlined as well as other prediction methods. These include fuzzy mathematic methods, frequency analysis, and rock engineering systems tools.

Finally, the literature review ends with an overview of remote sensing techniques. Here, the focus is on case studies of the utilization of remote sensing techniques in evaluating slope instability. Geotechnical studies of the Thulamela Municipality are examined before a thesis is formulated for the combined use of numerical analysis and remote[1].

---

[1] A portion of the literature has been published as a review paper in the International Journal of Geotechnical Engineering under the reference: Sengani, F., and Mulenga F., (2020) A Review on the Application of Particle Finite Element Methods (PFEM) to Cases of Landslides. International Journal of Geotechnical Engineering, https://doi.org/10.1080/19386362.2020.1814027.

2.1 Introduction

The concept of rockfall is one of the oldest that has been widely documented along river banks, slope cuts, and mountain ranges (Corominas et al., 2005). Historically, rockfalls have been established as the "detachment of a rock from a steep slope along a surface on which little or no shear displacement takes place" (Cruden and Varnes, 1996). This is because the belief has been that rockmass descends very quickly by falling, bouncing, and rolling. Another school of thought believes that a clear distinction should be made between detachments and rockfalls. Selby (1982) for example considers a rockfall as a small mass movement to contrast with the detachment of an individual rock. The latter involves large-scale rockmass in the form of rockslides and rock avalanches (Cruden and Varnes, 1996).

Several scholars have restricted the use of the term rockfall based on maximum kinetic energy (Spang and Rautenstrauch, 1988). Others (e.g. Whalley, 1984) have done the same based on volumetric terms such as debris falls (< 10 m^3), boulder falls ($10 - 100$ m^3), a block falls (> 100 m^3), cliff falls ($100 - 106$ m^3) and Bergsturz (> 106 m^3). In recent studies, the terms rockfall, rockslides, and rock avalanches are often used in non-equivalent meaning with no consensus on the actual definition (Hungr et al., 1999; Chau et al., 2003; Dussauge-Peisser et al., 2002; Guzzetti et al., 2003).

Rockfalls are the most common type of slope movement that makes rock cuts along transportation corridors in mountainous regions hazardous (Parise, 2002). It is essential to understand the deformation characteristics and failure mechanism driving the instability of slopes (Yang et al., 2017; Mohammedi et al., 2014). Slope stability refers to the potential of the earth's surface material (soil and rocks) on inclined slopes to withstand or undergo movement. The strength and cohesion of the slope material as well as the amount of internal friction between materials help in maintaining the stability of the slope. Stability is determined by the angle of the slope and the strength of the constitutive material. The steepest angle that a cohesionless

slope can maintain the mass without losing its stability is referred to as its angle of repose. Slope stability also refers to the relationship between the driving and the resisting forces. The ratio of resisting forces to driving forces is known as the factor of safety of the slope. The gravitational force is evidently the main driving force acting on a slope. The gravity-induced driving force is directly proportional to the slope inclination. The existence of discontinuities in the rock leads to uneven distribution of strength and stress in all directions. Elastic properties of the rock mass are consequently altered leading to the disrupted balance of rock mass strength as well as landslides. The orientation of discontinuities is another major factor affecting rock stability and rock failure alike (Wyllie and Mah, 2004).

Rock slope failures can be classified depending on the type and degree of structural control. The most encountered rock slope failures include planar, wedge, toppling, and circular failures. The geometry of the slope, the characteristics of the potential planes of failure, surface drainage, and groundwater conditions are the main internal factors controlling rock slope stability. Rainfall, seismicity, and man-made activities, on the other hand, are external factors. The combination of these factors is responsible for the conditions of stability of a slope (Raghuvanshi, 2017).

The analysis of rock slope stability is generally performed to assess how safe and functional excavated and natural slopes are. Eberdhart (2003) argues that the analysis is aimed at assessing slope conditions, potential failure mechanisms, and slope response to external factors that can trigger failure. Moreover, the analysis can be used not only to determine the most effective options for support stabilization but also to optimally design safe, reliable, and economical excavation slopes. This analysis mostly revolves around the concept of the factor of safety.

The Factor of Safety (FoS) can be defined in three different ways: limit equilibrium, force equilibrium, and moment equilibrium (Abramson et al., 2002). The three types of FoS are illustrated in Figure 2.1. It should be noted that the factor of safety of a rock slope is usually assessed through a

detailed comparison of the calculated FoS against the acceptable FoS. Hoek (1991) argued that the acceptable standard threshold value of FoS is 1.5 for road rock slopes before failure occurs.

Limit equilibrium:

$$F = \frac{s_u}{\tau} \quad \text{(Total stress)}$$

$$F = \frac{c' + \sigma' \tan\phi'}{\tau} \quad \text{(Effective stress)}$$

Force equilibrium:

$$F = \frac{\text{Sum of resisting forces}}{\text{Sum of driving forces}}$$

$$F = \frac{S_a}{W\sin\alpha} = \frac{cL + N\tan\phi}{W\sin\alpha}$$

where,

L = total length of the sliding plane

Moment equilibrium:

$$F = \frac{\text{Sum of resisting moments}}{\text{Sum of driving moments}}$$

$$F = \frac{R\int_0^L s_u\, dl}{W.x}$$
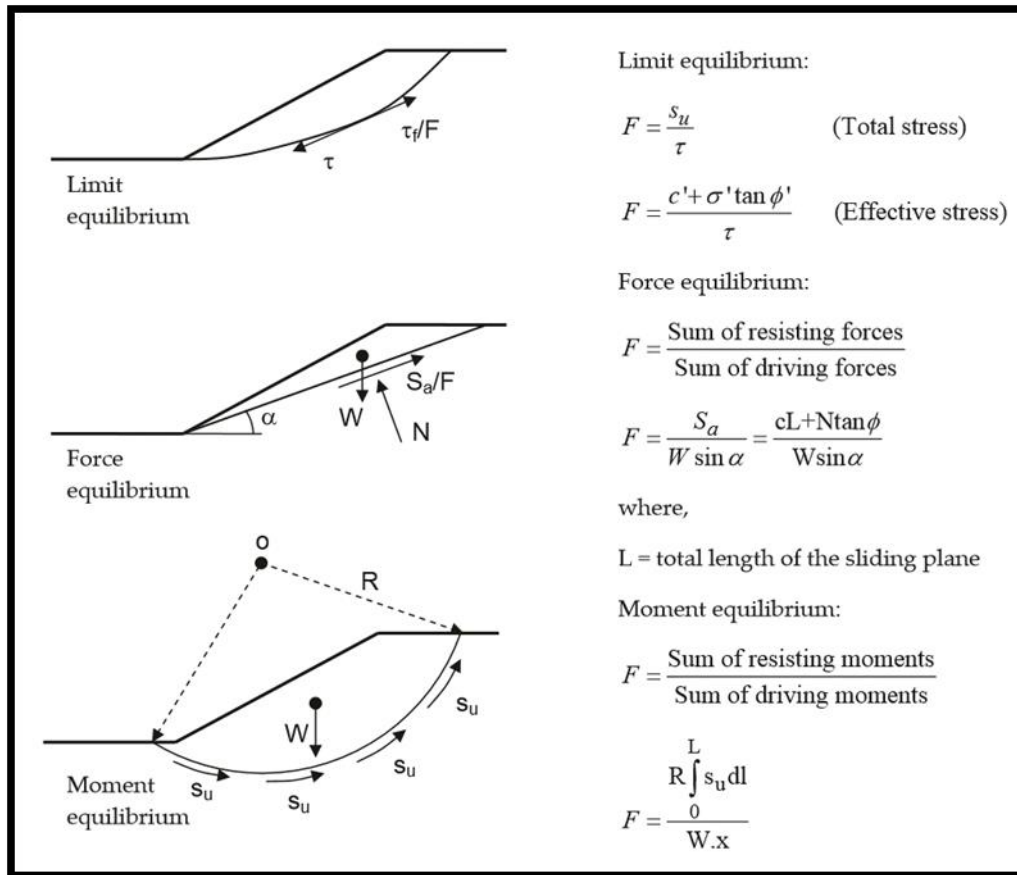
Figure 2.1 Illustration of the three classical definitions of the factor of safety FoS (Abramson et al., 2002)

Limit equilibrium methods are known to suffer from the uncertainty associated with estimated input parameters amongst others. To overcome this, probability methods are usually resorted to (Christian et al., 1992). Most of these methods replace FoS values with a probability of failure as a measure of slope stability (Oka and Wu, 1990; Scavia et al., 1990; Koukis and Ziourkas, 1991; Carter, 1992; Sah et al., 1994; Chowdhury, 1988 & 1994; Leung and Quek, 1995; Einstein, 1996). A review of landslides, rockfalls, and slope stability analysis centered on limit equilibrium methods is done in the subsequent sections.

2.2 Fundamentals of rock slope stability

Rockfall, landslides, and slope instability have caused a number of injuries and accidents worldwide (Rabie, 2013). They have incurred economic losses especially in mountainous parts of the world (Göktepe and Keskin, 2018). A major case of the landslide in which about 100 000 lives were lost has been well documented by Petley (2004). From an economic point of view, the rehabilitation of the landscape and the compensation of affected parties may amount to as much as $ 4 billion per year in Japan. Countries like the United States of America, Italy, and India have reported expenditure of the order of $ 1 – 2 billion per year (Schuster, 1996).

Factors responsible for rockfalls and landslides include landslide toe loading, urban and industrial development in areas, deforestation, and increased regional precipitation. In this section, the differentiating elements between rockfalls and landslides are highlighted. The underlying dynamics governing rockfalls and landslides are also presented. Finally, the prominent types of rockfalls and landslides are reviewed.

2.2.1 Landslides

Maerz et al. (2008) define a landslide as "the downslope movement of soil or rock material under the influence of gravity." Heavy rains, deforestation, and land use are factors that can accelerate landslides. Deforestation for instance can weaken the integrity of the topsoil and reduce slope strength leading to landslides. The most important factor contributing to landslides is arguably the slope angle (Göktepe and Keskin, 2018). The slope angle is directly proportional to the shear stress in the soil or any unconsolidated material. This means that if the slope angle increases, the shear stress within the material increases thereby initiating landslide.

Landslides are classified based on the type and speed of movement as well as the failure mechanisms involved (Collin et al., 2008). Despite how

complex they can be, landslide movements are considered to fall into three groups: flows, falls, and slides.

Flow refers to a water-soaked mass of loose soil, rock, and sediments that behaves like a viscous fluid. The characteristics of flow depending on its water content, particle size, the degree of particle sorting, the angle of the hillside slope, and the width of the flow channel. All these features make flow difficult to study; however, earthflow, mudflow, and debris flow are the main types of flow(Laing, 1991). Figure 2.2 illustrates the generic profile of an earth type of flow.
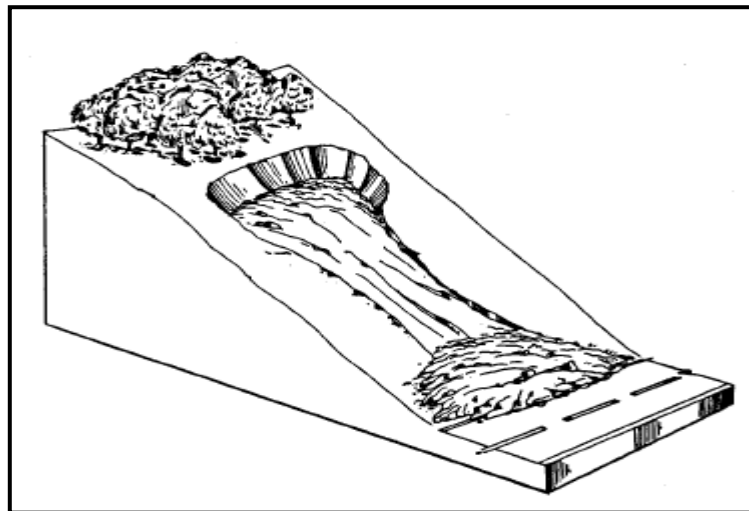
Figure 2.2 Schematic of an earthflow (Collin et al., 2008)

A fall is a type of landslide commonly associated with rocks or highly compacted soil. It usually occurs in very steep slopes that are the result of improper excavation of roads, highways, or benches. Falls tend to be short-term failure events that happen along with artificial excavations, riverbanks, and rock mass with vertical joints (Wills et al., 2008). Figure 2.3 shows schematically the occurrence of rockfalls.
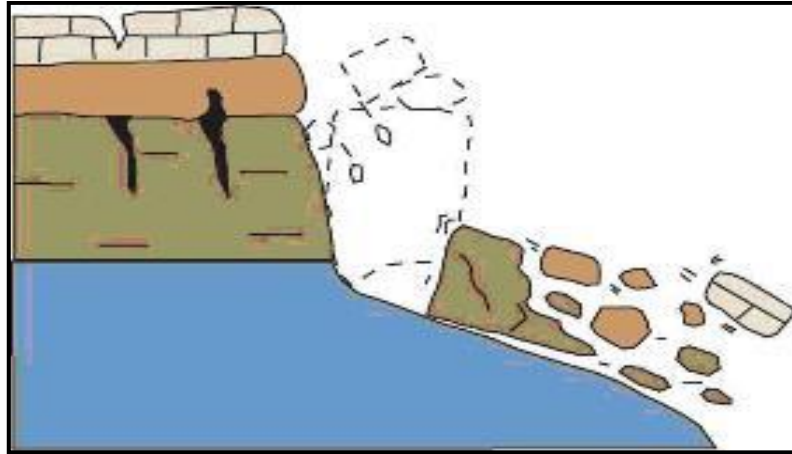
Figure 2.3 Schematic of rockfalls (Collin et al., 2008)

A slide or a slump is a downslope movement of soil or rock mass occurring in a rockmass surface experiencing intense shear strain. Three common categories of slides exist: rotational, translational, and compound (Collin et al., 2008). In most cases, slides associated with circular rotational slips occur in soft rocks. Non-circular rotational slips, on the other hand, are associated with initially compacted clay soil or intact rockmass that has been weathered. A circular rotational slide is depicted in Figure 2.4.
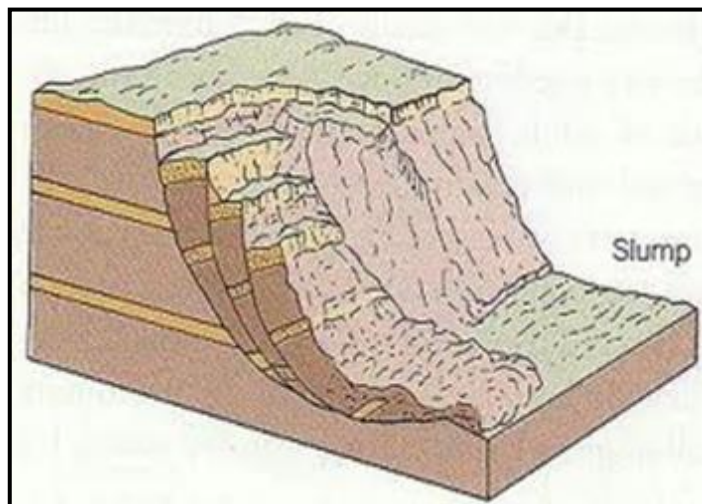
Figure 2.4 Schematic of slumps (Collin et al., 2008)

Although rockfalls are a type of landslide, their analysis necessitates special tools that may not apply to other types of landslides. This is what is discussed in the next section.

2.2.2 Rock slope failures

Rock-slope failures can be categorized into four classes: planar failures, wedge failures, toppling failures, and circular failures.

Planar failures are a type of rock slope failure in which movement occurs by sliding on a single discrete and approximately plane surface. Owing to its simple geometrical setting shown in Figure 2.5, this type of failure is generally analyzed as a two-dimensional problem (Hoek, 1991).
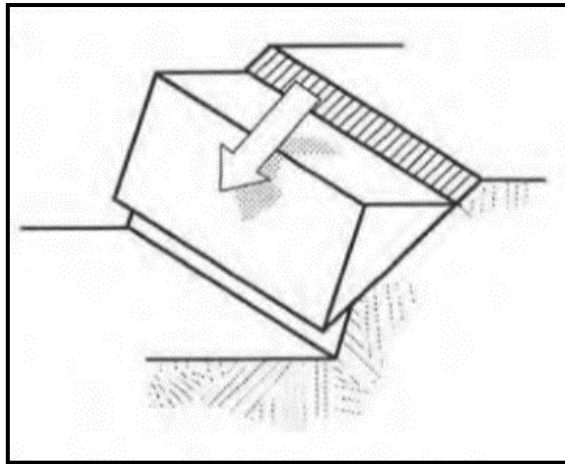
Figure 2.5 Planar rock slope failure (modified after Hoek and Bray, 1981)

The lateral extent of planar failures is generally controlled by the density of discontinuities in the rockmass (Hoek, 1991). The plane of failure is usually located at the nose of the rock slope while the lateral size of the failure can range from a few meters to several kilometers.

Rock failure can occur in the form of wedges with a portion of the rock unit dis-locked from the rockmass. Such a failure mode is known as wedge failure. Figure 2.6 illustrates a wedge failure where a block slides along two intersecting discontinuities. The discontinuities dip out of the cut slope at an oblique angle relative to the cut slope and result in the wedge block.
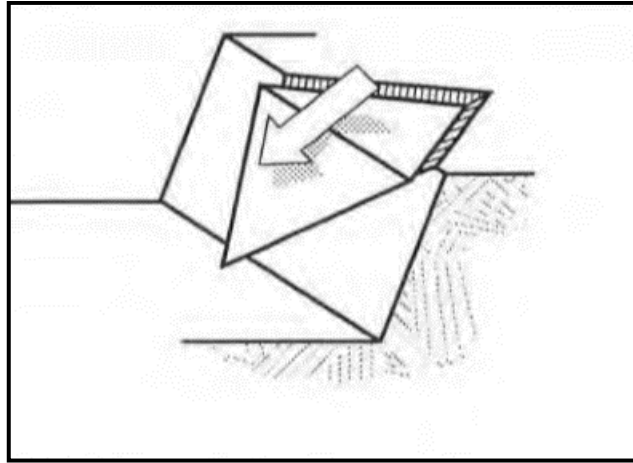
Figure 2.6 Wedge failure (modified after Hoek and Bray, 1981)

Wedge failures are normally observed in fractured and steep rock slopes. Their occurrence also depends on the strength of the material and the forces acting along the boundaries of the rock units (or blocks). Wedge failure can be continuous or regular while its size can range from a few meters to several kilometers.

Toppling failures are another type of landslide that occurs predominantly in rock masses comprised of a series of rock slabs. These slabs are formed by a fracturing network along a dip steep slope as shown in Figure 2.7.
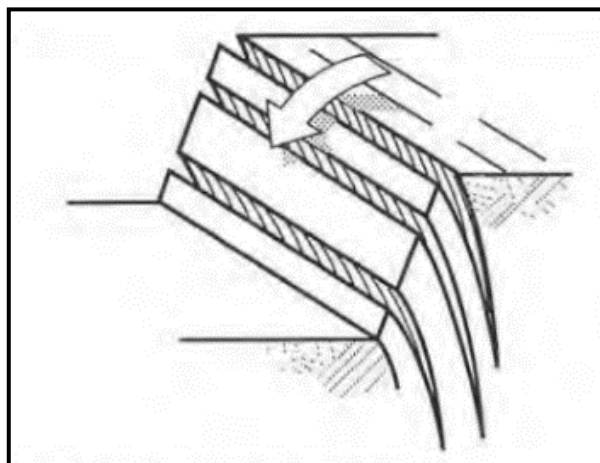
Figure 2.7 Rock toppling failure (modified after Hoek and Bray, 1981)

Rock slabs fail by rotating about an essentially fixed point or near the base of the slope while slipping takes place. Columnar basalts and sedimentary

or metamorphic rocks with well-developed bedding or foliation planes are most prone to this type of failure (Hoek and Bray, 1981).

The last type of rock failure is circular failure. Here, rock fails in a manner that is not controlled by structural discontinuities. The material slips along a surface that describes approximately the arc of a circle as exemplified in Figure 2.8. Weathered rock masses have been reported to be most likely to experience such type of rock slope failure (Hoek, 1991).
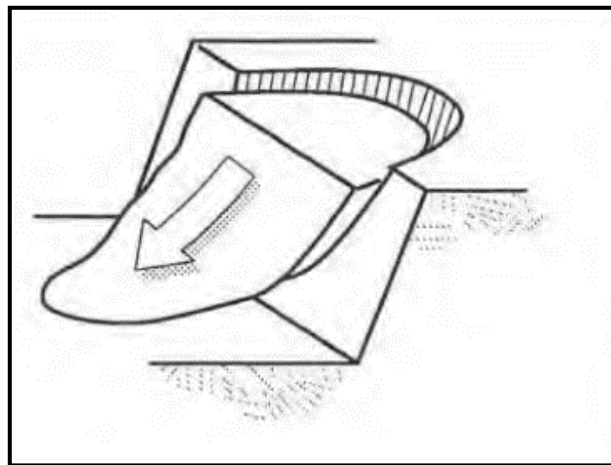
Figure 2.8 Circular rock slope failure (modified after Hoek and Bray, 1981)

2.3   Limit equilibrium analysis of rock slope stability

Historically, Limit Equilibrium Methods (LEM or LE analysis) have been extensively used to analyze landslides (Abolmasov et al., 2015; Antronico et al., 2015; Barla et al., 2010; Borrelli et al., 2014; Pilot, 1984; Yin et al., 2010). The majority of reported cases have been the toppling and rotational analyses of landslides.

Kinematic analysis is an alternative set of techniques that can also be used for the analysis of rock slope stability. The term generically refers to any empirical method dealing with landslides and rockfalls from the premise of their specific geological structures, physical properties of the material involved, groundwater regime as well as slope geometry (Michoud et al., 2012).

Kinematic analysis is commonly used to identify the translational failures that occur due to the formation of wedges or planes (Laribi et al., 2015; Simeoni and Mongiovì, 2007). Kinematic techniques can be regarded as useful tools for the simplified analysis of rock slope stability. But their relevance is limited to desktop studies beyond which limit equilibrium methods are better suited.

Limit equilibrium analysis finds relevance in the study of the complex failure of the heavily fractured and weathered rock mass. It is in this light that the analysis techniques are reviewed in this section. A note is made of numerical modeling programs built upon fundamentals of limit equilibrium analysis.

2.3.1   Toppling analysis

The appreciation of whether a rock is likely to slide or topple along a slope is generally based on a chart known as the toppling and sliding chart. Illustrated in Figure 2.9, the chart enables one to categorize slope instability as sliding, toppling, or both sliding and toppling.
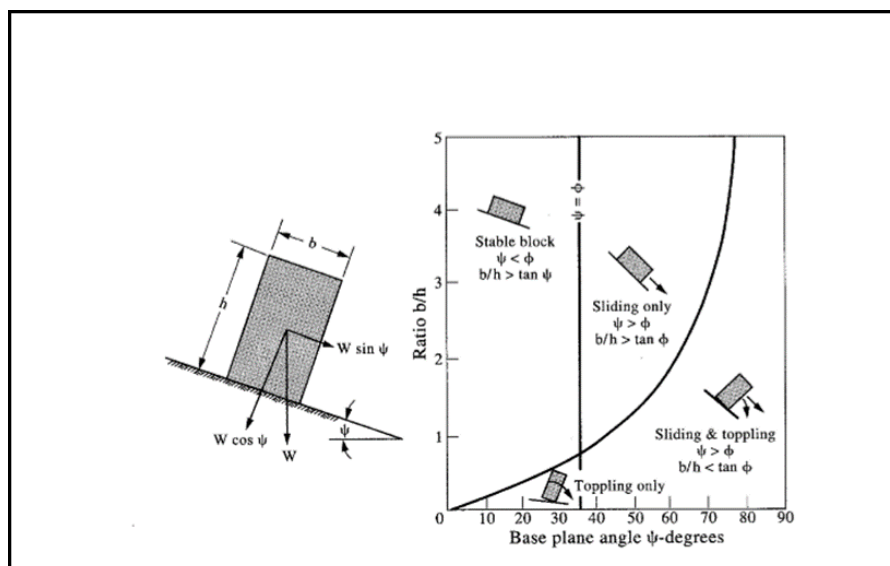
Figure 2.9 Toppling and sliding chart for instability of the solid block (after
Hoek and Bray, 1991)

Hoek and Bray (1991) who developed the chart argued that direct toppling occurs when the center of gravity of the discrete rock mass lies outside of the overall base of the block. The conventional approach to rock toppling and sliding is based on the above premises.
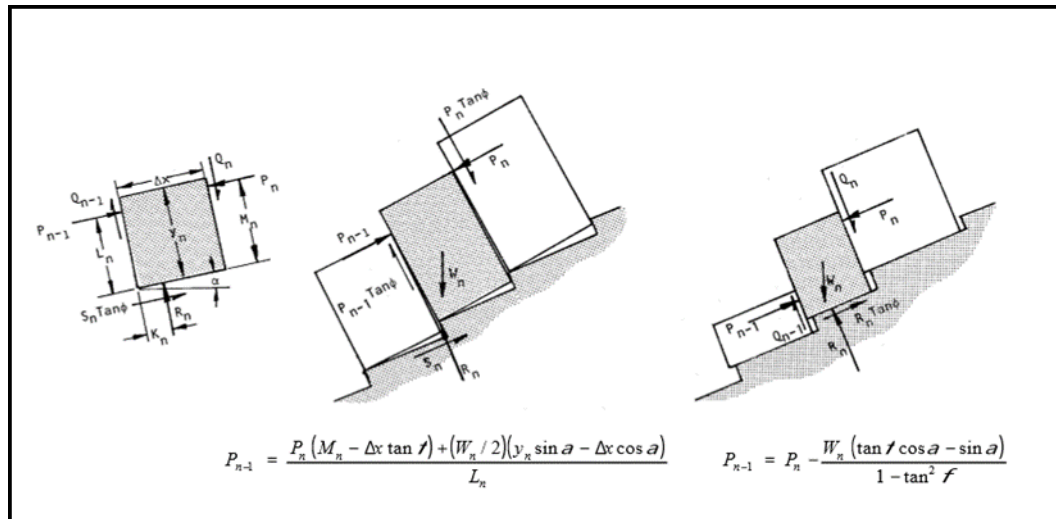
Figure 2.10 Limit equilibrium conditions for toppling and sliding with a number of variables established in the diagram (after Hoek and Bray, 1991)

The basic criterion by Hoek and Bray (1991) can be further elaborated upon in the case of multiple blocks as shown in Figure 2.10. And despite the complexity of the system, advances in technology make it possible to study toppling and sliding using numerical modeling tools.

2.3.2   Transitional analysis

Like toppling, the transitional analysis was also introduced by Hoek and Bray (1991). The technique assumes that there is transitional sliding of a riding body along the plane of weakness as illustrated in Figure 2.11. It is crucial to indicate that all the forces pass through the centroid of the block because sliding does not experience rotation. In addition to this, it is always assumed in limit equilibrium solutions that "all points along the sliding plane(s) are on the verge of failure" (Eberhardt, 2003). This assumption

makes the problem statically determinate and allows for the smooth calculation of the Factor of Safety (FoS).

The resisting forces are governed by the shear strength of the sliding block. The driving forces, in contrast, are due to the down-slope weight component of the sliding block and water pressure along the boundaries of the block. The resisting forces and driving forces within and around a sliding block as well as the safety factors (FoS) can be seen in Figures 2.11 and 2.12.

$$SF = \frac{c'(H-z)\csc\psi_p + (W\cos\psi_p - U - V\sin\psi_p)\tan f}{V\cos\psi_p + W\sin\psi_p}$$

Where:

SF = safety factor
c' = effective cohesion
f = effective friction angle
ψ_p = dip of slide plane
W = weight of block
U = uplift force due to water pressure along slide plane
V = force due to water pressure in tension crack
H = slope height
z = tension crack depth

γ_w = unit weight of water
γ = unit weight of rock
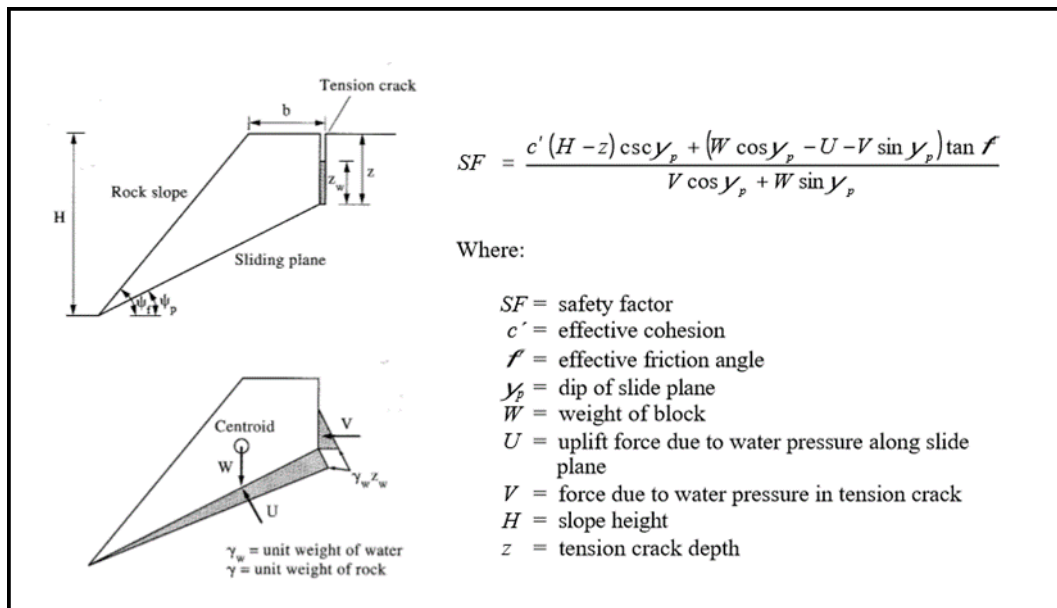
Figure 2.11 Planar failure of limit equilibrium (Hudson and Harrison 1997)
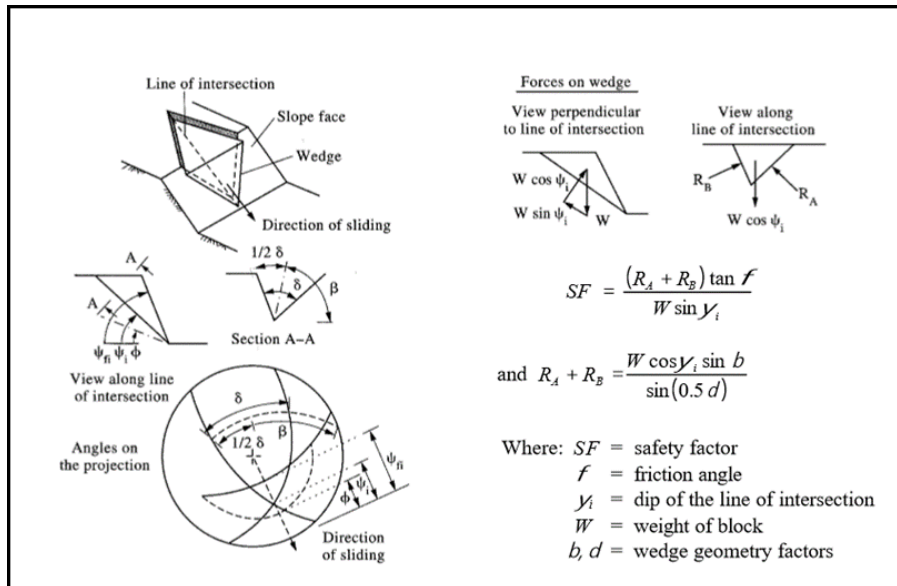
Figure 2.12 Wedge failure under dry conditions consisting of frictional strength only and using limit equilibrium solutions (after Hudson and Harrison, 1997)

The translational analysis method has been implemented in numerical simulation tools such as SWEDGE and RockPlane among others. These computer programs provide quick and interactive means to evaluate the stability of surface wedges. The computer programs also enable one to perform probabilistic analysis as well as FoS simulations. An example of computer-based analysis using SWEDGE is illustrated in Figure 2.13.
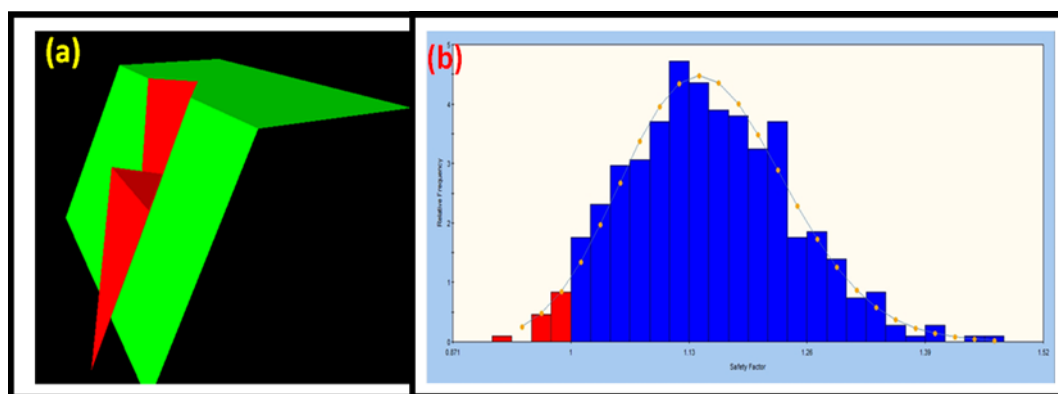
Figure 2.13 (a) Wedge simulated using SWEDGE and (b) Probabilistic limit equilibrium wedge analysis with the relative frequency defined as "the number of valid wedges formed by the Monte Carlo sampling of the input data" (Eberhardt, 2003)

2.3.3   Rotational analysis

The rotational analysis is a LE technique that differs from the transitional analysis covered earlier. This analysis technique specifically applies to circular rock slope failure.

Circular landslides usually occur within a weak rock or soil material of strengths of a magnitude similar to that of the induced stresses (Antronico et al., 2013; Grana and Tommasi, 2014; Gullà, 2014; Maiorano et al., 2015; Uzielli et al., 2015; Vaunat and Leroueil, 2002). In such cases, a simplifying assumption is made to exclude geological structures. This then leads to the production of landslides that occur along with a circular or rotational failure profile. A graphical summary of this rotational analysis is provided in Figure 2.14.
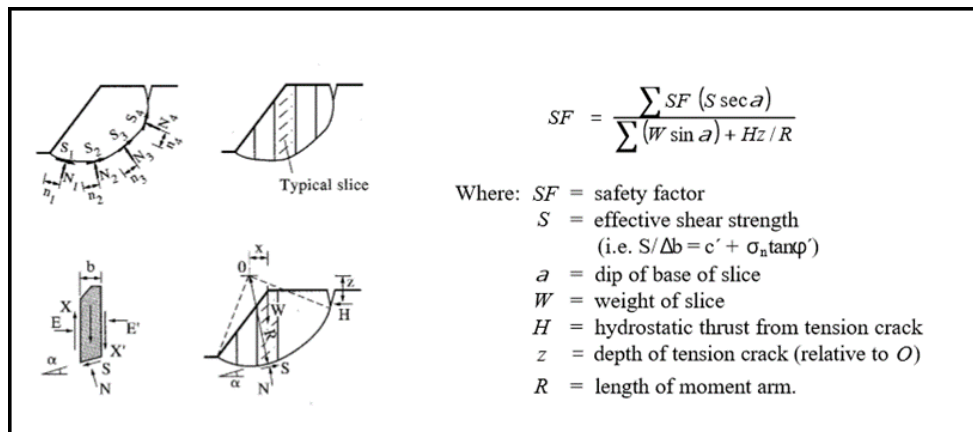
Figure 2.14 Limit equilibrium analysis of the solution of a rotational or circular failure (after Hudson and Harrison, 1997)

The two-dimensional (2D) numerical software called SLIDE is based on the rotational analysis in Figure 2.14. SLIDE finds use in the analysis of slip surfaces and the determination of safety factors along landslides involving materials of soil-like properties.

2.3.4 Note on the limit equilibrium family

The limit equilibrium (LE) family consists of several analysis methods. Fellenius (1936) introduced the first LE method which was referred to as the Ordinary or Swedish method for a circular slip surface. A few decades later, Bishop (1955) presented an advanced method built from the ordinary one. Bishop's method is basically a refined relationship for the base normal force of the sliding rock block. The method led to the development of a nonlinear equation of the safety factor (FoS). In the meantime, Janbu (1954) developed a simplified method specifically applicable to non-circular failure surfaces. Janbu's method divides the rockmass into several vertical slices as shown in Figure 2.14 and evaluates the potentials of each slice and of the rockmass to slide. Janbu (1973) later improved his method and proposed what is known as the generalized Janbu method. During this period, other LE methods were developed by several scholars such as Morgenstern-Price (1965), Spencer (1967), and Sarma (1973).

From this historical review, it is clear that LE methods are all based on certain assumptions for the interslice normal and shear forces. However, the central difference amongst the LE methods resides in how these forces are defined, determined, or assumed (Abramson et al., 2002; Krahn, 2004). For example, the ordinary method assumes that the interslice normal and shear forces are non-existent and therefore negligible. Bishop's methods, on the other hand, assume that side forces on slices are horizontal and of different magnitudes, while Janbu's simplified method considers equal magnitude for all slices. Janbu's generalized method is close to Bishop's methods with the assumption of variable forces from slice to slice. Several variants of Bishop's and Janbu's methods exist; they include Lowe-Karafiath's, the Corp of Engineers', Morgenstern-Price's, and Spencer's Method. Their details can be found in classical textbooks dealing with rock engineering (e.g. Abramson et al., 2002; Hudson and Harrison, 1997; Krahn, 2004). Suffice to say that Figure 2.15 summarises the forces at play within and around a rock slice. All the above-mentioned methods can be

reproduced by applying momentum and force equilibrium equations to each slice. Furthermore, different FoS values can be arrived at depending on how each interslice force is defined.
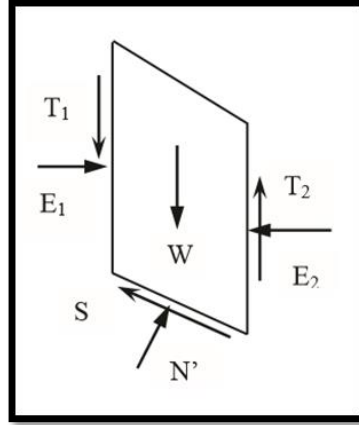
Figure 2.15 Forces considered in limit equilibrium analysis

Bishop's simplified method assumes that the absence of tangential interslice forces (i.e. $T_1 = T_2 = 0$ in Figure 2.15) while normal forces (E_1 and E_2) are applied against the slices. Following this, a force balance is performed to ensure force equilibrium and overall moment equilibrium. This leads to the following (Duncan, 1996; Abramson et al., 2002):

$$N' = \frac{1}{m_\alpha} \Sigma \left(W - \frac{c'\, l \sin \alpha}{B_f} - u\, l \cos \alpha \right) \tag{2.1}$$

Where $m_\alpha = \cos \alpha \left(1 + \tan \alpha\, \frac{\tan \emptyset'}{B_f} \right)$ $\qquad$ **(2.2)**

In Equations (2.1) and (2.2), α, c', φ', u, l and B_f represent the inclination of the slip surface in the middle of the slice, the cohesion, the friction angle, the pore pressure, the slice base length, and Bishop factors respectively.

Bishop's FoS is determined by applying several iterations to Equations (2.1) and (2.2) following the algorithm proposed by Duncan (1996). Janbu's generalized method, on the other hand, does not require any iterative process. The method considers the existence of all the forces in Figure 2.15. This enables the computation of Janbu's FoS as follows (Duncan, 1996):

$$FoS = \frac{\sum[\{C'\, l + (N - u\, l) \tan \emptyset'\} \sec \alpha]}{\sum\{W - (T_2 - T_1)\} \tan \alpha + \sum(E_2 - E_1)}$$ **(2.3)**

Perhaps the most important point to make is that Bishops' and Janbu's methods are very popular in geotechnical engineering. They are considered to yield the most accurate outputs and have been used as the basis for most numerical tools on the markets. Janbu's generalized method has the ability to handle irregular slopes and irregular failure surfaces. Bishop's simplified method, on the other hand, produces higher FoS values by approximately 5 % from Janbu's (Abramson et al., 2002). It is therefore crucial that the selection of the most appropriate analysis method be made with care based on the problem at hand.

2.4   Prediction of rockfalls

Rockfalls are widespread in mountain ranges, coastal cliffs, volcanos, riverbanks, and slope cuts. Although most take place in remote places, they also threaten residential areas and transport corridors (Chau et al., 2003; Corominas et al., 2005). Their unpredictable nature is often a cause for concern by authorities and decision-makers. Rockfalls can be of limited size but their underlying processes are extremely rapid with high kinetic energies and damaging capabilities. After an extensive study of rockfall events, Turner and Jayaprakash (2012) were able to demonstrate that small volumes of rocks may cause significant damage and traffic disruption. Petley (2012) argued that losses due to landslides and rockfalls are concentrated in countries lacking appropriate resources and research capacity. Rockfalls may be mitigated with stabilization and protection works. But more often than not, engineers have to make difficult judgments based on large uncertainties associated with the prediction of the size and frequency of the potential events.

A rockfall can be defined as the detachment of a rock from a steep slope along a surface on which little or no shear displacement takes place (Cruden

and Varnes, 1996). The main feature here is that the mass descends very rapidly through the air by falling, bouncing, and rolling. In addition to this, almost no interaction takes place between the moving fragments and the substrate (Hungr et al., 2014). Rockfalls generally refer to relatively small mass fragments or a small number of individual fragments detaching from the rock mass (Selby, 1982). In contrast, the detachment of large-scale rock masses is termed rockslide and rock avalanche (Cruden and Varnes, 1996).

The following are considered to be the main sources of rock slope failure: lithology, rockmass strength, and geological features. This is because the frequency, orientation, and spacing within the network of existing discontinuities determine the quality of the rockmass (Hoek and Bray, 1981). Rockfalls can also be triggered, to a limited extent, by the degree of weathering, cleft water pressure, and erosion (Budetta, 2004).

Conventional kinematic and limit equilibrium analysis techniques have been tested on cases of rockfalls. Success cases investigated involve simple slope geometries and basic loading conditions. However, these conventional methods can neither account for rock discontinuities nor can they provide information behind the mechanism responsible for the failure. Numerical techniques such as the traditional Lagrangian Finite Element Method are bridging the gap (Eberhardt et al., 2003 & 2004).

Finite Element Method (FEM) encompasses a set of numerical techniques used in solving problems of solid mechanics. Simply put, the solid is subdivided into several basic geometric shapes known as finite elements. Equilibrium equations are then formed and solved for the displacements at the finite number of nodes scattered across the model of the solid (Dow, 2015). The mechanical behavior of the solid is extracted from the nodal displacements based on the stress and strain field generated.

Although the FEM framework produces acceptable approximation results (Yuan et al., 2020), it cannot solve certain problems. For example, the FEM technique cannot predict the occurrence of slope failure in the form of

landslides or rockfall. Failure mechanism and landslide deposit are the other outputs that the FEM falls short on (Monforte et al., 2016 & 2018; Yuan et al., 2019a; Zhang et al., 2018a, 2019a & b). The main reason for this is that FEM is geared towards the modeling of solid continuum systems and not liquid-like systems such as landslides.

Zhang (2014) identified two major limitations of the FEM technique in terms of predicting the occurrence, failure mechanism, and deposit of landslides. The first is to do with the geometry of the rock system to be modeled. Indeed, the geometry of the material can change significantly depending on the magnitude of the internal deformations experienced. This then leads to the severe distortion of the mesh grid descriptive of the numerical model. The geometry of the frame representing the rockmass system changes to the point that numerical integration from a one-time step to the next becomes difficult. To circumvent this deficiency, the Arbitrary Eulerian-Lagrangian (ALE) method has been proposed with limited success (Nazem et al., 2006; Oliver, 2007; Nguyen, 2008). Remeshing and Interpolation Technique with Small Strain (RITSS) technique is another solution to large mesh distortion (Hu and Randolph, 1998; Tian et al., 2014; Yu et al., 2012). The key to RITSS is to re-mesh the computational rockmass domain at every incremental step while state variables such as displacement, stress, and strain are mapped from the previous mesh to the new mesh.

Owing to the previous discussion, the ALE and RITSS techniques address some limitations inherent to the FEM, cases where the original boundaries of the rockmass system change during the deformation process still yield poor prediction results (Yuan et al., 2019b; Zhang et al., 2018b).

The second limitation associated with FEM pertains to solving the underlying momentum balance and nonlinear constitutive equations. The Newton-Raphson scheme has been applied as a way to minimize the imbalance in the FEM framework with limited success. The Newton-Raphson method is an adaptive scheme that relies on the accuracy of the FEM results between computation time-steps. In cases where large

changes occur over small time steps, final output results can be of a low level of accuracy.

The two problems associated with the implementation of FEM in rock engineering are still topical. Several case studies have been reported on the finite element modeling of rockfalls and slope stability with varying success (Tian et al., 2014; Yuan et al., 2019b). Notwithstanding this, several numerical Limit Equilibrium analysis tools have been introduced to deal with rock-slope stability problems. All these tools use the Mohr-Coulomb constitutive model as a predictor of slope failure (Abramson et al., 2002).

The Mohr-Coulomb constitutive model is a set of analytical equations that establish a relationship between the shear strength of the material, on the one hand, and its cohesion, normal stress, and angle of internal friction, on the other. It can be summarised in Equation (2.4) (Rocscience, 2004):

$$f = \frac{I_1}{3}\sin\phi + \sqrt{J_2}\left[\cos\theta - \frac{1}{3}\sin\theta\sin\phi\right] - C\cos\phi \qquad (2.4)$$

Where f Factor of Safety

ϕ is the angle of internal friction of slope

C is the cohesion of the slope

$$I_1 = \sigma_1 + \sigma_2 + \sigma_3 = 3\sigma_m \qquad (2.5)$$

$$J_2 = \frac{1}{2}\left(s_x^2 + s_y^2 + s_z^2\right) + \tau_x^2 + \tau_y^2 + \tau_z^2 \qquad (2.6)$$

$$\theta = \frac{1}{3}\sin^{-1}\left[\frac{\sqrt[3]{3J_3}}{2J_2^{3/2}}\right] \qquad (2.7)$$

In Equations (2.4) and (2.5), $s_x = \sigma_x - 3\sigma_m$, $s_y = \sigma_y - 3\sigma_m$, and $s_z = \sigma_z - 3\sigma_m$ while $J_3 = s_x s_y s_z + 2\tau_{xy}\tau_{yz}\tau_{zx} - s_x\tau_{yz}^2 - s_y\tau_{xz}^2 - s_z\tau_{xy}^2$.

The Mohr-Coulomb Material model required six material properties (i.e. input parameter for the analysis): friction angle ϕ, cohesion C, dilation angle ψ, Young's modulus E, Poisson's ratio v, and unit weight of soil γ.

In a study by Goktepe and Keskin (2018), Young's modulus and Poisson's ratio were set at $E = 10^5$ kN/m^2 and $v = 0.3$ respectively. By assuming no dilation within the material, the numbers of input parameters were reduced to three: friction angle ϕ, cohesion C, and unit weight of soil γ. Upon applying the FEM framework, the two researchers noted that the FEM offers real benefits over-limit equilibrium methods in a case of slope instability. They were also able to show a good correlation between LEM and FEM results (see Table 2.1). The discrepancies were attributed to the fact that factors such as groundwater and dilation were not considered in the analysis.

Table 2.1 Slope stability analysis: compared performance of LEM and FEM methods (after Göktepe and Keskin, 2018)

Methods		FoS	
		Slope/W	Slide
LEM	Fellenius	1.275	1.161
	Bishop	1.279	1.164
	Janbu	1.246	1.125
FEM		1.115	

Despite the relative success (Göktepe and Keskin, 2018), the application of the FEM framework to the prediction of landslides still has a long way.

Other predictive methods of rock-slope stability have been documented in the literature. They include the rock mass rating (Hoek and Bronw, 1991) and the overlaying hazard maps (Ellison, 1978; Ellenberger, 1981; Seegmiller, 1983; Adoko et al., 2020). These rather empirical methods are very limited in their prediction ability as they generally fail to capture the complexity of landslides. It is because of the above that techniques such as fuzzy inference methods (Nguyen, 1985) and rock engineering system methods (Mazzocola and Hudson, 1996) have been tested.

Considering the scope of this thesis, prominent fuzzy inference or fuzzy mathematics methods are summarised in Table 2.2.

Table 2.2 Summary of fuzzy mathematics methods in use in geotechnical engineering (modified after Adoko and Wu, 2011)

Fuzzy techniques	Subcategory of fuzzy techniques	Example of applications
Basic fuzzy set / fuzzy logic and inference	None	Rock mass classification (Nguyen and Ashworth, 1985), slope stability (Kacewicz, 1987; Juan et al., 1998), sawability classification of building stones (Tutmez et al., 2007) and risk assessment for rock stability (Wang et al., 2011).
Advanced fuzzy inference systems	Mandani type systems	A new Mandani-based model to predict burden from rock geomechanical properties (Monjezi and Rezaei, 2011) and Mandani fuzzy inference model prediction of the blastability designation of rock (Azimi et al., 2010)
	Sugeno type systems	Rock engineering classification system (Jalalifar et al., 2011), rock slope stability assessment (Chen et al., 2011).
	Systems using Neural Network	Constitutive modelling of undrained response of sand mixtures (Calabar et al., 2010) and prediction of maximum charge per delay in surface mining (Alipour and Ashtiani, 2011).
	Systems using Genetic Algorithm	Slope stability (Zhang and Lin, 2006; Xue et al., 2007)
	Hybrid formulation	Soft computing techniques based model of the angle of shearing resistance of soils (Kayadelen et al., 2009)
Fuzzy probability theory	None	Slope reliability (Dodagoudar and Venkatachalam, 2000)
Fuzzy plasticity theory	None	Cyclic constitutive modeling (klisinski, 1988), rock fragmentation (Mishnaevsky and Schmauder, 1996) and soil-water hysteresis model for unsaturated sands (Min and Phan, 2010)

The next prediction methodology is what is generically known as rock engineering systems.

Rock engineering system methods were originally developed to provide a framework for the evaluation of underground designs (Hudson, 1992). The methods have since been adopted in tackling rock-slope stability problems (Mazzocola and Hudson, 1996). Common rock engineering systems in use in rock-slope stability analysis include quantitative risk analysis, rational approach, and frequency analysis (Corominas et al., 2017). A brief description of each approach is outlined below.

Quantitative Risk Analysis (QRA) is considered to be a powerful tool for the prediction of rockfall risk (Fell et al., 200). The advantage of QRA is that assumptions made in traditional methods such as the rock mass rating are explicitly accounted for here. A group of researchers (Corominas and Mavrouli, 2011; Corominas et al., 2014) has pointed out that QRA enables objective decision-making by removing the use of ambiguous terms. QRA results are easily repeatable and consistent; they also provide valuable input parameters for the cost-benefit analysis of different scenarios. Like any other technique, QRA presents limitations from a rockfall perspective (Corominas et al., 2017). Foremost is the need for prior knowledge of the probability of rock-slope failure for a range of factors. These include the expected trajectories, the fragmentation of detached blocks, and the impact of falling or rolling mass on the ground.

As an analytical method, QRA can be summarised in the mathematical expression as shown in Equation (2.8) (Corominas et al., 2014):

$$R = \sum_{M_i} P(M_i)\, P(X_j|M_i)\, P(T|X_j)\, X_{ij}\, C \qquad \text{(2.8)}$$

Where:

R is the risk due to the occurrence of a rockfall of magnitude M_i on an element at risk located at a distance X from the landslide source with an intensity j

$P(M_i)$ is the probability of occurrence of a rockfall of magnitude M_i

$P(X_j|M_i)$ is the probability of the rockfall reaching a point located at a distance X from the landslide source with an intensity j

$P(T|X_j)$ is the probability of the element being at the point X_j at the time of the rockfall occurrence

X_{ij} is the vulnerability of the element being impacted by a rockfall of magnitude i and intensity j

C is the value of the element at risk.

In developing Equation (2.8), Corominas et al. (2014) acknowledged that the rupture of the rock wall and its probability $P(M_i)$ are the most challenging to estimate for use in the QRA. That is one key reason why the rational approach and frequency analysis are suggested.

The term rational approach broadly refers to analytical tools for slope stability (Hoek and Bray, 1981) and numerical simulation tools that consider the strength of the rockmass (Eberhardt, 2008; Stead et al., 2006). Analytical tools have been touched on earlier whereas numerical tools are summarised in the next paragraphs. The latter include continuum modeling, discontinuum modeling, and hybrid modeling.

Numerical simulation tools are appropriate for the analysis of slopes with heavily jointed rockmass, intact rock, weak rocks, and solid-like material (Coggan et al., 1998; Eberhardt, 2008). Underlying models allow material to deform so that complex mechanical behaviors of the rock mass are captured. The most widely used numerical tools considered as part of the rational approach are summarised in Table 2.3 along with some of their limitations.

Table 2.3 Numerical methods of rock slope analysis (modified after Coggan et al., 1998)

Analysis method	Critical parameters	Advantages	Limitations
Continuum modelling (e.g. finite element, finite difference)	Demonstrative slope geometry; constitutive criteria include elastic, elasto-plastic, creep, Other inputs parameters include groundwater characteristics; shear strength of surfaces; in-situ stress state.	Deformation and failure of the material can be simulated with the Factor Safety concept included. Complex behaviour and mechanism of the rockmass can be model, with 3D view capabilities. The processing or run time is reasonable, while the effect of pore pressure, creep deformation and dynamic loading can be computed.	The codes suffer from the boundary effects, it presents meshing errors, hardware memory is required and time restrictions of the simulation. The model requires training and experience in using the code. The input data are generally poor, due to requiring input data that are not routinely measured. The models are limited when simulating heavy jointed rockmass and difficulties in analysing sensitivity due to run time.
Discontinuum modelling (e.g. discrete element)	Demonstrative slope geometry; constitutive criteria includes elastic, elasto-plastic, creep. Other inputs parameters include groundwater characteristics; shear strength of surfaces; in-situ stress state.	The advantages of Discontinuum are similar to Continuum Modelling exposing that the Discontinuum has the ability to combine material and discontinuity behaviour coupled with hydromechanical and dynamic analysis); the effects of parameter variation on instability can be assessed.	The limitations are similar to those listed above while the effects of scale has to be taken into consideration, the discontinuity geometry has to be simulated representatively (spacing, persistence, etc.); there is always limited data on joint properties available (e.g. jkn, jks).
Hybrid modelling	Combination of input parameters of Continuum and Discontinuum models.	Intact rock fracture propagation and fragmentation of jointed are possible simulated by coupling finite-distinct element models.	High memory required when analysing complex problems and continuous calibration of the model is required.

Hungry (2016) argued that numerical models should always be based on sufficient data; otherwise, they provide misleading results. So, in the absence of sufficient validation data, an empirical method such as frequency analysis may be a viable alternative.

Frequency analysis methods resort to statistical analysis to calculate the probability of the failure based on past events (Hungr et al., 1999; Dussauge-Peisser et al., 2002; Guzzetti et al., 2003). The understanding is that phenomena such as landslides repeat themselves but occur as a natural event (Corominas and Moya, 2008). Therefore, the temporal occurrence of these events gives an opportunity to be expressed in terms of frequency, return period, or exceedance probability. Based on the above assumption, landslides and similar natural events can be described using Equation (2.9) (Corominas et al., 2017):

$$\log_{10} N(> M) = \alpha - bM \tag{2.9}$$

Where N is the cumulative number of landslides greater than magnitude M; α is a coefficient representing the measure of the level of landslide activity while b is a coefficient indicating that higher values correspond to a larger proportion of small landslides and conversely lower values correspond to a smaller proportion of small landslides.

Equation (2.9) has been successfully used in the description of debris flows (Guthrie and Evans, 2004; Hungr et al., 2008) and rockfalls (Hungr et al., 1999; Chau et al., 2003; Guzzetti et al., 2003). However, a complete inventory of the landslide is usually required to perform the frequency analysis which could be a hurdle (Hungr et al., 1999; Dussauge-Peisser et al., 2002). More sophisticated methods such as Finite Element Methods (FEM) are gaining interest in the field of geotechnical engineering. Particle Finite Element Method is a recent subset of FEM that is seeing slowly growing applications to geotechnical problems. A detailed description of the method is outlined in section 2.5.

2.5   Particle Finite Element Method

In the PFEM framework, both fluid and solid domains are modeled using the updated Lagrangian formulations. This enables one to solve issues relating to mesh distortion and liquid-like behavior (Zienkiewicz and Taylor, 2005; Monforte et al., 2017 & 2018).

In terms of computation, all variables associated with a domain are assumed to be known in their current configuration at time t. The new set of variables is then calculated for the updated configuration at a time $t + \Delta t$. All the continuum mechanics equations are solved using FEM techniques applied to each subdomain. The basic steps underpinning the PFEM are summarised below with the illustrative reference in Figure 2.16:

1. A PFEM simulation in fluid-solid-structure interaction commences with a cloud of points that defines the domain of analysis at each time step. Suppose ^nC represents that cloud at a time $t = t_n$.

2. The next step is to identify the boundaries for both fluid and solid domains so as to define the analysis domain ^nV. Some boundaries might be severely distorted during the computation as can be seen with flying subdomains in Figure 2.16. Re-entering and separation of the nodes, therefore, becomes crucial. An algorithmic framework known as α-shape method is used to solve the distortion problem (see Figure 2.17 for reference).

3. The Finite Element (FE) mesh ^nM is used to discretize the continuum domains. In most cases, an innovative mesh generation scheme based on the extended Delaunay tessellation is used and is expand on later (Idelsohn et al., 2003a, 2003b & 2004).

4. The discrete governing equations characteristic of FEM techniques are then solved to obtain the displacement of the nodes.

5. The mesh nodes are then moved to a new position ^{n+1}C where $n+1$ denotes the time $t_n + \Delta t$ in terms of the time increment size. This step is typically a consequence of the solution process of step 4.

6. The positions of the nodes are updated so as to arrive at the new cloud of points ^{n+1}C.

7. The iterative process can finally be repeated from step 1 to step 6 for the next computational cycle.
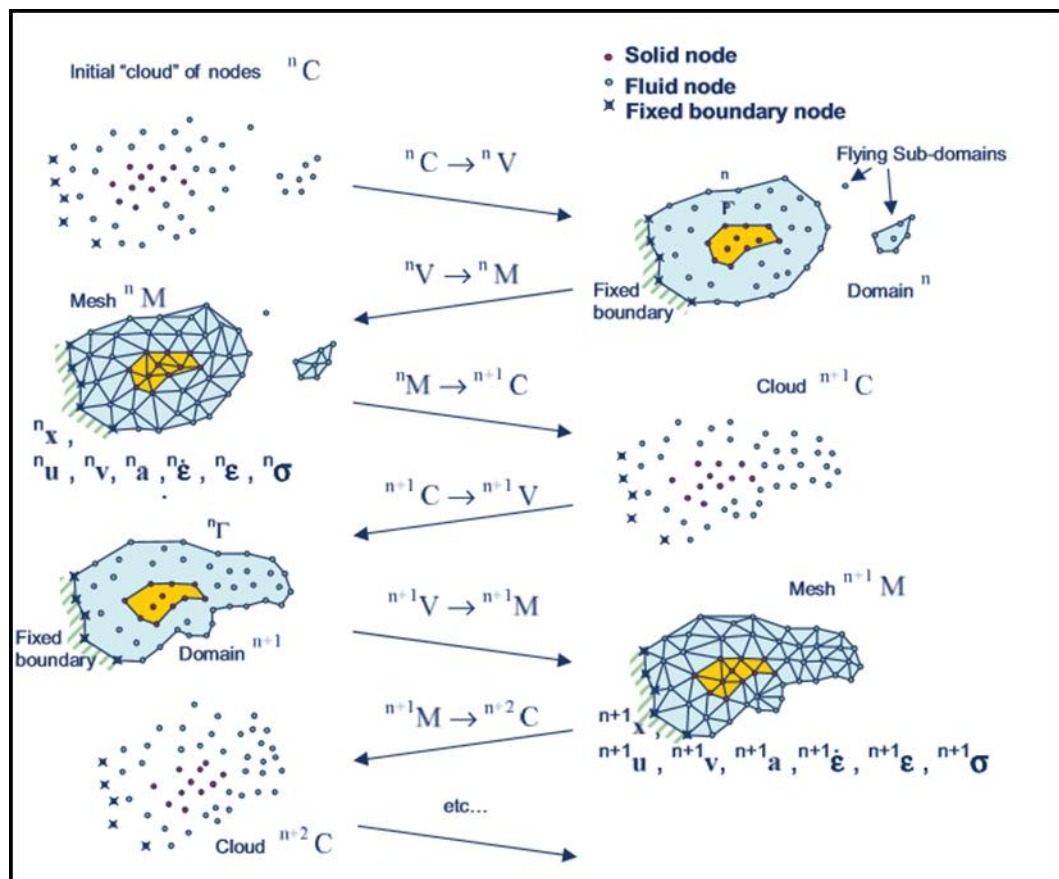
Figure 2.16 Sequence of steps between times $t = t_n$ and $t = t_n + 2\Delta t$ needed to update a cloud of nodes representing a domain containing fluid and solid fractions (after Onate et al., 2011)

The above procedure of PFEM has the advantage of treating solid and fluid simultaneously. However, solids slightly differ from fluids as their mapping of state variables and physical properties from old to new mesh is required

once re-meshing is done. The details of the implementation of the PFEM technique are presented in the subsequent sections.

2.5.1   Domain detection

One of the challenges of PFEM is the identification of the computational domain ^nV defined from the cloud of points ^nC. In most cases, there are no unique solutions for this problem; however, Idelsohn et al. (2004) have proposed a solution referred to as the alpha-shape method. The method was initially developed by Edelsbrunner and Mucke (1964) for computer graphics applications. It has been subsequently adopted in PFEM for the identification of computational domains.

The basic principle of the alpha-shape method is as follows: A cloud of points is considered with a characteristic spacing h. Then, for some predefined value of a parameter α (alpha), all nodes on an empty sphere with a radius greater than αh are considered boundary nodes. Simply put, for each point in the domain, one can examine if it is possible to place a sphere of radius αh such that it contains only that point. If possible, the point is a boundary point and if not, it is an internal point. Figure 2.17 shows an example of boundary detection using the alpha-shape method.
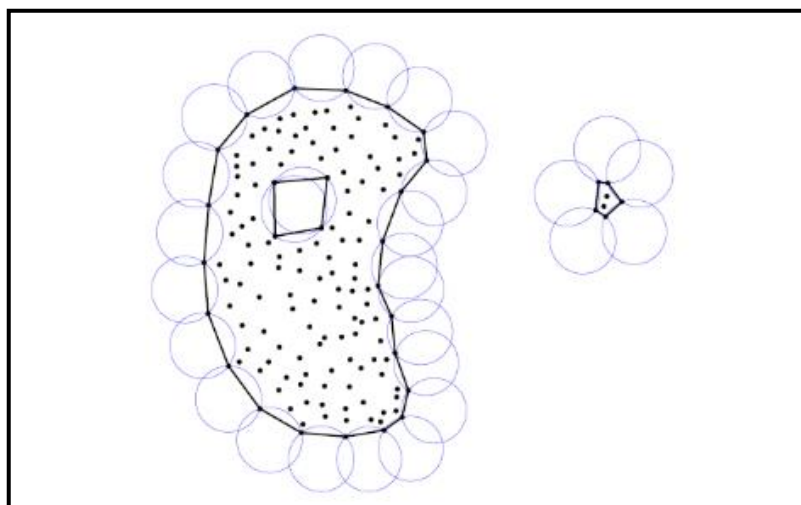
Figure 2.17 Alpha-shape methods (after Cremonesi et al., 2014)

Although the technique in Figure 2.17 is simple and straightforward, the quality of the identified domain is controlled by the appropriate choice of the value of the parameter α. Note that the optimal value of α is problem-dependent as shown in Figure 2.18, but the range of possible values is rather limited from 1.3 to 1.6 (Zhang, 2014).
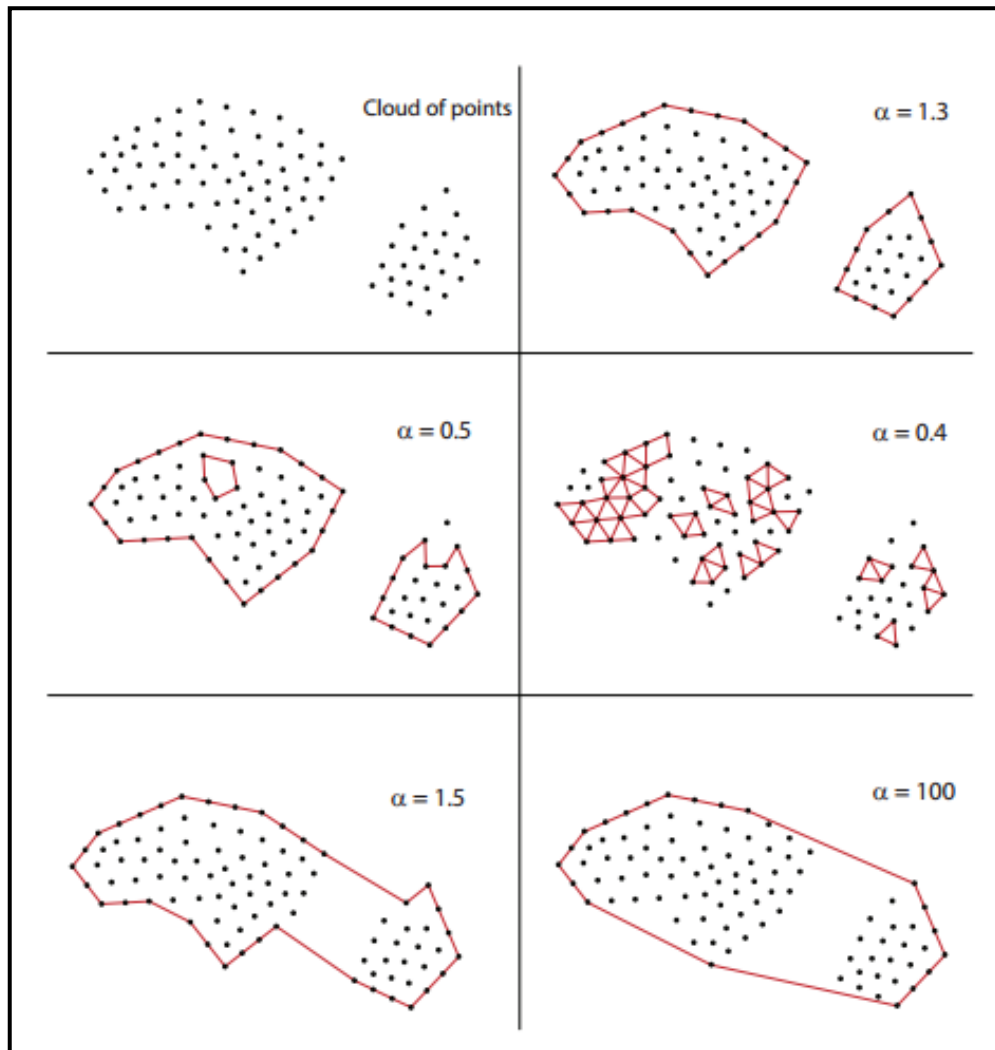
Figure 2.18 Dependency of the definition of the computational domain with the value of alpha (Zhang, 2014)

From Figure 2.18, a value of $\alpha = 1.3$ produces a set of boundaries that in many cases is considered reasonable. Any value of $0.9 \leq \alpha \leq 1.3$ produces this set of boundaries (Zhang, 2014). Internal voids are generated at $\alpha = 0.5$ while the external boundaries disintegrate for $\alpha = 0.4$. On the other hand, when $\alpha > 1.3$, the two initially distinct sets of points coalesce (see $\alpha = 1.5$).

Larger values of α generate a solid defined by the convex hull inscribing the cloud of points. Figure 2.18 demonstrates that a value of α slightly greater than 1 is appropriate and produces results consistent with physical observations (Zhang, 2014).

2.5.2 Mesh generation

Extremely large deformation is expected when applying PFEM to solid systems (Zhang, 2014). Remeshing of the detected domain is therefore critical. Mesh generation for solids can be performed with the help of the open-source code *Triangle* (Shewchuk, 1996 & 2002). The computer code is a two-dimensional quality mesh generator and Delaunay Triangulator with high efficiency. Re-meshing in PFEM closely resembles RITSS discussed sections below (Hu and Randolph, 1998; Zienkiewicz and Taylor, 2000). Indeed, re-meshing is periodically applied in RITSS using triangulation, h-adaptive techniques, and mesh smoothing. However, the difference between RITSS and PFEM re-meshing lies in the details of the algorithmic implementation of the triangulation.

2.5.3 Variable mapping

The remeshing of the detected computational domain is always expected when using PFEM to solve problems. In most cases, once a new mesh is generated, the remapping of state variables from the old finite element mesh to the new one is required for an extremely large deformation situation. As outlined in Section 2.5.2, there exist a number of variable mapping methods. But, for the purpose of this research, two remapping schemes are briefly described: Inverse Distance Algorithm and Unique Element Method.

The first scheme known as the Inverse Distance Algorithm (IDA) was proposed by Shepard (1968). To illustrate the scheme, let us assume a stress state σ at a collection of old Gauss points (see black points in Figure

2.19a). The stress state at the new Gauss point x (see the cross in Figure 2.19) can be estimated by using the stress states at its neighboring old Gauss points (see blue points in Figure 2.19b) as follows:

$$\sigma(x) = \frac{\sum w_i\,\sigma_i}{\sum w_i} \tag{2.10}$$

Where σ_i is the stresses at the i-th neighboring Gauss point, and w_i is its weighting function defined as:

$$w_i = d_i^{-c} \tag{2.11}$$

In Equation (2.11), d_i is the distance between the i-th neighboring Gauss point and the new Gauss point while c is a constant parameter usually between 2 and 4 with a recommended default value of 3.5 (Gadala et al., 1983; Cheng and Kikuchi, 1986).
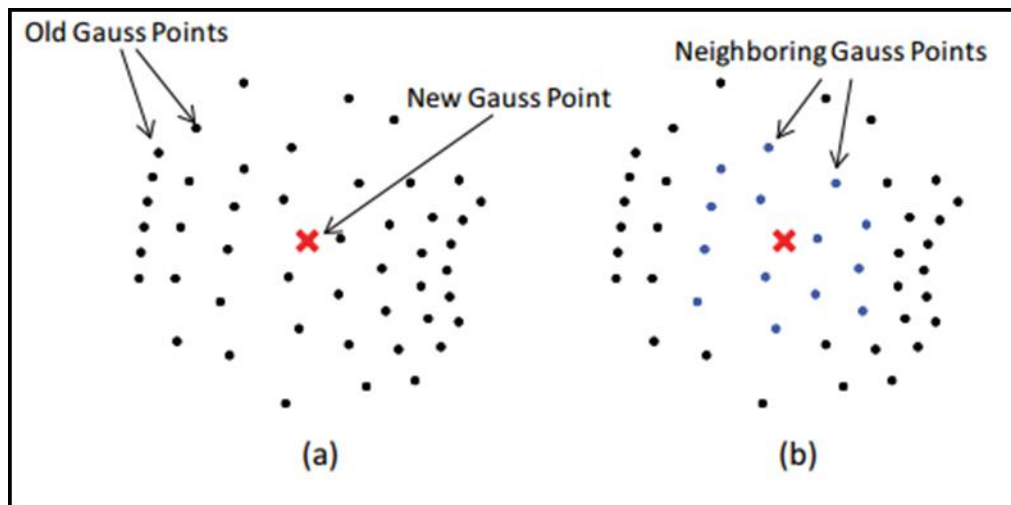
Figure 2.19 Illustration of the variable mapping by Inverse Distance Algorithm (modified after Zhang, 2014)

The second remapping scheme is the Unique Element Method (UEM) popularised by Hu and Randolph (1998). The UEM scheme is purported to be more stable than the IDA (Hu and Randolph, 1998; Zhang, 2014).

The UEM scheme hinges on the use of a six-node triangular element. The transfer of stresses from the old to the new Gauss points involves a few

steps. First, the old finite element mesh in which the new Gauss point is located (see an orange cross in Figure 2.20a) has to be identified. For that, the stress at the new Gauss point is interpolated or extrapolated using the stresses at the old Gauss points of the identified old finite element mesh (see red crosses in Figure 2.20b). This is done with the understanding that stress varies linearly within the six-node triangular element (Zhang, 2014).
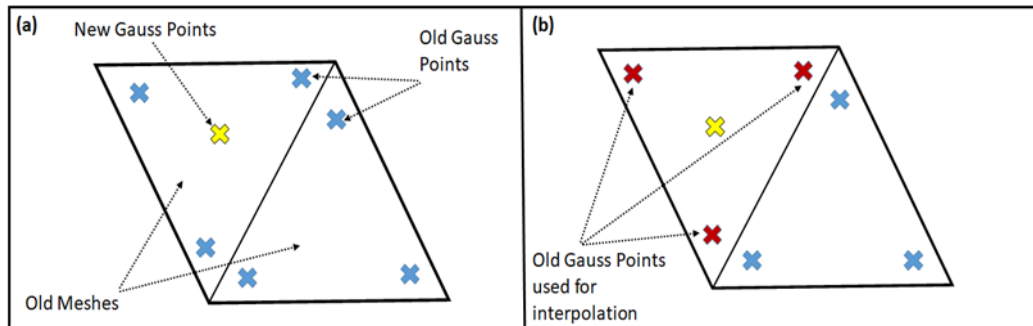
Figure 2.20 Illustration of the variable mapping by Unique Element Method (modified after Zhang, 2014)

2.5.4   Mathematical formulation of the framework

The mathematical formulation of the PFEM framework followed in this section includes the lagrangian continuum in PFEM, governing equation, local integration, contact discretization, and mesh mapping. All the above-mentioned items are fully described in the subsections below.

2.5.4.1 Lagrangian continuum in PFEM

Recall that PFEM is a numerical modeling paradigm that resorts to the Lagrangian formulation of particulate systems for its resolution. Basically, PFEM is a combination of finite element and meshless finite element methods that has witnessed much development (Aubry et al., 2004; Idelsohn et al., 2003a, 2003b & 2004; Onate et al., 2003 & 2004).

Originally, the PFEM was employed as a method for solving systems involving solid particles interacting with fluids (Idelsohn et al., 2003 & 2004; Onate et al., 2004; Zhang, 2014). The popularity of PFEM in the fluid dynamics community stems from its ability to handle mesh distortion, free fluid surfaces, fluid-solid interactions, and multi-fluid flows breaking waves to name but a few (Idelsohn et al., 2003 & 2004; Onate et al., 2004, 2008, 2011a & 2011b; Zhang, 2014). However, PFEM has received little attention in geotechnical engineering yet the formulation might not differ from fluid mechanics. A critical review of the underlying governing and constitutive equations is covered in the subsequent sections. The derived framework generally referred to as the Geotechnical Particle Finite Element Method (or G-PFEM) in the geotechnical fraternity is also discussed as well as local integrations, contact discretization, and mapping.

2.5.4.2 Governing equations

Governing equations defining the mathematical implementation of the FEM model of a solid system are encapsulated in Equations (2.12 − 2.16). Assuming an infinitesimal deformation is to be simulated, the equations can be expressed as follows (Zienkiewicz et al., 2005)

$$\varepsilon = \nabla u \tag{2.12}$$

Where $u = \begin{bmatrix} u_x & u_y & u_z \end{bmatrix}^T$ are the displacements while the strains ε are given by

$$\varepsilon = \begin{bmatrix} \varepsilon_x \\ \varepsilon_y \\ \varepsilon_z \\ 2\,\varepsilon_{xy} \\ 2\,\varepsilon_{yz} \\ 2\,\varepsilon_{zx} \end{bmatrix} = \begin{bmatrix} \dfrac{\partial u_x}{\partial x} \\[4pt] \dfrac{\partial u_y}{\partial y} \\[4pt] \dfrac{\partial u_z}{\partial z} \\[4pt] \dfrac{\partial u_x}{\partial y} + \dfrac{\partial u_y}{\partial x} \\[4pt] \dfrac{\partial u_y}{\partial z} + \dfrac{\partial u_z}{\partial y} \\[4pt] \dfrac{\partial u_z}{\partial x} + \dfrac{\partial u_x}{\partial z} \end{bmatrix} \tag{2.13}$$

In Equations (2.12), the term ∇ is the usual linear strain-displacement operator taking the following form

$$\nabla = \begin{bmatrix} \frac{\partial}{\partial x} & 0 & 0 \\ 0 & \frac{\partial}{\partial y} & 0 \\ 0 & 0 & \frac{\partial}{\partial z} \\ \frac{\partial}{\partial x} & \frac{\partial}{\partial y} & 0 \\ 0 & \frac{\partial}{\partial y} & \frac{\partial}{\partial z} \\ \frac{\partial}{\partial x} & 0 & \frac{\partial}{\partial z} \end{bmatrix} \qquad \textbf{(2.14)}$$

The general three-dimensional differential equations of equilibrium are given by

$$\nabla^T \sigma + b = 0, \text{ in V} \qquad \textbf{(2.15)}$$

Where $\sigma = [\sigma_x \quad \sigma_y \quad \sigma_z \quad \sigma_{xy} \quad \sigma_{yz} \quad \sigma_{zx}]^T$ are the stresses, $b = [b_x \quad b_y \quad b_z]^T$ are the body forces stemming for example from self-weight, and V is the domain under consideration.

The implementation of Equations (2.12 – 2.15) is generally prone to numerical instability known as volumetric locking. To address this, Zienkiewicz and Taylor (2000) expressed the governing equations with a mixed displacement and mean pressure formulation. This enabled the split of the Cauchy stress into the deviatoric and volumetric tensors as shown by Equation (2.16):

$$\begin{cases} \nabla \cdot \sigma^d + \nabla p + b = 0 \\ p - \frac{1}{3}\,tr(\sigma) = 0 \\ \mu(u) = 0 \end{cases} \qquad \textbf{(2.16)}$$

Where $\boldsymbol{\sigma^d}$ is the deviatoric part of the Cauchy stress tensor; p is the Cauchy mean pressure; u represents solid displacement; and μ stands for the initial and boundary conditions with respect to fixed displacements and prescribed tractions.

The resolution of Equation (2.16) using the same PFEM procedure in Figure 2.21 leads to reduced volumetric locking. And despite the heavy numerical requirement, integration using the pressure Laplacian technique or the polynomial pressure projection suppress the problem (Zienkiewicz and Taylor, 2000; Dohrmann and Bochev, 2004; Bochev et al., 2006; Preisig and Prévost, 2011).

Zhang (2014) approached the mathematical formulation of the PFEM framework by considering the boundary conditions. He was then able to argue that the boundary conditions used in the PFEM can be either of essential (geometric) or natural (traction) type. He applied several compatibility conditions to the model (Zienkiewicz and Taylor, 2000; Dohrmann and Bochev, 2004; Bochev et al., 2006; Preisig and Prévost, 2011) and eventually expressed the boundary conditions as shown in Equation (2.17):

$$N\sigma = t, on\ S \tag{2.17}$$

where S is the boundary; t is the given tractions, and

$$N = \begin{bmatrix} n_x & 0 & 0 & n_y & 0 & n_z \\ 0 & n_y & 0 & n_x & n_z & 0 \\ 0 & 0 & n_z & 0 & n_y & n_x \end{bmatrix} \tag{2.18}$$

To sum up, the governing equations underpinning the PFEM can be represented by Equation (2.17). However, the latter equation does not lend itself to mitigation against the volumetric locking problems associated with the Particle Finite Element Method.

2.5.4.3 Constitutive equations

Constitutive equations of the material (solid or liquid) provide a relationship between stress and strain under different conditions. There is still a lack of consensus in terms of the most suitable constitutive equations for geotechnical problems. Suffice to say that Simo and Hughes (2006)

identified two prominent schools of thought in the description of large elasto-plastic deformations. The first approach is based on an additive decomposition of the plastic and elastic strains as well as the use of hypoelastic rate constitutive models. Geotechnical problems are very complex and mostly associated with a rigid material (Nazem et al., 2006). Therefore, this approach extends the usual small strain formulations by incorporating additional terms to deal with geotechnical problems. By contrast, the second approach assumes the multiplicative decomposition of the deformation gradient and hyperelastic behavior. Most studies recommended the second approach as appropriate for geotechnical applications (Bathe, 2006; Nazem et al., 2006; Simo and Hughes, 2006; Monforte et al., 2017).

This brings us to talk about the next topic, that is, the mathematical formulation of the constitutive equations. In the first approach, additive decomposition of the strain tensor is assumed. In doing so, the characteristic of the material is represented by the existence of yield criterion that effectively limits the magnitude of the stresses as shown in Equation (2.18):

$$F(\sigma) \leq 0 \tag{2.18}$$

Where F is the yield function; it should be noted that $F(\sigma) < 0$ corresponds to stress states within the elastic domain while $F(\sigma) = 0$ corresponds to yield, that is, the current stress point is on the yield surface.

The strain tensor or total strain ε can now be decomposed into elastic and plastic components denoted ε^e and ε^p respectively as shown in Equation (2.19):

$$\varepsilon = \varepsilon^e + \varepsilon^p \tag{2.19}$$

In order to obtain the relation between stress and strain, geotechnical materials are usually assumed to be isotropic with the linear elastic property. This can be expressed mathematically as shown in Equation (2.20):

$$\varepsilon^e = \mathbb{C}\sigma \qquad \qquad \textbf{(2.20)}$$

Where σ is stress and $\mathbb{C}$ is the elastic compliance modulus.

Most geotechnical problems are strongly related to events that take place as time progress. As such, it makes sense to express Equation (2.20) in terms of time-dependent rates as shown in Equation (2.21):

$$\dot{\varepsilon}^e = \mathbb{C}\dot{\sigma} \qquad \qquad \textbf{(2.21)}$$

where the superposed dot indicates differentiation with respect to pseudo-time.

In order to obtain the plastic strain rate, the plastic strain is assumed to be derivable from the plastic potential G so that the plastic strain is given by Equation (2.22):

$$\dot{\varepsilon}^p = \dot{\lambda}\nabla\sigma\mathrm{G}(\sigma) \qquad \qquad \textbf{(2.22)}$$

where $\dot{\lambda}$ is the plastic multiplier that satisfies the complementarity conditions as shown in Equation (2.23):

$$\dot{\lambda}\,F(\sigma) = 0, \dot{\lambda} \geq 0 \qquad \qquad \textbf{(2.23)}$$

The parameter $\dot{\lambda} \geq 0$ in Equation (2.23) is a nonnegative function called the consistency parameter. It is assumed to obey the following Kuhn-Tucker complementarity conditions, this can be expressed by Equation (2.24) as follows:

$$\begin{cases} F(\sigma) \leq 0 \\ \dot{\varepsilon} = \mathbb{C}\dot{\sigma} + \lambda\dot{\nabla}\sigma\mathrm{G}(\sigma) \\ \dot{\lambda}\,F(\sigma) = 0, \dot{\lambda} \geq 0 \end{cases} \qquad \qquad \textbf{(2.24)}$$

Equation (2.24) represents the constitutive equations based on the additive decomposition into elastic and plastic strains.

The second approach involves the application of multiplicative decomposition to the deformation gradient with hyperelastic behavior assumed. The following is a chronological summary of its development: the

approach goes back to the work conducted by Taylor (1938), then, expanded by Hill (1966), Hill and Rice (1972), Asaro and Rice (1977), and later Asaro (1979).

The most important feature defining the multiplicative approach is the introduction of an intermediate local configuration relative to which the elastic response of the material is characterized. The multiplicative decomposition has been widely reported on (Lee and Liu, 1967; Lee, 1969; Kroner and Teodosiu, 1972; Mandel, 1964 & 1974; Kratochvil, 1973; Sidoroff, 1974; Nemat-Nasser, 1982; Agah-Tehrani et al., 1986; Lubliner, 1984 & 1986; Simo and Ortiz, 1985; Simo, 1988). And from a phenomenological standpoint, the total decomposition gradient F is split into the elastic and plastic components. Elastic refers to reversible deformation while plastic applies to an intermediate configuration of an irreversible deformation. The multiplicative decomposition can now be expressed by Equation (2.25) (Monforte et al., 2018):

$$F = \frac{\partial \varphi(X,t)}{\partial X} \equiv F^e . F^p \qquad (2.25)$$

Where F^e is the pure elastic loading and F^p is pure plastic deformation.

The elastic deformation can be decomposed into volumetric and deviatoric parts multiplicatively as follows: $F^e = F_v^e \cdot \overline{F^e}$. The volumetric component is then given by $F_v^e = J^{e\left(\frac{1}{3}\right)}\mathbb{1}$ while the deviatoric one is $\overline{F^e} = F^e \cdot (F_v^e)^{-1}$ with $J^e = \det(F^e)$ being the elastic Jacobian.

By assuming elastic deformation to be hyperelastic with uncoupled volumetric and deviatoric responses, can be written by the following Equation (2.26)(Monforte et al., 2018):

$$\tau = 2b^e \frac{W(b^e)}{\partial b^e} = \tau(b^e) = JP(J^e) + s\overline{(b^e)} \qquad (2.26)$$

Where τ is the Kirchhoff stress tensor related to the Cauchy stress through $\tau = J\sigma$ while $J = \det(F)$ is the determinant of the deformation gradient; W is the stored energy function; and b^e is the elastic left Cauchy Green tensor.

The latter is the volumetric state denoted by $b^e = F^e \cdot F^{eT}$ with its deviatoric component given by $\overline{b^e} = \overline{F^e} \cdot \overline{F^{eT}}$.

The plastic term of the decomposition gradient (Equation 2.27) will require the specification of the yield criterion (f), a hardening law (h), and a flow rule (g) as well the addition of the Kuhn-Tucker conditions and is expressed by Equation (2.27) (Simo, 1998):

$$\begin{cases} f(\tau, q) \leq 0 \\ q = h(F^p \cdot F^{pT}) \\ l^p = \dot{\gamma} \frac{\partial g(\tau, q)}{\partial \tau} \end{cases} \tag{2.27}$$

Where $f(\tau, q)$ is the yield surface; h represents the hardening parameters; g is the plastic potential; $\dot{\gamma}$ is the plastic multiplier; and l^p is the plastic velocity gradient.

For elastic and perfectly plastic analyses, the hyperelastic model can be expressed by Equations (2.28 and 2.29) (Monforte et al., 2018):

$$p = \frac{2G(1+v)}{3(1-2v)} \frac{\ln J^e}{J} \tag{2.28}$$

$$S = 2G \frac{\ln \overline{b^e}}{2} \tag{2.29}$$

Where G and v are the shear and Poisson moduli.

For isochoric plastic deformation, the elastic and total volumetric strains can be expressed as follows $J = J^e J^p = J^e$ while $J^p = 1$. This reduced the perfect plastic case to a model with a smoothed Tresca yield surface given below in Equation (2.30) (Monforte et al., 2018):

$$\begin{cases} f(\tau, q) = J_2 \cos(\theta) - S_u \leq 0 \\ q = 0 \\ g = f \end{cases} \tag{2.30}$$

Where J_2 is the second invariant; θ is the Lodes Angle of the Kirchhoff stress; and S_u is the undrained shear strength.

In summary, the two approaches presented above constitute the constitutive equations underpinning the G-PFEM. The second approach is deemed to be the most appropriate for geotechnical problems. Solving equations emanating from either approach is covered in section 2.5.5.

2.5.5 Local integrations

The accuracy of the finite element analysis depends on the local integration scheme of the constitutive equations (Monforte et al., 2017 & 2018). Simo (1998) has indicated that the algorithm is mostly implicit in time when dealing with multiplicative strain decomposition formulations, resulting in the re-mapping algorithms. This has since been explored in several studies. Perez-Foguet and Armero (2002) for instance pointed out the lack of numerical convergence when dealing with implicit methods. This may be ascribed to the fact that implicit methods depend on the second-order convergence of the constitutive equations (Rouainia and Wood, 2006). To solve the problem, an explicit integration scheme should be implemented for multiplicative finite strains of elasto-plasticity instead. The explicit scheme is based on the assumption that an exponential function should be used to approximate variations of the plastic deformation gradient (Simo, 1998; Monforte et al, 2017 & 2018). This is expressed by Equation (2.31) as follows:

$$F_{n+1}^p = \exp\left(\Delta t \overline{L_n^P}\right).F_n^P \tag{2.31}$$

Substitution of Equation (2.31) into Equation (2.25) yields the following expression by Equations (2.32 and 2.33):

$$F_{n+1} = F_{n+1}^e.\exp\left(\Delta t (F_n^e)^{-1}.l_n^p.F_n^e\right).F_n^p \tag{2.32}$$

$$F_{n+1} = F_{n+1}^e.(F_n^e)^{-1}.exp\left(\Delta\gamma \frac{\partial g(\tau,q)}{\partial t}\right).F_n \tag{2.33}$$

The elastic Left Cauchy Green tensor from Equation (2.34) becomes:

$$b_{n+1}^e = F_{n+1}.F_n^{-1}.exp\left(-\Delta\gamma\frac{\partial g(\tau,q)}{\partial t}\right).b_n^e.exp\left(-\Delta\gamma\frac{\partial g(\tau,q)}{\partial t}\right).F_n^{-T}F_{n+1}^T \qquad \textbf{(2.34)}$$

In summary, from Equation (2.34), one can define the new elastic configuration, the new stress state, and the new deformation gradient at step $n+1$. The definition of step $n+1$ is based on the previous configuration n. Finally, note that the explicit stress integration scheme can be implemented by means of adaptive sub-stepping (Sloan et al., 2001).

2.5.6   Contact discretization

G-PFEM problems generally involve the analysis of contacts between a rigid object/material and a deformable soil. Wriggers (1995) was able to show that the penalty method could be used to model the contacts. The penalty method is summarised below in the form of the linear momentum balance equation as shown by Equation (2.35) (Wriggers, 1995; Monforte et al., 2017 & 2018):

$$C_c = \int_{\Gamma_c} \boldsymbol{\omega}.(\sigma_n\boldsymbol{n} + t)dy \qquad \textbf{(2.35)}$$

Where Γ_c is the part of the boundary in contact, σ_n is the normal total contact stresses, $\boldsymbol{n}$ is the outwards and t is the tangential contact stress. Furthermore, the total normal contact stress is given by Equation (2.36):

$$\sigma_n = \epsilon g_n^- \qquad \textbf{(2.36)}$$

With ϵ being the penalty parameter while g_n^- is the penetration function.

From Equation (2.36), normal stress is directly proportional to the amount of penetration of the deformable body within the rigid material. Furthermore, the tangential component of the contact condition is usually modeled using the concept of elasto-plastic analogy. This is because, in G-PFEM, stick conditions have been found to obey elastic regimes while slip conditions mimic plastic flows. This can be summarised by Equation (2.37) as follows (Monforte et al., 2018):

$$
\begin{cases}
\mathbf{g}_t = \mathbf{g}_t^e + \mathbf{g}_t^s \\
\mathbf{L}_v \mathbf{t} = \epsilon_t \mathbf{g}_t^e \\
f_s(\mathbf{t}, p_n, \mathbf{g}_v) = |\mathbf{t}| - \overline{f_s}(p_n, \mathbf{g}_v) \leq 0 \\
\dot{\mathbf{g}}_t^s = \dot{\gamma} \frac{\partial f_s}{\partial t} = \dot{\gamma} \mathbf{n}_t \\
\dot{\mathbf{g}}_v = \dot{\gamma}
\end{cases}
\tag{2.37}
$$

Where $\mathbf{g}_t$ is the tangential gap; $\mathbf{g}_t^e$ is the elastic decomposition; $\mathbf{g}_t^s$ is the plastic part of the tangential gap.; and $\mathbf{L}_v \mathbf{t}$ is the tangential contact stress.

It should be noted that the solutions to Equation (2.33) should comply with the Kuhn-Tucker conditions. In this thesis, Kuhn-Tucker conditions are the irreversible nature of plastic flow by means of loading and unloading conditions, which are usually presented by $\gamma \geq 0$, $f(\sigma, \alpha) \leq 0$, $\gamma f(\sigma, \alpha) = 0$, where $\gamma \geq 0$ is the rate at which slip takes place. When this is the case, an implicit time integration scheme can then be applied which is equivalent to a one-dimensional (1D) return mapping of the elasto-plastic constitutive equations.

2.5.7 Application of PFEM to rockfall and slope stability

We preface this section by stating that the PFEM was originally intended to solve problems of fluid mechanics. The framework is now gaining a lot of interest in geotechnical engineering. The simulation of large displacements and deformations, intermittent separation, and fusion of bodies are some of the potential applications (Monforte et al., 2018). However, there are limited known cases that describe the performance and application of this framework. Hereafter is a non-exhaustive list of work that pioneered the use of the PFEM in geotechnical engineering: Carbonell et al. (2010 & 2013), Zhang (2014); Zhang et al. (2017 – 2019), Salazar et al. (2016), Monforte et al. (2017 & 2018), Wang et al. (2019).

It should be highlighted that Carbonell et al. (2010 & 2013) and Salazar et al. (2016) did not investigate landslide problems. Therefore, they will not be dealt with in the subsequent paragraphs in this thesis.

To the best of my knowledge, it seems that the first documented study on the application of PFEM to landslide could be attributed to the doctoral work by Zhang (2014). The author developed a PFEM model and applied it to the Yangbaodi landslide that occurred in a hilly region at an altitude of 104 – 385 m in Southern China. Few soil parameters were used in the simulation while the landslide was modeled as a 2D problem. The fluid-like landslide was modeled as a single-phase material. The sliding of the mass was then described using Equations (2.15 – 2.21) in which the effect of liquid was assumed inexistent. To put it another way, the rock mass was assumed to experience no deformation until internal stresses exceeded the yield. Upon reaching this threshold, plastic deformation ensued. A total of 600 incremental finite element nodes (with the cross-section with the horizontal distance of 350 m and a maximum elevation of 250 m) were considered for the simulation of the entire sliding slope with time increment Δt = 0.05 s. Additive decomposition of the strain tensor was used to solve the constitutive equations governing the framework. Encouraging results were produced demonstrating the potential of the PFEM tool for the estimation of rock sliding and its final run-out distance (see Figure 2.21).
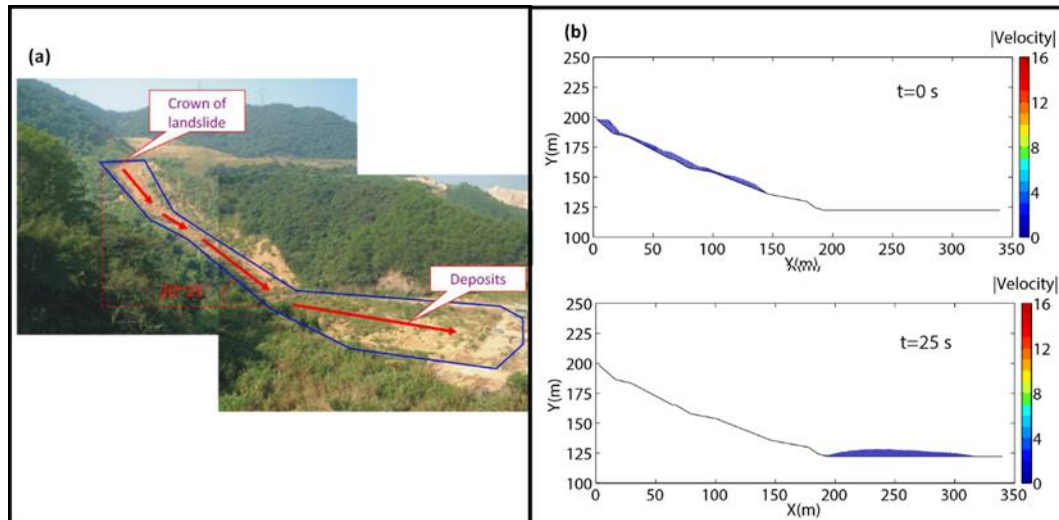
Figure 2.21 (a) Landslide event (after Li et al., 2012) and (b) flow evolutions with velocity contour (after Zhang, 2014).

Zhang et al. (2017, 2018 & 2019) have gone on to further validate their doctoral PFEM model with other cases. And despite few shortcomings, the model has given reasonable results. It should be conceded that the framework by Zhang (2014) still experiences the type of volumetric locking problems expanded on in Section 2.5.5.

Building from Zhang's algorithm, Monforte et al. (2017 & 2018) presented a numerical framework for the simulation of total stress problems. The new framework is basically the Lagrangian Finite Element method integrating constitutive equations allowing for hyperelastic behavior. Contrasting from Zhang (2014), Monforte et al. (2017 & 2018) applied a multiplicative decomposition approach with low-order elements and frequent remeshing. This decomposition together with the application of the displacement-mean pressure formulation enabled them to suppress volumetric locking. In addition to this, the system was modeled as a pro-mechanic continuum composed of two phases: a solid skeleton and water. The penalty method reviewed in Section 2.5.6 was used to model the elasto-plastic character of contacts. Nevertheless, Zhang et al. (2019) conducted another study on the application of PFEM in landslides case, the authors found that their "computational framework is capable of quantitatively reproducing the multiple rotational retrogressive failure process as well as the final run-out

distance and the retrogression distance of the Saint-Jude landslide" the results of the model is shown in Figure 2.22.
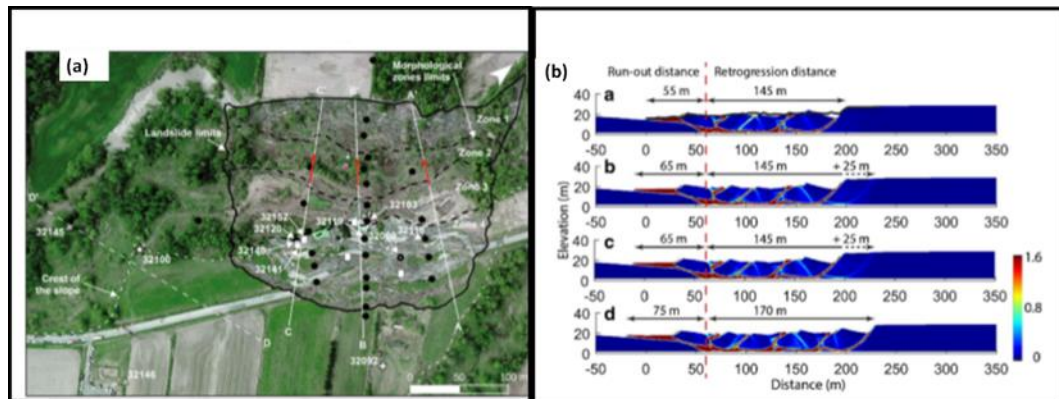
Figure 2.22 (a) Landslide event (after Locat et al., 2017) and (b) Landslide run-out distance and retrogression distance (after Zhang et al., 2019).

This brings us to talk about the last and most recent study on the application of PFEM to geotechnical engineering.

Wang et al. (2019) attempted to simulate the evolution of shallow landslides using the PFEM. The researchers were able to generate encouraging results. The computational algorithm followed a procedure similar to that presented in Zhang et al. (2016, 2017 & 2018). The final PFEM model was then used to explore the Cà Mengoni landslide. This was a landslide that occurred as a mass-movement event in 2013 in the northern Apennines, Italy (Zhang 2017.). The group of researchers reached the conclusion that their PFEM model has the ability to predict the landslide deposit point. They were also able to obtain a partial estimation of the mechanism behind the occurrence of the event. This is noteworthy considering that their model is simple yet could capture aspects of the complex phenomenon. What is still outstanding is to extend the model beyond the shallow types of slope instability it was calibrated against.

2.5.8   Future outlook

As a starting point, it should be stated that PFEM was initially intended to simulate complex problems of computational fluid dynamics. The method is now finding its way in rock mechanics with its implementation in the *Triangle* open-source code for example (Zhang et al., 2018 & 2019). Subsequent to this has been the birth of G-PFEM dedicated to geotechnical engineering applications in general and rock mechanics in particular.

The majority of studies on PFEM fall primarily in the field of fluid mechanics and not solid mechanics. This has made it difficult to find appropriate applications of the method to landslides. Indeed, PFEM is a novel technique still in its infancy as far as solid mechanics is concerned. Therefore, there is a lot of scope for research and development. One pressing research gap is the determination of the mechanism of slope sliding and rockfalls as well as the associated re-occurrence (Monforte et al., 2016; Yuan et al., 2019.). The other problem is the extension of the G-PFEM beyond the general-purpose finite element environment it was built for. The endeavor should accommodate for instance the effects of fluid-solid interaction and temperature on landslides (Monforte et al., 2018).

Overall, the application of the PFEM framework and particularly the G-PFEM sub-framework to rock engineering has potential. However, for the development and refinement of the technique to happen, experimental and actual field data needs to be compiled. Remote sensing technologies could be an option for addressing the shortfall. Specific technologies that have been successfully used in geotechnical engineering applications are succinctly reviewed in section 2.6.

2.6   Remote sensing in geotechnical engineering

Remote sensing has been widely used as a means for the collection of data essential for the construction of landslide susceptibility maps (Rawat et al.,

2015; Ghosh et al., 2017; Ramesh et al., 2017; Gupta et al., 2018; Ramos-Bernal et al., 2018). The capacity of remote sensors to repeatedly visit the same area over time makes remotely-sensed data ideal for monitoring changes in causative factors leading to landslide occurrence. This also contributes to the effort of issuing early warnings of landslide occurrence (displacement of the mass and slipping of material from slopes) in areas susceptible to such (Tyoda, 2013).

The rapid development of computing power over recent years has contributed to the establishment of remote sensing technologies. For example, artificial intelligence techniques have been introduced to process remotely-sensed data (Arnone et al., 2014; Dehnavin et al., 2015; Zhang et al., 2017). This type of data resulting from, say, the monitoring of rock slopes can be acquired using for example a Phased Array type L-band Synthetic Aperture Radar (PALSAR) or an Advanced Spaceborne Thermal Emission and Reflection Radiometer (ASTER). The latter is the object of this section owing to the easy access of ASTER images.

2.6.1   ASTER imagery

The Advanced Spaceborne Thermal Emission and Reflection Radiometer (ASTER) was launched on 18 December 1999 as part of the NASA Terra satellite shuttle. The earth observing instrument was installed and placed in orbit with the initial aim of monitoring volcanic activities (Pieri and Abrams, 2004; Urai, 2004; Carter et al., 2010; Ramsey et al., 2012).

The ASTER detects the activity of the earth's surface at multiple spatial-spectral resolutions and from different viewing points. The instrument has three sensors with independent bore-sighted telescopes. The three sensors have 14 spectral channels in total in the shortwave infrared (SWIR), the thermal infrared (TIR), and the visible/near-infrared (VNIR) regions (Yamaguchi et al., 1998). The SWIR instrument, designed to exploit 1.6 – 2.43 µm waves, failed in 2008. It was originally set with six channels for a

spatial resolution of 30 m/pixel. The TIR instrument, on the other hand, has five channels at a spatial resolution of 90 m/pixel and emits 8.13 – 11.65 µm rays. The VNIR sensor beams rays of wavelength 0.52 – 0.86 µm. It has three spectral channels with a spatial resolution of 15 m/pixel paired and one additional channel looking backward to create digital elevation models (DEMs). This VNIR instrument is the focus of most landslide susceptibility projects; it is of interest to this doctoral thesis. This is primarily because ASTER-based VNIR data is freely accessible with wide coverage, high spatial resolution, and DEM-oriented output.

The availability of ASTER data provides an opportunity for the scientific analysis of areas with no topographic, soil, and vegetation maps. These maps can be generated by inference even for inaccessible areas. ASTER imagery is therefore central to concepts such as landslide susceptibility mapping. Several studies have exploited DEMs by successfully processing ASTER images (Welch and Marko, 1981; Lang and Welch, 1999). Interestingly, Lang and Welch (1999) were able to generate absolute DEMs accurately to within 7 – 50 mm in vertical elevation. This alone is an incentive for the utilization of the ASTER as a reliable source of images for risk hazard analysis of landslides. Several analysis techniques are available in the literature; however, only landslide susceptibility mapping and normalized difference vegetation index are covered in section 2.6.2.

2.6.2   Landslide susceptibility mapping

Landslide susceptibility mapping (LSM) is considered to be one of the most recent risk hazard analysis techniques. It relies on ASTER imagery to manage, plan and mitigate the risk of and the measures against landslides (Arabameri et al., 2019).

Various approaches to LSM have been explored worldwide; however, they can be grouped into three categories: heuristic, deterministic, and probabilistic. Heuristic techniques basically rely on the expert's knowledge

to rank landslide-prone areas from high to low probability risk. Heuristic mapping is very subjective but does provide good insight into the areas. It is often used to analyze large areas with a known history of landslide occurrence. Deterministic techniques, on the other hand, hinge on the numerical description of the physical mechanisms controlling slope failure (Zhang et al., 2019). They are appropriate for large-scale mapping but become impractical in highly heterogenous rockmass. The need for large data representing the mechanical properties of the rock also exacerbates the problem as the underlying numerical models may fail to capture key features. The last techniques are known as probabilistic; they are built on the non-deterministic nature of rocks and on the use of statistical laws to describe landslides. Dehnavin et al. (2015) have argued that probabilistic LSM is the most promising approach to landslide detection. However, the production of reliable results is heavily dependent on the proper filtering of input parameters known as causative factors.

Causative parameters are factors that may trigger landslides and control their occurrence (Rawat et al., 2015; Ghosh et al., 2017; Gupta et al., 2018). Three types of causative parameters are generally defined: static, variable, and triggering factors. Static factors are unlikely to change within a short period of time. Geology, geomorphology, and the type of vegetation are examples of static factors (Sarkar and Kanungo, 2004). In contrast, variable factors experience anything from seasonal to daily variations. They include the water content in the soil as well as the density, health, and productivity of the vegetation. During the dry season, for instance, the rapid deterioration and loss of vegetation cover can increase the likelihood of landslide occurrence. Last, triggering factors are such factors as heavy rainfalls and earthquakes that can set off landslides besides static and variable factors (Tyoda, 2013).

Different techniques can be used to weight the contribution of causative parameters to the rendered landslide susceptibility maps (Quan and Lee, 2012; Ramesh et al., 2017; Ramos-Bernal et al., 2018). The weight of the

evidence approach is the most widely used technique for the quantification of the relative importance of causative factors to slope failure (Sarkar and Kanungo, 2004; Tyoda, 2013; Gupta et al., 2018).

The Weight of Evidence (WOE) approach is based on the construction of a 2D grid overlaying the surface area being mapped. Then, a cell of size Δ_s is defined by sequentially considering a 3×3 cellular network made of 9 nodes with altitude values Z_1 to Z_9. The process is iteratively repeated for the input dataset of landslide points defining the whole grid. Next, topographical descriptors including Landslide Susceptibility LS are calculated as shown by Equations (2.38 to 2.48) (Singh et al., 2011):

$$Slope = \sqrt{H^2 + G^2} \tag{2.38}$$

$$Aspect = arctan\left(\frac{H}{G}\right) \tag{2.39}$$

$$Plan\ Curvature = -\frac{Q^2\,R - 2\,Q\,S + P^2\,T}{(P^2 + Q^2)\left(\sqrt{1 + P^2} + Q^2\right)^3} \tag{2.40}$$

$$LS = \left(\frac{A_S}{22.13}\right)^{0.6} \tag{2.41}$$

$$G = \frac{df}{dx} = \frac{Z_3 + Z_6 + Z_9 - Z_1 - Z_4 - Z_7}{6\,P} \tag{2.42}$$

$$H = \frac{df}{dy} = \frac{Z_1 + Z_2 + Z_3 - Z_4 - Z_8 - Z_9}{6\,P} \tag{2.43}$$

$$P = \frac{Z_3 + Z_6 + Z_9 - Z_1 - Z_4 - Z_7}{6\,\Delta_S} \tag{2.44}$$

$$Q = \frac{Z_1 + Z_2 + Z_3 - Z_7 - Z_8 - Z_9}{6\,\Delta_S} \tag{2.45}$$

$$R = \frac{Z_1 + Z_3 + Z_4 + Z_6 + Z_7 + Z_9 - 2\,(Z_1 + Z_2 + Z_3)}{3\,\Delta_S^2} \tag{2.46}$$

$$S = \frac{-Z_1 + Z_3 + Z_7 - Z_9}{4\,\Delta_S^2} \tag{2.47}$$

$$T = \frac{Z_1 + Z_2 + Z_3 + Z_7 + Z_8 + Z_9 - 2\,(Z_4 + Z_5 + Z_6)}{3\,\Delta_S^2} \tag{2.48}$$

The above flow of information together with other relevant factors such as hydrology, geology, weather, and soil characteristics are processed using the scheme in Figure 2.23. Random forest, decision tree, and Fisher's linear discriminant analysis are relied upon for this purpose. Finally, the landslide susceptibility map of the area is rendered.
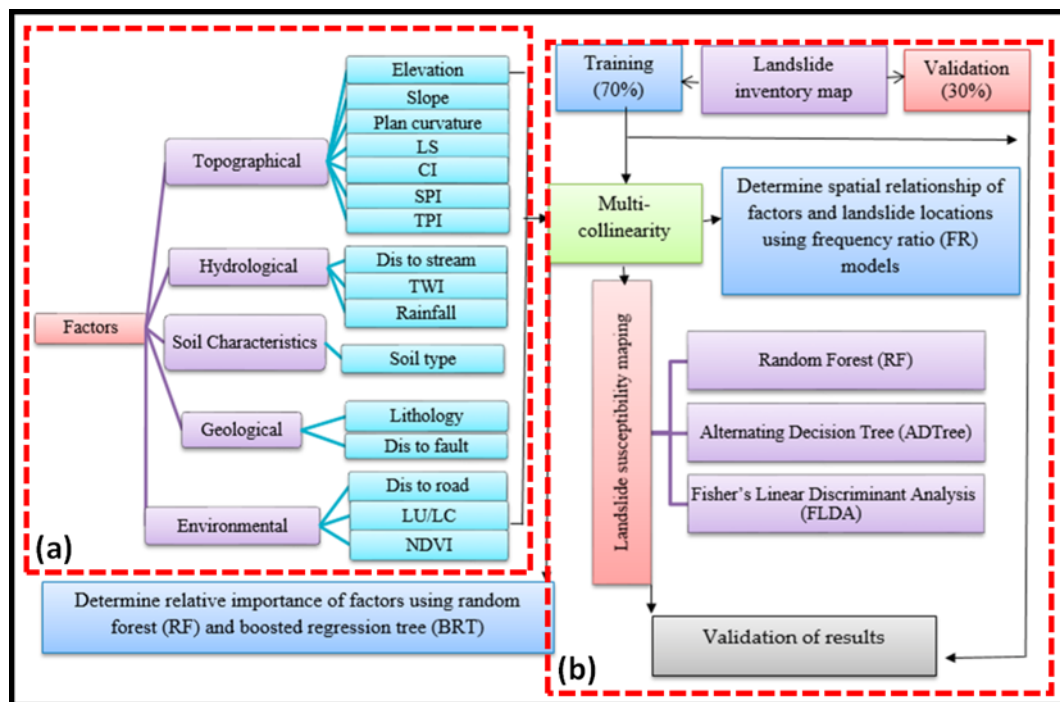
Figure 2.23 (a) Causative parameters for landslide susceptibility mapping and (b) processing of input data (after Arabameri et al., 2020)

The study by Roy et al. (2019) exemplifies well the application of the WOE approach in the context of LSM. It can be seen from Figure 2.24 that Roy et al., (2019) has presented several outputs parameters that were used in order to develop classes of landslide hazard zones within the study area. The authors used the so-called WOE model in which previous data and current data outputs are the most crucial aspects. As shown in Figure 2.30, the Authors were then being able to categorize the study area into four classes (low, medium, high, and very high landslide susceptibility) these results were validated by the previous or post landslides that occurred within the study area. A summary of the Weight of Evidence models and their parameters is demonstrated in section 2.6.4.2.
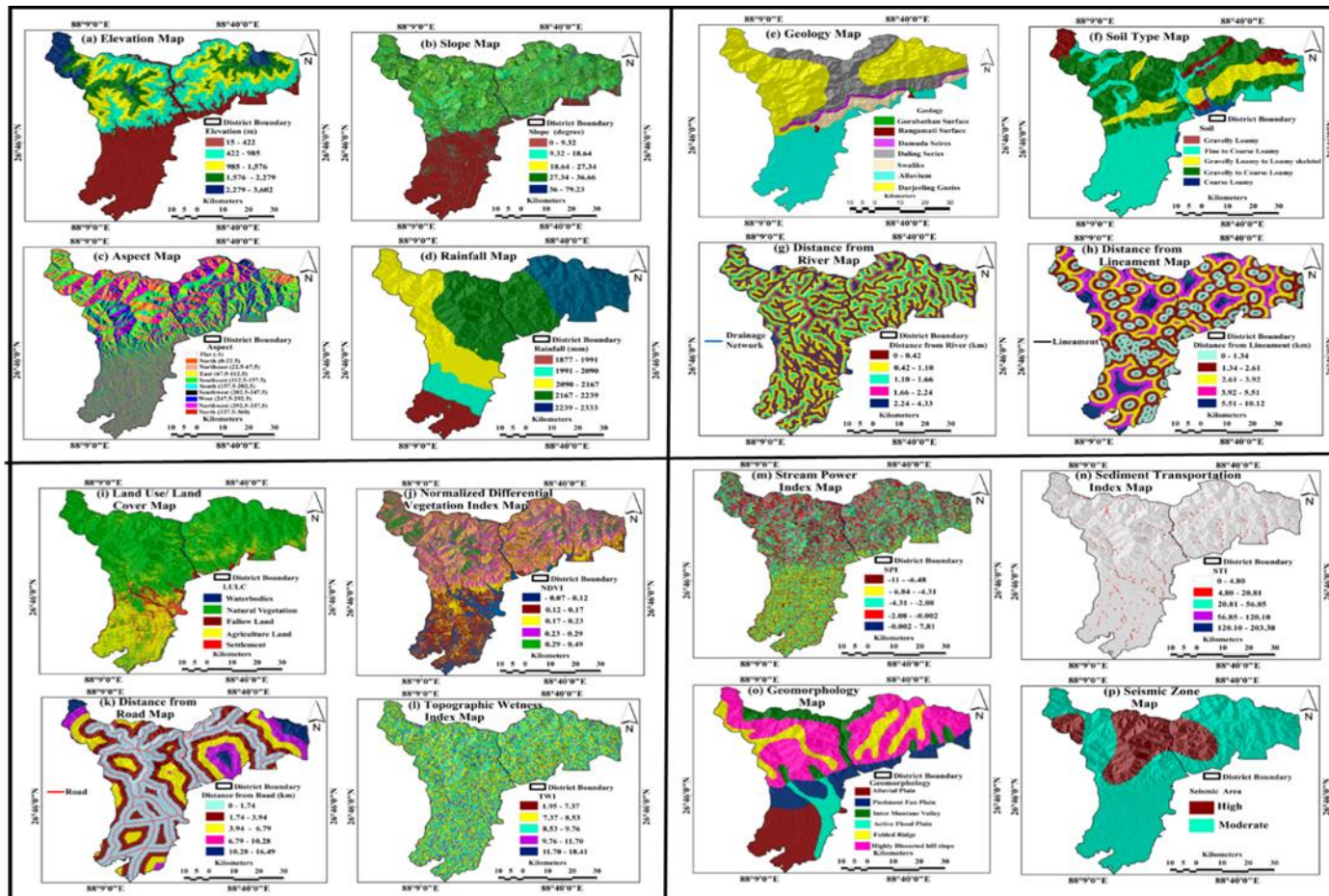
Figure 2.24 Typical output rendering of the application of the WOE approach to LSM (Roy et al., 2019)

2.6.3 Normalised difference vegetation index

The Normalized Difference Vegetation Index (NDVI) is a remote sensing metric characteristic of the condition of the vegetation associated with an area (White et al., 2005). It has gained wide acceptance after its successful use in the discrimination of contiguous Mediterranean habitats (Grignetti et al., 1997; Alcaraz-Segura et al., 2009; Feret et al., 2015).

The NDVI can be used as a proxy for tracking the Spatio-temporal changes in the vegetation of a geographical area. Classical applications of the NDVI are mostly found in agricultural studies (Phua et al., 2008). Here, plant growth and greenness, vegetation cover, and biomass production are measured and monitored from multispectral satellite data. The NDVI offers a simple, quick, and compact way for the identification of vegetated areas as well as their conditions. It remains the most widely used index for the inferential characterization of live green plant canopies from multispectral remote sensing data. Phua et al. (2008) even claim that once the detection of vegetation has been demonstrated, researchers and practitioners alike tend to extend the use of the NDVI to quantifying the photosynthetic capacity of plant canopies. This is because the NDVI somehow captures features such as changing illumination, surface slopes, and the presence of vegetation (Wang et al., 2003). The NDVI has also been demonstrated to be a good indicator of thriving plants as well as plants under stress due to lack of water (Jensen, 2005).

In terms of LSM studies, the NDVI is being primarily employed to describe the removal of vegetation in time and space as a result of a landslide. The index, therefore, has relevance where the slope instability of such areas and the probability of landslide should be estimated.

The NDVI is computed by taking for example bi-weekly satellite images of an area. These photographic frames are stitched in the form of a pixel-based time series. Following this, the NDVI technique was implemented using

near-infrared and red bands of the log-residuals-calibrated multispectral image. The principle of applying the NDVI in vegetation mapping is that the vegetation is highly reflective and absorptive in near-infrared (NIR) and visible red, respectively. The difference between these bands was used to indicate the presence and greenness of vegetation (see Equation 2.49).

$$NDVI = \frac{NIR - Red}{NIR + Red}$$ **(2.49)**

where NIR and Red are the normalized reflectance values of NIR and red bands, respectively. The NDVI resulting values range from -1 to +1 and the common range for green and healthy vegetation is 0.2 to 1 (Jensen, 1986), while bare soil is typically represented by values < 0. The pixel-based images can now be processed by means of what is known as the principal component analysis through the conditional expectation (Yao et al., 2005).

The NDVI is one of the techniques that could be easily established in comparing changing illumination such as surface slopes, and the presence of vegetation, this ability of the technique allows it to clearly predict and identify landslide zones within the terrain. Its ability has attracted several scholars to explore its ability in geotechnical problems such as slope instability, a brief review of landslide susceptibility models that are used in conjunction with NDVI and ASTER imagery are presented below.

2.6.4 Landslide susceptibility models

Regardless of the way the value of the NDVI is arrived at, specific models are to be used to extract the index from the ASTER data meaningfully. Such models may differ in their definition, but they intrinsically serve the same purpose. The most important ones from an LSM viewpoint are covered in this section.

2.6.4.1 Frequency ratio

The frequency ratio method has been implemented in numerous studies. It is purported to be simple to generate landslide susceptibility maps with (Ozdemir and Altural, 2013; Lepore et al., 2012; Lee and Talib, 2005; Shahabi et al., 2014; Park et al., 2013; Mohammady et al., 2012).

The commonly used definition of the Frequency Ratio (FR) to be assigned to a unit cell of a landslide-prone study area is given below (Wang et al., 2013; Lepore et al., 2012; Regmi et al., 2010):

$$FR_i = \frac{AI_i/AI}{AC_i/AC} \tag{2.50}$$

$$LSI = \sum_{j=1}^{n} FR_j \tag{2.51}$$

Where AI_i is the number of landslide cells of the category (i); AI is the total number of landslide cells; AC_i is the number of cells of the category (i); AC is the number of cells; FR_i is the FR value for the chosen class of factor (i); n is the total number of factors included in the study; and LSI is the Landslide Susceptibility Index based on the calculated FR values.

An important point to make is that for FR > 1, there is a high probability of landslide occurrence. On the contrary, for FR < 1, a low probability of landslide occurrence is registered.

2.6.4.2 Weight of evidence

Weight of evidence (WOE) is a Bayesian probability model that uses the weights of factors to generate landslide susceptibility maps (Lee et al., 2002; Regmi et al., 2010; Meyer et al., 2014). Factors can be positive weights (W+) or negative weights (W−).

The weights associated with individual factors included in the model are estimated based on the presence or absence of landslides within the area

of interest. One way of defining weights is summarised below (Van Den Eeckhaut et al., 2009):

$$W^+ = \ln\left[\frac{AI_i/AI}{AC_i/AO}\right]$$ **(2.52)**

$$W^- = \ln\left[\frac{1-AI_i/AI}{1-AC_i/AO}\right]$$ **(2.53)**

Where AI_i is the number of landslide cells of the category (i); AI is a total number of landslides cells; AC_i is the number of cells of the category (i); AO is the number of cells outside the landslides i.e. number of study area cells minus a total number of landslides cells.

From Equations (2.52) and (2.53), the weight contrast (C) can be computed as the difference between the W+ and W− (Mohammady et al., 2012; Meyer et al., 2014; Ozdemir and Altural, 2013; Corsini et al., 2009).

$$C = W^+ - W^-$$ **(2.54)**

$$P = exp\left[\sum W^+ + \ln P_{p(s)}\right]$$ **(2.55)**

$$P_{p(s)} = \frac{Number\ of\ lanslide\ cells}{Number\ of\ total\ study\ area\ cells}$$ **(2.56)**

The magnitude of the contrast obtained from Equation (2.54) represents the overall factor associated with landsliding. Furthermore, a negative contrast shows a negative spatial correlation and conversely.

The final probability of landsliding is calculated as the sum of weights of each predicting factor in Equation (2.55) and their prior probability (see Equation 2.56).

2.6.4.3 Logistic regression

Logistic Regression is a modeling approach that has been successfully implemented in a number of cases (Guzzetti et al., 1999). The probability of

absence and presence of landslide is defined between one and zero following the multivariate model (Othman et al., 2015; Kleinbaum and Klein, 2011):

$$P = \frac{1}{1 + \theta^{-Z}}$$
(2.57)

$$Z = \alpha_0 + \beta_1 X_1 + \beta_2 X_2 + \cdots + \beta_n X_n$$
(2.58)

Where α_0 is the intercept of the model; n is the number of variables; β_i are the beta values associated with each of the independent variables; P is the probability of landsliding with values between 0 and 1 on an S-shaped curve; and Z varies from $-\infty$ to $+\infty$ on an S-shaped curve.

2.6.4.4 Probit regression

Probit regression shares some similarities with the logistic regression discussed in the previous section. The Probit Regression (PR) is based on some form of binomial statistical regression. The model is centered on the probit link function; this function represents the inverse of the cumulative distribution function of the standard normal distribution. In doing so, probabilities are transformed to the standard normal variable. The following Equations (2.59 and 2.60) is used for the purpose of probit regression (Aldrich and Nelson, 1984; McCullagh and Nelder, 1983):

$$Z = \Phi^{-1} P$$
(2.59)

$$\Phi(Z) = \frac{1}{\sqrt{2\pi}} \int_0^Z exp\left(\frac{-t^2}{2}\right) dt$$
(2.60)

Where Φ denotes the cumulative normal distribution function; P represents the probability of landsliding; and Z varies from $-\infty$ to $+\infty$.

2.6.5 ASTER in geotechnical engineering

ASTER satellite data has been successfully employed to evaluate landslides. To the best of our knowledge, the following are the most relevant studies: Crowley et al., 2003; Liu et al., 2004; Santini et al., 2009; Roy et al., 2019; Dou et al., 2019. They are briefly summarized here in chronological order.

Crowley et al. (2003) have explored remote sensing techniques in the identification of potential rockfalls. A critical comparison of the remote sensing data sets was performed, the study revealed the possibility of remotely sensed data in the evaluation of the altered rock masses that could result in potential volcanic debris flow sources.

Liu et al. (2004) have studied the Three Gorges of China rating it as an area of high to low landslide hazard. The study presented the use of ASTER imagery as a useful tool to extract the topographic and spectral data which could be used to develop a landslide hazard map of the area.

Santini et al. (2009) conducted a critical investigation on the influence of varying terrain procedures techniques toward the final results of slope stability prediction using Terra ASTER, DEMs. The DEMs procedures were revealed to affect the implementation of the countermeasures against slope stability. Regardless, their findings the study denoted remote sensing as a useful tool to predict landslides (slope instability).

Roy et al. (2019) were able to produce landslide susceptibility maps with the help of remote sensing data. Four classes of susceptibility to landslide occurrence were defined for the purpose: low, medium, high, and very high. The results of their study highlighted areas of the high probability of landslides as can be seen in Figure 2.25.
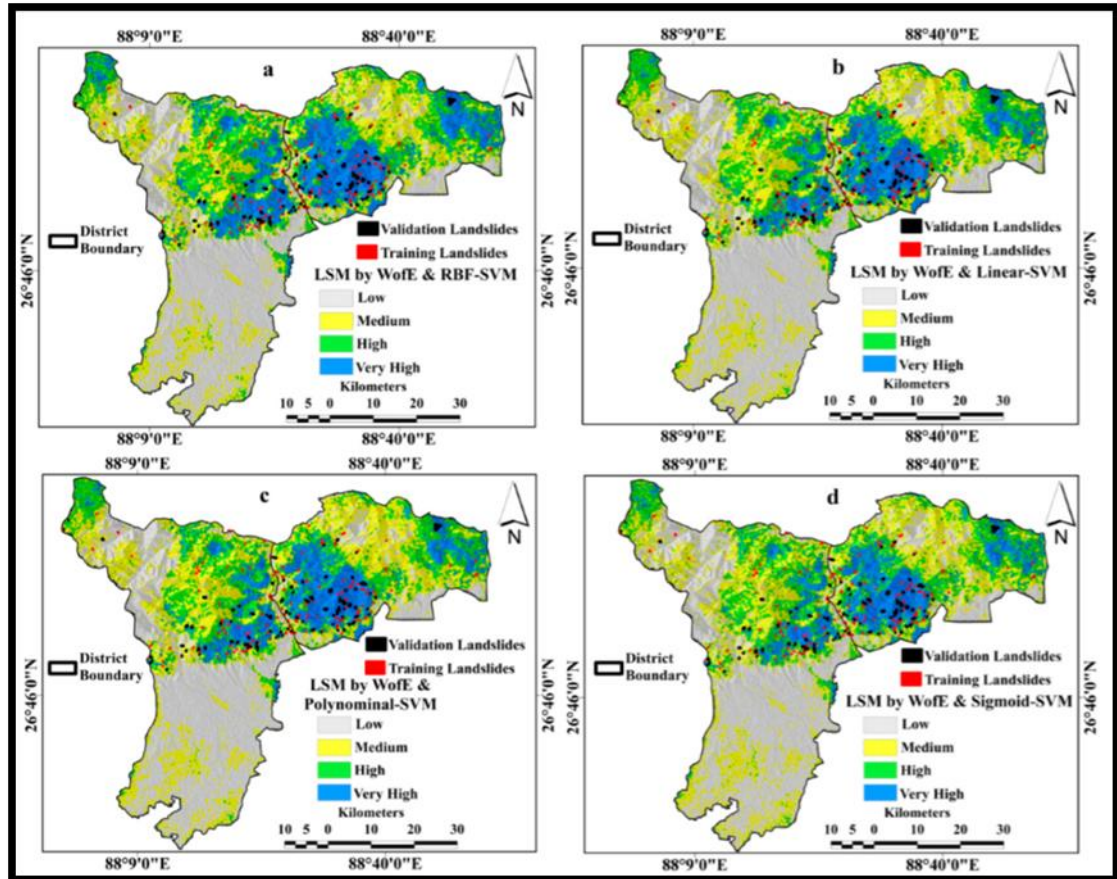
Figure 2.25 Landslide susceptibility maps (Roy et al., 2019)

Dou et al. (2019) borrowed the analysis procedure initially performed by Roy et al. (2019). Their results also highlighted areas of high as well as medium to low landslide susceptibility. The study by Dou et al. (2019) complements that of Roy et al. (2019) and in a sense builds confidence in the proposed LSM technique. Finally, Dou et al. (2019) concluded that their processing technique for ASTER data can be extended to areas experiencing landslides due to both rainfall and earthquake. Figure 2.26 gives an overview of the types of landslide susceptibility maps they were able to produce. Clear demarcation of areas prone to landslides can be seen; these are allocated a high landslide susceptibility index.
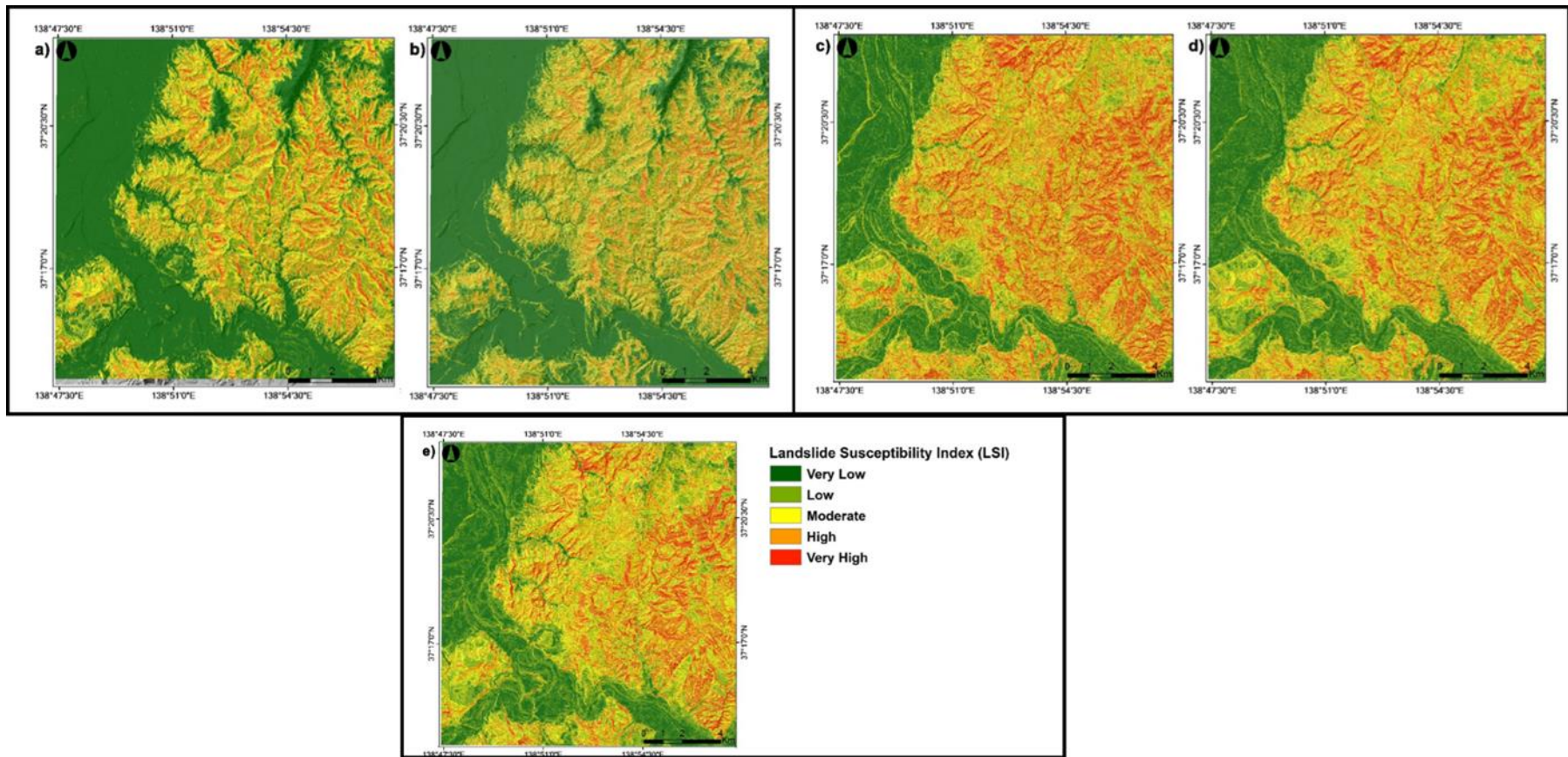
Figure 2.26 Example of Landslide Susceptibility Index (Dou et al., 2019)

2.6.6   Closing comments

It appears from the review covered in Section 2.6 that techniques for the analysis of remote sensing data are still to gain momentum in rock mechanics. The picture is very different in fields such as agricultural engineering, environmental sciences, and related disciplines. This is evidenced by the very limited number of scientific articles dealing with remote landslide susceptibility mapping; yet, the underlying analysis protocols are well established. It is, therefore, our opinion that there is room for the exploration of LSM techniques to solve rock mechanics problems.

It must be conceded that alternative theoretical techniques have been in existence for tackling landslide problems. However, the study area that is the object of this doctoral research has limited information in the literature that fully describes the occurrence and mechanisms associated with rock-slope instability. It is strongly believed that ASTER and LSM have the potential to contribute towards a better understanding of rockfalls in the Thulamela area. But before proceeding, a review of past work in the area of interest is done in the next section. This is expected to outline some of the missing links the present research is aimed at addressing.

2.7   Past case studies in the Thulamela Municipality

Looking at the background of the study area, Thulamela Municipality roads are located in the northern region of Limpopo province in South Africa. Most of these roads are situated in the rugged topography of the Southpansberg Group. These roads serve as significant access from villages to the surrounding townships. The stability of road slopes is therefore critical as this contributes to the social welfare in the region.

It should be noted that Thulamela roads had been excavated using blasting and mechanical operation. The excavations were carved through topographically challenging terrain with high slopes and fractures (Sengani

and Zvarivadza, 2019). As a result of this, road construction has subjected the area to intensive rockmass movement. This has disturbed the original balance of driving and resisting forces. The groundwater regime has also been affected to the point that unstable conditions have been prevalent since. Deforestation and compounding heavy rainfall have worsened the situation. These two factors have led to weakened soil structures, reduced rock strength, and increased internal rockmass stress (Bennet and Doyle, 1997; Abbott, 2002; Göktepe and Keskin, 2018).

Regional roads of the Thulamela Municipality have been reported to the scene of extensive rockfalls and slope instability during the wet season (Mutanamba, 2013; Sengani and Zvarivadza, 2019). Several remedial measures were suggested and implemented; however, rockfalls and slope instability are still experienced at an alarming rate.

To the best of my knowledge, Mutanamba (2013) is the only study so far who have conducted a scientific study on slope stability in the Thulamela Municipality. Indeed, the researcher analyzed the stability of the cut-slope along the R523 road between the Thathe Vondo and Khalavha area using conventional methods. He first surveyed the area and collected observational data relating to the specific geological structures, the properties of the rock material, and the groundwater regimes. The field data was appropriately processed for soil classification and then used as inputs to the various analytical methods. These included slope stability charts, translational analysis, toppling analysis, and rotational analysis. The initial findings suggested the existence of two types of slope failures: rotational slump and rock toppling. Both failure mechanisms were observed to occur close to the roadside with extensive damage to the support system previously installed. Mutanamba (2013) conceded that it is yet to be established how natural drainage patterns and rainfall in summertime amongst others could be contributing factors to rockfalls. Equally, a similar study by Sengani and Zvarivada (2019) could not outline the underlying

mechanisms of rockfalls. This study also highlighted the need for a better understanding of rockfalls in the Thulamela Municipality.

To sum up, natural slopes along the R523 road have been disturbed by road construction that in turn has altered natural drainage patterns. This has contributed to the increasing instability further exacerbated by heavy summer rainfalls. It is however not clear how rainwater and any other factors have been contributing to rockfalls and rock instability. Follow-up work by Sengani and Zvarivadza (2018) was conducted using the data collected by Mutanamba (2013). In this case, concordant findings were reported even though LEM-based simulation techniques were used.

It is in cognisant of this background that the Finite Element Method (FEM) and Remote Sensing data from the Advanced Spaceborne Thermal Emission and Reflection Radiometer (ASTER) techniques could bring value to the study. The proposed joint techniques have the potential to describe the mechanism of rockfalls and slope failure in the Thulamela Municipality.

2.8   Concluding remarks

In addressing the limitations of conventional analysis techniques, the combination of FEM and ASTER image techniques is brought in as a viable alternative. The combination of advanced geotechnical methods and remote sensing techniques is purported to provide results of rock slope instability. From the literature review, it is evident that the two techniques have not been paired before to solve geotechnical problems. The present doctoral research is an opportunity to bridge that gap and contribute to a better understanding of rockfalls. The two methods may finally not necessarily solve existing problems but they may at least provide good insights into the phenomenon of rockfalls.

Chapter 3   Collection of experimental, field, remote sensing, and simulation data

This chapter details the methodology followed in this thesis for the collection of supporting data. This includes field observation and measurements, laboratory analysis, kinematic analysis, limit equilibrium analysis, numerical simulations, and ASTER images processing for landslides susceptibility.

3.1   Introduction

The data collection methods followed in this thesis entailed desktop study, field observation, field measurements, experimental tests, and numerical simulation. In the desktop study, relevant materials were collected and reviewed in order to gain an understanding of rock-slope stability and their methods of analysis. This data collection technique was used to lay the foundation for field and laboratory work. In essence, the desktop study served the purpose of devising an efficient and meaningful program for the acquisition of field and laboratory data.

The second stage of data collection was to perform field observations and measurements. Here, geological mapping and field measurements of the rock mass structures were conducted within the selected study areas. Both soil and rock samples were collected for the characterization of the mechanical properties and geotechnical parameters of the sites. Laboratory tests were the third stage; soil samples were tested for particle distribution, Atterberg's limit, soil classification while rock samples were prepared for thin section.[2]

---

[2] Sections of this chapter has been used in several articles mentioned on the list of publications in this thesis. The information will appear in a variety of papers based on the content of the paper.

In the third stage, kinematic analysis and limit equilibrium analysis were performed. These numerical techniques were employed to evaluate slope stability and identify the underlying mechanisms of rockfalls. The following numerical programs were used for the analysis: SLIDES, DIPS, SWEDGE, RocPlane, and Phase2. Finally, the last stage was to perform the analysis of rock slope stability using ASTER image, WOE and NDVI. This together with the kinematic and Limit Equilibrium analyses made it possible to develop slope stability hazard prediction charts. Thereafter, rockfall analysis was performed using the Rock Mass Rating method as well as DIPS and RocFall simulations. These methods later made it possible to develop a rockfall hazard matrix chart also known as a rockfall hazard prediction chart.

This chapter is specifically devoted to describing the details of the methodology adopted for the collection of actual raw data. The chapter also covers the testing protocols used in the field and in the laboratory. The experimental program for the simulation work is also presented as well as the manner in which supporting software packages were set up. The analysis of the entire dataset and the interpretation of the results is done in the next and subsequent chapters.

3.2   Geotechnical testing programs

The aim of field observations and measurements was to collect important data for the validation of simulation results. The field data was to give room for realistic simplifications of mathematical equations descriptive of the behavior of the in-situ rockmass.

Fieldwork entailed visual observations, field measurements, and rainfall statistics of the selected study area. Further details are provided in this section.

3.2.1 Visual observation and field measurements

Visual observation was extensively used to circumscribe the rockfall problem associated with the selected study areas. Field trips were made to identify the types of soils present in the study areas. The dimensions or extent of the unstable slopes along Thulamela Municipality roads were also measured.

To this end, the width and height of the micro landslides were measured using a geological tape measure as shown in Figure 3.1b. The width and height were measured within the boundaries of the micro landslides. The above-mentioned procedure was followed by collecting soil samples, Soil samples were collected random sampling (see sampling location points in Figure 1.1) with the emphasis that samples should be collected from the depth of 0.5m (the depth of 0.5m was used to acquire fresh sample) within the affected slopes. In order to simplify the process of soil sampling, a handheld Auger was used to collect soil samples (18 samples were collected with three samples per sampling point), with a sample bag of 5kg (see Figure 3.1f). Samples were named from each selected point of the study area to avoid mixing of data, and samples were stored separately (Samples were separated based on the location in which they were obtained, in short, there were three sets of samples with three samples each). In the meantime, some of the geological features (joints, faults, and dykes) revolving around the study area were recorded by measuring the strike and dip of the feature using campus (see Figure 3.1h), other parameters such as the properties of the features including infill, the width of the features were also recorded in a notebook (see Figure 3.1d-e example of the notebook). Geotechnical and geological mapping(using a geological compass) was also conducted with the focus of identifying dip and dip direction of the wedges developed along with the micro landslides and also measure the slope angle, the orientation of tension cracks. A figure showing annotated micro landslide is denoted in Figure 3.1.

Figure 3. 1 Sampling and geological tools used for the study (a) handheld Auger, (b) Tape measure, (c) Clipboard, (d-e) Pen and Notebook, (f) 5kg Sample bag, (g) Geological harmer, (h) Campus, (i) Hand-held GPS
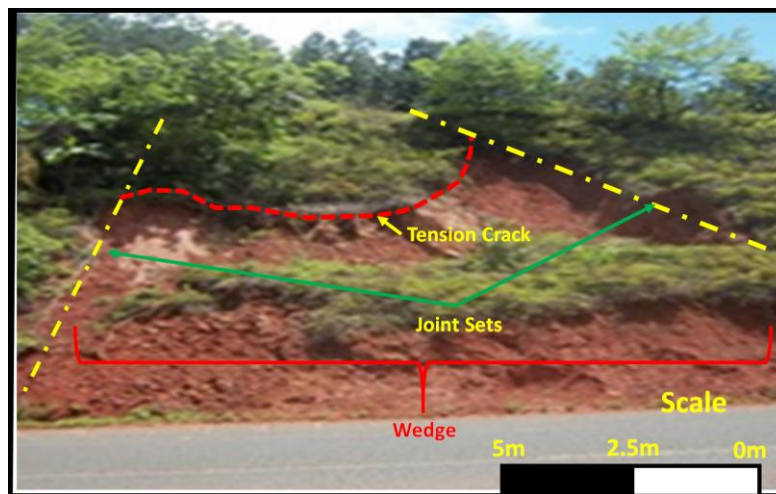
Figure 3. 2 Annotated Micro landslides of the study

Visual observation was supplemented with field measurement that consisted of geotechnical mapping also referred to as geological mapping.

Geotechnical mapping followed the common procedure required to rate the quality of the rock mass such as those of Bieniawski between (1972 and 1973). The key parameters that were measured are listed in Table 3.1.

Table 3.1 Geological or geotechnical mapping parameters

	Symbol	Units
Sites	S	
Joint Set	Jn	
Joint Spacing	JS	mm
Joint Persistence	JP	m
Joint Aperture	JA	mm
Joint Roughness Coefficient	JRC	
Joint Infilling	JI	kPa
Joint Weathering	JW	
Rock Mass Rating class	RMR	

The identification of the parameters in Table 3.1 was aimed at compiling input data for later numerical simulation work. The information was also to be used in the classification of the rock mass of the study areas. Indeed, the parameters capture the mechanical behavior of the rock mass and assist in designing an appropriate support system for the area. The parameters in Table 3.1 included the documentation of the set of joints, their spacing, and their persistence amongst others.

In terms of actual implementation, three major steps were followed during the geological mapping: planning and preparation; construction of the map in the field; and production of the final map.

The planning component of the study was composed of visiting the study area and deciding on the size of the map as well as designing the traverses that should be followed using a constructed topographical of the area (see Figure 3.3). The developed traverses were about 500m wide and 1.7km long, and five traverses were developed across the study area. The planning process was limited to the reconnaissance survey so that the starting map of the study area could be drafted. Although this research is not geological in nature, the geology of the study area was crucial to the understanding of the behavior of the material present. After developing

reasonable traverses, geological mapping commenced, the traversing process took 2 days, with the fact that some areas were not accessible while others were dominantly covered with topsoil and fewer outcrops were denoted across the study area. Geological harmer, clip broad, notebook, pen, and topographical map were used to fulfill the purpose of geological mapping, rock samples were also collected (this collection was done per outcrop encountered) to further the understanding of rock types within the study area. The geological map was later drafted and compared with a large-scale geology of the study area.
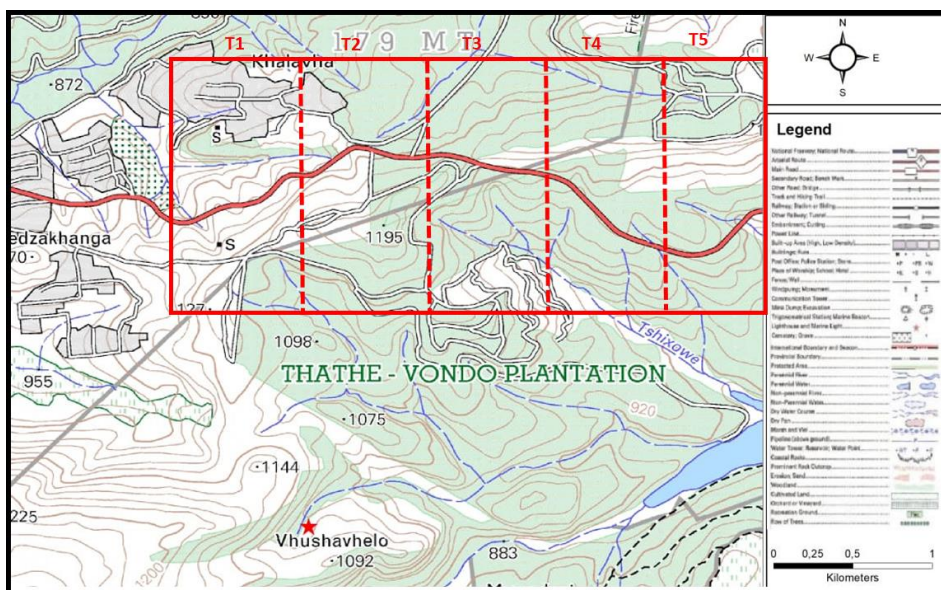
Figure 3.3 Topographical map of the study area with the designed
traverses across an area of interest

3.2.2 Laboratory tests

Most geotechnical investigations associated with landslides involve the characterization of the soil. In order to acquire such information, soil samples were collected in the vicinity of the active landslides. The purpose of the exercise was to identify the types of soils present in the study area and perform the appropriate classification.

Sample bags containing approximately 5 kg of soil samples were labeled. As already indicated that the Auger was utilized to acquire soil samples as deep as 0.5 m from the soil surface. The samples were prepared in the laboratory for particle size analysis, Atterberg's limit testing, and measurement of the mechanical properties of soil. The protocols are described below.

3.2.2.1 Sieve analysis

Particle size analysis (also known as sieve analysis) was carried out to classify the soil materials, determine their textures, and estimate the size of the grains. The latter is known to greatly influence the behavior of the soil mass; hence, its determination.

The following apparatuses were used: a stack of sieves with the pan at the bottom and a top cover, a Sartorius balance accurate to within 0.01 g, a mechanical sieve shaker, a plate, and the Vacutec drying oven.

To determine the grain size distribution, the samples were placed in the Vacutec oven and dried overnight. The dried soil was sieved through a stack of sieves placed on the mechanical shaker. Sieves were arranged from top to bottom starting with coarser and ending with a smaller opening. The amount retained on each sieve was collected and weighed. This was later used to calculate the fraction of material passing each sieve as a percentage of the total sample being sieved.

Before commencing with sieving, all sieves, as well as the bottom pan, were cleaned, weighed, and their initial weights were recorded. The sieves were then assembled from the bottom up in ascending order of sieve number starting with the finest #200 (0.075 mm) sieve (see Figure 3.4). An oven-dried sample was prepared and weighed on the Sartorius balance. The sample was poured into the top 7 mm sieve and was gently shaken by hand before placing the lid cover on the stack. The loaded stack was placed on

the mechanical shaker and shaken for an hour (60 min). Upon removing the stack, the material retained on each sieve was carefully weighed and expressed as percentage passing plotted on a logarithmic graph. From the plotted gradational curves, the coefficient of uniformity (C_u) and curvature (C_C) were calculated as follows:

$$C_u = \frac{D_{60}}{D_{10}}$$ (3.1)

$$C_C = \frac{D_{30}^2}{D_{10} \times D_{60}}$$ (3.2)

Where D_{10}, D_{30}, and D_{60} are respectively the grain size corresponding to 10%, 30%, and 60% passing.

Figure 3.4 Sieves used for particle size analysis

3.2.2.2 Atterberg's limits

The objective of testing for Atterberg's limits was to determine the basic index nature of the soil. This gives an idea of the strength and settlement characteristics of the material in-situ. It is also the primary form of classification of fine-grained soils. Atterberg's limits are used to determine the boundaries between the different states of fine-grained soils. The

classical states associated with clay are liquid, plastic, semisolid, and solid. However, the laboratory tests were performed to determine only the plastic and liquid limits of fine-grained soil because of the logistical limitation of the laboratory.

The liquid limit (LL) is defined as the water content at which a pat of soil in a standard cup and cut by a groove of standard dimensions flows together at the base of the groove for a distance of 13 mm (1/2 in.). When subjected to 25 shocks from the cup being dropped 10 mm in a standard liquid limit apparatus operated at a rate of two shocks per second (Das, 1997).

The liquid limit property of the fine-grained fractions of the samples was tested using a Casagrande liquid limit device, a grooving tool, a water bottle, mixing dishes, a spatula, and the Vacutec drying oven.

The testing procedure began by cleaning up and calibrating the Casagrande equipment. The calibration involved the setting of the drop of the cup to a consistency drop height of 10 mm. The soil was then passed through a #40 sieve, collected, and air-dried. The fraction of soil was thoroughly mixed with a small amount of distilled water until it turns into a smooth uniform paste. The moist sample was placed on the Casagrande's cup and smoothening to the maximum depth of 8 mm (see Figure 3.5). The groove was cut at the centreline of the sample in the cup. Next, the device was cranked at 2 revolutions per second until the two halves of the soil pat come into clear contact of about 13 mm long at the bottom of the groove. The number of blows (N) that caused the closure was counted and recorded. The sample in the pat was collected, weighted together with the Can, labeled, and dried in the oven at 110°C for 6 hours. The weight of the dried sample was also determined. The test was repeated 3 times at different moisture contents; this enabled the production of successively lower numbers of blows to close the groove. The number of blows in each trial was then plotted against the water content. The best-fit straight line through the plotted data points was constructed for which the liquid limit (LL) was determined as the water content corresponding to 25 blows.
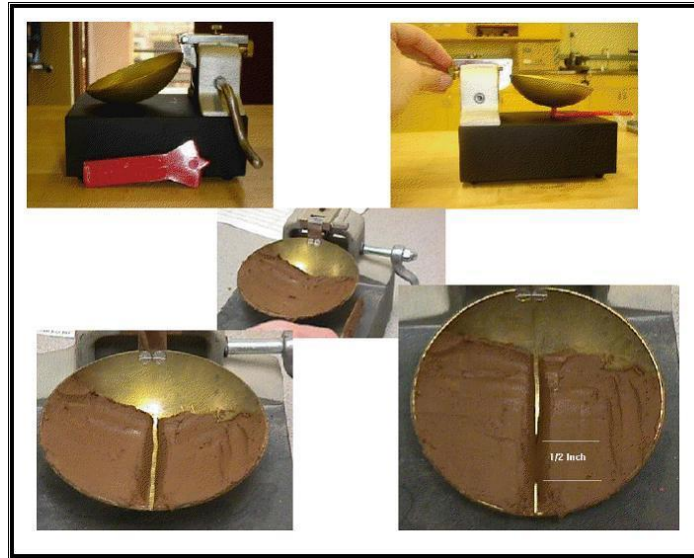
Figure 3. 5 Example of Casagrande's cup and the procedure (Modified After Muhammad, 2017)

In plotting the limit liquid data, some samples do not conform well to the expected straight line. This may be ascribed to the inadequate mass of soil in the brass cup, inadequate rate of blows, or inadequate height of fall. To compensate for this, Equation (3.3) was used (.Das, 1997):

$$LL = W_n \left(\frac{N}{25}\right)^{0.121}$$ **(3.3)**

Where LL is the liquid limit of the soil; N is the number of blows in the liquid limit device; and W_n is the corresponding moisture content.

The plastic limit testing of the soil samples was looked at next. The plastic limit (PL) of soil is defined as the water content at which the soil begins to crumble when rolled into a thread of 3 mm in diameter (Das, 1997).

In terms of the test work itself, the plastic limit was tested by taking 3 ellipsoidal-shaped masses of the sample. The masses were rolled using a plastic limit device with a calibrated opening of 3.18 mm until the soil crumbles. The thread was crumbled until it reaches a uniform diameter of 3 mm, and once they have reached the uniform diameter of 3 mm, the soil was considered to be at its plastic limit. The mass was rolled between the palm or the fingers of the hand and the glass plate. Sufficient pressure was

used to roll the mass into a thread of uniform diameter at about 90 strokes per minute. From the perspective of sample preparation, a stroke is one complete motion of the hand forward and back to the starting position. The thread was deformed until its diameter reaches 3.2 mm (1/8 in.); this took no more than 2 min. When the thread reached the correct diameter, it was broken into several pieces. Kneading, reforming of the pieces into ellipsoidal masses and re-rolling ensued. This was done until the thread crumbled under pressure and could no longer be rolled into a 3 mm diameter thread. At this critical point, the soil was considered to be at its plastic limit.

The crumbled soil was collected and weighed, dried and weighed again for water content. It should be noted that the mass of the can was determined beforehand so that the crumbled soil and the containing can be weighed as a single entity. Three replicates of each plastic index test were performed for consistency. The water content was deemed to represent the plastic limit PL of the soil. Finally, the plastic index was calculated as follows (Das, 1997):

$$Plastic\ index\ PI = LL - PL \qquad\qquad \textbf{(3.4)}$$

Where LL and PL are the liquid limits and the plastic limit values of the soil.

In addition to Equation (3.4), Table 3.2 was used to interpret the description of the plasticity index of the soil samples.

Table 3.2 Classification of the plasticity index (Burmister, 1949)

Plasticity Index %	Description
0	Nonplastic
1 – 5	Slightly plastic
5 – 10	Low plasticity
10 – 20	Medium plasticity
20 – 40	High Plasticity
>40	Very High Plasticity

3.3 Remote sensing-based measurement

Rock slope instability is commonly noticed through the disturbance caused by the vegetation coverage. This can therefore be used as a proxy for the extent and recurrence of rock slope instability. The remote sensing techniques of Normalized Difference Vegetation Index and Weight of Evidence covered in Section 2.6.4 were used in this thesis. Relevant details of their implementation are described below.

3.3.1 Normalized Difference Vegetation Index

The Normalized Difference Vegetation Index (NDVI) involved two main procedures: the compilation on one hand as well as the processing and classification of ASTER data on the other. The NDVI technique was used to detect the change in the vegetation of the study area with time.

ASTER images were used in order to perform the analysis of the NDVI. These images are rendered with pixels of 15 m resolution capable of reproducing small change taking within the area.

The dataset was from the ASTER L1T which is a Precision Terrain Corrected Registered At-Sensor Radiance Product. Two ASTER scenes, from Path 169 and Row 76, acquired in November 2004 and 2017 were retrieved from https://lpdaac.usgs.gov. The database is maintained by the NASA Land Processes Distributed Active Archive Center (LPDAAC) at the USGS/Earth Resources Observation and Science (EROS) Center, Sioux Falls, South Dakota. Only the bands in VNIR spectral region were used in the present study. The VNIR region was selected based on the fact that its spectral resolution is capable of detecting vegetation conditions (Jensen, 1986). Moreover, its spatial resolution is deemed appropriate for the level of spatial details required for the type of land in the study area (Table 3.3).

Table 3.3 Wavelength ranges and spatial resolution of ASTER bands

Spectral region	Band number	Wavelength range (μm)	Spatial resolution (m)
VNIR	1	0.52 – 0.60	15
	2	0.63 – 0.69	
	3	0.78 – 0.86	

This brings us to talk about the second part of the NDVI methodology, that is, the processing and classification of the ASTER data. This was carried out using the ENVI 5.0 Image Analysis Software. The three VNIR bands were stacked together to build a new multispectral image. The resultant image was a subset of the size of the study area. The log residuals calibration was used to remove solar irradiance, atmospheric transmittance, instrument gain, topographic effects, and albedo effects from radiance data. The calibration tool converted radiance data to a pseudo reflectance image which is useful in vegetation mapping (Green and Craig, 1985).

In addition to this, supervised classification of the types of land cover in the study area was implemented on the log-residuals calibrated ASTER multispectral image of 2017. This was conducted to evaluate the relationship between NDVI values and the types of land cover. Furthermore, the true colour satellite image from Google Earth Pro which was acquired in 2017 was used as the gathering tool of the training classes of the types of land cover. The following land covers characteristics of the study area were identified: evergreen forest, tea plantation, vegetation, bare soil/rock, built-up land, and waterbody. The extracted representative Regions-of-Interest (ROI) of the land cover were examined for separability. This is crucial as it greatly affects the accuracy of the subsequent supervised classification. In this study, the pairs of all types of land cover attained separability values in the range of 1.9 to 2 indicative of excellent separability. The equation followed in the determination of NDVI is denoted by Equation 2.49.

The ROIs of the land covers formed the training dataset which was used for supervised classification using the Minimum Distance algorithm. This algorithm uses the mean vectors of each ROI and calculates the Euclidean distance from each unknown pixel to the mean vector for each class. Pixels in the image were then classified into the closest class.

3.3.2   Construction of the landslide susceptibility maps

The Weight of Evidence (WOE) model was utilized to analyze landslide susceptibility. The modeling exercise was implemented based on the theories covered in Section 2.6.4.

Firstly, the spatial analysis tool ArcGIS version 10.5 was used to reclassify the ASTER datasets in terms of slope, aspect, land cover types and elevation on a scale of 1 to 5. The lithology, stream, road, and lineament were acquired as either polygons or polylines; therefore, their subsequent raster maps were reclassified to create ranked maps on a scale of 1 to 5. In other words, the subclasses of each thematic layer were assigned a value between 1 and 5. A subclass assigned a value of 5 was considered to be the most influential one and the least influential subclass was assigned a value of 1. For instance, the slope angle between 0-6°, 6-12°, 12-18°, and 18-68° was assigned a value of 1, 2, 3,4 and 5 respectively.

Each thematic layer was given a value based on its significance as far as its contribution to landslide occurrence is concerned. Thematic layers that are deemed to be more significant are given a higher value. For example, the slope was given a weight of 8 because it is considered the most important out of the eight thematic layers used. The entire exercise is summarised in Table 3.4 for the eight thematic layers. The weight of the causative factor (or thematic layer) was then multiplied by the rank of subclasses in that thematic layer. Finally, the intermediary result was summed for all eight thematic layers to produce the landslide susceptibility index.

Table 3.4 Weights and ranks for the causative factors to model an expert based landslide susceptibility map

Thematic class	Subclass	Rank	Weight	Thematic class	Subclass	Rank	Weight
Slope (°)	0-6	1	8		Flat & E	1	
	6-12	2			S	5	
	12-18	3		Aspect	SE & SW	3	4
	18-68	5			N, NE & NW	2	
Road (m)	0-20	5	7	Geology	Arenite	4	
	20-30	4			Basalt	2	3
	30-40	3			Norite	2	
	40-50	2			0-20	5	
	>60	1			20-30	4	
Elevation (m)	1250-1250	5		Stream (m)	30-40	3	2
	1100-1250	4	6		40-50	2	
	900-1100	3			>60	1	
	705-900	1			0-20	5	
Land cover	Evergreen forest	1		Lineament (m)	20-30	4	
	Vegetation	2			30-40	3	
	Tea plantation	2	5		40-50	2	
	Waterbody	3			>60	1	1

3.4   Assessment of rock-slope stability

Three approaches were followed in order to investigate the rock-slope stability of the study area. They are the kinematic analysis, the limit equilibrium and numerical simulation.

The kinematic approach consisted of analysis relating to planar failure, wedge failure, circular failure and topping failure. Two computer programs were used to perform kinematic analyses: DIPS and SWEDGE. The limit equilibrium approach, on the other hand, looked at toppling, transitional and rotational analyses. Toppling analysis was done by means of conventional toppling and sliding charts covered in Section 2.3.1 while transitional and rotational were performed using RocPlane as the numerical program.

The kinematic and limit equilibrium approaches are covered in Section 3.4 while the computer-based simulation of the rock-slope stability is presented in Section 3.5.

3.4.1   Kinematic analysis

The kinematic analysis was utilized in an attempt to describe the translational failures that may occur around the wedge and plane formations present in the area of study. Nonetheless, for the analysis to make sense, several input parameters were needed. These include the structure of the rock mass structure and the geometry of the material (i.e. soil and rock). The effects of these parameters are critically evaluated to identify the possibility of the material failing.

In this thesis, the kinematic analysis was carried out using Stereonet plots generated by the DIPS computer program (see Figure 3.6). DIPS was chosen because it has been reported to have the ability to visualize and determine the

kinematic feasibility of the rock slope using friction cones, daylights and toppling envelopes (Rocscience, 2001a). To this end, geological mapping data conducted along all unstable slopes were used to generate Stereonet plots as exemplified in Figure 3.7.
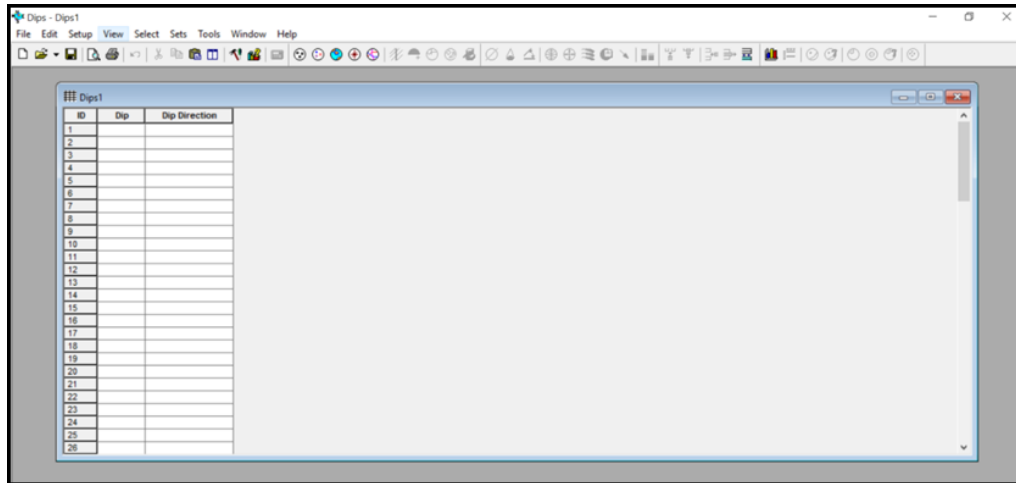
Figure 3.6 Starting a new project in DIPS
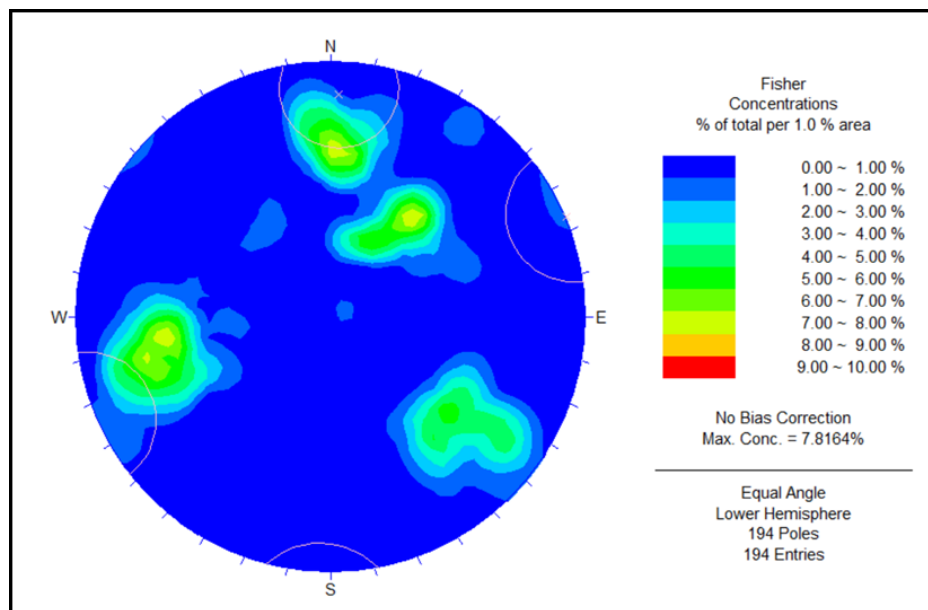
Figure 3.7 Example of a Stereonet plot generated in DIPS

Although the Stereonet technique appears to be suitable for the research problem at hand, it has some shortfalls. The technique can only recognize a

potential sliding failure that involves single discontinuities. It cannot cater for failures involving multiple joints or joint sets, internal deformation and fracture. Because of this, the SWEDGE program was brought in to supplement the Stereonet technique. Indeed, SWEDGE can estimate the factor of safety (FoS) of a wedge failure. It also incorporates the probabilistic analysis of variations in the properties of joint sets on the FoS (Rocscience, 2001b). Computer-based tests were performed by importing Stereonet data into SWEDGE for six selected landslides along the Thulamela Municipality roads.

The following paragraphs present the procedure employed in setting up DIPS and SWEDGE for the purpose of kinematic analysis.

In DIPS, the first step was to create a new project as shown in Figure 3.5. Next, the geotechnical data collected during the geological mapping covered in Section 3.2 was used as the input parameters to DIPS. Dip, strike and dip direction of the geological features mapped on-site were inputted. This enabled the computation of Stereonet plots for later use and analysis. The Fisher concentration was also tested for the identification of zones prone to failure based on the concentration of wedges created within the area.

SWEDGE followed the same basic workflow as DIPS; however, the difference was the input parameters required. Here, the dips and dip directions of the set of joints, the upper face, and the slope face were entered. In addition to this, the dip, dip direction, and trace length of tension cracks were incorporated. The cohesion of the soil obtained from the laboratory tests presented in Section 3.2.2 was also included as shown in Figure 3.8. From this, the analysis was run as per theoretical models in Section 3.2.1 while the options for displaying end results can be either probabilistic or deterministic (see Figure 3.9).
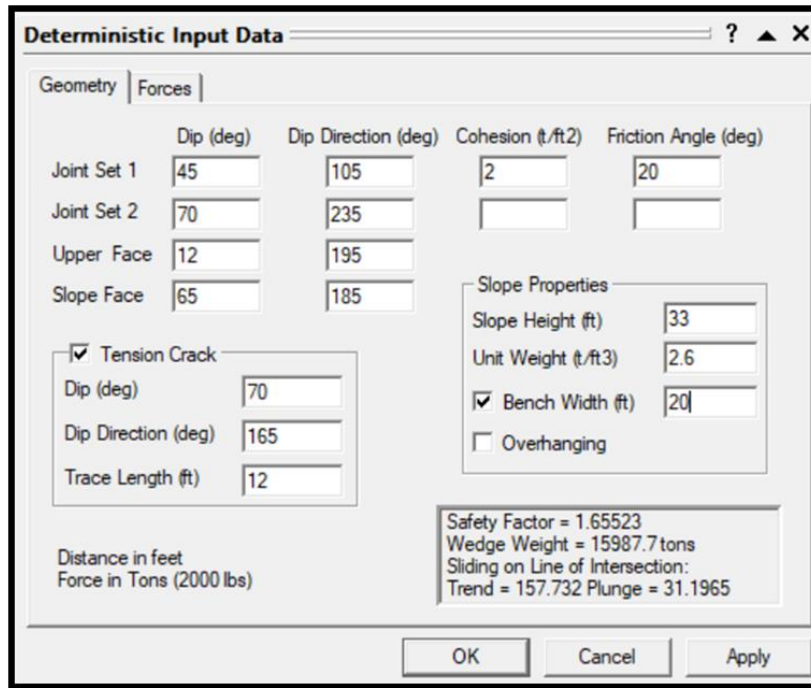
Figure 3.8 Entering the input data in SWEDGE
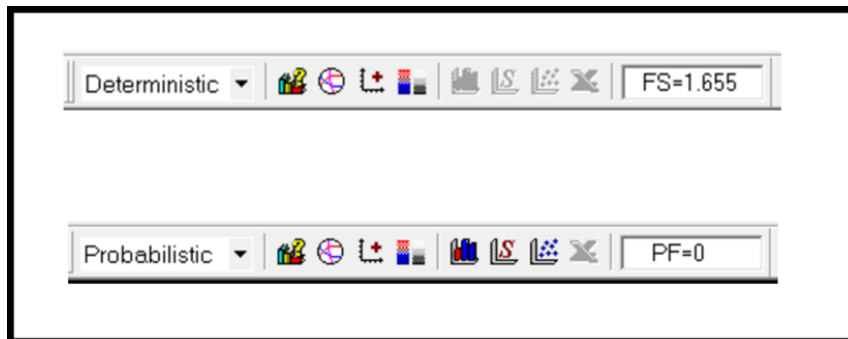
Figure 3.9 Analytical approaches available in SWEDGE

The deterministic option presents the results as a force field of the slope with a wedge in it. The benefit is the possibility of seeing how the wedge would rotate in time steps once the stability conditions of the area are changed. The additional benefit is the possibility of determining the expected extent of the deposition of the falling wedge as exemplified in Figure 3.10.
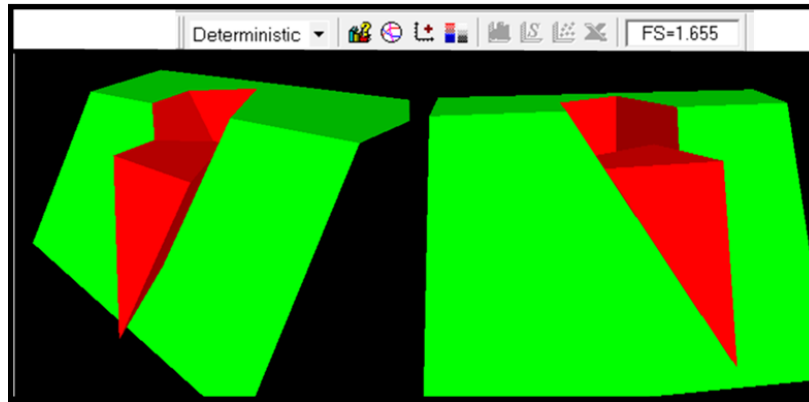
Figure 3.10 Example of a SWEDGE simulation output rendering

The probabilistic option renders the SWEDGE results in two ways: a histogram plot of FOS versus relative frequency or a scatter plot of FoS versus wedge weight, wedge length, a tension crack friction, and joint strength among others (see Figure 3.11). The probabilistic interpretation was extensively used in this thesis to describe the behavior of the rock and soil mass. An example showing the probabilistic analysis of both the histogram and scatter plots is illustrated in Figure 3.12.
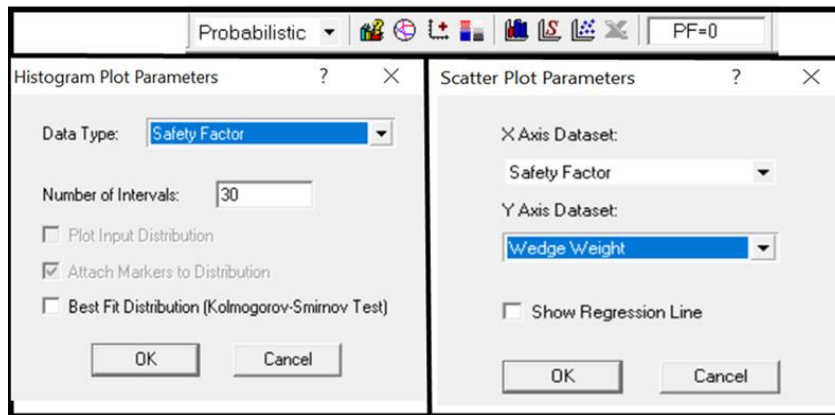
Figure 3.11 Probabilistic rendering of SWEDGE results
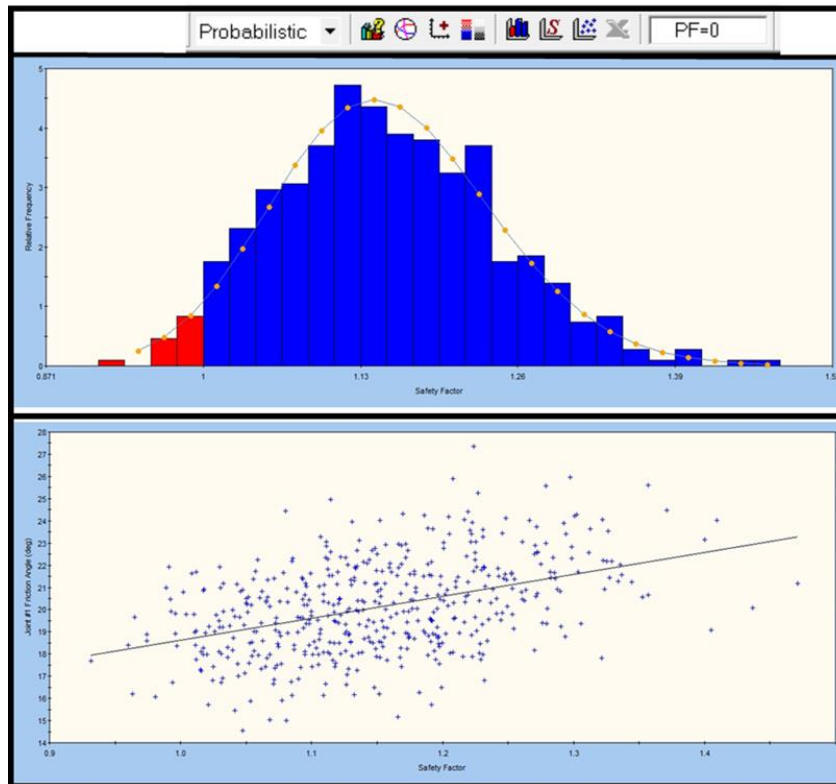
Figure 3.12 Example of the histogram and scatter plots rendered in
SWEDGE

3.4.2 Limit Equilibrium analysis with SLIDES and RocPlane

Limit Equilibrium analysis is based on the classical models of Bishop and Janbu
presented in Section 2.3.4. The numerical implementation of these analytical
models is available in SLIDES and RocPlane. The two computer programs
were selected because they are purported to be adequate for a wide-scale
range of geotechnical problems (Rocsience, 2011a).

RocPlane was set up following the steps similar to SWEDGE; however, the
notable difference was the input parameters needed: angle and height of the
slope, the direction of tension crack, angle of the upper face, and cohesion of
soil (see Figure 3.13).
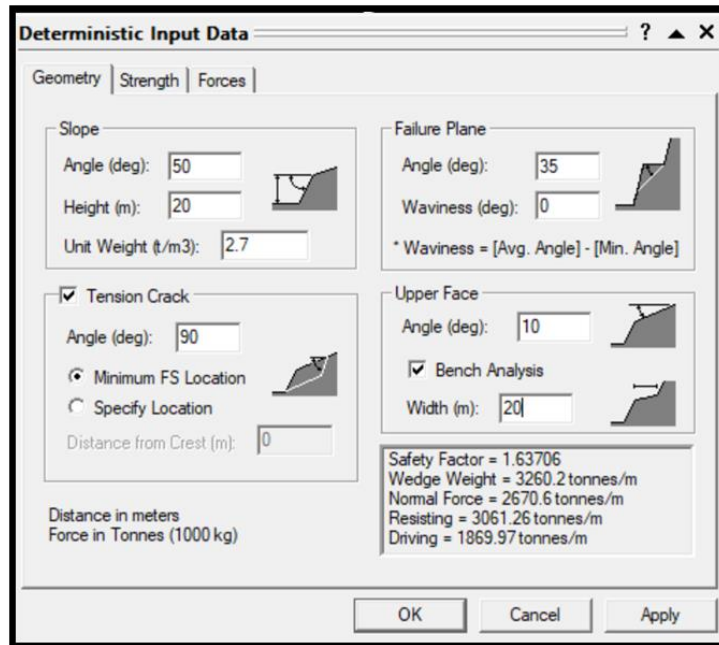
Figure 3.13 Entering the input data in RocPlane

For the limit equilibrium analysis performed in this section, deterministic and probabilistic representations of simulation results are also available like with SWEDGE. They can be invoked and rendered in a similar fashion as Figure 3.12. The expected deposition of the falling wedge can also be predicted (see example in Figure 3.14).
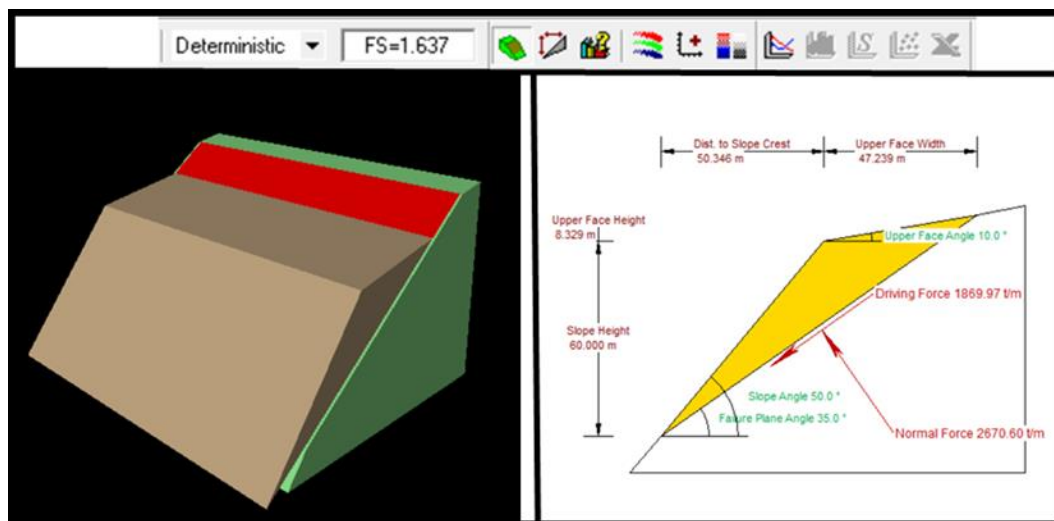
Figure 3.14 Example of a RocPlane simulation output rendering

The procedure used in setting up SLIDES has already been described in the previous paragraphs. It is however noteworthy to state here that SLIDES was utilized to estimate the FoS values of the slope for several scenarios. The FoS values can be computed following various models covered in Section 2.3.4. The different outcomes can be compared at once.

In terms of model building, the exercise starts with the creation of a new project (see Figure 3.15).
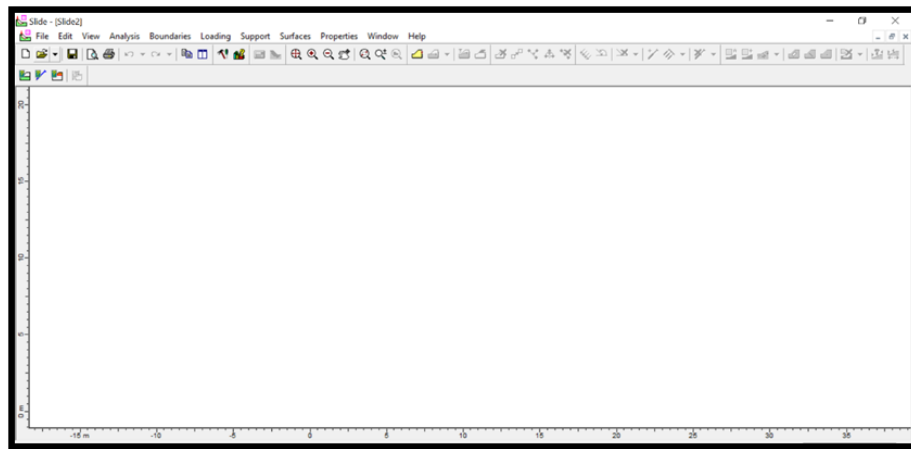
Figure 3.15 New Project in SLIDES

Similar to other modeling platforms, the new project required the delimitation of the model limitation in XY coordinates. For that, various X and Y coordinates defining the region were entered. The ultimate goal of this step was to draw the model of the region as shown in Figure 3.16.
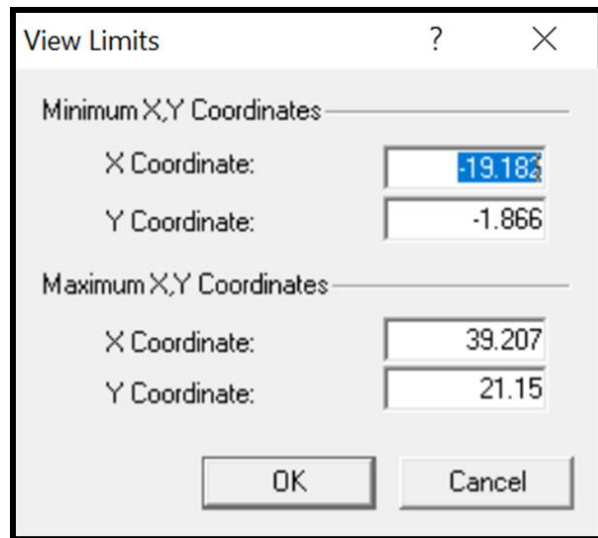
Figure 3.16 Generating limits of the model in SLIDES

Upon generating the boundaries of the model, the actual initial conditions of the simulation are defined next for the project. Inputs such as the statistics associated with groundwater conditions, the computational methods, and the failure directions are captured. This is illustrated in Figure 3.16. Several tabs associated with Figure 3.17 are also illustrated in Figures 3.18 – 3.20. The models behind these tabs were also presented in Chapter 2 while the choice of input data was guided by the results of the tests described in Section 3.2. The correct values of input data and the appropriate selection of procedural approaches were of paramount importance. This is because the study determined how realistic the computer modeling of the actual rockmass associated with the study area would be. For a thorough interpretation of the results, several methods of analysis were considered as per Figure 3.18. The motivation was to compare various approaches to the problem. However, corresponding results were interpreted based on the performance of each approach as was reviewed in Chapter 2.
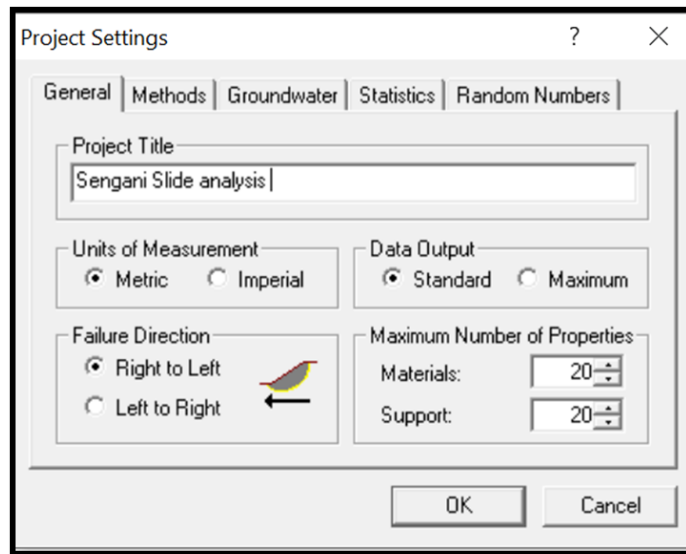
Figure 3.17 Project settings using the SLIDES model
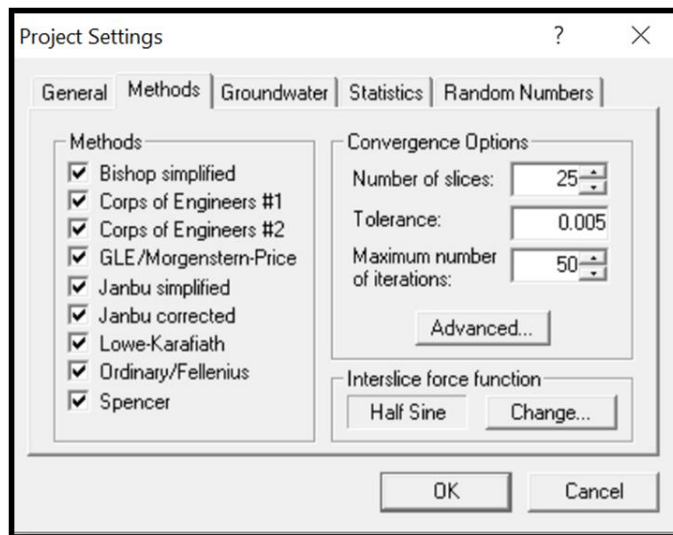
Figure 3.18 Methods used for analysis

The other important factor was the groundwater regime set at 9.81 KN per cubic meter. This value was estimated in the laboratory after performing several tests on soil material. Statistics of the yearly rainfalls in the area were also considered in estimating the groundwater regime (see Figure 3.19).
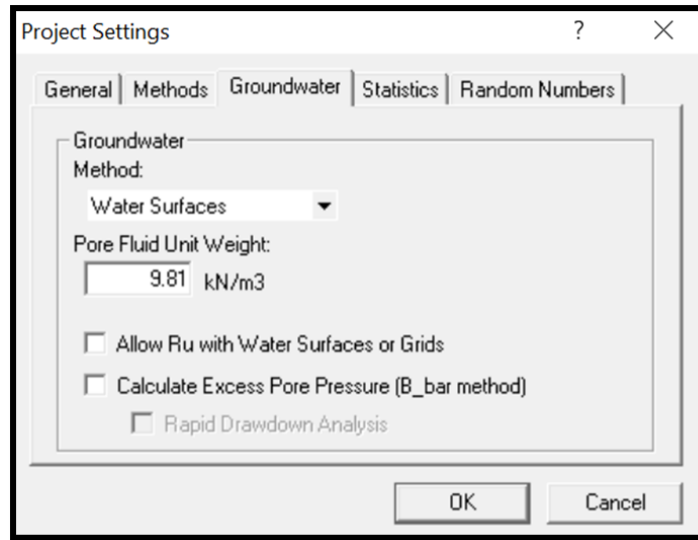
Figure 3.19 Setting of groundwater conditions

It is important to stress that theoretical models underpinning all these computer programs are generally based on simplifying assumptions. These depart from the real behavior of soil and rock masses and diminish the value of output results. To circumvent the limitation, a degree of randomness and unpredictability is supposed to be allocated to the modeling frameworks. In this thesis, the exercise was implemented by resorting to the probabilistic analysis built upon the Monte-Carlo sampling method. Indeed, the Monte-Carlo method refers to the allocation of randomness to a phenomenon by means of random number generators. Figure 3.20 illustrates how this was set in SLIDES while the properties of the material measured based on the laboratory tests and field observations are inputted as shown in Figure 3.21.
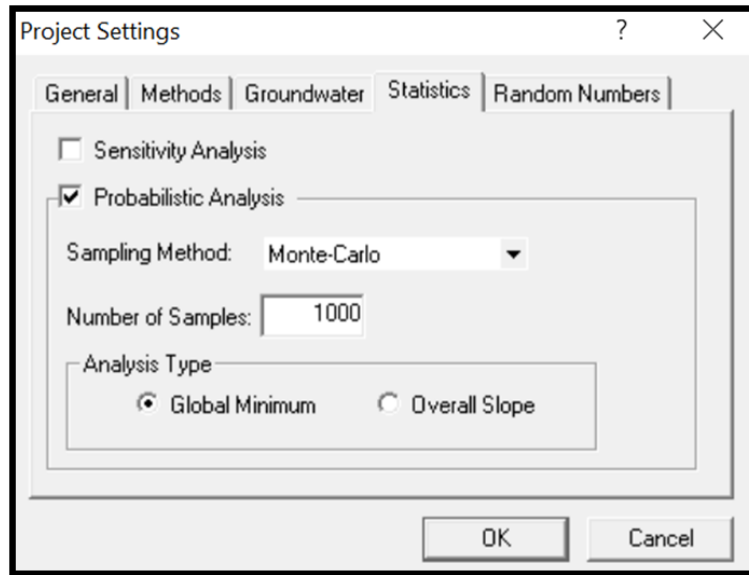
Figure 3.20 Statistics methods used
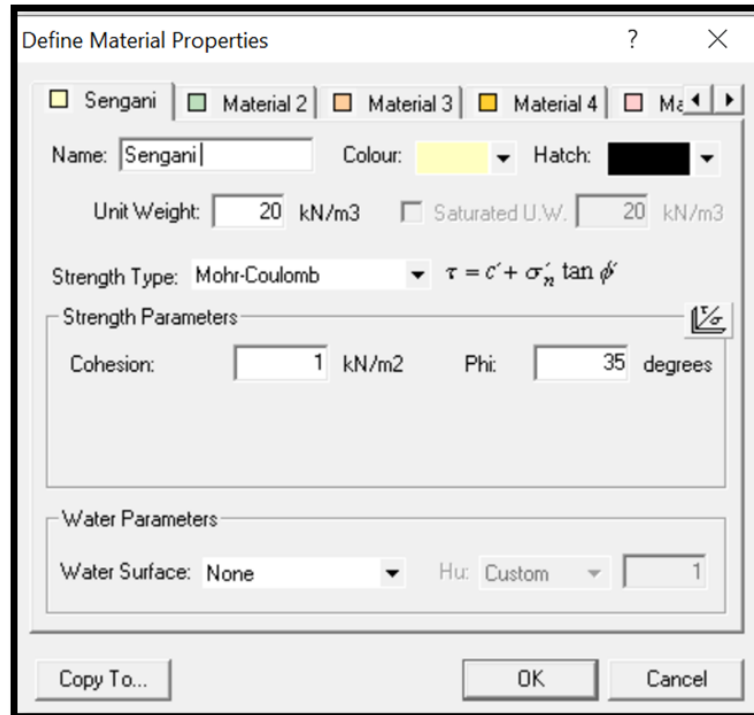
Figure 3.21 Definition of the properties of the soil and rock mass

The next step was the definition of the boundaries of the excavation upon which the roads were constructed. An example is indicated in Figure 3.22 with

coordinates entered based on field surveying and existing maps of the region. The inputs in Figure 3.22 are rendered automatically and diagrammatically as the excavation model in Figure 3.23.

```
Enter vertex[esc=quit]: 15 4
Enter vertex[u=undo,esc=quit]: 6.5 4
Enter vertex[u=undo,esc=quit]: 4.5 4
Enter vertex[c=close,u=undo,esc=quit]: 1 4
Enter vertex[c=close,u=undo,esc=quit]: -1 4
Enter vertex[c=close,u=undo,esc=quit]: -10 4
Enter vertex[c=close,u=undo,esc=quit]: -10 -8
Enter vertex[c=close,u=undo,esc=quit]: 15 -8
Enter vertex[c=close,u=undo,esc=quit]: c
```

Figure 3.22 Procedure adopted when entering external boundaries (modified after Rocscience, 2001), the number in bold black are the coordinates used to generate the excavation boundaries
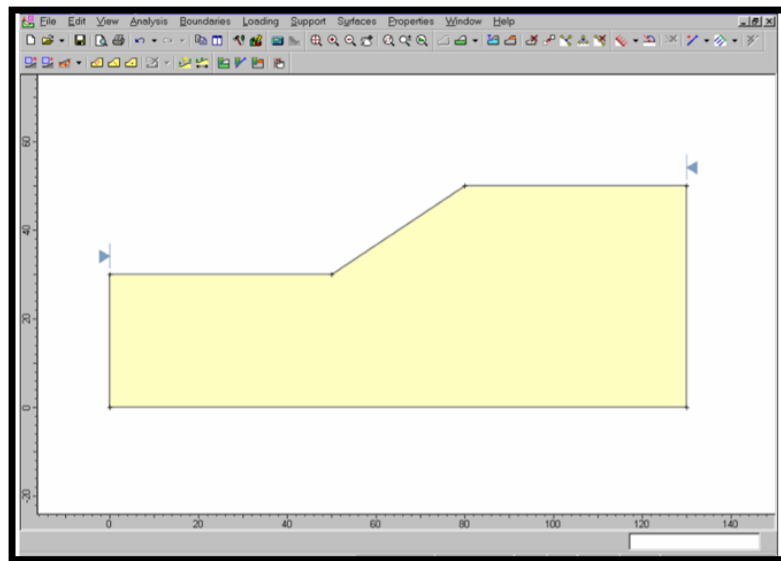
Figure 3.23 Excavation boundaries

Finally, computational routines are selected and defined in terms of grid spacing of the limit equilibrium analysis of the excavation model. The theoretical background of the computation steps executed in SLIDES was presented in Section 2.3. Other relevant input parameters are also incorporated

before the model is finally solved. The convergence solution to the problem is exemplified in Figure 3.24 with the most likely FoS defined in the inset.
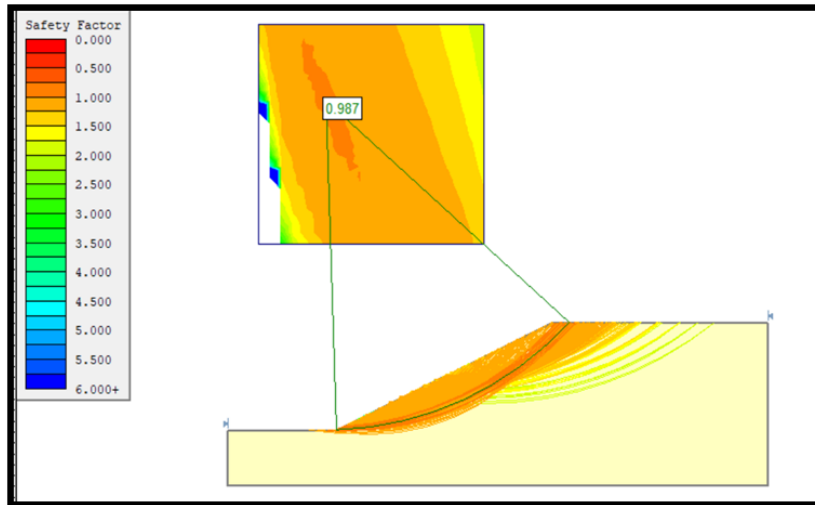
Figure 3.24 Illustration of a modeled excavation mapped with an FoS scale

Various scenarios were simulated and their output results were recorded for later analysis. Several techniques were used for the purpose; they are presented in Section 3.5.

3.5   Numerical analysis of rock-slope behavior

Rock engineers are mostly interested in predicting the conditions for the likely occurrence of landslides and rock failure. To do that, they need to understand the fundamental behavior of the material (soil and rock). This is captured in the shear strength and stress of the material and its interaction with the surrounding environment. In this study, the RocData software was utilized to generate such a fundamental behavior of the solid mass while taking the FoS values computed in Section 3.4.2 by SLIDES into account.

The FEM-based analysis was supplemented with data generated from the RocFall program. The latter was used to trace the most likely trajectory paths

of falling rock blocks. RocFall relies on output data imported from the DIPS covered in Section 3.4.1 and rendered as Stereonet plots. The rationale of the numerical analysis is presented in the subsequent sections (Section 3.5.2).

3.5.1 Mechanical properties of the in-situ material

The mechanical properties of the in-situ material are central to geotechnical engineering. They are used to perform numerical simulations under various conditions. Without them, complex systems become difficult to analyze.

In this thesis, the mechanical properties of the soil and rock characteristics of the Thulamela area were measured (see Section 3.2). The properties that could not be measured were sourced from existing literature on the region. Table 3.5 summarises the properties used as simulation input parameters.

Table 3.5 Input parameters to numerical rock slope analysis of the study area

	Symbol	Units	Values
Density	ρ	kg/m^3	1900
Unit Weight	γ	kN/m^3	18
Poisson's ratio	υ		0.39
Young's Modulus	E	MPa	3
Undrained Compressive Strength	q_u	kPa	45-66
Shear Strength	T	KPa	90-250
Cohesive Strength	c	kPa	95-188
Angle of Internal Friction	ϕ	°	20°
Compressibility	m_v		0.15-0.17
Soil Sensitivity	S_t		1

3.5.2   Simulation program with RocData and RocFall

RocData was selected as the simulation tool for the behavior of the rock slope along the Thulamela roads.

Similarly, to other numerical tools, a new project was defined and the mechanical properties in Table 3.5 were captured in various forms. These steps are illustrated in Figures 3.25 and 3.26.
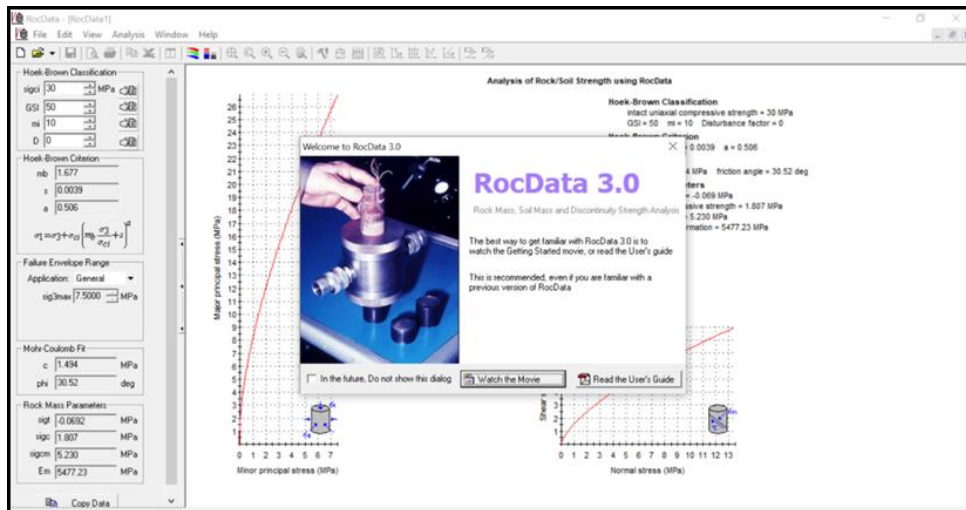
Figure 3.25 New project for the rock slope analysis under RocData
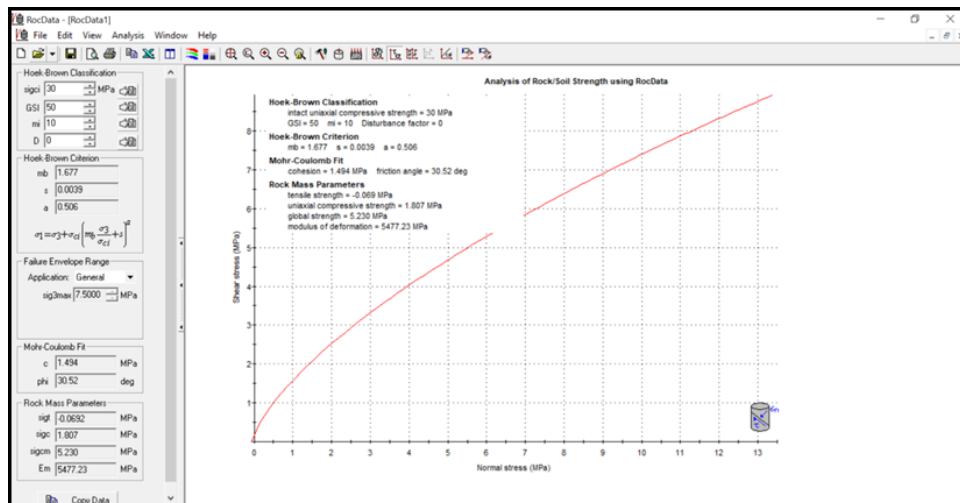
Figure 3.26 Processed of rockfall/soil strength outputted in RocData

RocData was used to estimate the probability of rock failure up the slope, the size of falling rock blocks and their mode of failure. From this information, the RocFall model in Figure 3.27 was set up to track the falling motion of blocks.
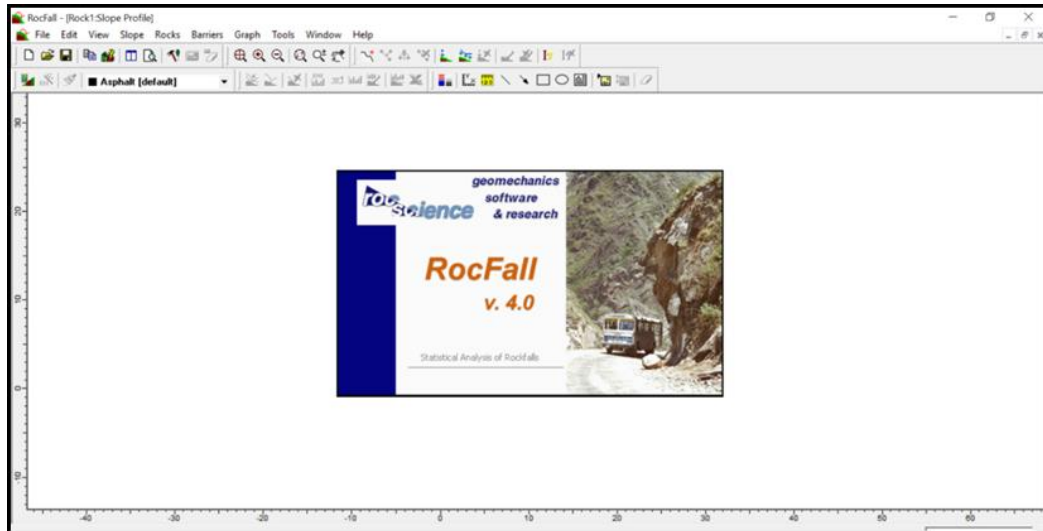
Figure 3.27 New project Window in RocFall

RocFall is a rock trajectory simulator that makes an inventory of the mechanical energies of the rock mass as it rolls, impacts, bounces down the slope, and overshoots into the road past the hill toe. The inventory is solved for the velocity and position of individual rock blocks as shown in Figure 3.28.
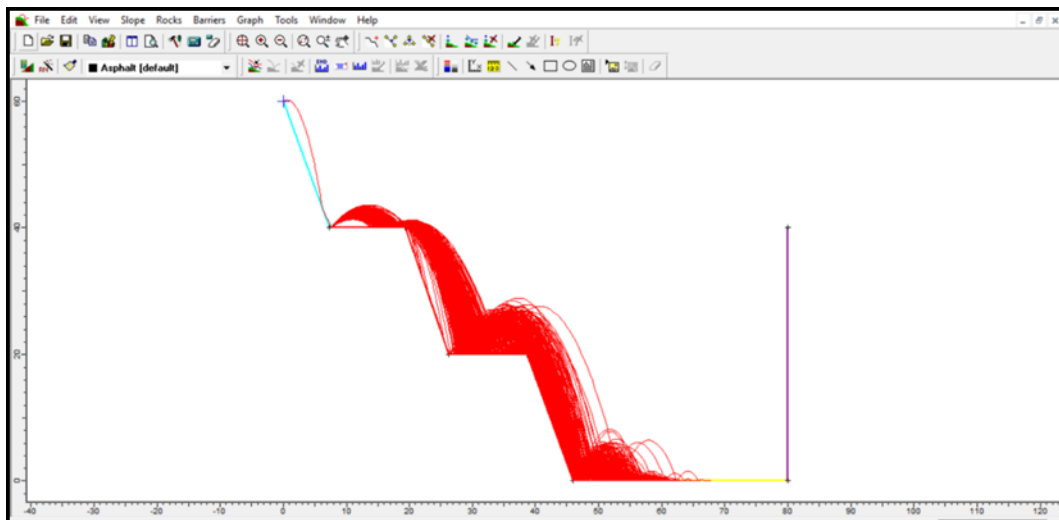
Figure 3.28 Example of trajectory analysis in RocFall

Finally, note that the RocFall model also includes input parameters from fieldwork such as the height of the slope and the properties of the rock.

3.5.3   Influence of rainfall intensity

Extreme rainfall has been recognized as an important factor in slope stability analysis (Lazzari et al., 2013, Lazzari and Piccarreta, 2018). That is why monthly rainfall data of the study area were considered. The statistics of the Thohoyandou and the Thulamela areas were extracted from the database maintained by the South African Weather Service (SAWS). This database is readily available online and freely accessible to the public. Rainfalls between 1989 and 2018 were used with the purpose of identifying major trends and variations within the study area. The intention was to ascertain whether there is a correlation between rainfall statistics and the reported recurrence of slope failure. The analysis of the rainfall patterns helped pinpoint the months of the high likelihood of slope failure. This information finally assisted in understanding the contribution of water to slope failure in the study area.

3.5.4   Complementary simulation work

The numerical experimentation adopted in Section 3.4 hinges entirely on the LEM framework presented in Section 2.3. From the literature review, it was highlighted that the framework suffers some limitations. The most important shortcoming is the failure of LEM to consider strain and displacement compatibility. The Finite Element Method (FEM) enjoys much preference as it overcomes this type of problem.

A set of complementary simulations performed using the Phase 2 software package was initiated. The idea was to validate the numerical models against field observations and hopefully identify the mechanisms behind slope failure.

The theoretical background of the FEM implemented in Phase 2 was presented in Sections 2.5.2 and 2.5.4. Several steps are followed to set up the simulation and input all the relevant parameters before the model is finally solved. These involve the construction of boundaries, mesh generation, boundary conditions, adding traction, field stress, assignment of material properties, and lastly simulation.

Phase 2 was used to simulate stress, strain, and shearing of the material around the road development. Like with all the previous tools, a new project was launched for each simulation scenario as shown in Figure 3.29.
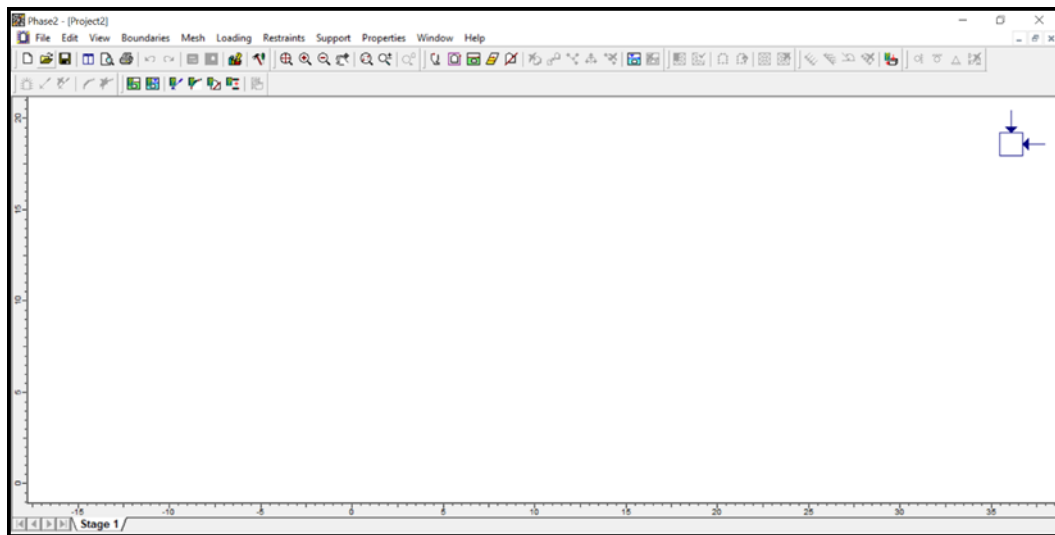
Figure 3.29 New project in Phase 2

The next step was to generate the limits of the road excavation and rockface slopes using existing coordinates of the cross-sectional view of the road. The required coordinates were inputted based on information collected in the field and in the various archival maps of the region. A snapshot of one of Windows

to go through in the definition of the key coordinates of the systems and thereby eventually generating its limits is shown in Figure 3.30.
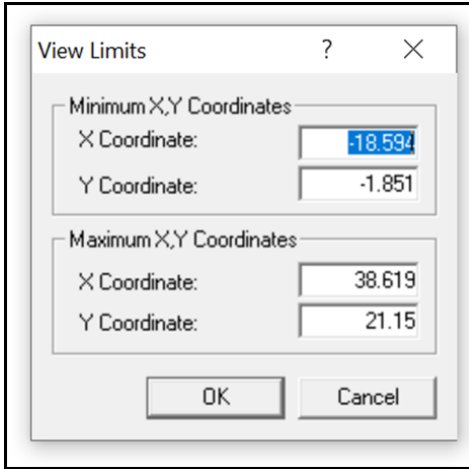
Figure 3.30 Generating limits using Phase 2 model

Next was to define the project settings, that is, the initial and boundary conditions of the model to be used once the Phase 2 solver was launched. In addition to this, the number of iterations and the convergence criteria of the numerical computation were decided upon (see Figure 3.31).
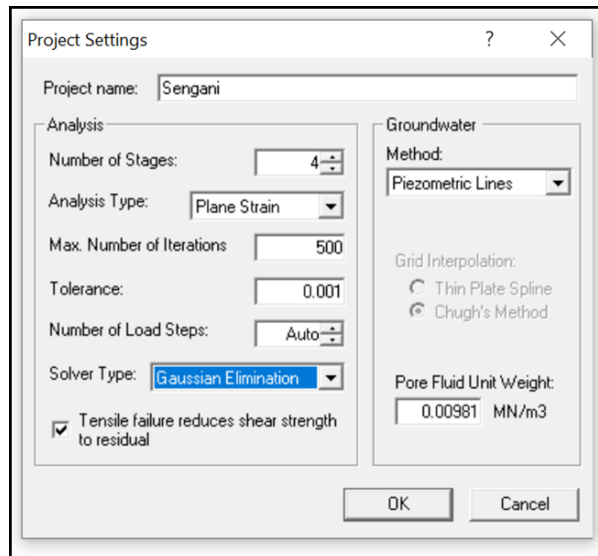
Figure 3.31 Project settings using the Phase 2 model

Upon setting up the Phase 2 solver, it was necessary to enter the boundary geometry and conditions. This critical step was also the opportunity to define the boundary functions of the excavation. Boundary functions specifically refer to the loading conditions of the site. These may include the vibration created on the road surface as vehicles pass by and the effects of rainfall and groundwater amongst others. Figures 3.32 – 3.34 illustrate how boundaries were generated as well as their type and external conditions entered.


```
Enter vertex[a=arc,esc=quit]: 4.5 4
Enter vertex[a=arc,u=undo,esc=quit]: 4.5 -1
Enter vertex[a=arc,u=undo,esc=quit]: 6.5 -1
Enter vertex[a=arc,c=close,u=undo,esc=quit]: 6.5 4
Enter vertex[a=arc,c=close,u=undo,esc=quit]: c
```
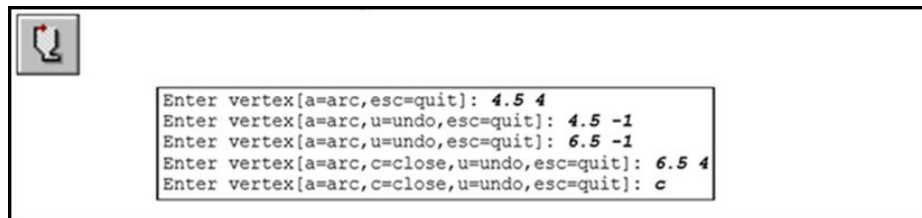
Figure 3.32 Definition of the excavation (modified after Rocscience, 2001)
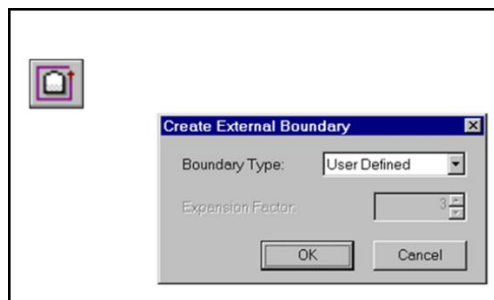
Figure 3.33 Settings followed when creating the external boundary

```
Enter vertex[esc=quit]: 15 4
Enter vertex[u=undo,esc=quit]: 6.5 4
Enter vertex[u=undo,esc=quit]: 4.5 4
Enter vertex[c=close,u=undo,esc=quit]: 1 4
Enter vertex[c=close,u=undo,esc=quit]: -1 4
Enter vertex[c=close,u=undo,esc=quit]: -10 4
Enter vertex[c=close,u=undo,esc=quit]: -10 -8
Enter vertex[c=close,u=undo,esc=quit]: 15 -8
Enter vertex[c=close,u=undo,esc=quit]: c
```
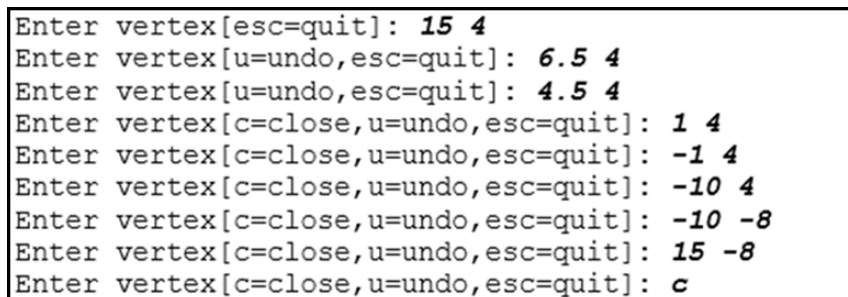
Figure 3.34 Procedure adopted when entering external boundaries (modified after Rocscience, 2001)

At this point, model discretization and meshing were to follow. Based on the level of details required of the FEM solution, graded meshing was used so that the vicinity of the excavation had finer meshes. The meshing element was a 3 noded triangle as this type tends to be numerically stable. Other factors were also defined by trial-and-error as shown in Figure 3.35. The discretized model was then created and meshed (see Figure 3.36).
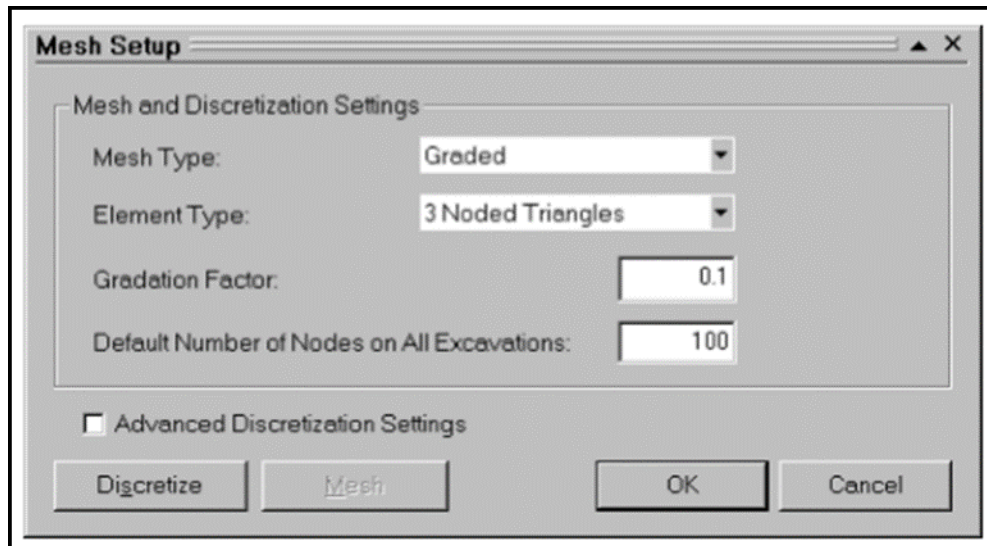
Figure 3.35 Settings selected for mesh generation
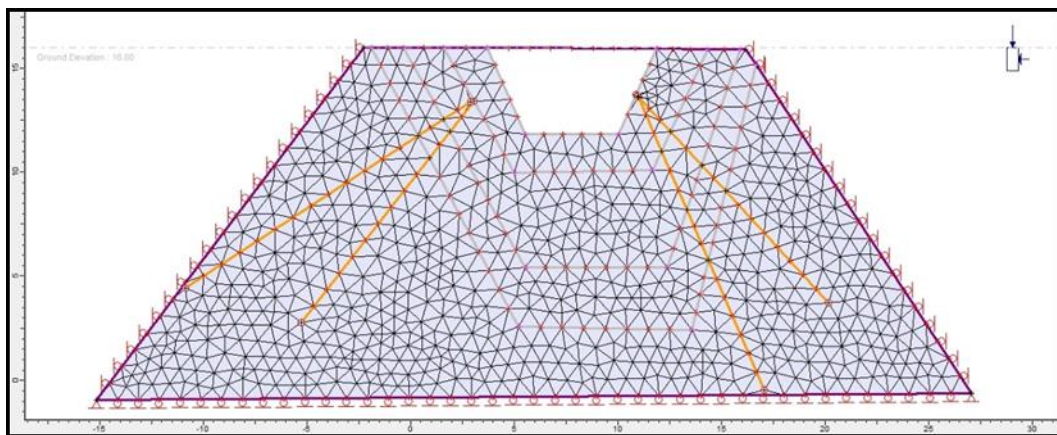
Figure 3.36 Mesh generated using Phase 2 with the road profile based on surveyed field measurements of the width and depth of the excavation

Note that in defining the boundary conditions, some segments of the model were restrained while others were freely movable as labeled in Figure 3.37.
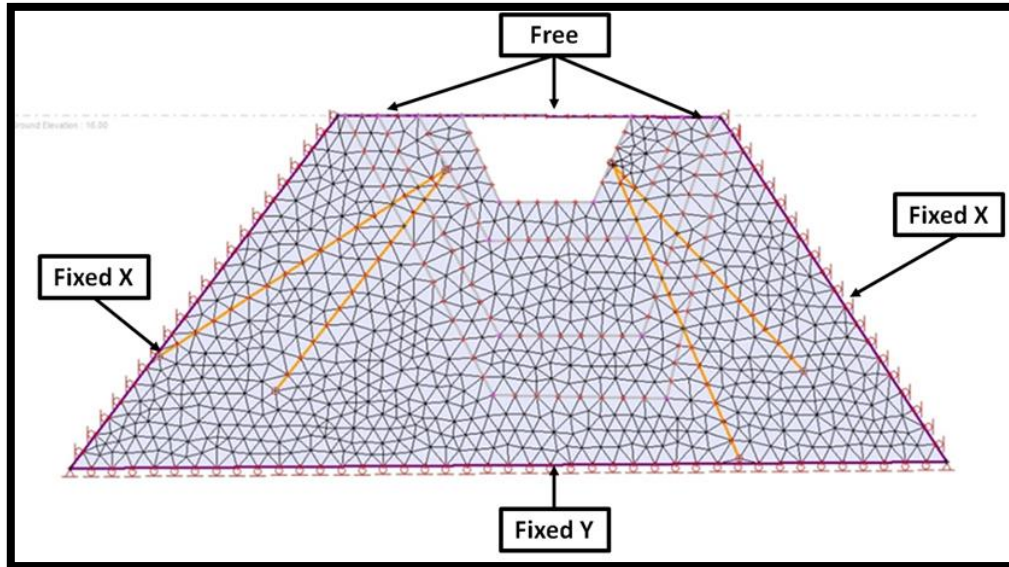
Figure 3.37 Example illustrating the definition of the boundary conditions

In several studies, traction is usually defined last. Traction refers to the loading conditions of the free segments; it is defined both for the horizontal and vertical components as shown in Figure 3.38.
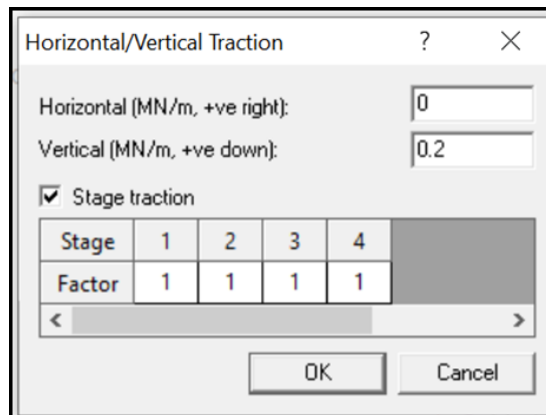
Figure 3.38 Adding traction: since blasting took place at every stage of road construction, traction was assumed to occur throughput but was kept at 1 to obtain reliable results while 0 means no traction

The next step was to define the field stresses at play around and within the rock mass model. Since the model is a surface excavation, the gravity stress field needed to be defined. Then, the vertical and horizontal distribution of the stress field was set at 1.5 throughout (This was done because surface excavations have high horizontal stresses than vertical stresses). The remaining entries were captured based on the measured properties of the corresponding type of material (see Figure 3.39).

Figure 3.39 Field stress inputs. The unit weight of overburden is from laboratory testing of the samples, the stress ratio was kept at the commonly used default value of 1.5 while the elevation was taken from remote sensing data

In the final leg of setting the simulation model, the material properties of the project were considered. The values used in the simulation models are listed in Table 3.3; they are based on the laboratory tests in Section 2.2.

The entry form for material properties for Phase 2 is shown in Figure 3.40. Note the selection of the Mohr-Coulomb as the failure criterion; this is to enable easy comparison between LEM and FEM outputs on the basis of the use of the same failure model. The theoretical framework of the failure model was extensively discussed in Section 2.4. It is indeed here in the prediction of the probability of occurrence of rock slope failure.

Figure 3.40 Material properties of the project

The last step before the simulation model could be run was to assign appropriate properties corresponding to the various layers making up the road. A similar assignment could be done for the various stages of road construction. This information was entered using the form in Figure 3.41 while the specifications of the road were sourced from the Thulamela Municipality.

Finally, a choice of the type of outputs to be made available for later interpretation was made as indicated in Figure 3.42. Once the solver had converged, the results of the model could be analyzed, refined, and reported for the various stages of road construction.
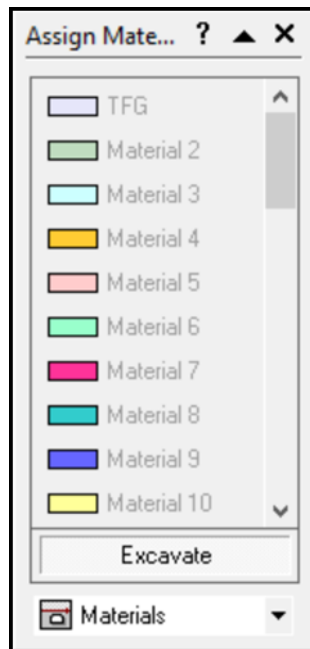
Figure 3.41 Process of excavating each stage
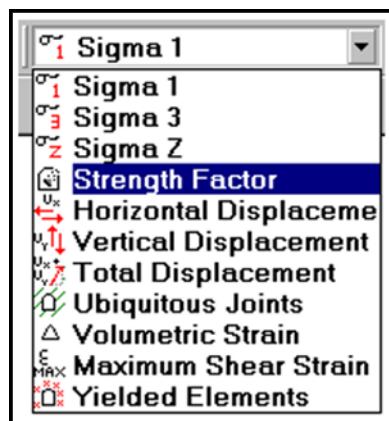
Figure 3.42 Interpreting criteria

3.6   Limitations and challenges encountered

One of the limitations of the experimental program presented in this chapter is that the study did not contemplate a three-dimensional analysis of the slopes. And although the development of such a numerical simulation tool would have

been a viable option, this was beyond the scope and the timeframe of the thesis.

Second, field stresses were assumed and not measured in any way. This is because field stress measurements require expensive equipment that could not be covered by the budget allocated for the study.

Third, access to some target locations of the study area was impossible as part of the fieldwork. The main reason is that the said locations were very steep or covered with a large and wild forest. In other instances, some areas were considered unstable to walk over for observation and surveying.

Fourth, a detailed laboratory test on rock strength using core samples was not performed. The core lobs and supporting hardware equipment failed when only 4 samples were collected for testing. In view of the small size of the core samples, it was decided not to perform any laboratory testing of rock strength. Estimates from past work done in the great Limpopo province were sorted for a reasonable substitute to be used in the Thulamela Municipality.

Last, it was wished to use the Particle Finite Element Method (PFEM), but the code was not readily available for use although from Zhang (2014). The researcher was approached but in the end, elected not to share his PFEM computer script.

Chapter 4   In situ evaluation of the mechanical properties of the soil: an empirical and experimental approach

The purpose of this chapter is to estimate the physical and mechanical characteristics of the soil samples collected along the R523 road. Key points within the active slopes are used for the in-situ evaluation of the soil material of the R523 road situated in Thathe, Limpopo. The study commences with detailed geological mapping, followed by soil sampling, and later laboratory testing of the soil samples.

From the geological mapping, it is shown that the study area is dominated by basalts, with arenite and norite found along the boundaries of basalts. It was also observed that almost all slope failures were located along basalt slopes created during road construction. Only one slope instability occurred at the contact zone of basalt and arenite. Most of the slope instabilities involve the sliding of topsoil. This soil is red clay, well known for swelling and expanding when exposed to rainfall. Laboratory analysis of the red clay evidenced high liquid and plastic properties as well as a high plasticity index. This suggests that the soil is prone to slope instability if no support system is installed.[3]

Finally, it was found that soil types and road construction activities along the roads are probably the key factors influencing slope stability in the area.

---

[3] Portion of this chapter has been published in a conference held in 2018 September under the following reference: Sengani, F., Zvarivadza, T., 2018. Evaluation of factors influencing slope instability: Case study of the R523 road Between Thathe Vondo and Khalvha Area in South Africa. Proceedings of the 18th Symposium on Environmental Issues and Waste Management in Energy and Mineral Production, SWEMP 2018, Springer, Cham
The other portions of this chapter have been published in some of the articles listed on publication list.

However, detailed geotechnical surveying and numerical simulation are required to consolidate these conclusions.

4.1   Introduction

Soils in nature rarely exist separately as gravel, sand, silt, clay, or organic matter. It is usually found as mixtures in varying proportions of these components. Grouping of soils on the basis of certain defining criteria would help the engineer to rate the performance of a given soil without the necessity of a lengthy description (Murthy, 2002). The soil can be rated for example as a good foundation for structures or a sub-base material for roads and airfield pavements.

Soil classification is empirically done by allowing for the particle sieving data and Atterberg's limit testing. Indeed, the size of particles present in the solid gives an indication of the probability of occurrence of such sizes of particles. In the same breadth, Atterberg's limits collectively refer to the shrinkage limit, plastic limit, and liquid limit. They are a basic measure of the critical water contents of fine-grained soil.

To understand the value of Atterberg's limits, let us consider dry clayey soil. It can take in a large volume of water and while doing that the soil undergoes distinct changes in behavior and consistency. Depending on the water content, the clayey soil may appear in four states: solid, semi-solid, plastic, or liquid. This is graphically illustrated in Figure 4.1.
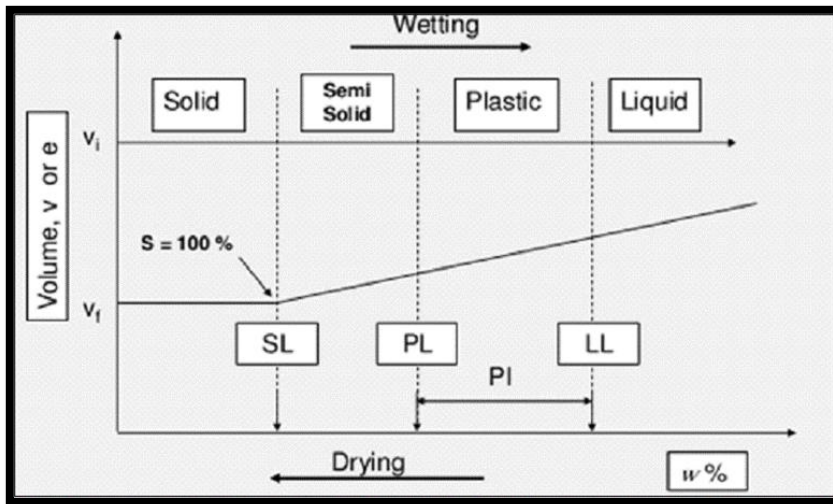
Figure 4.1 Summary of the index properties of soil (Sowers, 1979)

In each state, the consistency and behavior of the soil are different and consequently so are its engineering properties (Pandian, 2004). It becomes evident that the boundaries between the different states a solid can take define the changes in behavior. This has a bearing on the probability of landslides and rockfalls. At the same time, silts and clays for example have different particle fineness that can be established by sieving. Particle size can also expand or shrink with the moisture content while shear strength varies in this environment (Das, 2006). Particle size, mechanical properties such as shear strength, and Atteberg's limits are therefore interwoven.

It is the above observation that underpins the widely used tests performed in Section 3.2. This chapter reports on the findings associated with the field and laboratory work that basically consisted of collecting soil samples at unstable points of the active slopes. The types of soil found in the surveyed area of the Thulamela Municipality are empirically classified. The chapter is concluded with estimates of the physical and mechanical characteristics of the soil within the study area.

4.2 Approach to data collection and analysis

The initial approach to data collection consisted of two main steps: field observation and measurements as well as laboratory testing.

As part of data collection, the fieldwork commenced with the careful observation that led to the selection of active slope instability areas. Geological mapping was then conducted throughout the selected study area. Mapping was purposed to understand the lithological background and underlying structural controls. Traverses of the same sizes were also developed across the area.

The laboratory testing was done on the soil samples collected from selected points within the active slope instability area. The samples were analyzed for particle distribution, Atterberg's limits, and soil classification (refer to Sections 3.2.2 and 3.5.1). Critical properties of the soil and rock mass that could be measured in-situ or in the laboratory were sourced from the literature. These include cohesion, Young's modulus, and soil sensitivity amongst others.

The consolidated results of the field and laboratory study are presented in the subsequent sections (Section 4.3 and 4.4). The sections are covered in the chronological listing adopted in Chapter 3 starting with the lithology, the classification, and finally, the mechanical properties of the soil for rock slope stability analysis.

4.3 Initial results of the field observations

The initial walkabout showed that all discovered landslides were located along with the road benches or sidewalls. The ongoing road construction along this mountainous area also appeared to alter the surface drainage patterns, create unstable slopes and increase runoff (see Figure 4.2).
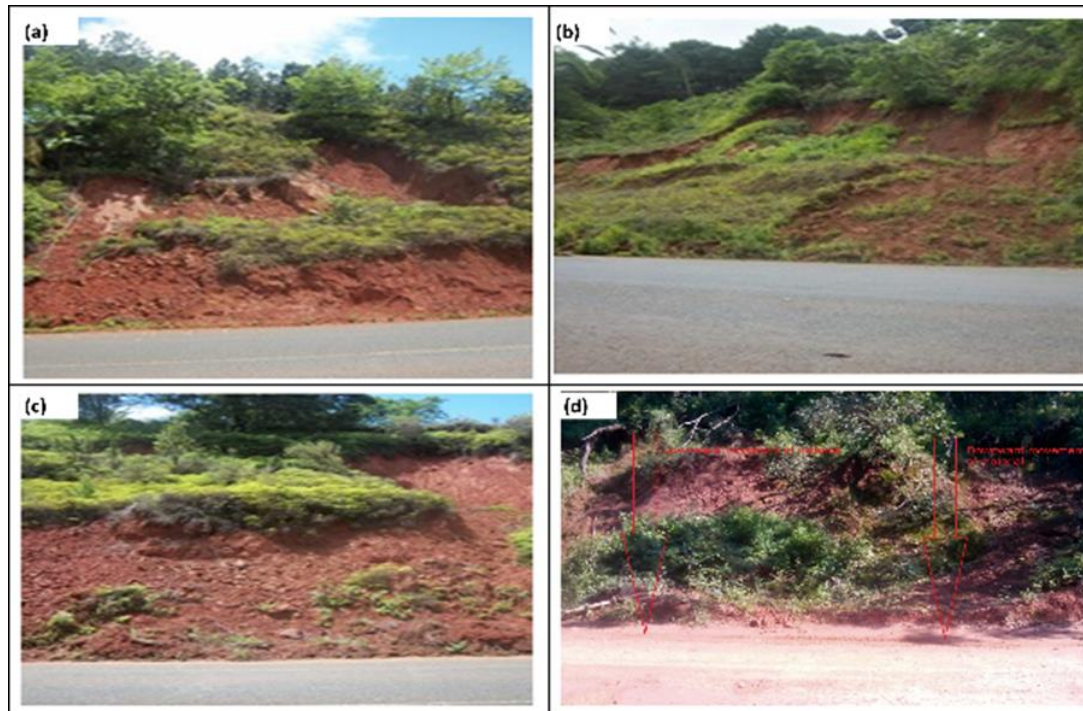
Figure 4.2 Downward movement of material (soil or rocks) along R523 road

The first empirical observation suggested that improper road construction could be the reason for the formation of water pools at the foot of the cut-slope. This became a non-negligeable driving force for accelerated slope failures. Second, altered drainage patterns led to an increased rate of surface runoff and increased probability of water washing soil down to the road. As a result of this, the surface drainage ditch was blocked while the foot of the slope became waterlogged. The rapid saturation of soil ensued also contributing to the frequent occurrence of landslides. This destabilized the R523 road and the side-cast material downslope; this also made the slope steeper than before (see Figure 4.3). Consequently, undercut natural slopes become unstable. Shear stresses in the soil within the slope increase with an increased probability for failure (Abramson and Thomas, 2002).

Figure 4.3 Occurrences of post landslides along the R523 road

Third, contrary to local accounts, evidence of previous landslides was noticed also where certain slopes were deemed inactive (see Figure 4.4). This prompted the implementation of mitigating measures to limit further slope failure (landslides). A gabion wall was erected to prevent future landslides. The gabion walls were noted to be effective where two-tiered steps were employed and to fail otherwise as shown in Figure 4.5. The ineffectiveness of the gabion translated into the collapse of the walls or the wash-away of soil material. In other instances, the failure of the gabion was created to the interruption of traffic due to soil slides blocking the road.

Figure 4.4 The effective gabion walls along R523 road

Figure 4.5 Damaged wire mesh of an ineffective gabion wall along the R523 road due to landslide re-occurrence

Another factor believed to contribute significantly to slope failure along the study areas is water pressure. Indeed, Duncan and Wright (2005) have shown that water naturally fills the cracks developed on the surface of the slope. The water then greatly decreases the shear strength of the soil as pore pressure within the slope increases. Supporting observations also showed that several cracks and a number of short streams were present in most areas with pronounced slope failure (see Figure 4.6).
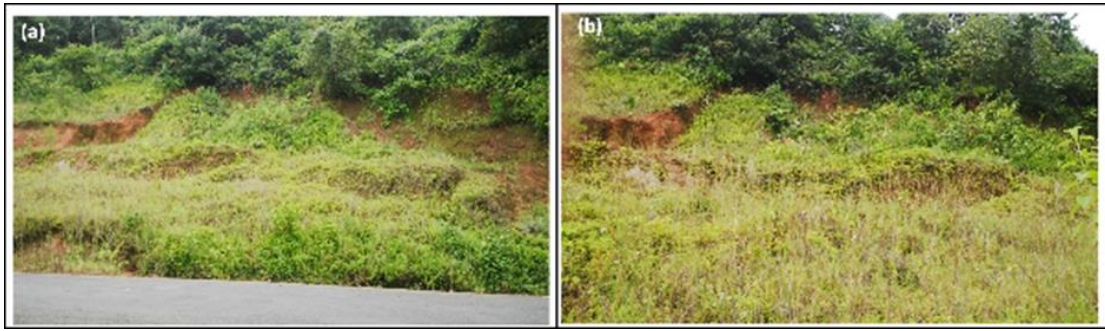
Figure 4.6 Tension cracks observed during the reconnaissance survey

In summary, the initial field observations enabled us to build an empirical picture of the occurrence of landslides along the R523 road. There is strong evidence that the cross-section profile of the constructed road encourages retention, instead of the flow, of water around the area. And because the majority of landslides occur during the rainy season (i.e. in December and January), the weathering profile of the region is to be further explored. Once this is done in subsequent chapters, a correlation between landslide occurrences and rainfall statistics may be established. The benefit of the analysis would be a more realistic simulation of the soil and rock mass.

4.4   Geological description of the study area

From the geological mapping, it was established that the study area is dominated by basalts. In contrast, arenite and norite are disturbed along the boundaries of basalt (see Figure 4.7). Following this, the majority of active unstable slopes were located along with basalts while at the contact zone of basalt and arenite, slopes are more stable. The geological mapping also revealed that post and active slope instability is mostly experienced in red clay soil where basalts are the country-rock. The other interesting observation was that slope failures were mostly composed of soil rather than rock. This reassured the sampling and testing of soil since the collection of core samples was stopped after an equipment failure. From the survey of the target section

in Figure 4.7, a cross-section of the study area was produced. What resulted from this is that top layers seating on top of the country rocks (see Figure 4.8) were likely to slide when their phase changes from solid to liquid due to rainfalls. One could argue that clay soil on the upper horizon may experience slipping movement along the disturbed boundaries of the study area.
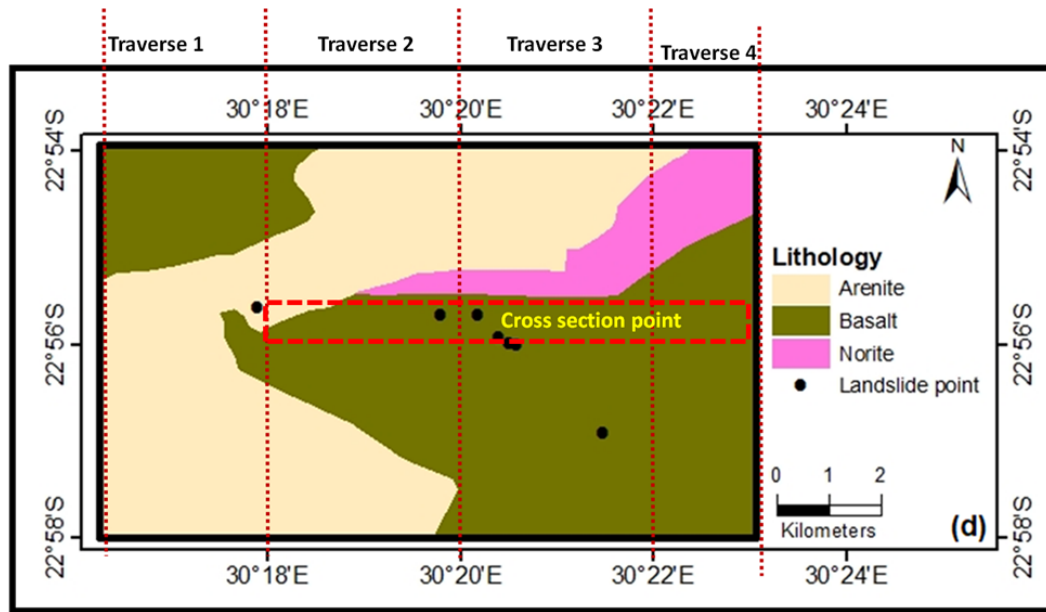
Figure 4.7 Constructed geological through geological mapping
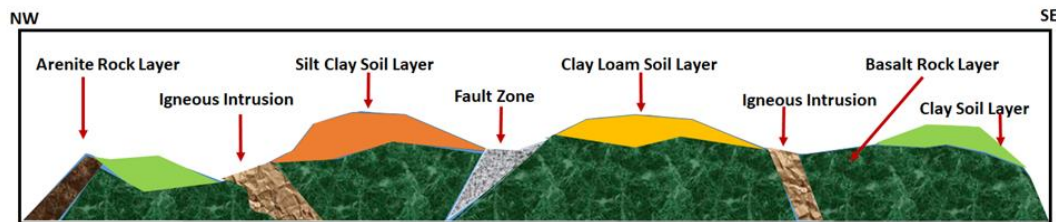
Figure 4.8 Cross-section view of the study area

A last note on the geological mapping is that road construction in the Thulamela Municipality took place in the mountainous area. Explosives were used for the initial excavation leaving behind fractures and compromised the stability of the rock mass. The fractures generated within the rock mass can readily disintegrate the material when exposed to extreme rainfalls. Large faults and multiple streams cutting across the area were also observed. These features

further strain the stability and internal movement of material in the study area. Created tension cracks propagate which in turn weakens the material and leads to gradual movement. Clayey layers capping the country-rock swell when exposed to rainwater and groundwater. The increased internal pressure finally forces rock slopes to collapse. In some cases, the disappearance of vegetation around the slopes is a precursor of a looming landslide.

4.5   Mechanical properties of the soil

In this section, the mechanical behavior of the solids found in the study area is qualitatively and quantitatively assessed. The following are presented: the particle size distribution, Atterberg's limits, and the classification of the soil.

4.5.1   Particle size distribution

Based on laboratory analysis, it was noted that the soil samples tested consisted mostly of clay material. This is because the fraction of material passing the coarsest sieve was high. The particle size distributions also have a small proportion of coarse material or silt soil as shown in Figure 4.9.

Figure 4.9 further shows that the percent fractions of particles passing through different sieves range from 25% to 100%. It was clearly observed that all samples are finer than the coarsest sieve used for laboratory analysis, i.e. 1mm. The fraction of soil passing through various sieves gradually also reduces with particle size. All the above suggests that the sample contained a fair fraction of pure and finely-grained clay soil.
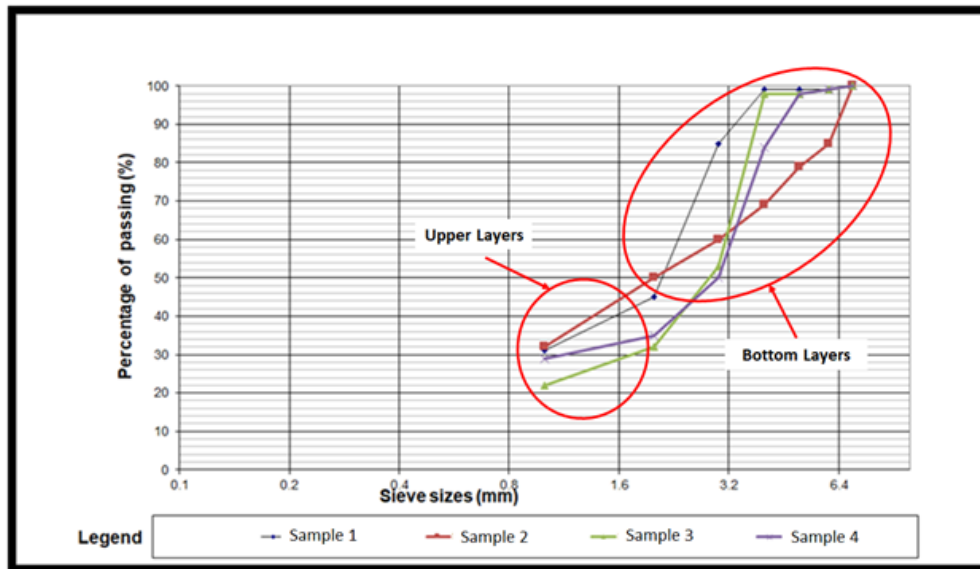
Figure 4.9 Gradation curve of the collected soil sample. The focus of this paper is on the upper layers. It is crucial to indicate that the gradation curves represent the mixture of the upper/top layer to the bottom layer of the soil mass.

In summary, all samples were mostly dominated with fine clay material and a small proportion of silt size material. This type of soil is known to be sensitive and prone to experience failure when exposed to extreme rainfall.

4.5.2 Atterberg's limits

Atterberg's limits are a set of index tests performed on finely grained soils to determine their relative activity to moisture. In this section, liquid limits, plastic limits and plastic index are presented.

It is important to state that soil samples collected across the study area were found to have similar Atterbeg's limits as shown in Figure 4.9. Indeed, the soil collected along the R518 and R523 roads was generally found to have 70% of the liquid limit on average. This result confirms that the soil is a very fine and clayey material with the ability to absorb large amounts of water within its pore

spaces. Consequently, the accumulated water takes time to pass through or evaporate for this type of soil. Such a soil also displays slipping and swelling characteristics especially in the presence of water. Conversely, this type of soil easily cracks when it dries up. Note that although the fourth sample appears to present less liquid limit, in reality, it falls under the same category (clay soil). The causing factor for this is the slightly higher amount of silt particles present in the sample.

Table 4.1 Summary of Atterberg's limits of soil samples

Samples	**Liquid limit (%)**	**Plastic Limit (%)**	**Plasticity Index (%)**	**Description**
Sample 01	71	37	34	High plasticity
Sample 02	66	34	32	High plasticity
Sample 03	70	37	34	High plasticity
Sample 04	56	26	30	High plasticity

Liquid limit alone cannot be used to draw a solid conclusion on the mechanical behavior of soil. It should be complemented with the analysis of the plastic limit and plastic index.

The plastic limit can be regarded as an indicator of the water content at which the soil begins to crumble. Based on the results in Table 4.1, it can be seen that all samples have a plastic limit ranging between 26% and 37%. The soil material of the entire study area can therefore be categorized as of high plasticity in accordance with Table 3.2. Indeed, the thread could be rolled out down to 3.2 mm at any moisture possible during the experiment. The soil has the ability to contain water at a very low percolation rate; it becomes plastic even after a short rainfall and does not hold well at a high slope angle. Plastic limit results also correlate well with liquid limit ones.

Talking about the plastic index, it can be said that it indicates the range of moisture content over which the soil is in a plastic state. Based on Equation (3.4), the plastic index is calculated as the numerical difference between the liquid limit and the plastic limit of the soil. Liquid and plastic limits are both dependent on the amount and type of clay in the soil, but the plasticity index is generally only dependent on the amount of clay present.

The results in Table 4.1 show that the plasticity index of the material is at an average of 32 % which is a classified as high plasticity index. This was confirmed by plotting the results in Table 4.1 onto the plasticity index chart as shown in Figure 4.10.
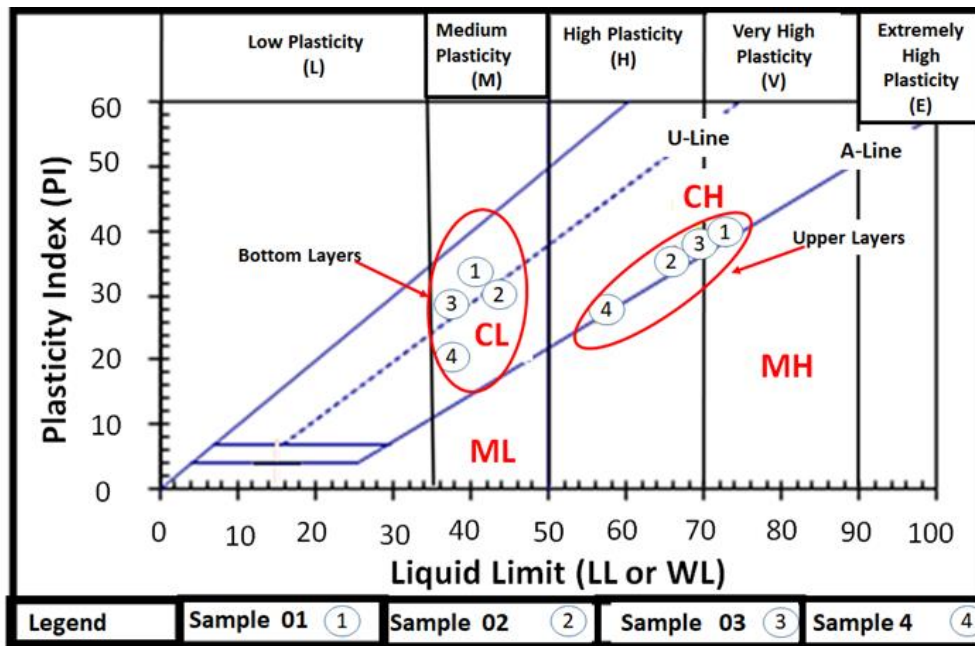
Figure 4.10 Plasticity index charts of collected soil samples

It is important to note that Atterberg's limits presented in this section mostly give a qualitative behavior of the soil subjected to different conditions.

4.5.3 Classifications and types of soils

Based on observations, the material found in the study area was classified. It consisted of soil significantly rich in silt clay, clay loam, and clay.

In an attempt to be less subjective, the soil was also classified based on soil classification charts in Figure 4.11.
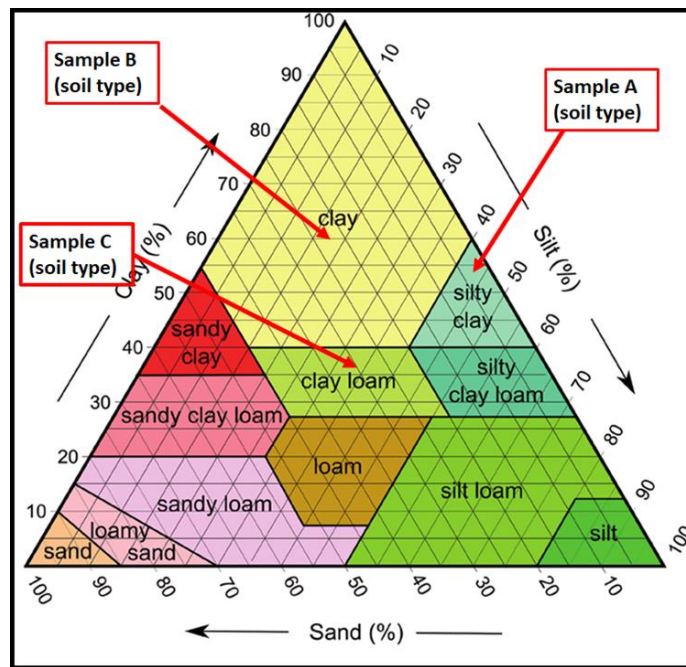
Figure 4.11 Soil texture chart of the study area.

It appears that the clayey soil within the study area is indeed prone to landslides. The soil also may become oversaturated under heavy rains, it may thereafter swell and slip easily. Cracks from drying and subsequent shrinkage are also to be expected.

4.5.4 Mechanical properties of soil

Input parameters for use in numerical simulations necessitated the soil samples to be further analyzed. To this end, additional standard tests were

done which resulted in the properties listed in Table 4.2. By and large, their values for the 3 sites considered were closely comparable. Differences attributable to site locations were noted for the cohesion, the shear strength, and the undrained compressive strength.

Table 4.2 Mechanical properties of soils in areas A, B, and C

	Area A	**Area B**	**Area C**
Density (kg/m^3)	1900	1600	1700
Unit weight (kN/m^3)	18	18	18
Poisson's ratio v (-)	0.39	0.39	0.39
Young's modulus E (MPa)	3	3	3
Undrained compressive strength (kPa)	66	55	45
Shear strength (kPa)	250	110	90
Cohesive strength (kPa)	96	188	95
Angle of internal friction	20°	20°	20°
Compressibility	0.17	0.15	0.17
Soil sensitivy	1	1	1

One noteworthy observation from Table 4.2 is that the types of soil within the study area can be classified as sensitive. This is corroborated by the findings reported in Section 4.5.2 whereby the soil contains large proportions of clay. Kaolinite and hematite were also noted to be the main forms of clay minerals in the study area. Such types of clay soil are usually associated with basalts and other igneous rocks (Blakemore and Swindale,1958; Kelly and Zumberge1961). Initial laboratory analysis further confirms that the geological mapping results in Section 4.4 make sense. Although the study area is clayey, silt and loam soils are also present. These have generally contributed to

undrained compressive strength, cohesive strength, shear strength and compressibility of the soil.

In conclusion, the soil material is not favorable to geotechnical work. This is because of its poor consistency and likelihood to fail when exposed to extensive rainfall or seismic movement. The qualitative description of the soil provides an understanding of the numerous slope failures observed along the sidewalls of the roads. It also gives insight into the unsuccessful mitigating measures against slope failures in the study area. The suggestion is that the soil properties and the morphological terrain of the study area could be the primary controlling factors of the recurrence of the slope instability.

Finally, in terms of landslide patterns, two types were noted: active slope instability and post slope instability. And although detailed slope stability analysis is discussed in the coming chapter, the initial findings reported here have enabled the identification of soil properties as a great contributor to slope instability.

4.6   Conclusion of the chapter

The results and discussion of the chapter have shown that the study area is dominated by basalt rocks with arenite and norite found at the boundaries. The majority of slope instabilities were noted in the sites associated with basalt rocks and clay soil.

Slope failures were observed to be distributed along the roadside walls rather than at the mountain top. The reason for this is believed to be the fractures generated during road construction by the use of explosives.

Finally, the red clay soil characteristic of the area was classified to be highly liquid and plastic. This means that the soil can swell under heavy rains and

cracks once the water has evaporated. The cracks create unstable slopes that lead to landslides.

Further analysis is required to quantitatively describe the mechanisms behind slope failures. This is covered in the following chapter using the classical kinematic and limit equilibrium analysis of slopes.

Chapter 5 Slope stability analysis using kinematic analysis, limit equilibrium, and numerical approach

The use of kinematic analysis, limit equilibrium methods and numerical simulation to cases of slope instability are presented in this chapter. The aim is to develop an understanding of the effects of common factors on landslides.

The kinematic analysis was performed using SWEDGE while limit equilibrium analysis relied on SWEDGE, SLIDE, and Phase 2. In doing so, a rich inquiry into the mechanisms governing slope instabilities was done. The safety factors of identified slopes in the study area were estimated using SLIDE.

It was shown that selected unstable or failed slopes could be described using wedge failure models. Limit equilibrium analysis, on the other hand, revealed that sliding types of toppling are common in the area of study. Finally, the majority of slopes in the study area consist of clay soil making them prone to instability. Owing to that, the effect of the slope angle on stability was assessed using RocPlane. It was noted that the steeper the slope is, the more unstable the slope tends to become.[4]

5.1 Introduction

Landslides, and to a large extent slope instability, have been documented to be a global threat to humans, the environment, and infrastructures (Haque et al., 2016; Stanley and Kirschbaum, 2017). However, Africa is the continent

---

[4] First paper has been accepted at the journal of sustainability with the following tittle "Application of Limit Equilibrium Analysis and Numerical Modeling in a Case Slope Instability". The second paper is under review at the journal os Soil and Foundations with the following tittle "Understanding the Mechanism of Slope Failure of a Regional Road (R523) by Different Slope Stability Analysis Methods".

leading in numbers with cases (Gariano and Guzzetti, 2016; Kirschbaum et al., 2015). One reason for this is the limited resources allocated to researching the mechanisms and the recurrence of landslides. The other reason is the difficult access to some remote areas and the scarcity of specialists in the field of study. Perhaps the most important reason is the fact that landslide susceptibility maps on the African continent are generated based on very little data (Hong et al., 2007; Kirschbaum et al., 2009; Nadim et al., 2006; Stanley and Kirschbaum, 2017).

The current study attempts to contribute towards building knowledge on a landslide in Africa using a case study. To this end, the ultimate aim of this chapter is to apply the kinematic analysis, limit equilibrium and numerical model to the analysis of landslides. In doing so, factors contributing to the slope instability of the R523 road in Thohoyandou (Limpopo Province, South Africa) are assessed. Numerical analysis is specifically employed to estimate safety factors, stresses, strain and displacement during and after road construction. This is expected to help identify post and active slope instability along the regional roads (R518 and R523) in the province.

5.2   Research approach

The methodologies utilized in this chapter are covered in detail in Section 3.4. They include kinematic and limit equilibrium analysis as well as numerical modeling.

Kinematic analysis entails wedge, planar, circular and toppling analysis. Limit equilibrium analysis, on the other hand, looks at toppling, rotational, and transitional analysis.

Numerical modeling complements the results of slope stability analysis with what-if scenarios. The Phase 2 computer software package is relied upon to do strain, displacement, and stress analysis.

Finally, it should be noted that the results of the study have been presented in two thematic sections: kinematic on the one hand and limit equilibrium on the other. Details of the results are covered.

5.3   Kinematic analysis with SWEDGE

Kinematic analysis is a common geotechnical approach to the study of landslides. This is because it can be employed to solve problems of Fluid-Solid-Structure Interaction (FSSI) such as the occurrence of landslides. In addition to this, the analysis has the ability to predict the formation of a wedge and its failure. Geological mapping data were utilized to simulate the possible wedge developed along the road walls. This data was collected along the recently active landslides where both tension cracks and joint orientations were clearly observed. Results are summarised in the subsequent sections.

5.3.1   Wedge simulations on stereonet

Based on the simulation results, it can be seen that the wedges developed along landslides were actually due to two joints sets. However, these joint sets were found to develop similar tension cracks throughout (see Figure 5.1).

Scenario analysis of the change in slope angle was implemented. It was noted that the wedges developed are more unstable at a very steep angle while slopes are expected to be stable at very low angles. The size of the wedges developed also increased with the slope angle provided that similar joint sets are present along the slope. This suggests that the increase in the slope angle

affects the size of the dislocked material and the stability of the slope. The results of the simulation are shown in Figures 5.1 to 5.3.
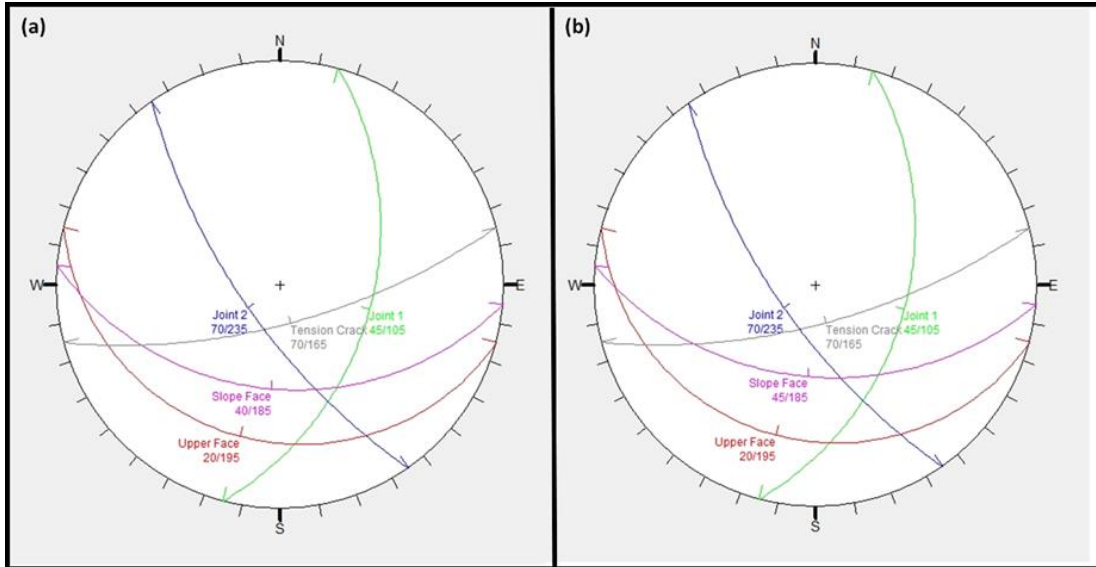
Figure 5.1 Stereonet simulation with two points and tension cracks: (a) at a 40° slope angle and (b) at a 45° slope angle
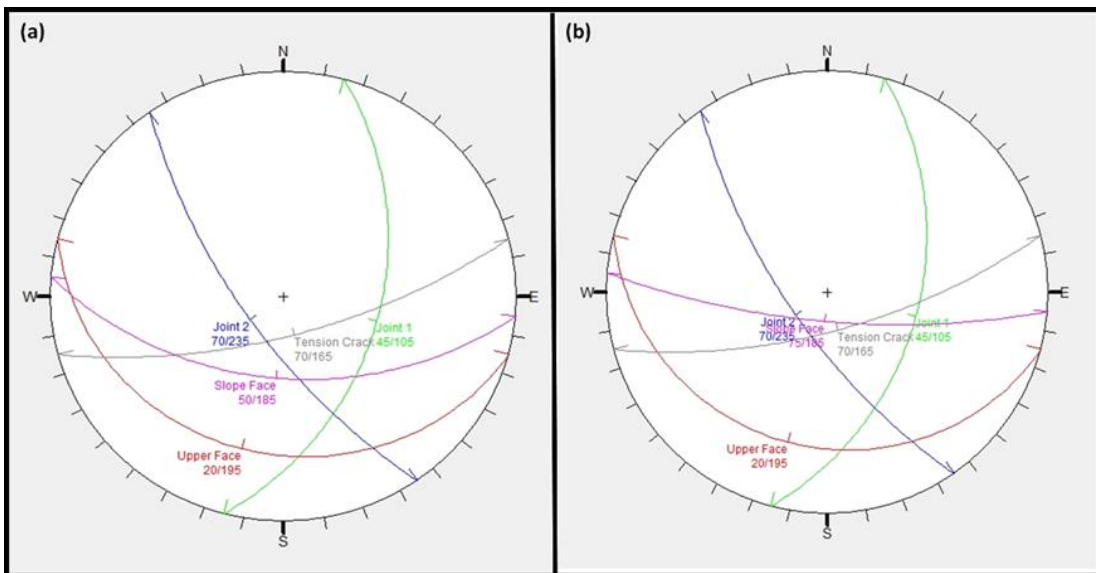
Figure 5.2 Stereonet simulation with two points and tension cracks: (a) at a 50° slope angle and (b) at a 75° slope angle
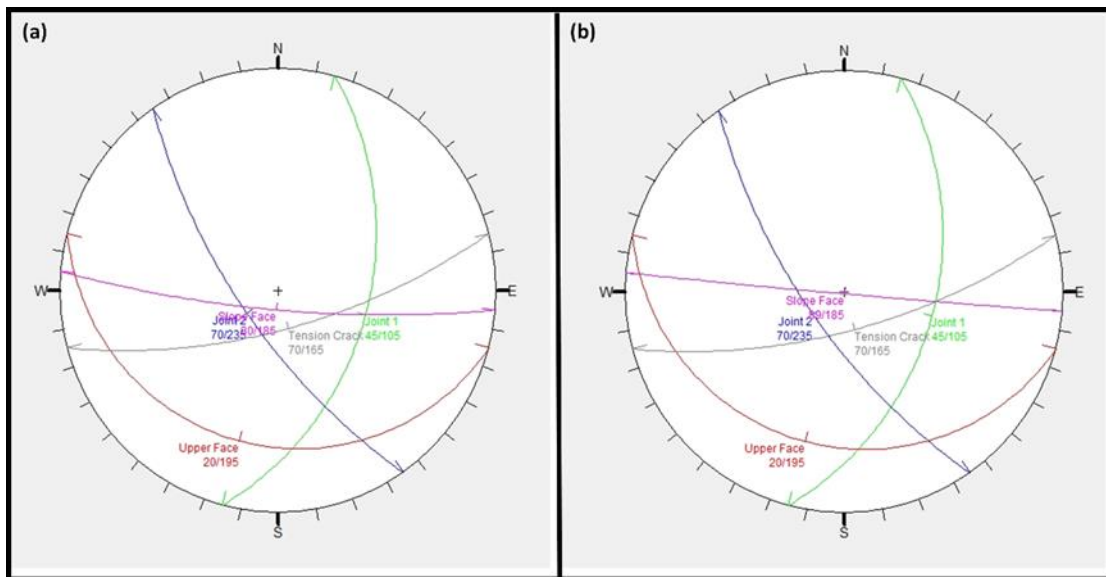
Figure 5.3 Stereonet simulation with two points and tension cracks: (a) at a 80°
slope angle and (b) at a 89° slope angle

5.3.2 Kinematic analysis using SWEDGE

The results presented in this section are based on two approaches:
deterministic and probabilistic analyses. The idea was to understand the
mechanisms associated with slope failure within the study area.

The deterministic results of the slope were simulated using SWEDGE. As
already explained in the previous chapter, the study area is dominated by clay
soil which swells and expands during heavy rainfalls. Upon drying, the soil
develops cracks that can be filled with water or any other material. Once
tension cracks are filled with water for a long duration, the soil material phase
usually changes from solid-state to liquid state. The sliding of the soil can also
ensue since the filling material within cracks plays a lubricating effect on the
soil granulates. This assumption was corroborated by the simulation model
through the use of time steps and assuming that the rainfall intensity remains

constant. The outcomes of the simulation work are summarised in Figures 5.4 and 5.5.
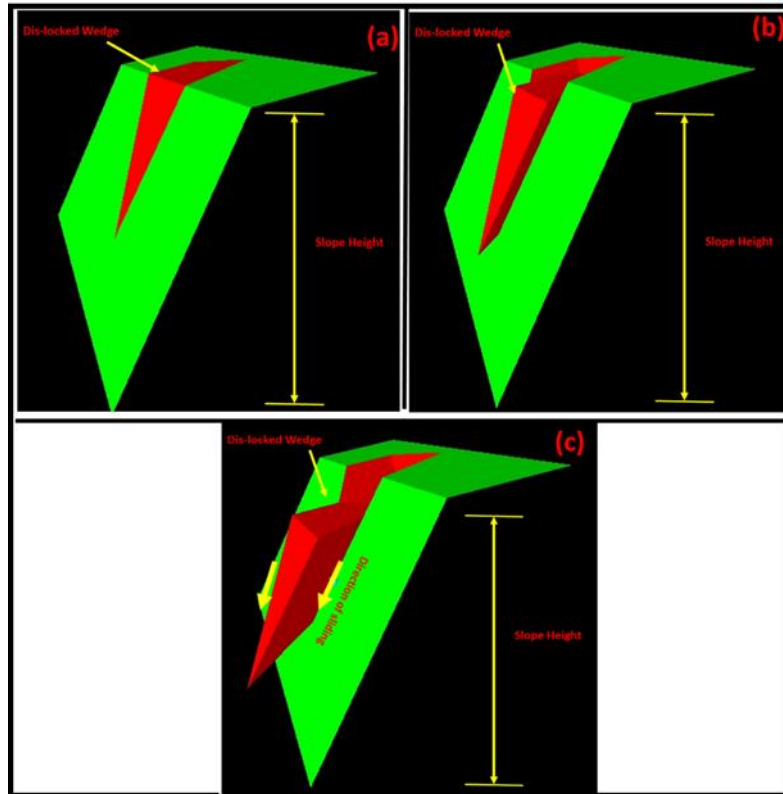
Figure 5.4 Simulation of the deposition of a selected landslide as a function of rainfall in SWEDGE
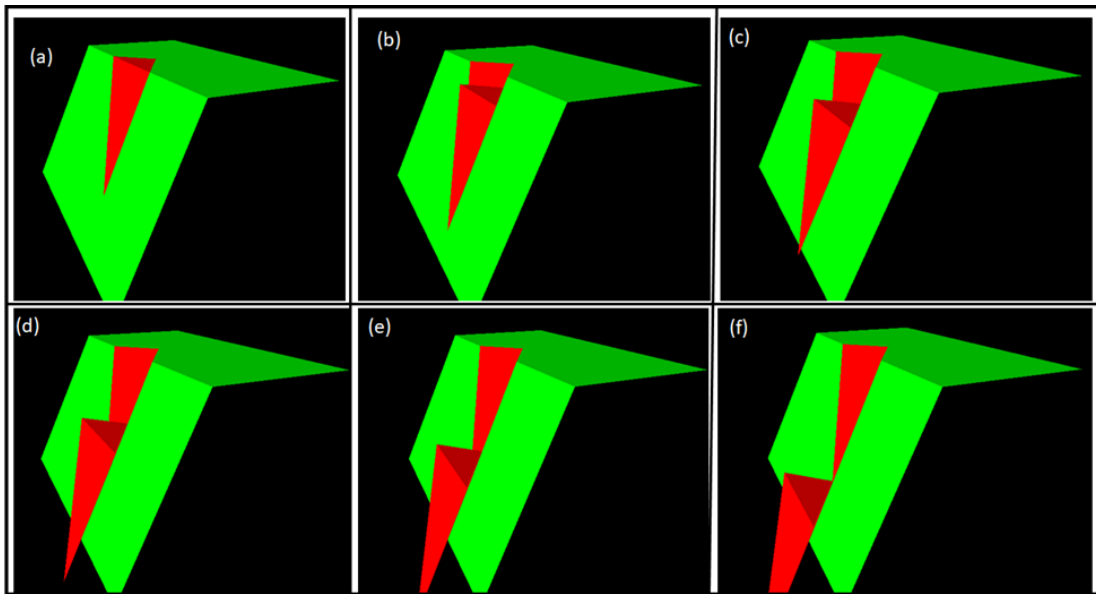
Figure 5.5 Wedge simulation using parameters of the second selected active landslides as a function of rainfall in SWEDGE

Figure 5.4 (a) to (c) shows that the final deposit of material appears to be controlled by the volume of water filling the voids. This is because when clay soil is subjected to heavy rainfall, the material slips easily and with less friction between soil particles. Previous studies (e.g. Abbott, 2002; Göktepe and Keskin, 2018) showed that a wedge usually fails to anchor the entire slope as its resistance along the boundaries rapidly reduces. The results in Figures 5.4 and 5.5 (a) to (f) follow the expected pattern with gradual movements along the weak zones. This suggests that extreme rainfall has a strong influence on the stability of jointed soils.

To consolidate the deterministic analysis in Figures 5.4 and 5.5, one would argue that the resistance of the slope wedges reduces as friction reduces. The phase change of the material from solid to liquid as a result of rainfall and developed weak zones is argued to be responsible for this. Nevertheless, the results of the model proposed in this thesis correlate well with recent studies (e.g. Zhang, 2014 – 2019; Monforte et al., 2017 & 2018). This is true even

though these studies were performed using more complex modeling frameworks such as SPFEM and PFEM.

Based on the above validation, it could be concluded that soil properties, geological features, slope angle, and rainfall are key contributing factors to instabilities. Following this, the probabilistic analysis was undertaking to understand the influence of the slope angle on the stability of the slope. Probabilistic analysis has the advantage of determining the influence of geological features on the safety factor of the slope.

In order to perform the simulation analysis of the effects of the slope angle, the relationship between relative frequency and safety factor of selected slopes within the study area was considered. The relative frequency refers to the number of valid wedges formed by the Monte Carlo simulation.

Based on the Monte Carlo simulation results, Table 5.1 shows that as the slope angle gets steeper, the factor of safety of the slope reduces.

Table 5.3 Monte Carlo simulation of the effects of slope angle on FoS

Slope angle (°)	FoS (-)
40	2.30 – 5.12
45	2.02 – 3.83
50	1.81 – 2.83
75	1.33 – 1.74
80	1.27 – 1.72
90	1.21 – 1.66

The results summarised in Table 5.1 were extracted from the bar charts in Figures 5.6 – 5.11. It should be stated that a slope with FoS < 1.5 is considered unstable (Hoek and Bray 1981; Hoek, 1991 .). From that point of view, the general trend observed in Figures 5.6 – 5.11 is that as the slope angle

increases, the number of wedges developed below the threshold FoS = 1.5 does the same. This is an indication that the change in slope angle has some influence on the recurrence of slope instability across the study area.
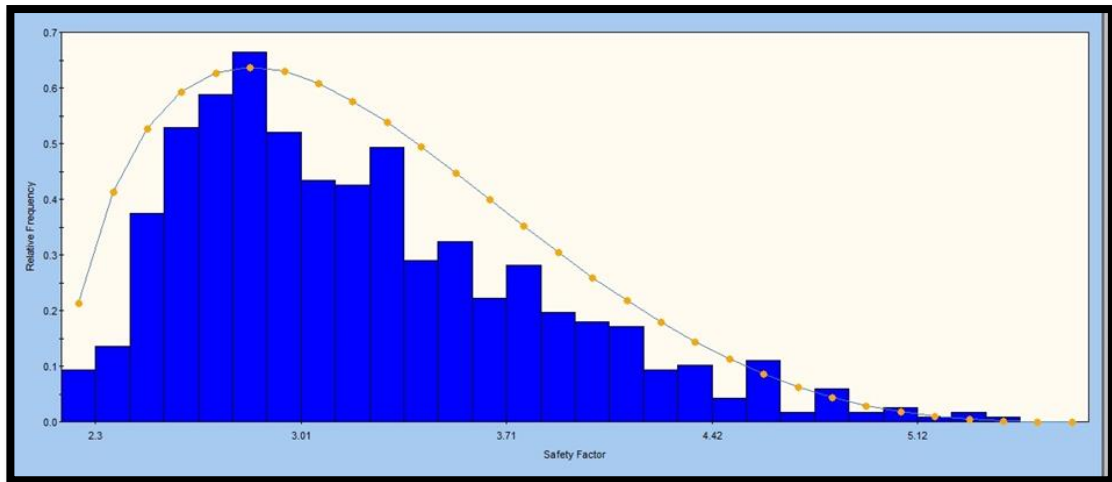
Figure 5.6 Relative frequency of FoS values at a 40° slope angle
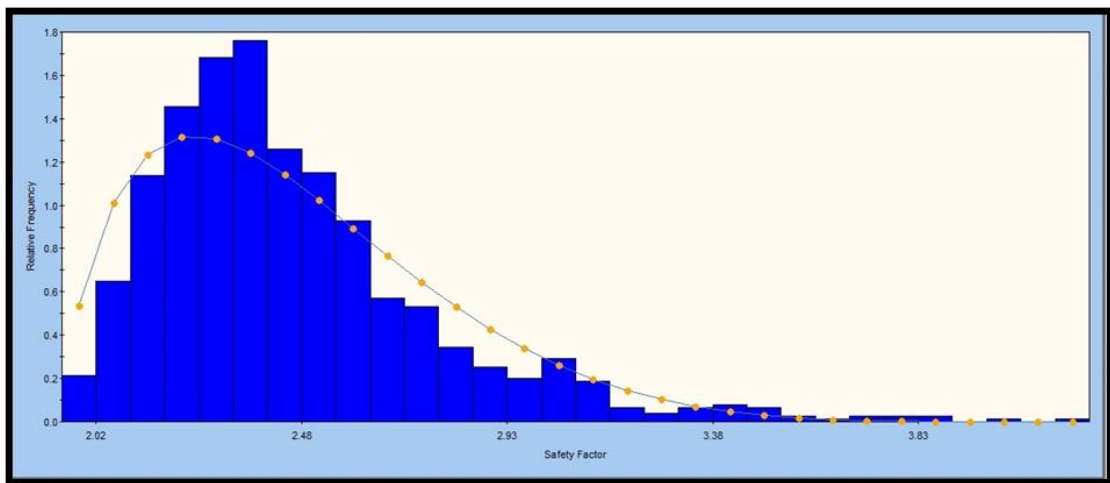
Figure 5.7 Relative frequency of FoS values at a 45° slope angle
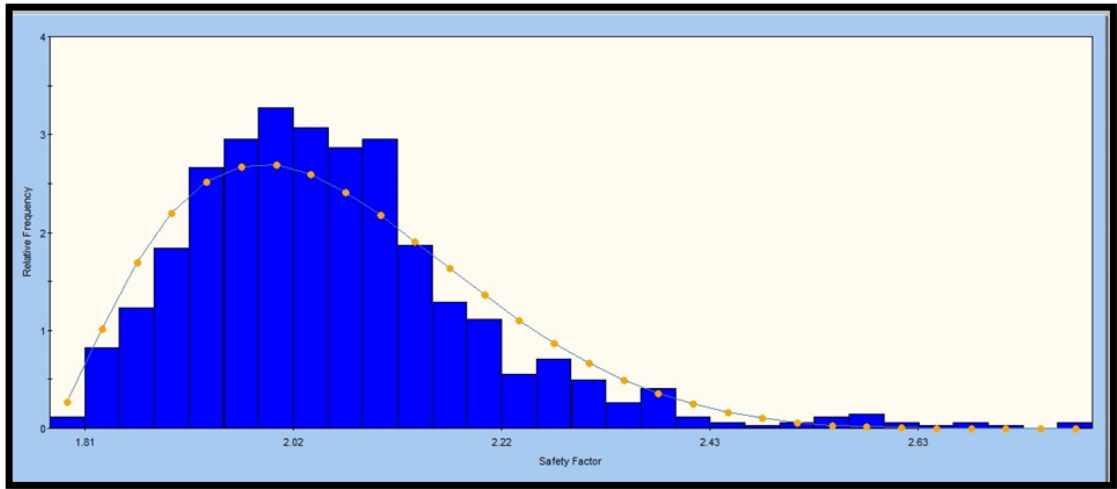
Figure 5.8 Relative frequency of FoS values at a 50° slope angle

Figure 5.9 Relative frequency of FoS values at a 75° slope angle
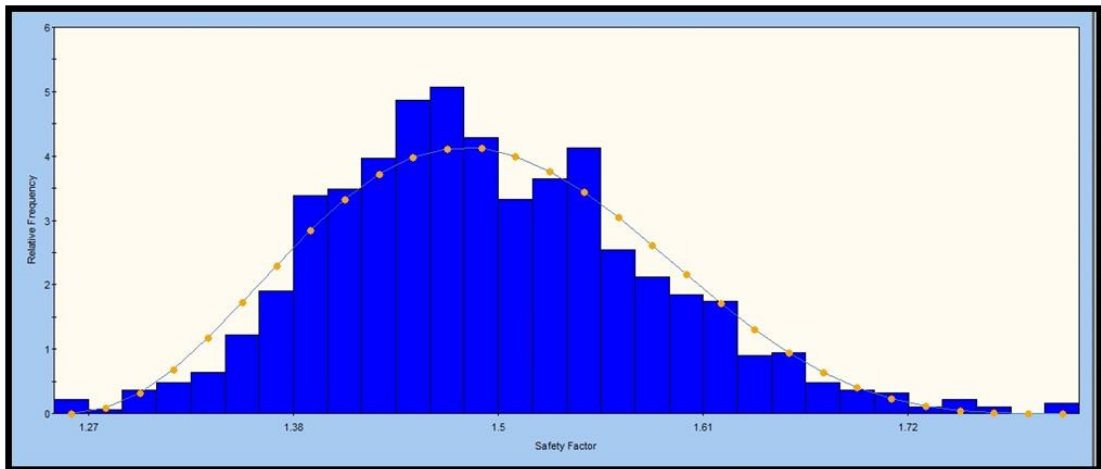
Figure 5.10 Relative frequency of FoS values at a 80° slope angle
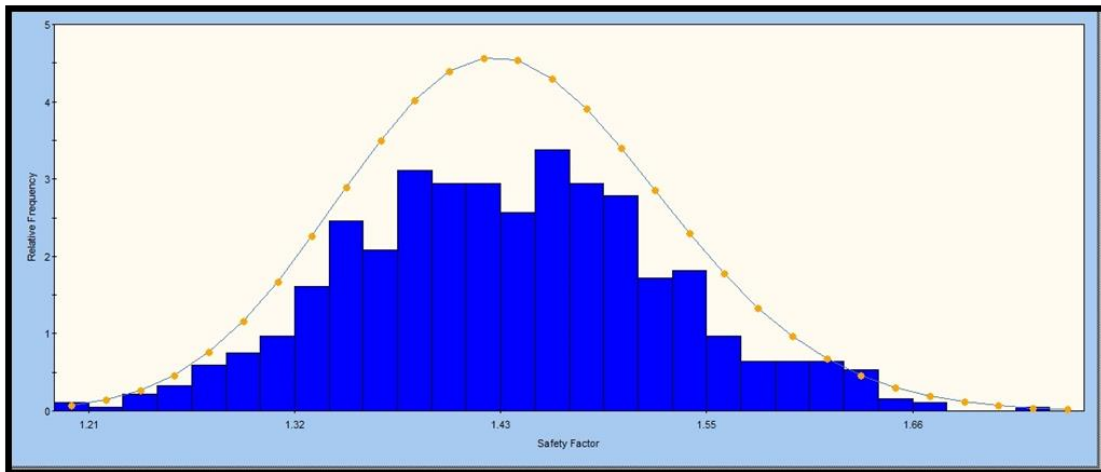
Figure 5.11 Relative frequency of FoS values at a 90° slope angle

Slope stability is also dependent upon geological descriptors such as the structural orientation and rock mass classification (Hoek and Bray, 1981). It is, therefore, crucial to analyze the influence of each joint set mapped along the boundaries of the wedges.

The analysis indicates that the selected slope was unstable with the majority of FoS values in the range 1.0 – 1.3 as shown in Figure 5.12.
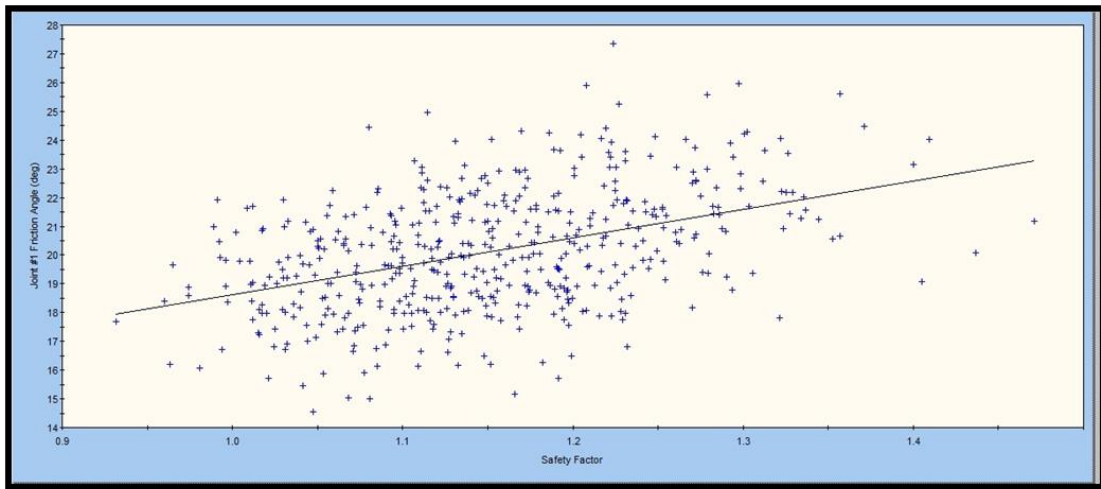
Figure 5.12 Relationship between safety factor and joint number 1 friction angle of the selected landslide

Figure 5.12 also suggests that the wedge is expected to be unstable along the selected joint set. Such behavior of the joint set may allow the sliding of the wedge triggered by water pressure as a result of rainfall.

Similar, to the first joint set, the second joint set also revealed that the FoS of the slope was unstable (see Figure 5.13). In other words, both joint sets defining the boundaries of the wedge have the ability to allow sliding of the block with minor movement.
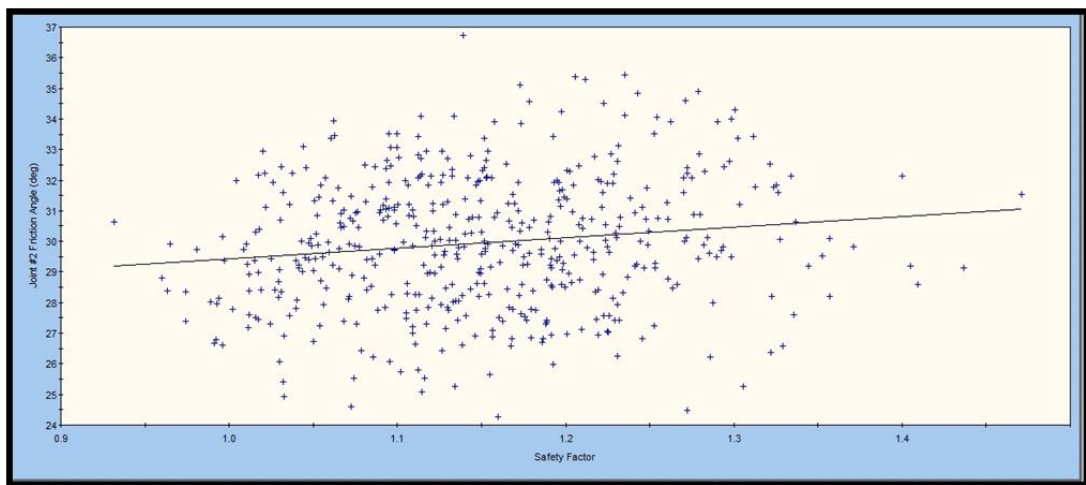
Figure 5.13 Relationship between safety factor and friction angle of joint #1

In conclusion, simulation results indicate that joint orientation and slope angle greatly influence slope stability within the study area. The next section looks at the shearing stress of the selected joint sets and their relation to slope stability. The analysis is implemented using the RocData software; this enables us to study the behavior of the material under stress.

5.3.3 Effects of shearing stress and stress on slope stability

Simulations of the effects of shearing stress relative to the minor stress acting along the slope were conducted. Figures 4.14 to 4.20 show the simulated relationship between shear stress and normal stress acting on the material, followed by major principal stress versus minor principal stress.
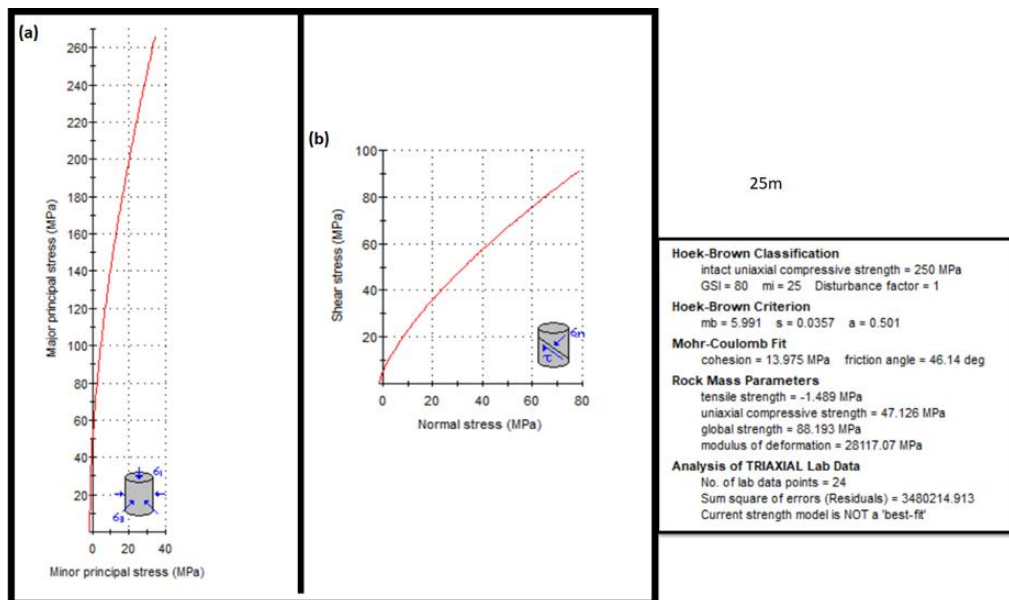
Figure 5.14 Shearing properties of the solid material from study area A (Area A is shown as point A in Figure 1.1, within traverse #5)
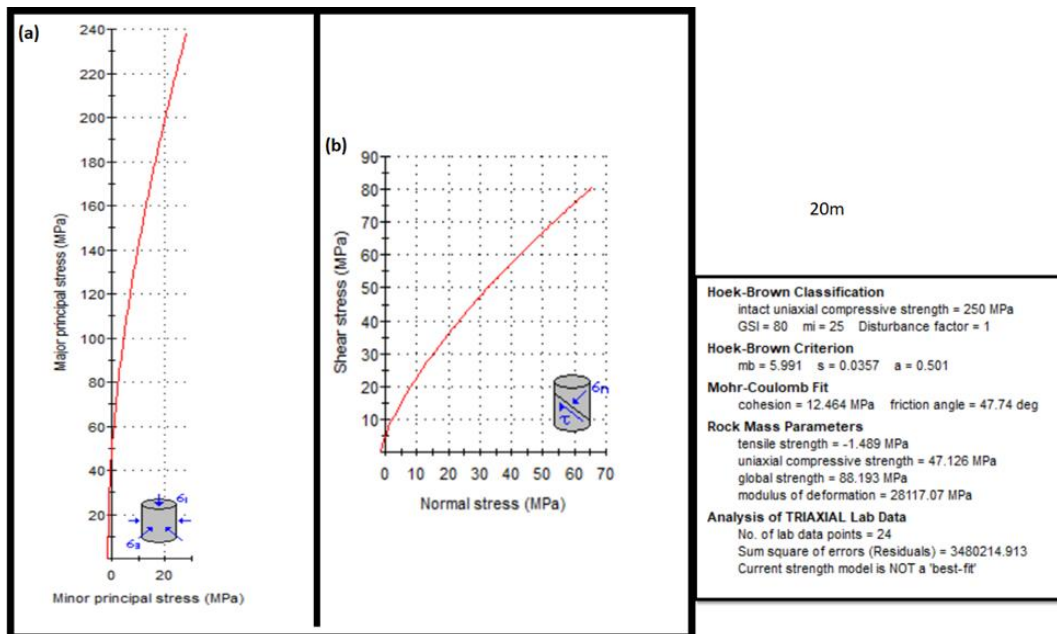
Figure 5.15 Shearing properties of the solid material from study area B(Area B is shown as point B in Figure 1.1, within traverse #4)
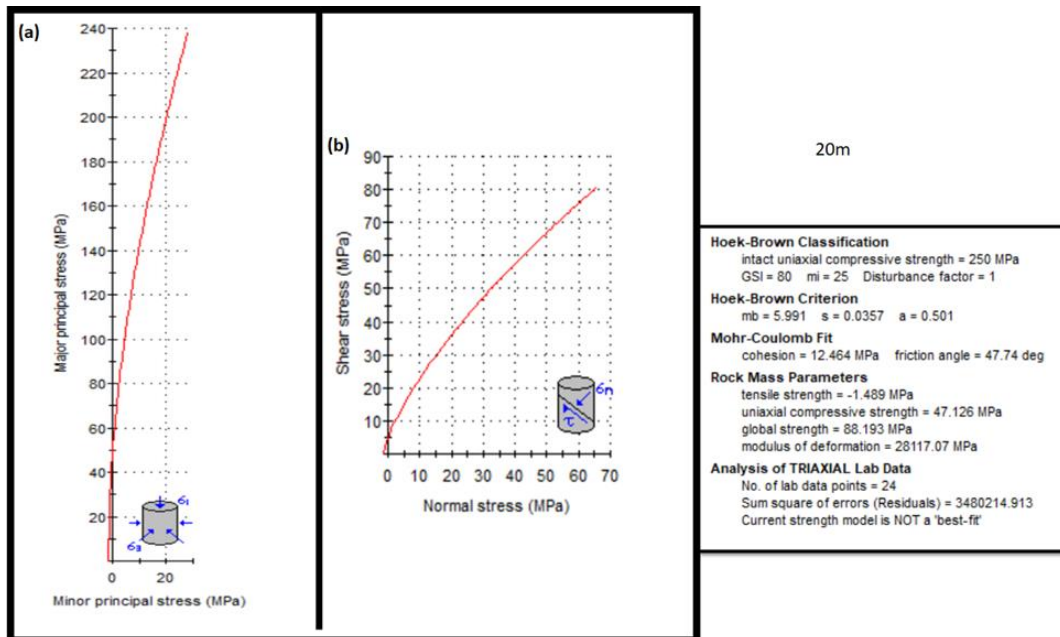
Figure 5.16 Shearing properties of the solid material from study area C(Area C is shown as point C in Figure 1.1, within traverse #4)
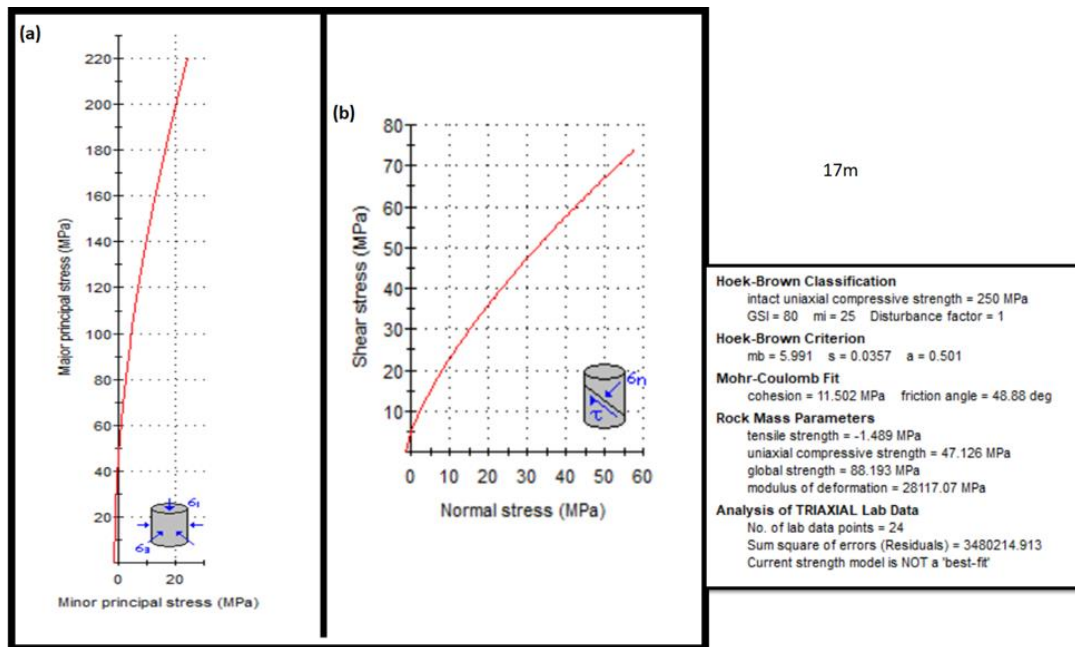
Figure 5.17 Shearing properties of the solid material from study area D(Area D is shown as point D in Figure 1.1, within traverse #3)
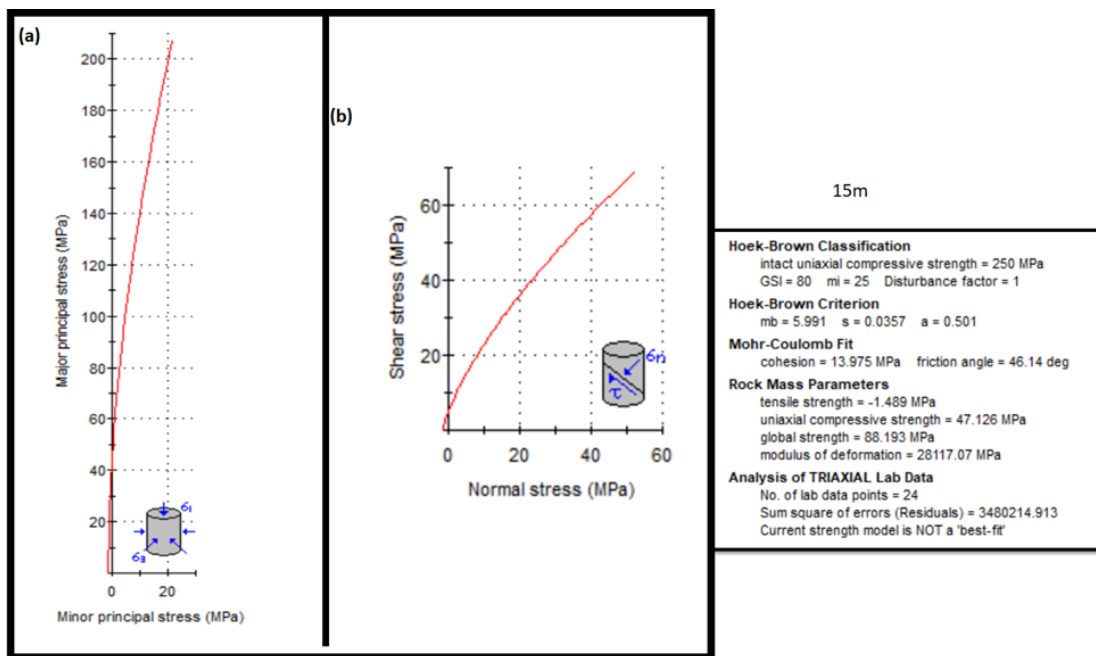
Figure 5.18 Shearing properties of the solid material from study area E(Area E is shown as point E in Figure 1.1, within traverse #3)
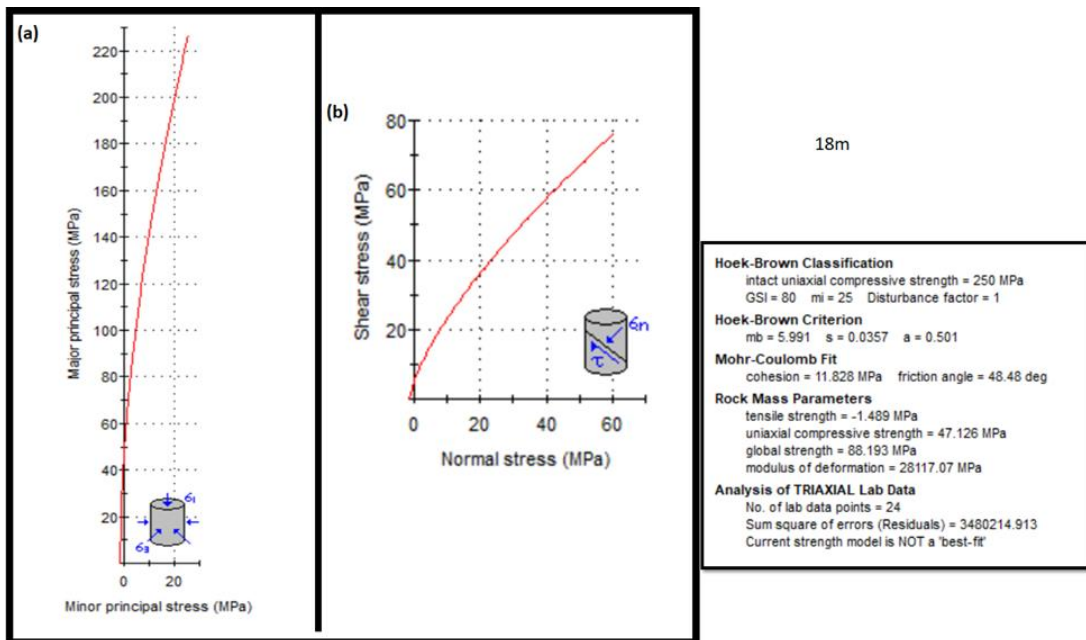
Figure 5.19 Shearing properties of the solid material from the study area F(Area F is shown as point F in Figure 1.1, within traverse #3)
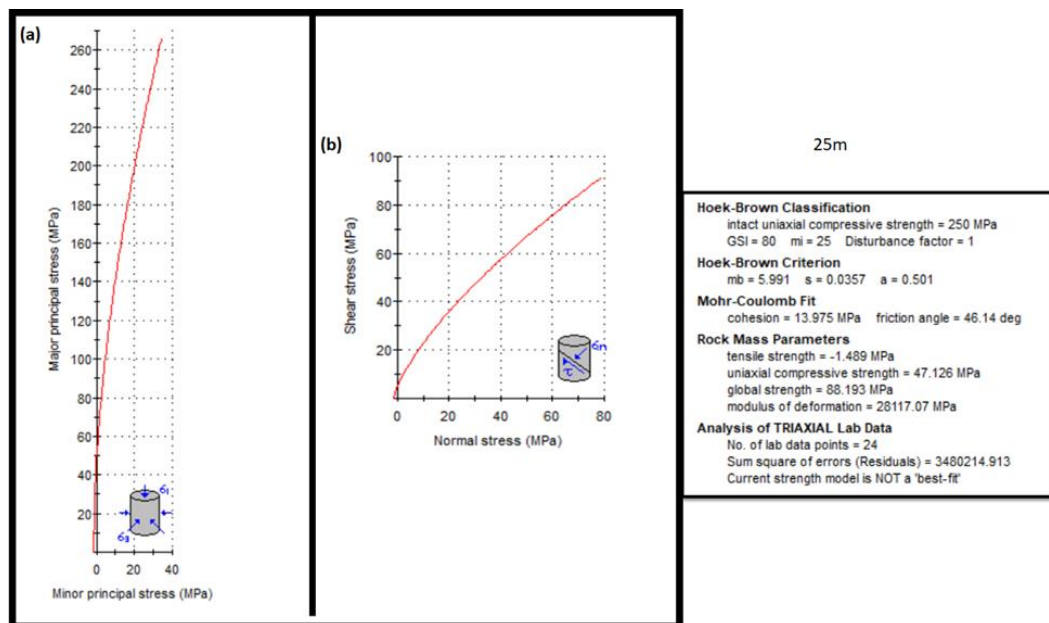
Figure 5.20 Shearing properties of the solid material from study area G(Area G is shown as point G in Figure 1.1, within traverse #1)

Based on the simulation results, it can be seen that the shear strength of the material gradually reduced with the increase in slope steepness. RocData has enabled evidence of the effects of the steepness and properties of the material on the slope. A significant influence on the stability of the material is noted (see Figures 5.16 – 5.20). The shear strength of the material was noted to be gradually reduced with the increase in slope steepness.

5.4   Limit equilibrium analysis

Results of toppling analysis, rotational analysis, transitional analysis, and advanced numerical modeling are presented in this section. The results are produced by using limit equilibrium (LE) analysis together with the FEM model.

5.4.1   Toppling analysis

The concepts of topping and sliding of blocks have been applied in six identified areas associated with slope instability. This has revealed that all the selected areas can be categorized as sliding rather than toppling as illustrated in Figures 5.21 – 5.26. This could be due to the composition of the material that is mainly clay soil and to the tension cracks surrounding the blocks.

It also appears that tension cracks were the most important aspect that initiate the sliding of the blocks. However, the initiation was also noted to be controlled by the amount of rainfall which in turn reduces the resistance of the material against sliding.
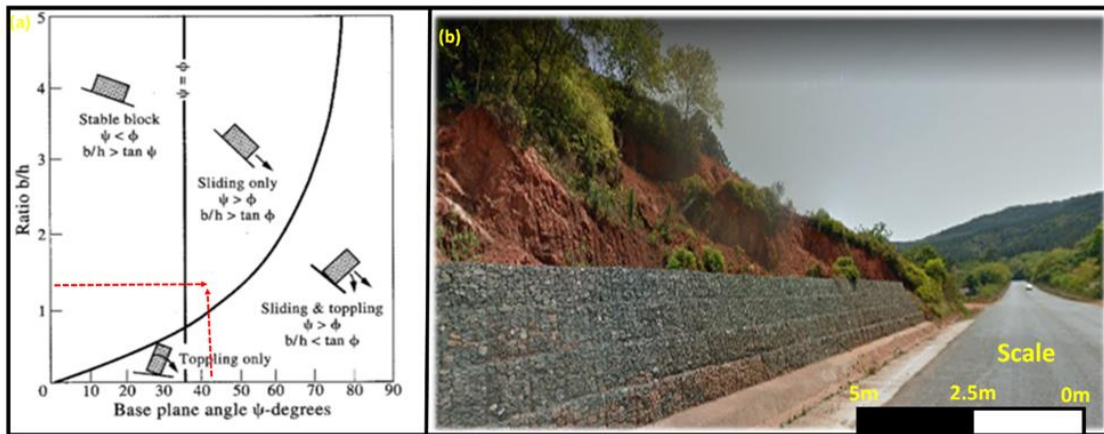
Figure 5.21 (a) Toppling analysis and (b) image showing study area A
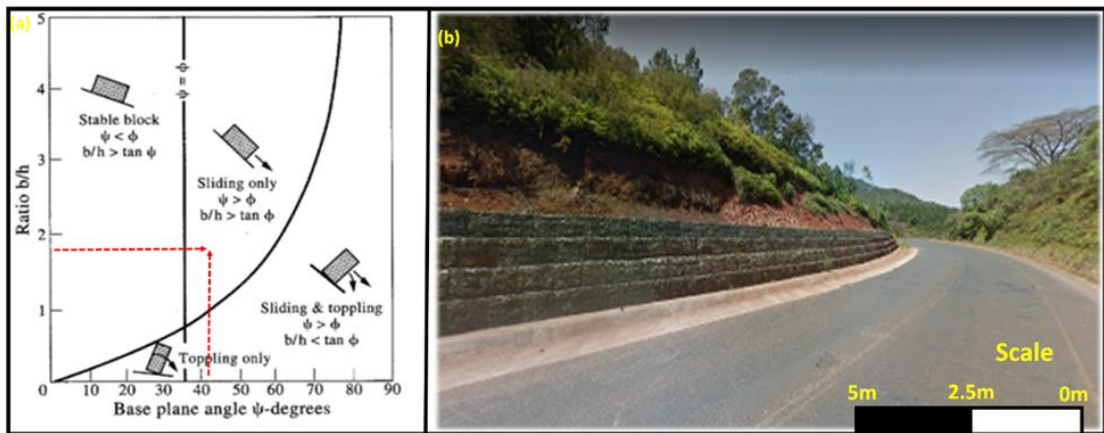
Figure 5.22 (a) Toppling analysis and (b) image showing study area B
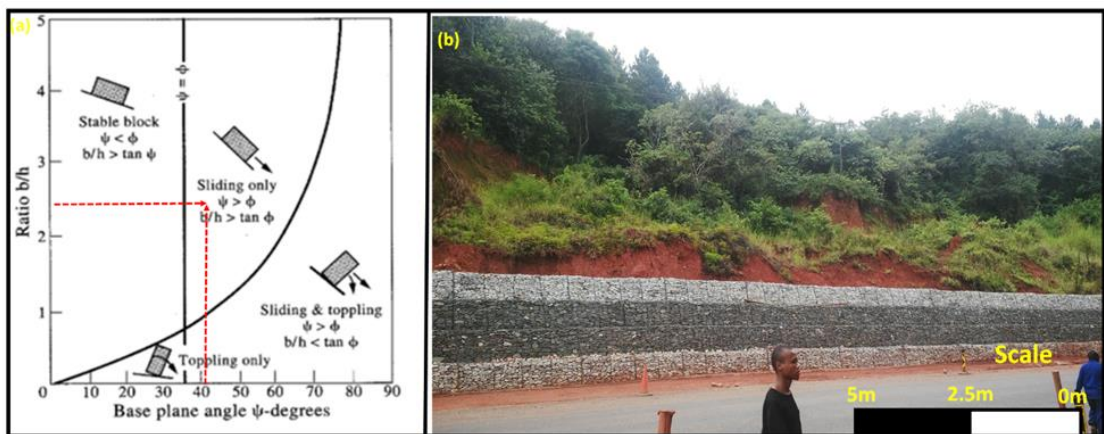
Figure 5.23 (a) Toppling analysis and (b) image showing study area C
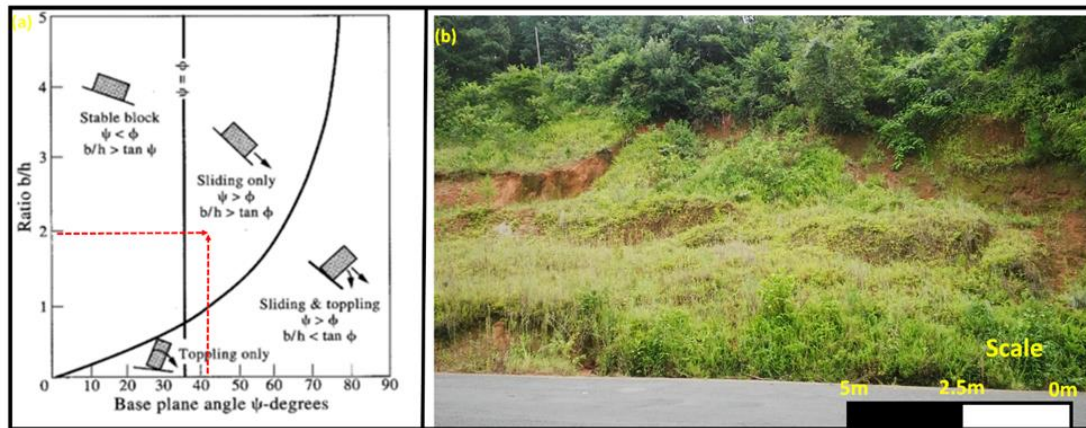
Figure 5.24 (a) Toppling analysis and (b) image showing study area D
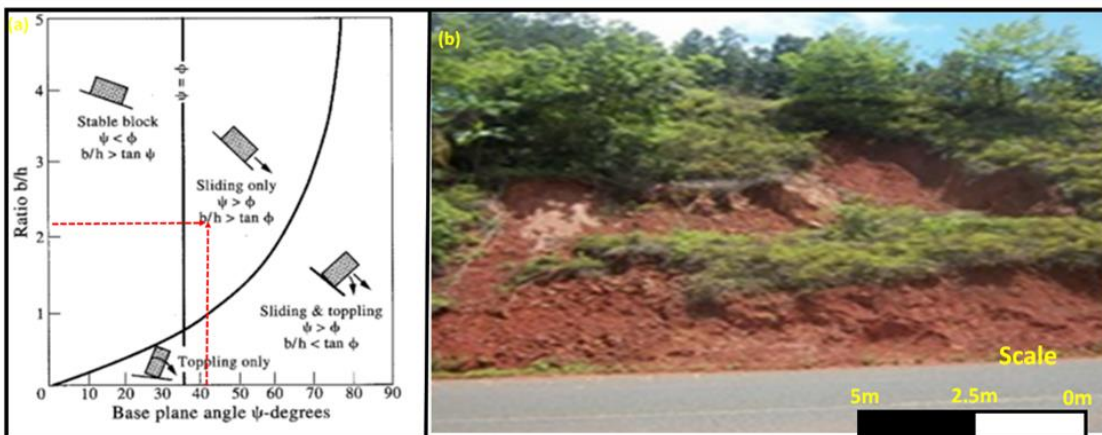
Figure 5.25 (a) Toppling analysis and (b) image showing study area E
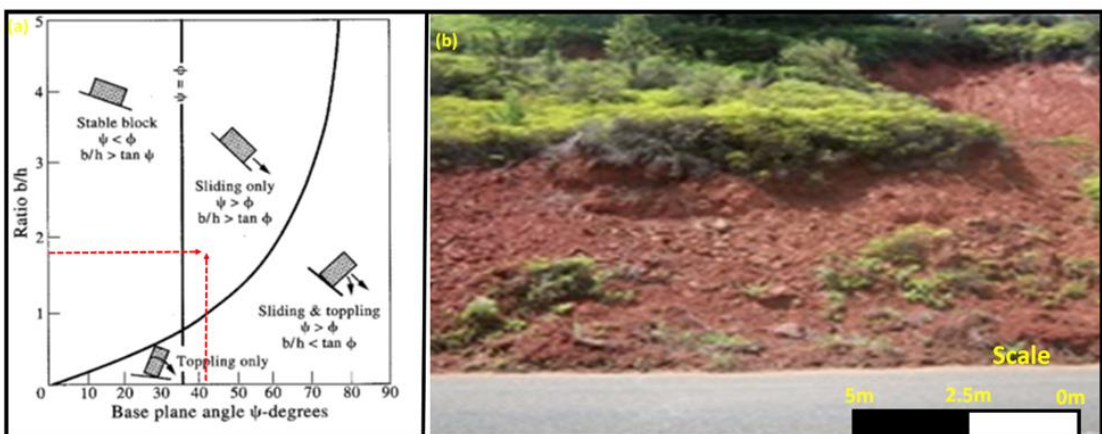
Figure 5.26 (a) Toppling analysis and (b) image showing study area F

153

Another aspect of toppling analysis is the common joint patterns around the area. These have been noted to influence the occurrence of the sliding of blocks since joints usually create wedges.

In summary, toppling analysis has shown that all active landslides are associated with sliding and to a certain extent a combination of toppling and sliding. Nevertheless, toppling analysis alone cannot give a broad view of the mechanisms associated with slope instability of the study area. That is why the next section presented the safety factors of six selected landslides estimated by simulation using SLIDES and RocPlane models. While the SLIDES software was used for rotational analysis, the RocPlane model took care of the transitional analysis. The purpose was to compare the impact of the slope angle on the recurrence of the slope instability.

5.4.2 Rotational analysis

The rotational analysis covered in this section is done on three soil types found around the six landslides within the study area. The simulation work underpinning the analysis focuses on the safety factor of several slices representing sections of the landslides. The results of the FoS of the clay soil slope and subsequent discussion are presented in the next paragraphs.

With reference to Figures 5.27 – 5.30, FoS values of the six locations with clay soil were found to be between 0.612 and 0.894 for all computation methods considered. The simulated minimum and maximum FoS values rate slopes in the area as unstable or prone to failure. It is clear that the material properties have played a major role in generating such low FoS. This is supported by field observations whereby the extent of slope failure was very wide in clay soils than in other soils. In a sense, simulated results mimic empirical analysis and observations. This provides a certain degree of reliability in the simulation model produced in this thesis.
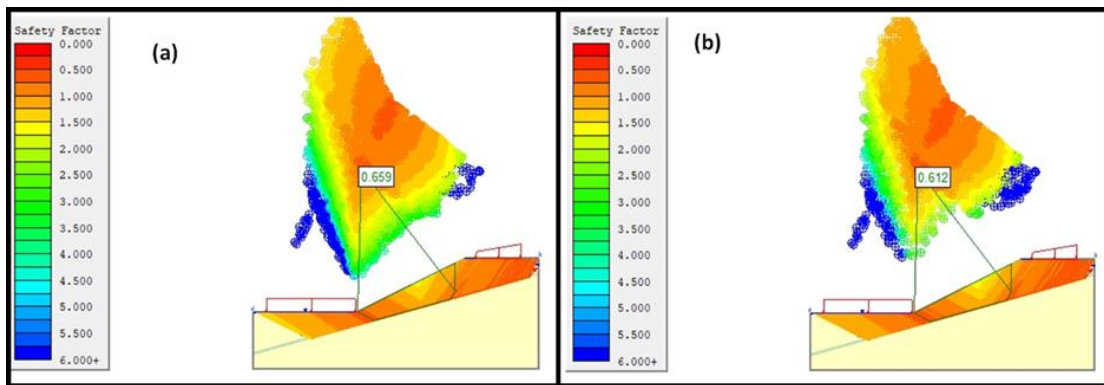
Figure 5.27 Safety factor simulated for drained to undrained conditions in clay soil slope using (a) Bishop's simplified method and (b) Janbu's simplified method
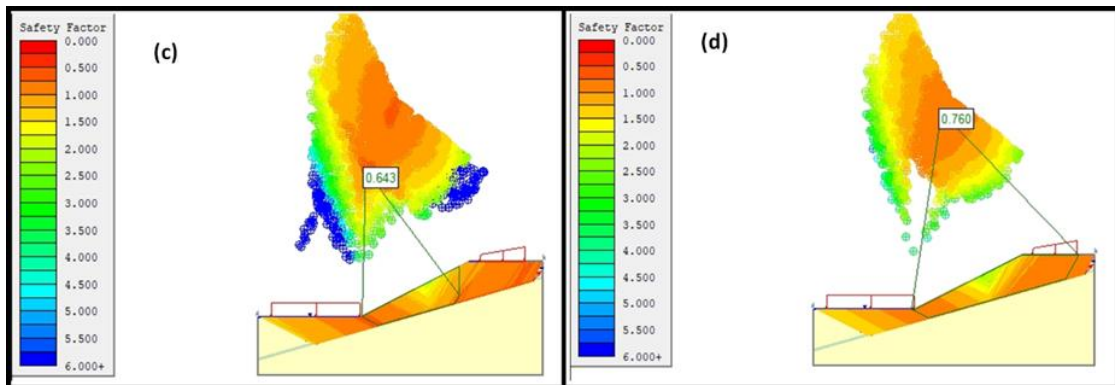
Figure 5.28 Safety factor simulated for drained to undrained conditions in clay soil slope using (c) Spencer's method and (d) the Corp of Engineers' Number One method
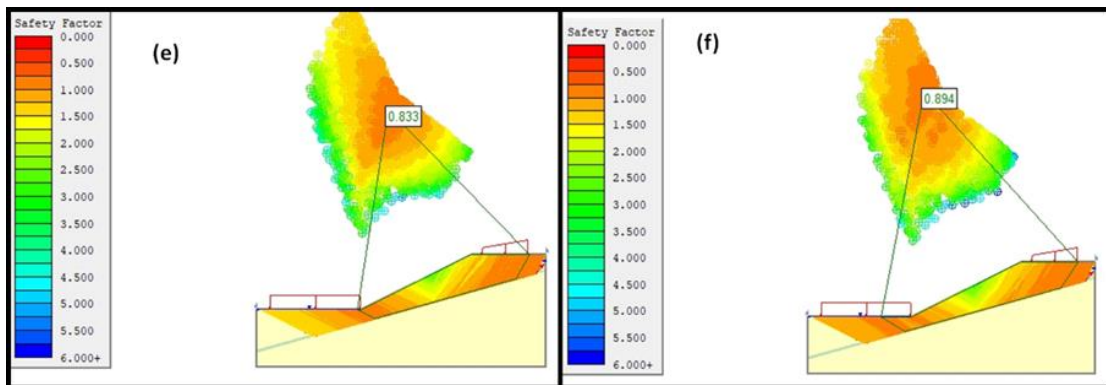
Figure 5.29 Safety factor simulated for drained to undrained conditions in clay soil slope using (e) the Corp of Engineers' Number Two method and (f) the Lower Karafiath method
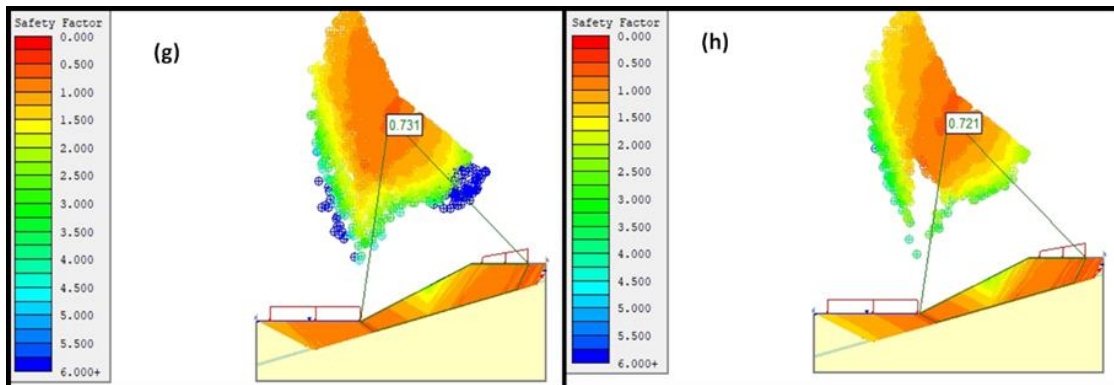
Figure 5.30 Safety factor simulated for drained to undrained conditions in clay soil slope using (g) the Lower Karafiath method and (h) the Gle/Morgenstern Price method

In Figures 5.27 – 5.30, eight methods are compared for consistency. All have shown that clay loam soil slopes are expected to collapse if mitigating solutions are inexistent. This is made worst by hydrometric streams that usually play a major role in triggering landslides (Lazzari and Piccarreta, 2018). The area of study was noted to have a number of periodical streams cutting across. Streams and geological features have the ability to weaken the material strength by reducing the resistance of the material. It is therefore arguable that extreme rainfalls reported within the study area may have also contributed to the observed cases of slope instability in the six locations.

The second type of soil simulated is silty clay. Results of the silty clay soil slope show that all areas are stable to a large extent. Indeed, estimated FoS values range from 1.424 to 1.717 as summarised in Figures 5.31 – 5.36. It is crucial to indicate that the standard safety factor for stable slope used in this study is 1.5 as per Hoek and Borwn (1981).
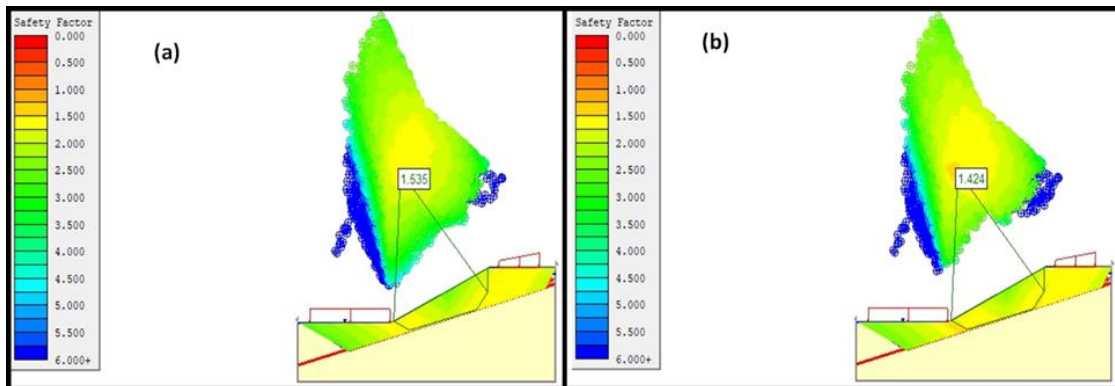
Figure 5.31 Safety factor simulated for drained to undrained conditions in silty clay soil slope using (a) Bishop's simplified method and (b) Janbu's simplified method
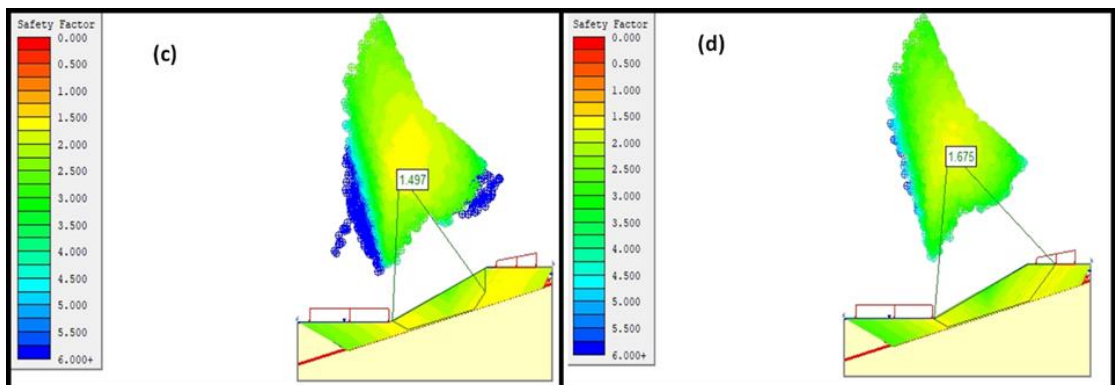
Figure 5.32 Safety factor simulated for drained to undrained conditions in silty clay soil slope using (c) Spencer's method and (d) the Corp of Engineers' Number One method
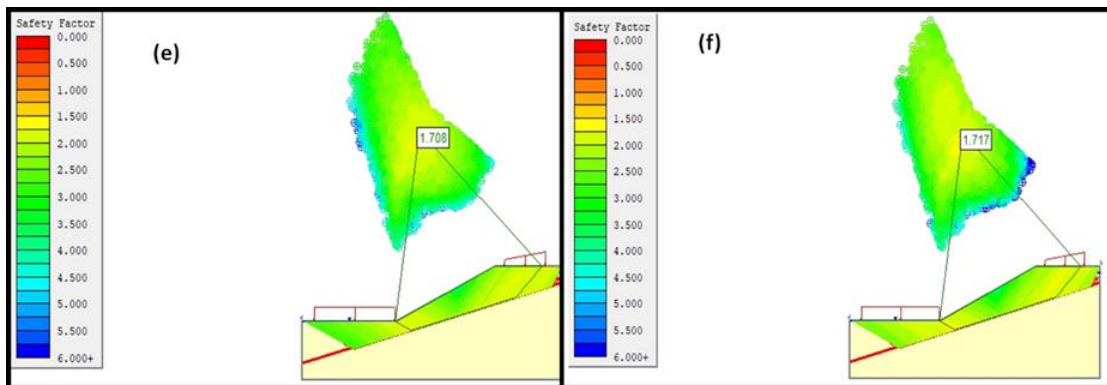
Figure 5.33 Safety factor simulated for drained to undrained conditions in silty clay soil slope using (e) Corp of Engineers' Number Two method and (f) the Lower Karafiath method
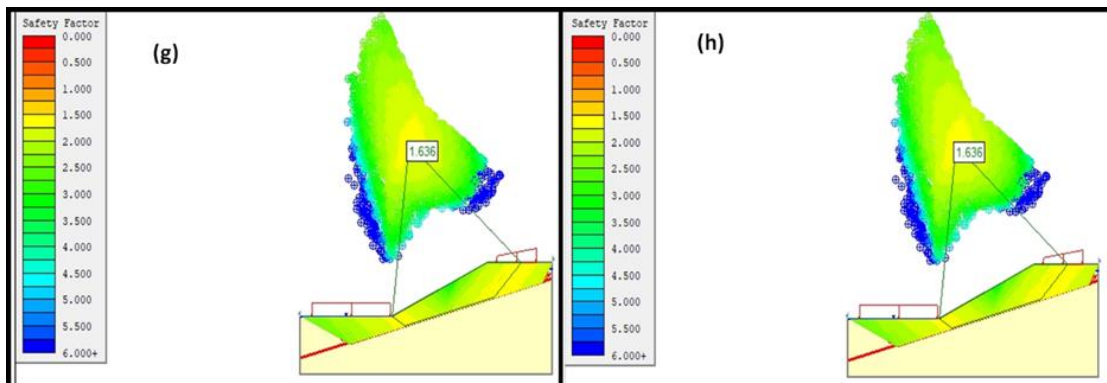
Figure 5.34 Safety factor simulated for drained to undrained conditions in silty clay soil slope using (g) the Lower Karafiath method and (h) the Gle/Morgenstern Price method

From the field observations and the empirical analysis, the slopes appeared to be less stable under normal conditions. But slope stability is expected to be compromised or reduced when rainfall occurs. Here also, conclusions similar to those applicable to the clay soil slope can be drawn. For example, the material properties affect the FoS. Numerical simulation results also make sense when compared to empirical observations. However, the extent of slope failure is moderate compared to pure clay soils. Finally, it is crucial to indicate that rainfall reduces the stability of the slope. The soil phase quickly changes during heavy rainfall and the soil material becomes liquid. At that stage, the

shear strength of the material rapidly drops and later the inter-particle binding weakens and allows deformation to occur at any given time.

The last simulations were undertaken to verify the performance of the clay loam soil material. Results show that slopes were stable for all simulation methods considered (see Figures 5.35 to 5.38).
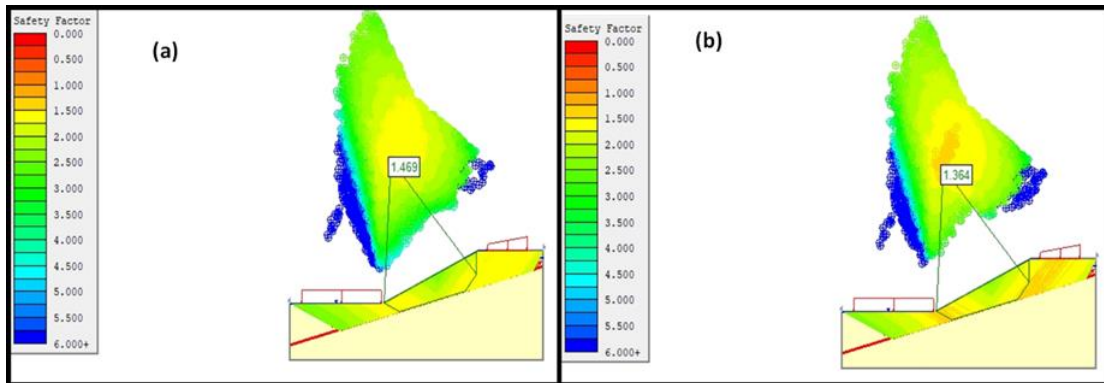
Figure 5.35 Safety factor simulated for drained to undrained conditions in claim loam clay soil slope using (a) Bishop's simplified method and (b) Janbu's simplified method
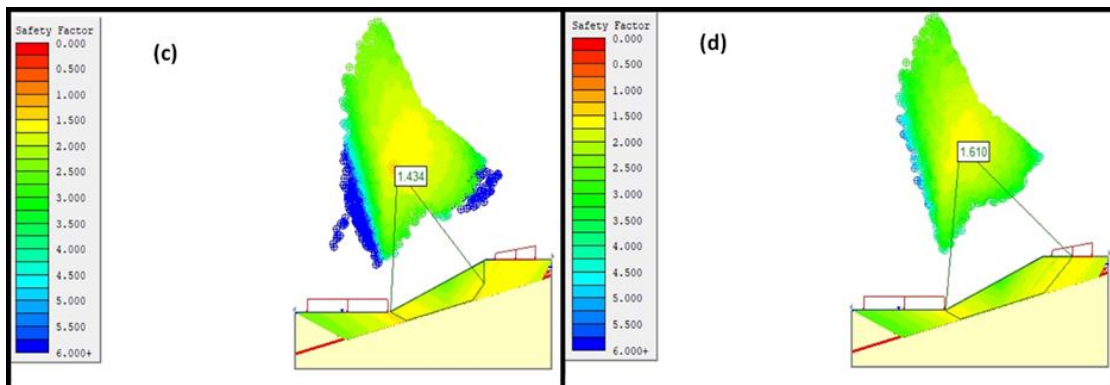
Figure 5.36 Safety factor simulated for drained to undrained conditions in claim loam clay soil slope using (c) Spencer's method and (d) the Corp of Engineers' Number One method
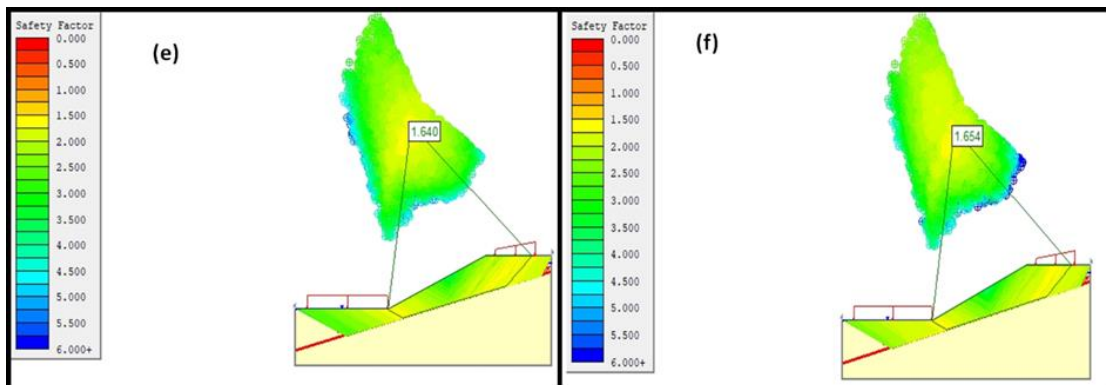
Figure 5.37 Safety factor simulated for drained to undrained conditions in claim loam clay soil slope using (e) the Corp of Engineers' Number Two method and (f) the Lower Karafiath method
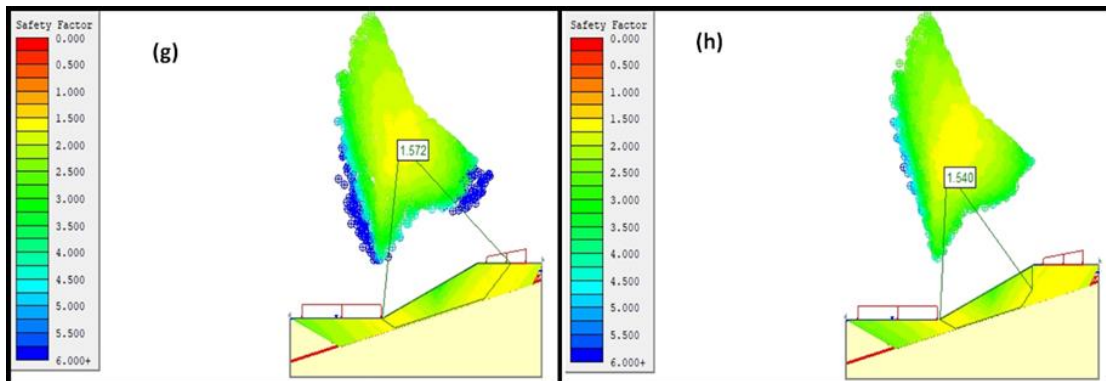
Figure 5.38 Safety factor simulated for drained to undrained conditions in claim loam clay soil slope using (g) the Lower Karafiath method and (h) the Gle/Morgenstern Price method

Figures 5.35 – 5.38 suggest that the selected slope is not prone to failure provided it is not exposed to extreme rainfalls. It is also important to highlight that the selected slopes are stable but in a very steep environment. So, geological structures and streams cutting across are expected to affect the simulated FoS which is mostly controlled by soil properties.

5.4.3 Transitional analysis

The transitional analysis is well established for the study of slope instability in highways and surface mining. The method is used in this section to simulate the safety factor, the slope behavior, and the effect of the slope angle. It was implemented using the RocPlane program.

Simulation results showed that an increase in slope angle leads to slope instability (See Figures 5.39 to 5.41).
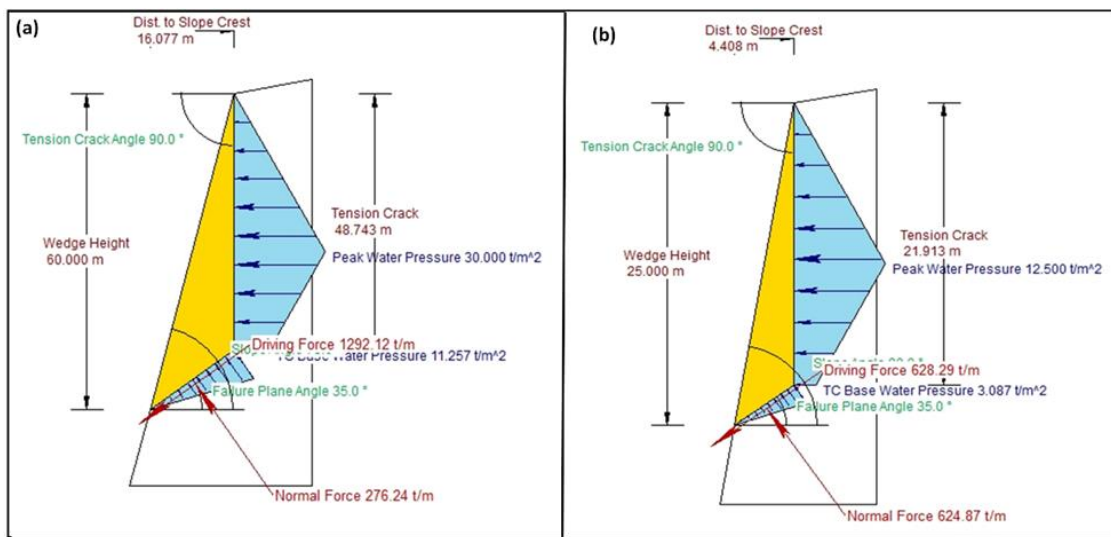
Figure 5.39 Simulation of slope behavior at (a) 90° and (b) 80° using RocPlane
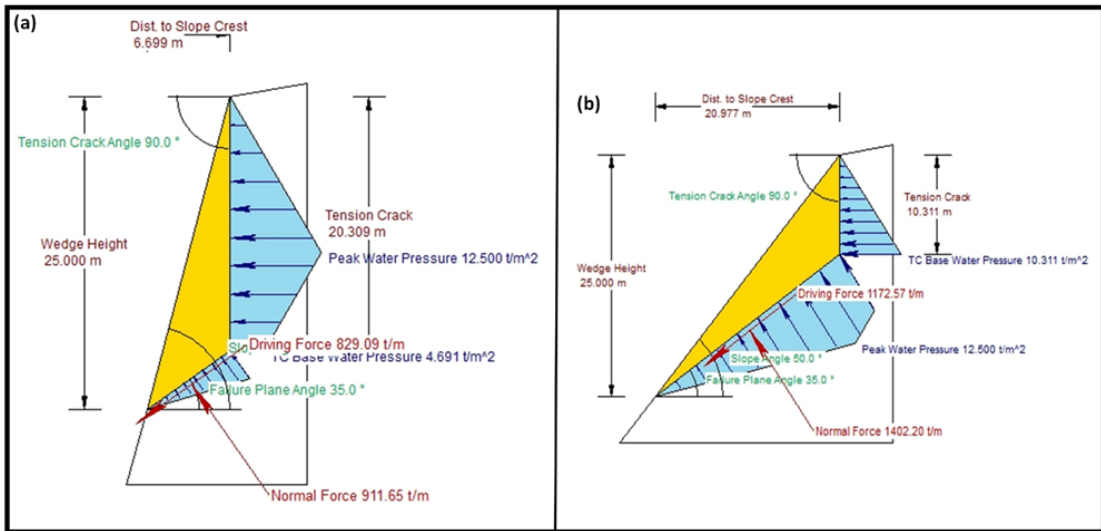
Figure 5.40 Simulation of slope behavior at (a) 75° and (b) 50° using RocPlane
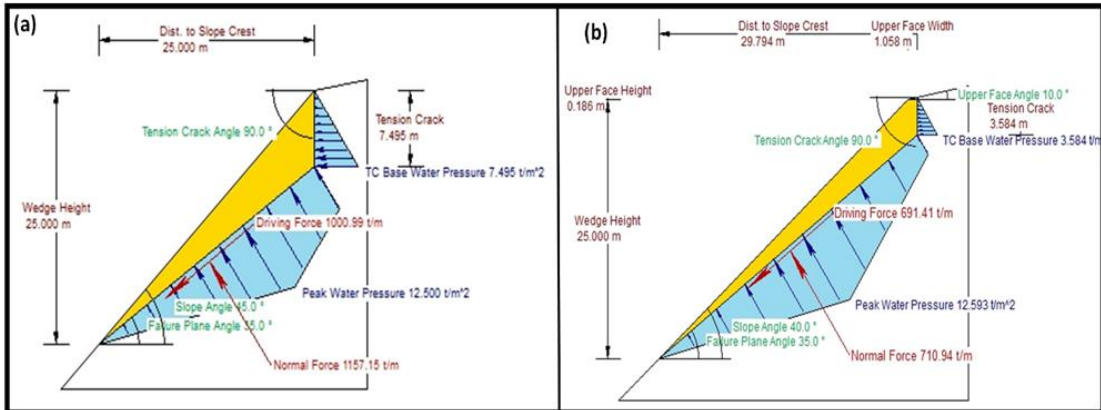
Figure 5.41 Simulation of slope behavior at (a) 45° and (b) 40° using RocPlane

It was also observed that the slope angle and water pressure increase the magnitude of the driving force. This eventually slides the solid material to the slope toe as evidenced in Figures 5.42 to 5.47. These results suggest that the presence of geological features (such as joints, Faults and Dykes), heavy rainfall, steepness of the slope and material properties are the common factors influencing the slope instability along the study area.

Figure 5.42 Simulation of safety factor at an angle of 90°
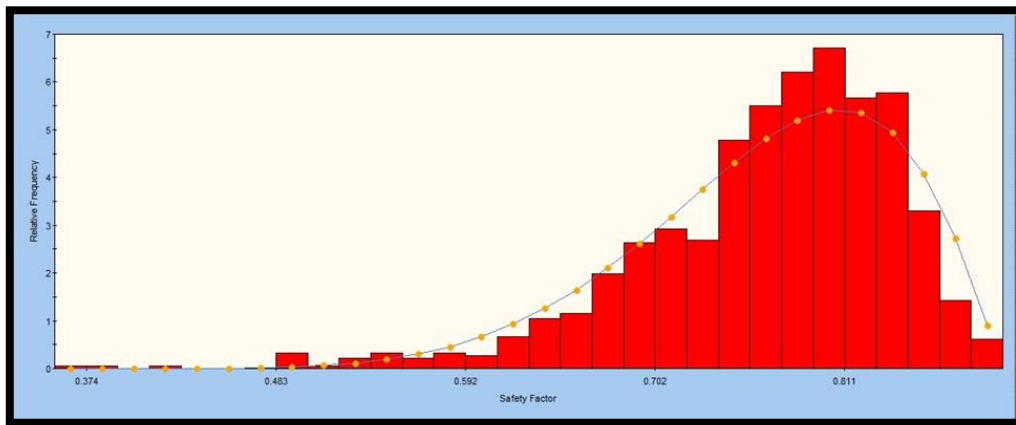
Figure 5.43 Simulation of safety factor at an angle of 80°
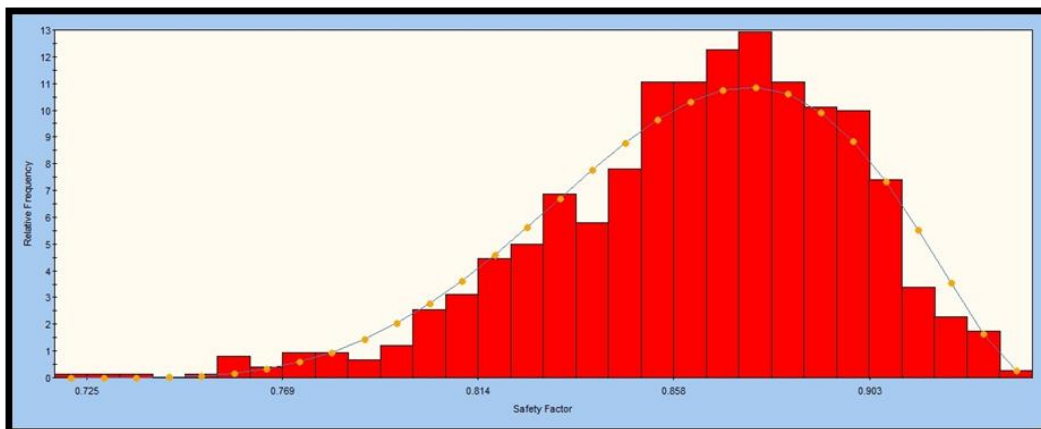
Figure 5.44 Simulation of safety factor at an angle of 75°
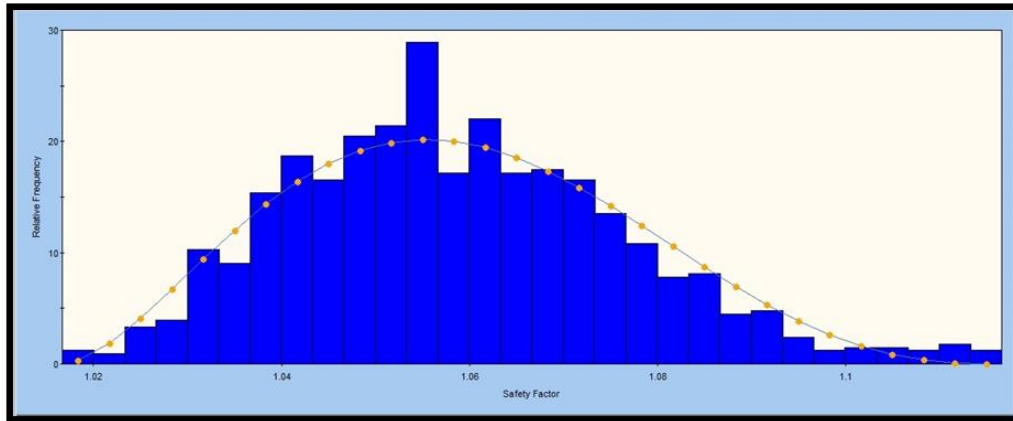
Figure 5.45 Simulation of safety factor at an angle of 50°
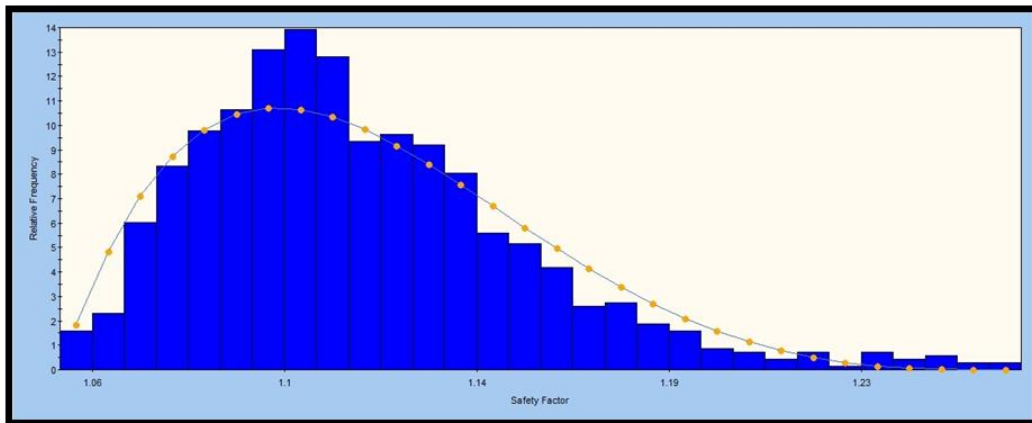
Figure 5.46 Simulation of safety factor at an angle of 45°
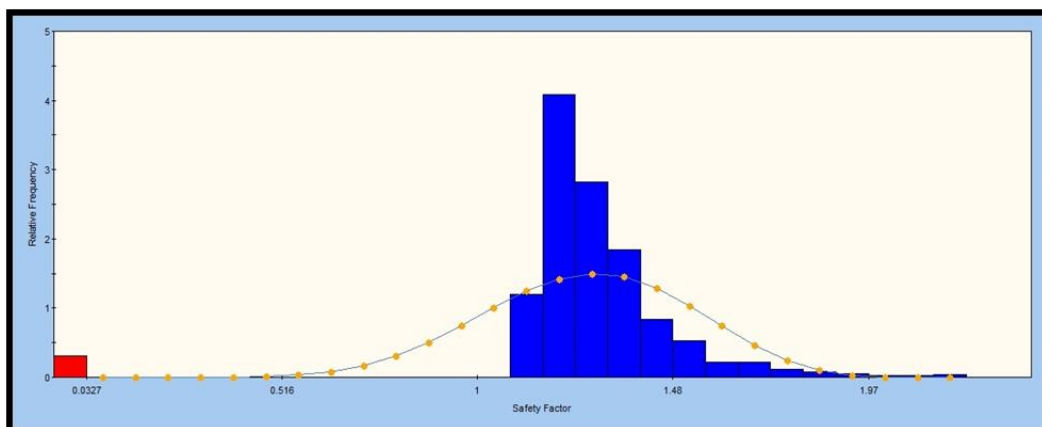
Figure 5.47 Simulation of safety factor at an angle of 40°

In summary, the results obtained from SLIDES and RocPlane were observed to agree well with each other. It was noted that material properties affect the stability of the slope in all situations. The steepness also plays a role in the stability of the slope with the simulated steep slope being prone to instability. The greatest challenge is that the wedge formation process cannot be simulated by the abovementioned technique. However, it can be inferred from the simulations that deformation or displacement within the Thulamela material is time-dependent. This is because it is activated by heavy rainfall and intersecting geological features.

5.5   Advanced numerical simulation of slope stability

The conventional techniques covered in the previous sections are generally limited to simplistic problems. However, many rock slope stability problems involve complexities such as in-situ stresses, seismic loading, and material anisotropy. Because of this, advanced numerical simulation becomes a viable alternative. In this section, stages that are normally followed during road construction were simulated using the Phase 2 software. The aim was to look into the change in stress, strain and shear as road construction progresses. The FEM-based results generated with Phase 2 are presented below.

5.5.1   Volumetric strain of slope in Phase 2

Simulation results rendered in Figure 5.48 for example show that during the first stage of road construction, the volumetric strain of the left and right slopes was minimal. This translated into little slope instability expected to occur from the upper part of the slope. Slope instability was nonetheless noted to gradually increase as the second stage of road construction was introduced (see Figure 5.49). However, it appears that much deformation was expected to occur on

the sides of the road walls during stage two. This is because the slope angle and height had rapidly increased (0.001 to 0.0149) which implied that the slope stability was to be affected largely.
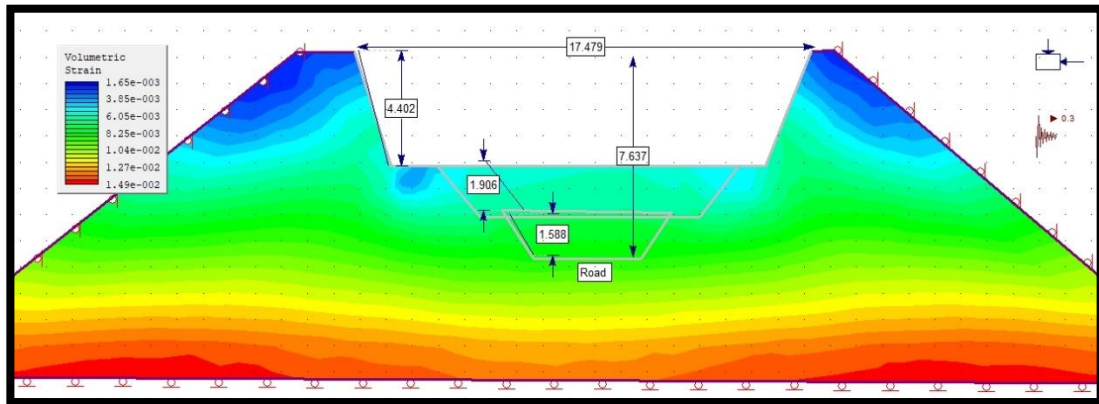
Figure 5.48 Simulated volumetric strain in the rockmass at the first stage of road construction
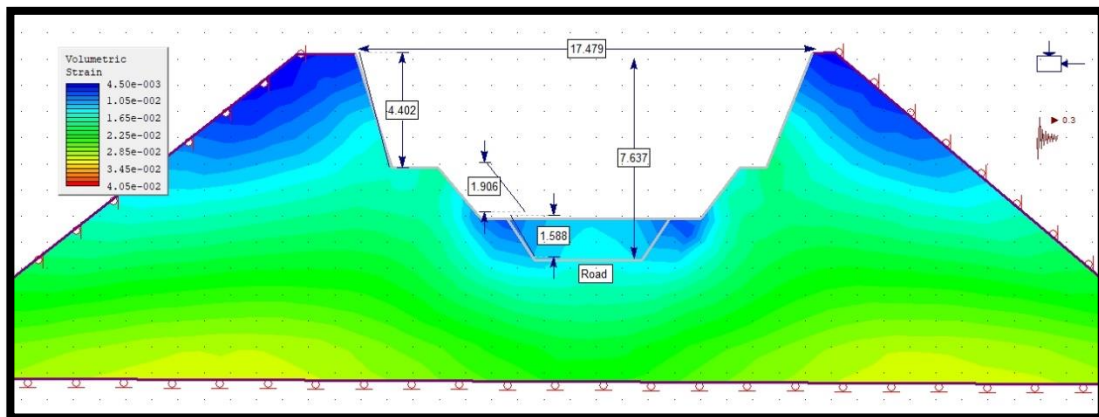
Figure 5.49 Simulated volumetric strain in the rockmass at the second stage of road construction

Unlike with other simulation tools used so far, Figures 5.48 and 5.49 indicate that a portion of the slope head is expected to slide into the excavation due to increased deformation. In reality, the model somehow agrees with reconnaissance and field observations as well as commonly accepted behaviors of slopes.

The final stage of road construction was also simulated as shown in Figure 5.50. It can be seen that the depth of the road, the slope height, and the slope angle have increased causing a proportionate increase in the volumetric strain of the slope.
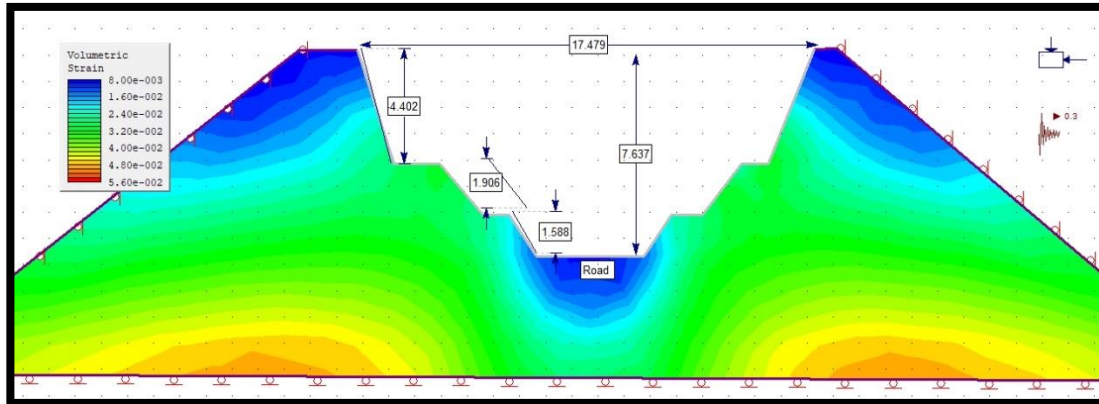
Figure 5.50 Simulated volumetric strain in the rockmass at the final stage of road construction

Ultimately, simulation results suggest that road construction has been disturbing the behavior and morphology of the slope. This has redistributed the total volumetric strain of the rockmass as blasting is used for excavation.

5.5.2   Maximum shear strain of slope in Phase 2

The same simulation outputs used to produce Figures 5.48 – 5.50 were used to extract the maximum shear strain. The results of the Phase 2 simulation model show that the strain due to the shearing of the material has been increasing from the first stage to the final stage of road construction. The output results summarized in Figures 5.51 – 5.53 suggest that the resistance of the material had been gradually dropping with each stage. This has affected the shear strength of the material as a result. Such inference could explain not only the tension cracks observed along the slopes but also the manner in which the slope failure has been happening along the road.
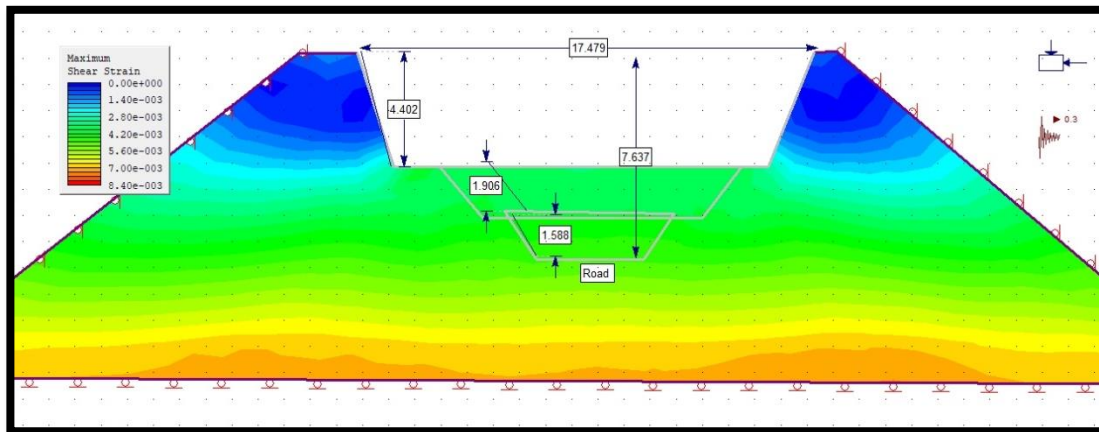
Figure 5.51 Simulated maximum shear strain in the rockmass at the first stage of road construction
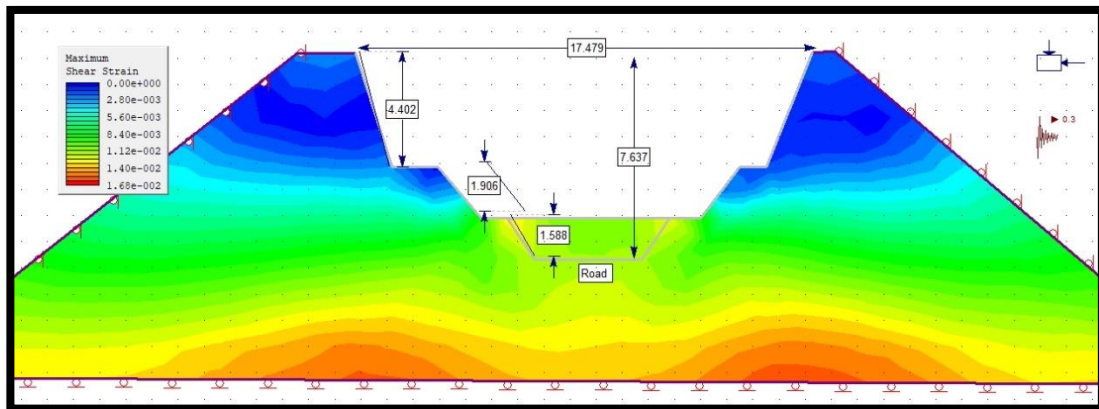
Figure 5.52 Simulated maximum shear strain in the rockmass at the second stage of road construction
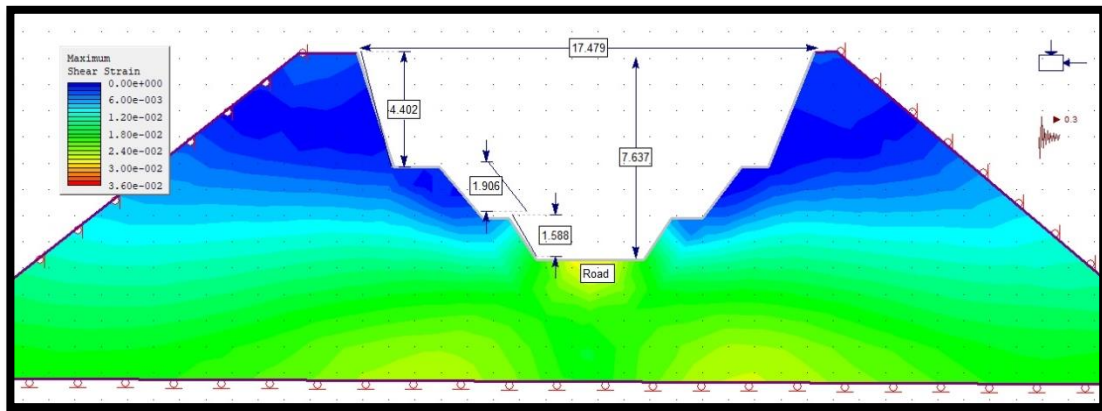
Figure 5.53 Simulated maximum shear strain in the rockmass at the final stage of road construction

One peculiar remark is the concentration of maximum shear strain around the middle part of the slope regardless of the stage of the road construction. This implies that material shearing is commonly expected around the middle section of the slope face. It is still not clear why the Phase 2 simulation model produced such an outcome.

5.5.3 Maximum shear stress of slope in Phase 2

Shear stress and strain were also analyzed from the Phase 2 simulation outputs. By comparing Figure 5.54 – 5.56 and Figures 5.51 – 5.53 at similar construction stages, it can be seen that the distribution of shear stress relates well with that of shear strain. However, the noticeable difference is that shear stress in Figures 5.54 – 5.56 steadily increases with the stages of road construction. This could be attributed to the fact that shear stress is generally proportional to the depth and width of the road (Sin et al. 2012).
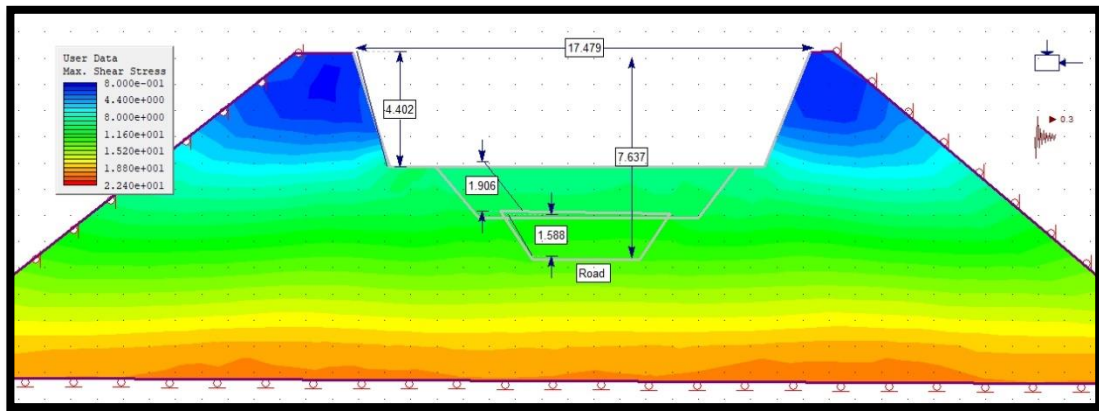
Figure 5.54 Simulated maximum shear stress in the rockmass at the first
stage of road construction
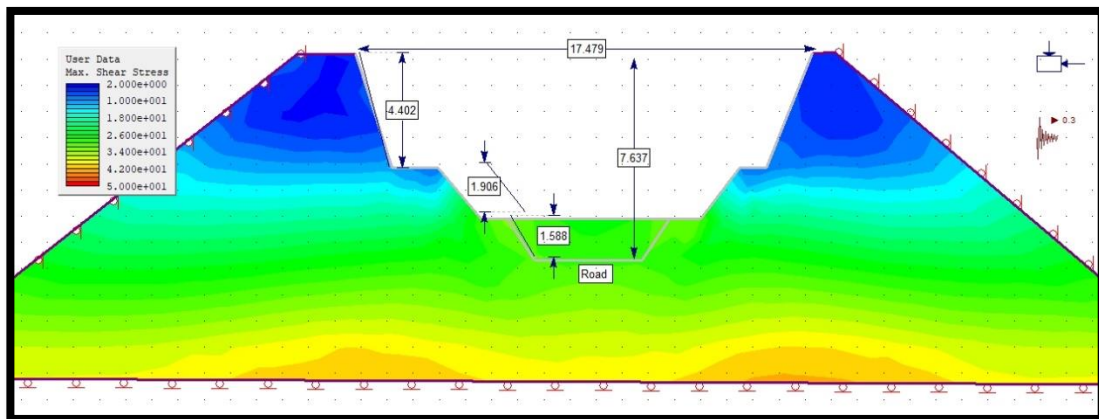
Figure 5.55 Simulated maximum shear stress in the rockmass at the second
stage of road construction
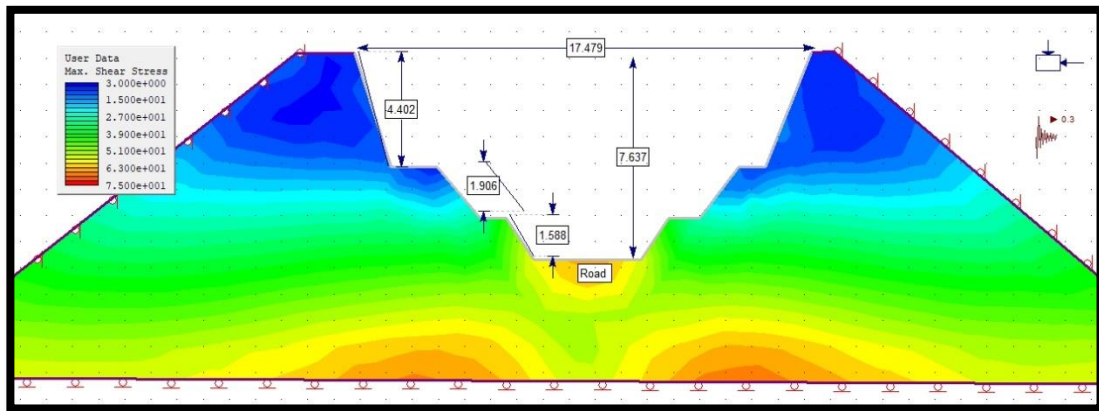
Figure 5.56 Simulated maximum shear stress in the rockmass at the final stage of road construction

Finally, shear stress was also found to be concentrated along the middle section of the slope face (see Figures 5.54 to 5.56). This simply means that the failure of the slope is expected to be initiated along that stress zone. In fact, most slope failures were observed not to occur from the mountain top but rather from the central area of the slope as shown in Figure 5.57.
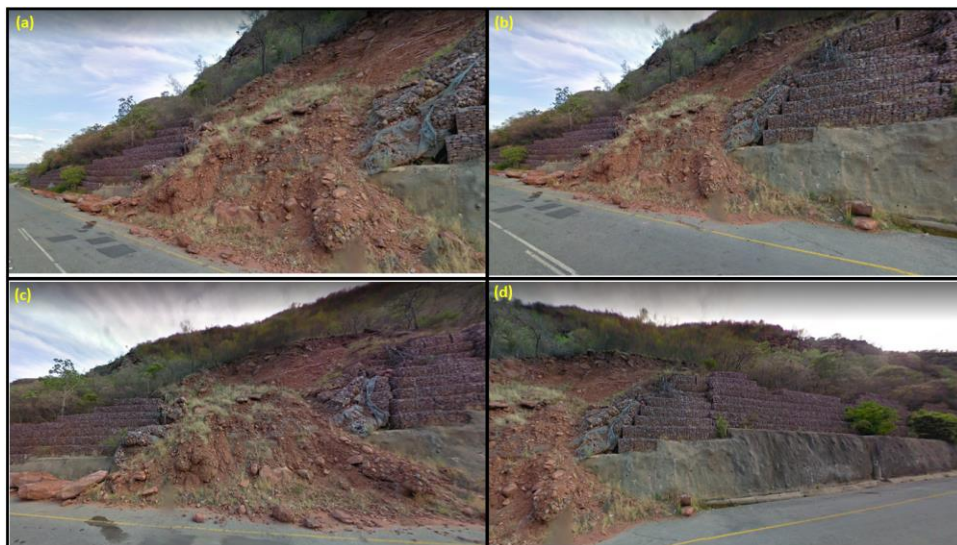
Figure 5. 57 Examples of the slope failure at the central area

5.5.4 Total displacement of slope in Phase 2

The total displacement of a slope is an important aspect to simulate as it gives an idea of the expected deformation as a result of rock excavation. The simulation results are summarised in Figures 5.58 – 5.60 for the three stages of road construction. Much development in the distribution of displacement can be seen throughout the stages. What is evident from Figures 5.58 to 5.60 is that displacement steadily increases from the first stage to the final stage of road construction.
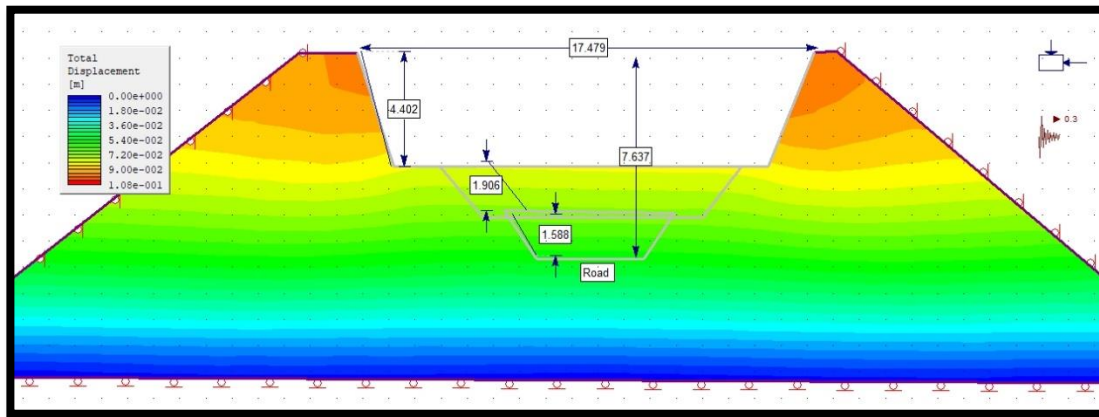
Figure 5.58 Simulated total displacement in the rockmass at the first stage of road construction
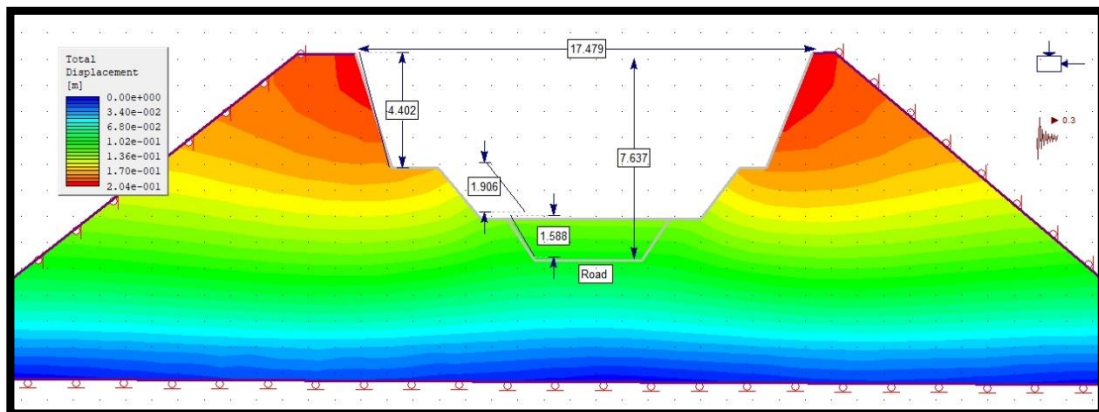
Figure 5.59 Simulated total displacement in the rockmass at the second stage of road construction
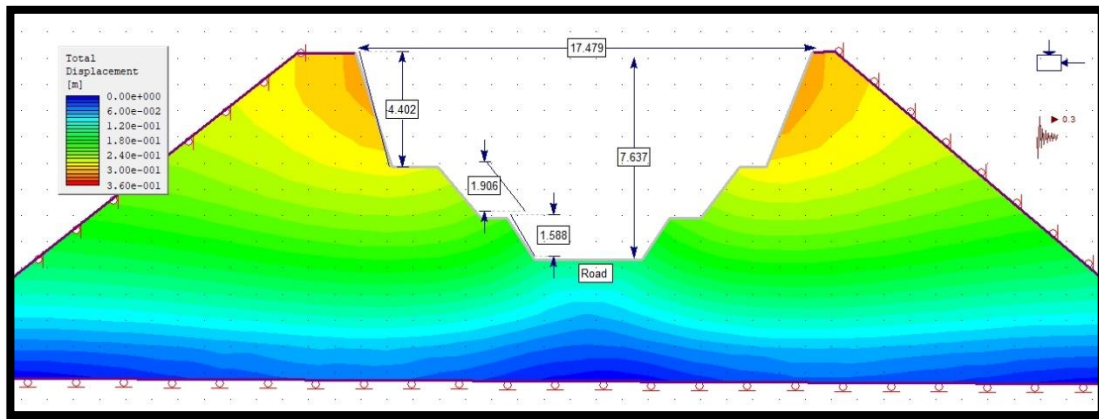
Figure 5.60 Simulated total displacement in the rockmass at the final stage of road construction

Lastly, the total displacement of the slope changes as the stages of construction progress. However, total displacement remains the highest on the road base and the foot of the slope at all stages. This has serious implications on the stability of the road foundation that requires a solid base and stabilizing gabions to curb the anticipated deformations and cracks.

5.5.5   Principal stress of slope in Phase 2

The last simulation outputs pertain to the minor and major principal stresses developed within the rockmass defining the slope.

Figures 5.61 to 5.63 summarise the simulation outputs of the minor principal stress (symbolically known as σ_1) at different construction stages. It can be seen from the stress distribution of the entire road excavation that the stress cloud is concentrated in the lower section of the slope. The findings are somewhat similar to the shear stress ones (see Figures 5.54 – 5.56 for comparison).
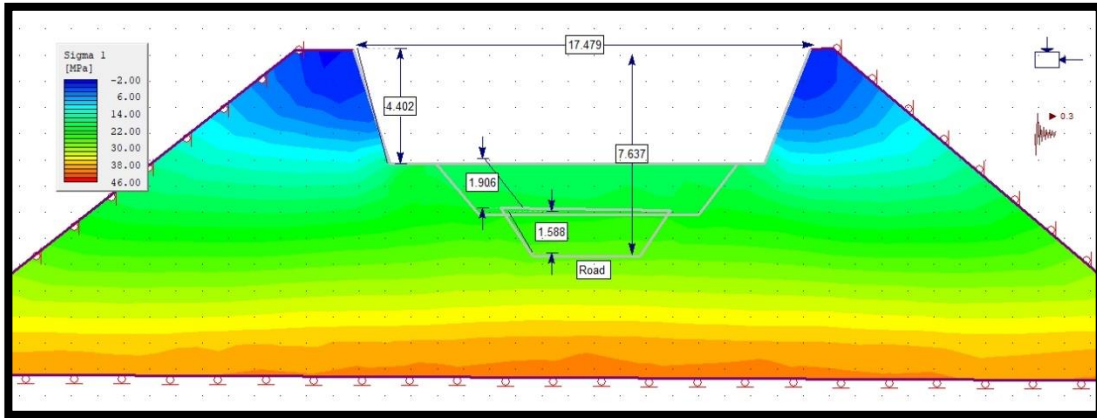
Figure 5.61 Simulated minor principal stress σ_1 at the first stage of road construction
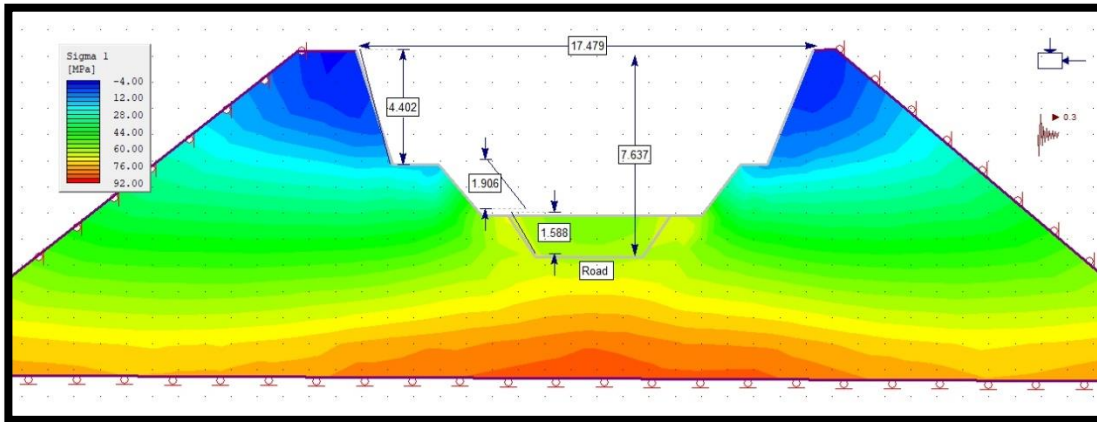
Figure 5.62 Simulated minor principal stress σ_1 at the second stage of road construction
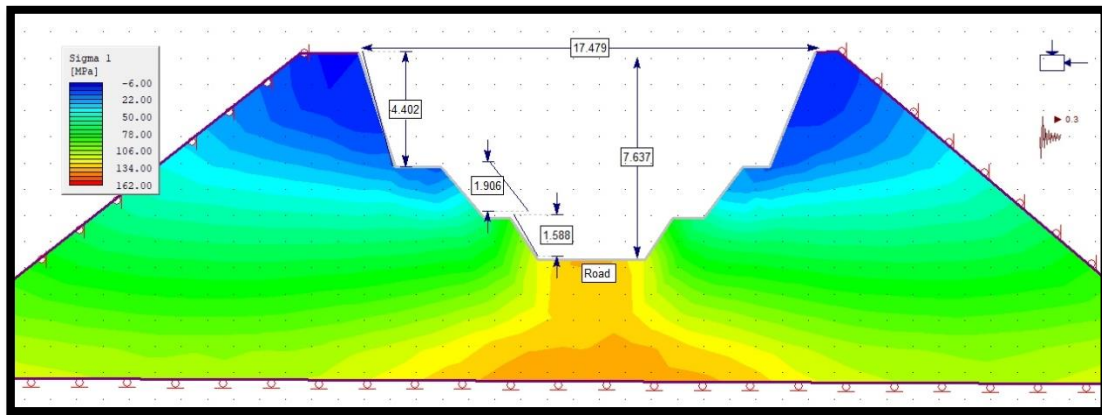
Figure 5.63 Simulated minor principal stress σ_1 at the final stage of road construction

Note that the concentration of principal stress σ_1 quickly changes between construction stages. Indeed, stress levels around the surface and for shallow excavation are minimal; then, develop and provides some indication of slope weakening with the deepening road excavation.
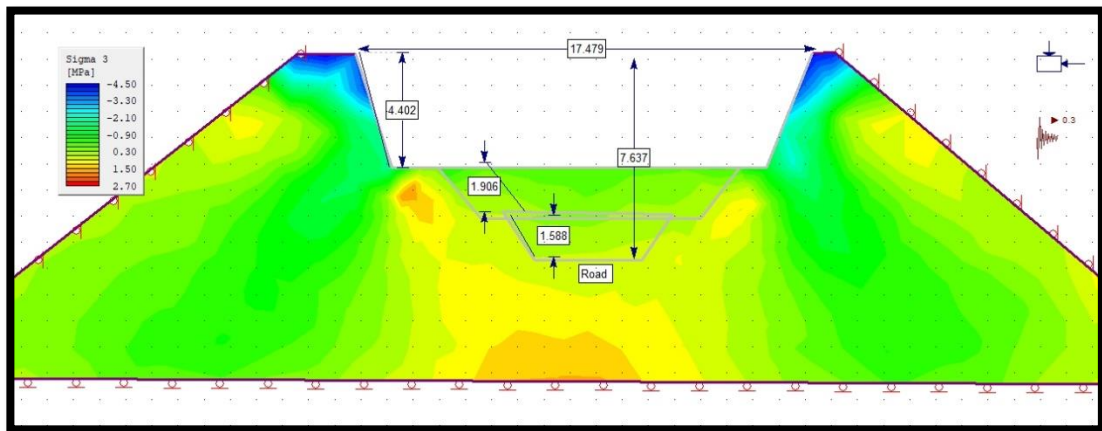
Figure 5.64 Simulated major principal stress σ_3 at the first stage of road construction
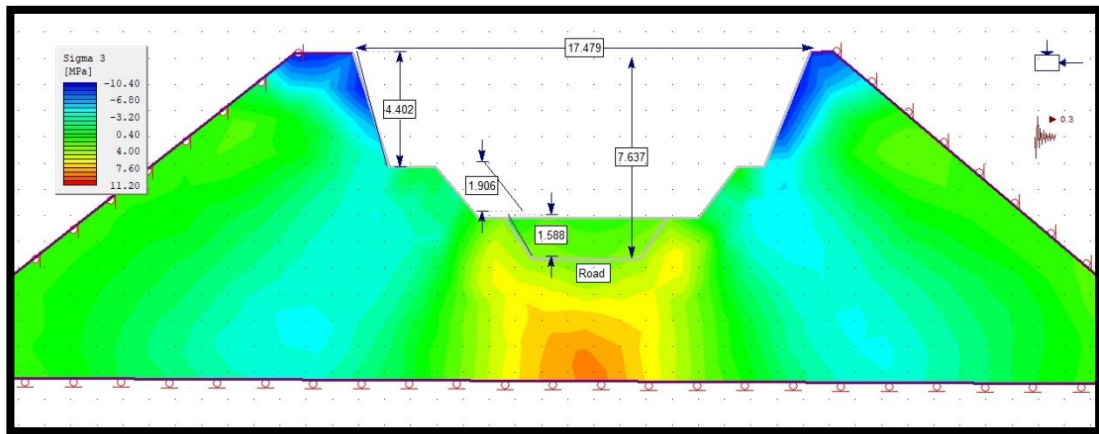
Figure 5.65 Simulated major principal stress σ_3 at the second stage of road construction
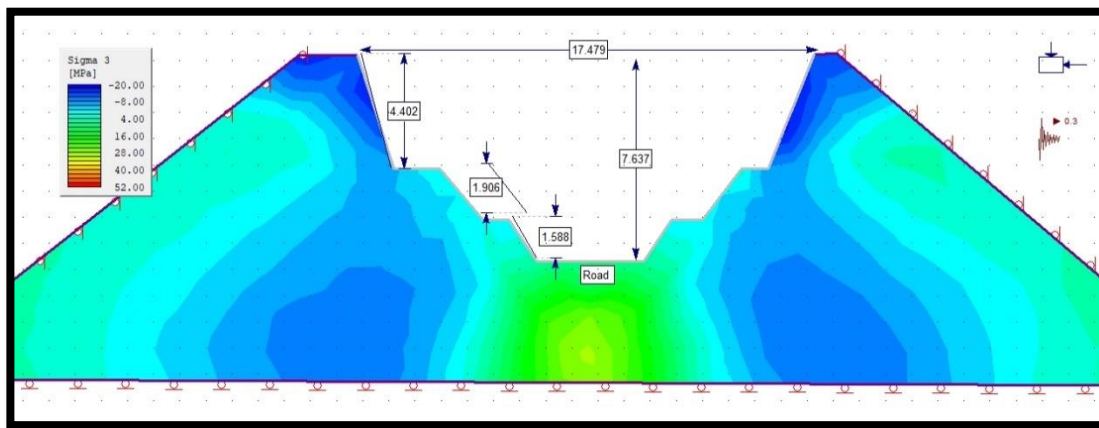
Figure 5.66 Simulated major principal stress σ_3 at the final stage of road construction

The last note is to state that the major principal stress σ_1 increases with the rate of excavation and blasting as evidenced in Figures 5.64 – 5.66. This implies that the strength of the road walls is compromised by the excavation.

5.6   Conclusion

The aim of this chapter was to implement kinematic, limit equilibrium and numerical analyses to cases of slope stability in the Thulamela area. The following computer packages were used: SWEDGE, SLIDES and RocPlane.

From the kinematic analysis, it was found that the most active slope instabilities in the area were associated with kinematic wedge failure. Failures occurred at steep slope angles with correspondingly low FoS values. Limit equilibrium analysis, on the other hand, revealed that the selected active and post slope instability areas happened in the form of sliding only rather than toppling.

The shearing strength of the material revealed that the slope angle influences the probability of the slope failing while geological features and extreme rainfall could be the driving forces of landslides.

In terms of FEM-based simulations, the computer code Phase 2 was employed to study volumetric strain, shear stress, shear strain, total displacement, and principal stress components of the slope. The outputs enabled us to show that all the above parameters increased with the stages of road construction thereby compromising slope stability. Perhaps the most important point to make is that improper road construction, steep slopes, extreme rainfalls, multiple geological features and water streams are the main drivers of slope instability in the Thulamela Municipality.

Chapter 6　Development of slope stability hazard assessment and prediction of recurrence chart

A simple slope stability chart of unsaturated soil in mountainous areas is described in this chapter. The chart is deemed most suitable for slope instability prediction in unsaturated clay soil. The WOE model, ASTER imagery and FEM simulations were used to identify the key factors governing slope instability in the selected study areas of the Thulamela Municipality.

The above techniques together with outcomes from the previous chapters have made it possible to develop the slope stability hazard prediction chart. Results show that the chart developed in this chapter is easy to use, does not require sophisticated interpretation techniques and is applicable to the selected study area. Most importantly, it was demonstrated from the chart that all active slopes in the study area can be considered unstable. The chart also captured well the influence of geological features, streams and slope steepness. Finally, it was concluded that remote sensing (ASTER imagery) and FEM (Phase 2 simulator) are both useful techniques for generating reliable charts that could predict slope instability in mountainous areas. [5]

6.1　Introduction

The analysis of conditions leading to landslide events is central to the identification of causative parameters (Ramesh et al., 2017; Gupta et al., 2018; Ramos-Bernal et al., 2018). These parameters are generally grouped into three

---

[5] There is a paper in review from this chapter in the Geosciences journal, with the following tittle: Development of slope stability hazard assessment and prediction of recurrence chart: ASTER images and FEM-based approaches.

categories: static, variable, and triggering factors (Tyoda, 2013). Causative factors that influence landslide occurrence in a certain area can be identified. Upon retrieval from remote sensing data of the area, they are turned into a landslide susceptibility map (Sarkar and Kanungo, 2004).

The preparation and construction of landslide susceptibility maps require the knowledge of the prevailing conditions of the area (Kanungo et al., 2009). These maps aim at predicting where failures are likely to occur without specifying when these would happen (Singh et al., 2011).

Different techniques can be used to weight the causative parameters of landslide and to model susceptibility maps (see Section 2.6.4). The appropriate technique is selected based on the nature of the problem, the observation scale and the availability of data descriptive of the causative factors (Sarkar and Kanungo, 2004). In this thesis, the Weight of Evidence (WOE) model was employed in combination with ASTER imagery. This was supplemented with FEM simulation in Phase 2 for validation purposes.

The results are divided into three main thematic sections. The first section discusses the results of the Normalized Difference Vegetation Index (NDVI). The next section identifies the causative factors of slope instability before the landslide susceptibility maps are produced. The last section is centered on exploring the effect of road construction on the stability of the road walls by means FEM simulation. The results of the chapter are outlined below.

6.2   Normalized difference vegetation indices in the selected areas

The Normalized Difference Vegetation Index (NDVI) values of nine pixels representing landslide area A are presented in Figure 6.1. Based on Section 2.6.3, high values for the year preceding landslide occurrence (2004) are noted

with an average value of 0.498 (Table A1). In contrast, the average NDVI in 2017 is relatively low at 0.106 with the lowest index at -0.371.
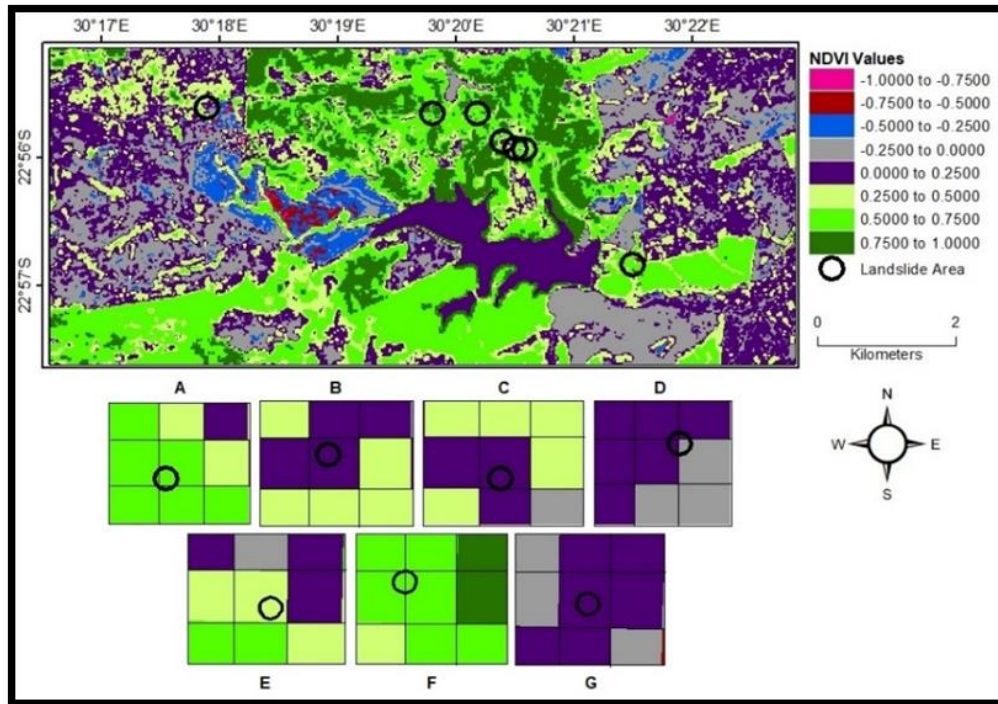
Figure 6.1 Maps showing the NDVI values derived from the ASTER data acquired in 2004. The nine pixels, covering an area of 45 m², represent each landslide

Landslide area B attained NDVI values exceeding 0.400 for the year 2004 indicative of good vegetation conditions (Jensen, 1986). On the contrary, most pixels in 2017 showed the deterioration of vegetation health with the exception of two pixels in which the NDVI value was noted to increase between 2004 and 2017 (see Table A2 and compare Figures 6.1 and 6.2). Eight pixels in the landslide areas C and D have high NDVI values in 2004 which subsequently drop in 2017 (Tables A3 and A4). As far as area E is concerned, low NDVI values are noted in 2017 relative to 2004 (Table A5). In 2004, area F was characterized by a very healthy and productive vegetation cover with an NDVI as high as 0.806. However, this pixel recorded the lowest NDVI of -0.578 in

2017 which suggests the prevalence of a land cover other than vegetation (Table A6). Landslide area G attained average NDVI values of 0.054 and 0.182 for the year 2004 and 2017 respectively (Table A7).
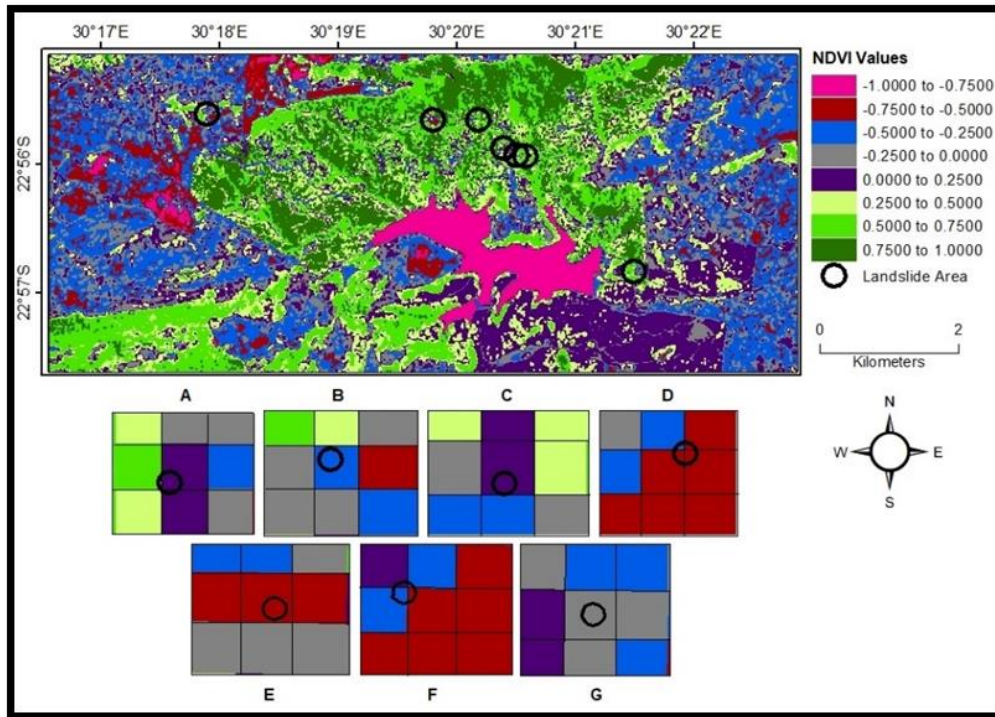
Figure 6.2 Maps showing the NDVI values derived from the ASTER data acquired in 2017. The nine pixels, covering an area of 45 m^2, represent each landslide

What is clear from the above analysis is that landslides in the Thulamela Municipality are well-pronounced as evidenced by the true-color satellite images of Figures 6.1 and 6.2. Furthermore, the NDVI values indicate a worrisome deterioration of the vegetation and an expansion of landslide localities over time. The latter can be attributed to the annual reactivation of landslide events in the active areas. The Western and Eastern parts of the study area also show a decline in NDVI values between 2004 and 2017 (Figures 6.1 and 6.2). These parts coincide with pixels classified as built-up land and bare soil/rock. They are indicative of human activities such as

deforestation, farming, and expansion of residential or commercial areas which can trigger slope failure (Garland and Oliver, 1993). Indeed, in this region, small-scale farmers frequently employ slash-and-burn techniques before December (Diko et al., 2014). The preparation of the fields for farming corresponds to a period of heavy rainfall. This in turn increases the likelihood of landslides.

6.4   Causative factors influencing slope instability

The slope steepness within the study area was simulated using the WOE model. Results have enabled the location of all active and post slope landslides along the slopes of steepness greater than or equal to 18° (see Figure 6.3). These findings matched those in Sections 5.3.2 and 5.4.3.
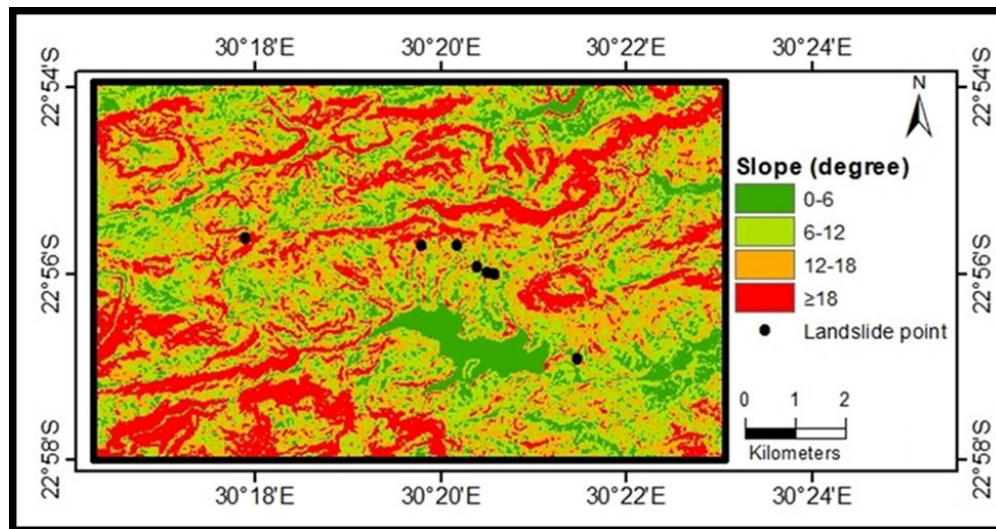
Figure 6.3 Slope angle simulated throughout the study area

Next was to analyze whether the orientation of the slope is a determining factor in the orientation of the slope collapse. Slopes were characterized to be orientated South-East, South-West, West, South and North-West (see Figure 6.4). The outputs also revealed that active slope instabilities are oriented

randomly with no apparent pattern. Consequently, it was difficult to ascertain whether slope orientation has an influence on slope instability. Following further analysis, it was noted that all active slope instabilities are located at the intersection of two slope orientations as evidenced in Figure 6.4.
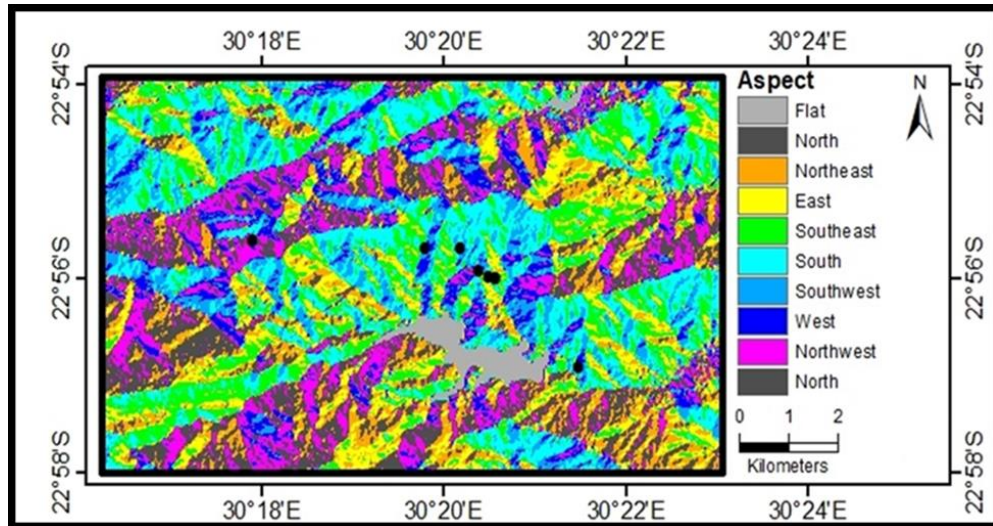
Figure 6.4 Slope orientations

The geographical elevation was also analyzed with the WOE modeling framework. Results show that the active slope instability happens at an elevation ranging from 900 m to 1100 m above sea level (see Figure 6.5). This strongly suggests that the selected study area in the Thulamela Municipality is at a high elevation or mountainous area. In addition to this, elevation and steepness contribute greatly to the stability of slopes.
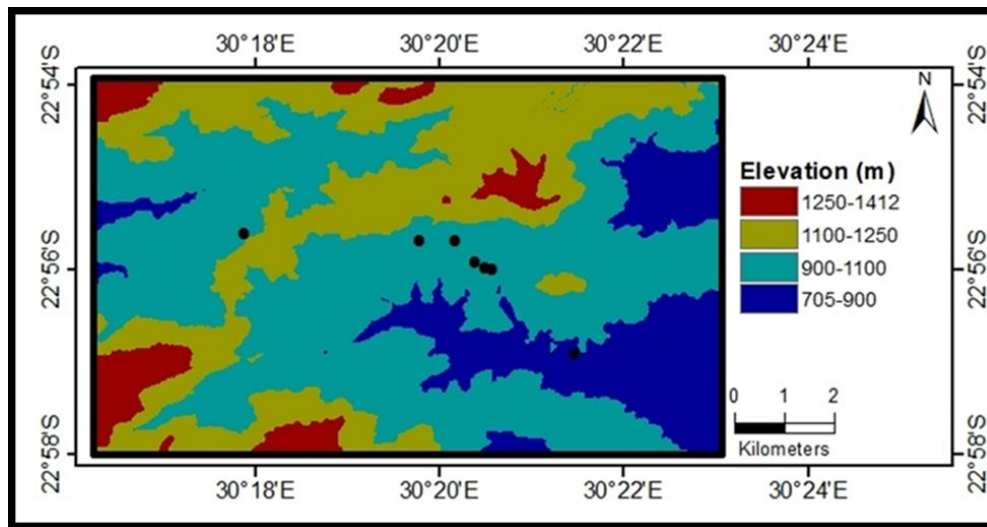
Figure 6.5 Elevation in the vicinity of the study area

Remote sensing data was finally utilized to study the contribution of geological features and water streams to the occurrence of slope instability in the area. The results of the endeavour are illustrated in Figures 6.6 and 6.7.
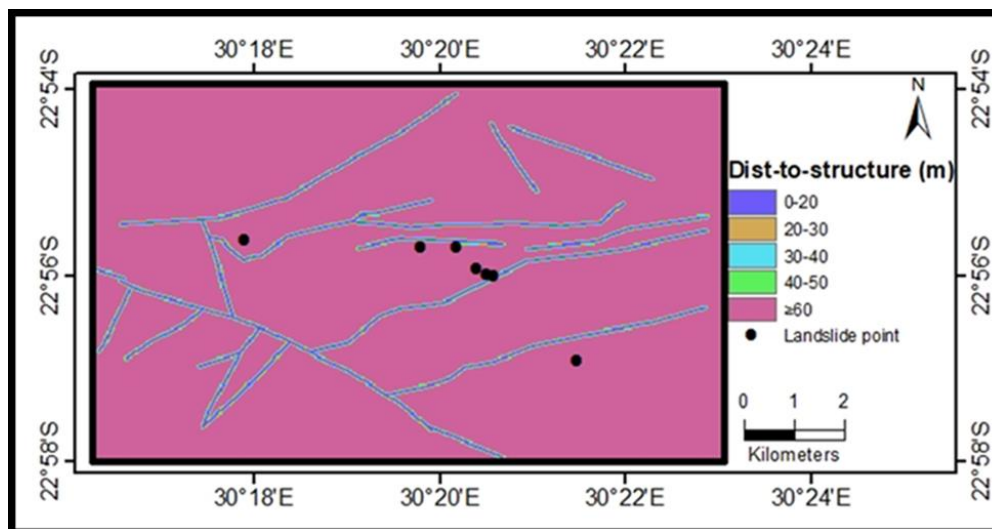
Figure 6.6 Locations of landslides relative to geological structures (Faults)
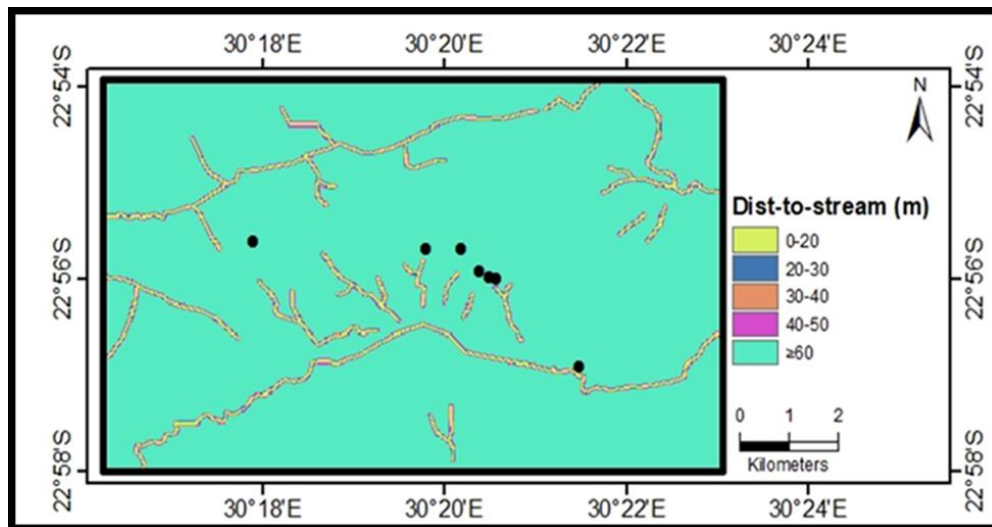
Figure 6.7 Location of landslides relative to water streams

Figure 6.6 shows the evidence of several geological features (Faults, Joints and dykes) of different sizes cutting across the study area. All active and post landslides are either located along the boundary or on the geological feature. This finding now confirms the assumptions made in Chapter 5 that geological features influence the recurrence of slope instability in the area. These geological features appear to generate weak zones and activate movement during the heavy rain season. Furthermore, the shear strength of the material and friction along the boundary of geological features are expected to gradually decrease during heavy rainfall and result in landslides.

It is always assumed that a geological feature cannot trigger a landslide alone. Water pressure or any other mechanism is to be involved. In line with this, water bodies or streams cutting across the area were identified as shown in Figure 6.7. Here also, the presence of streams seems to suggest some correlation with the locations of landslides. Although the road constructed has disturbed the path and flow of streams that may only affect slope stability through the overlain existing geological features.

This brings us to talk about landslide susceptibility mapping. As already indicated in Section 2.6.2, landslide susceptibility mapping requires several

input parameters. In this chapter, the following were included: slope angle, geological features, and rock types. Results show that indeed all selected active and post slope instability are highly susceptible to the occurrence of the slope instability (see Figures 6.8 and 6.9).
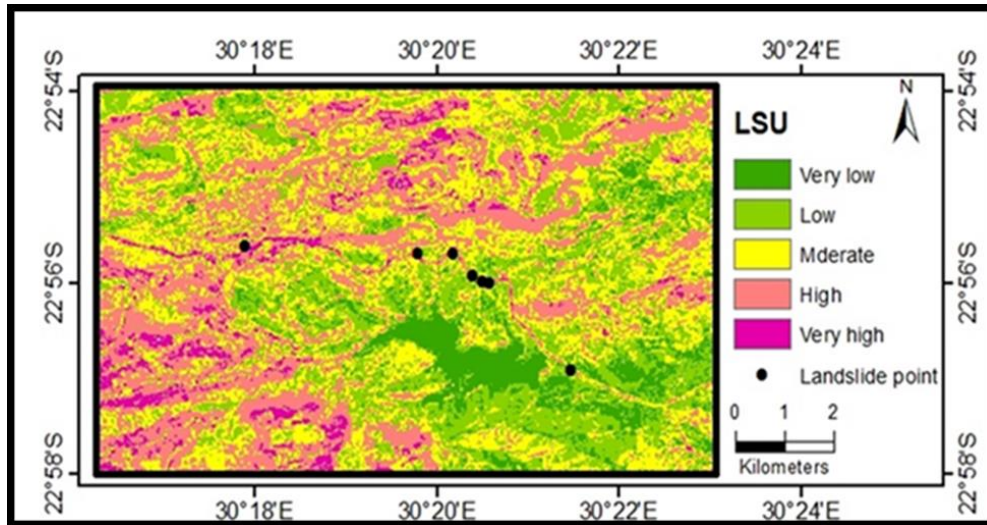
Figure 6.8 Landslide susceptibility map of the study area
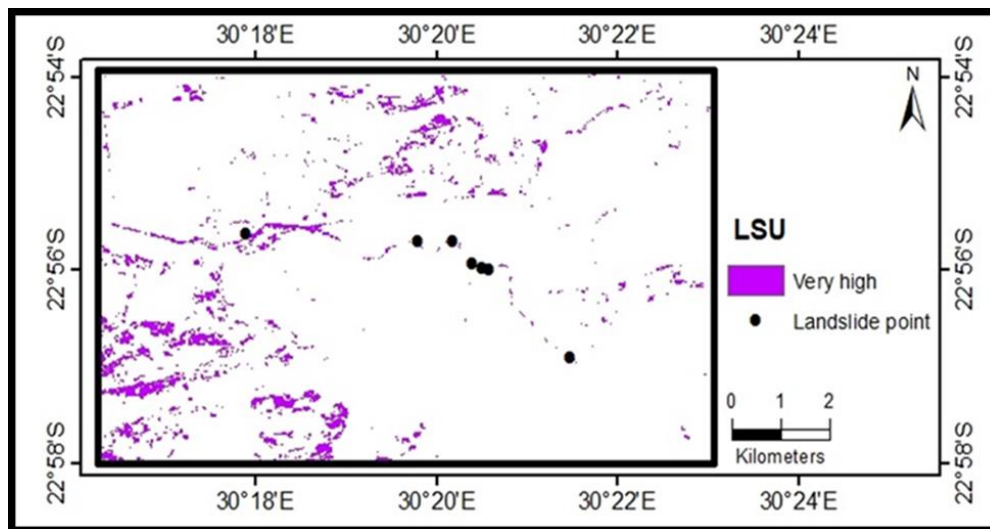
Figure 6.9 High-risk zones of landslide

The findings in Figures 6.8 and 6.9 supplements and consolidate the kinematic and limit equilibrium analysis presented in Chapter 5. This gives enough ground to consider that steepness, geological features, streams, improper road

construction are causative parameters of landslides in the region. It can be said that geotechnical and remote sensing techniques can be used jointly for a richer understanding of landslides. The outstanding factor is the effect of rainfall; this is addressed separately in Chapter 8.

6.5   Numerical simulation on the effects of geological features

The focus of this section was to simulate the strength factor and total displacement of the road material. Phase 2 simulator was used to explore the influence of geological features on rock stability. The strength factor and total displacement of the road slope were both simulated as the road excavation progresses. Simulations were implemented as a series of timesteps are outlined in the sections below.

6.5.1   Strength factor

This section looks at the relationship between strength factor and landslide susceptibility at various road construction stages. In order to proceed, four joints are created to cut across the rockmass and mimicking the creation of cracks as a result of rock blasting. In order to capture the progress of road construction, the simulation model is set at different timesteps corresponding to each stage as shown in Figures 6.10 to 6.13.
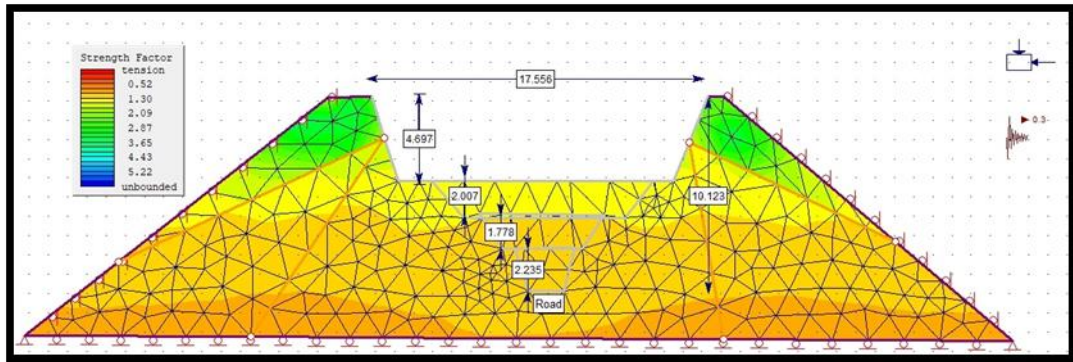
Figure 6.10 Strength Factor simulated at stage 1 of road construction
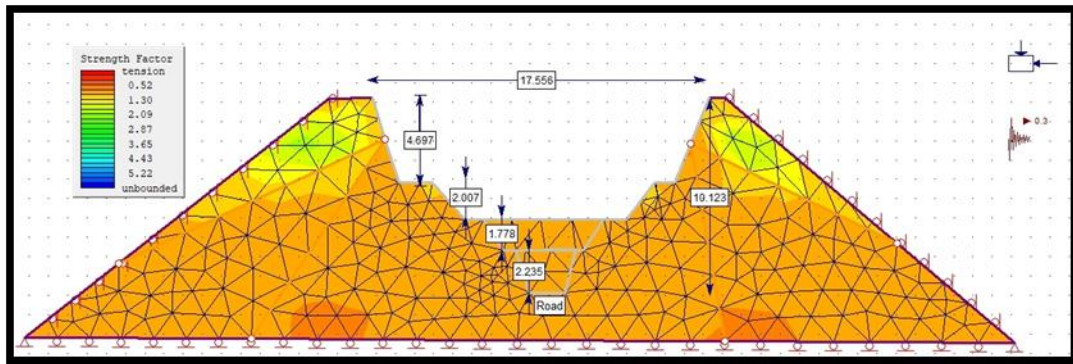
Figure 6.11 Strength Factor simulated at stage 2 of road construction
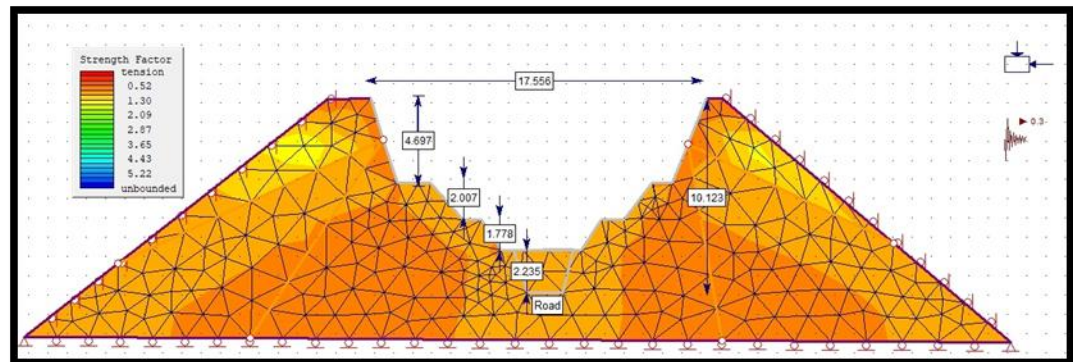
Figure 6.12 Strength Factor simulated at stage 3 of road construction
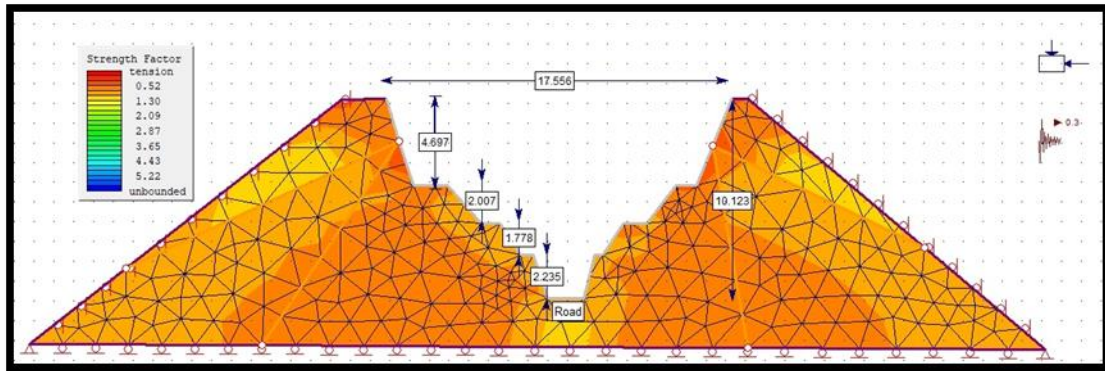
Figure 6.13 Strength Factor simulated at stage 4 of road construction

The numerical results in Figures 6.10 – 6.13 suggest that the strength of the rockmass along the road wall is expected to drop as road excavation progresses. The strength of the rockmass also appears to decrease around the four joints cutting across the rockmass. As a result of this, the rockmass may disintegrate and generate blocks and unstable ground conditions. The observations and ASTER-based analysis finally support the fact that geological features play a major role in the stability of slopes.

A close look into the relationship between the simulated strength factor and landslide susceptibility shows that landslide is most likely around the slope cuts and the four joints. The joints reproduce the effects of road construction on the steep mountainous areas characteristic of the Thulamela Municipality. So, as the road construction progresses, the computer model shows a gradual reduction in rockmass strength. At the same time, slope angle and depth increase and lead to the unstable rock face. The model finally shows that the presence of geological features along the slope has the potential to generate blocky and weak zones throughout the slope.

6.5.2   Total displacement

From the simulation outputs used to generate Figures 6.10 – 6.13, it was possible to also produce Figures 6.14 through 6.17 representing the total displacement or deformation of the rock mass. Here also, the effects of road construction and blasting (mimicked by the 4 joints) are analyzed.
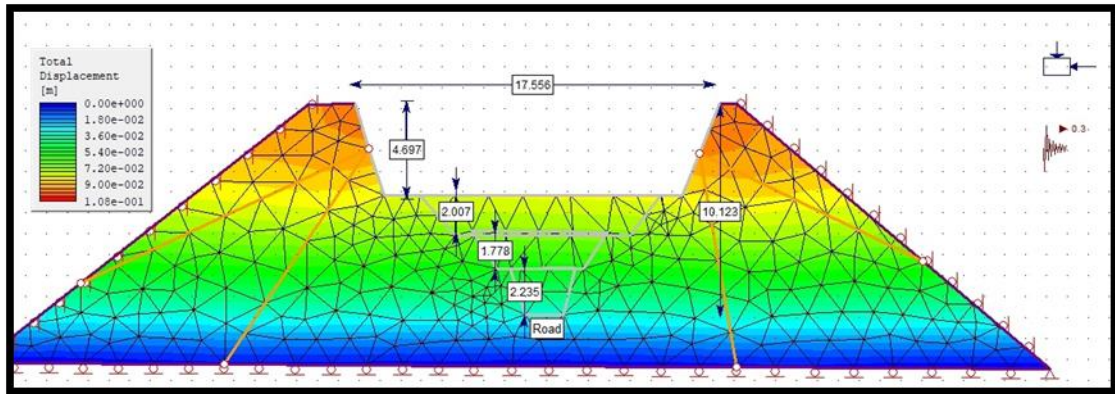
Figure 6.14 Total displacements simulated at stage 1 of road construction
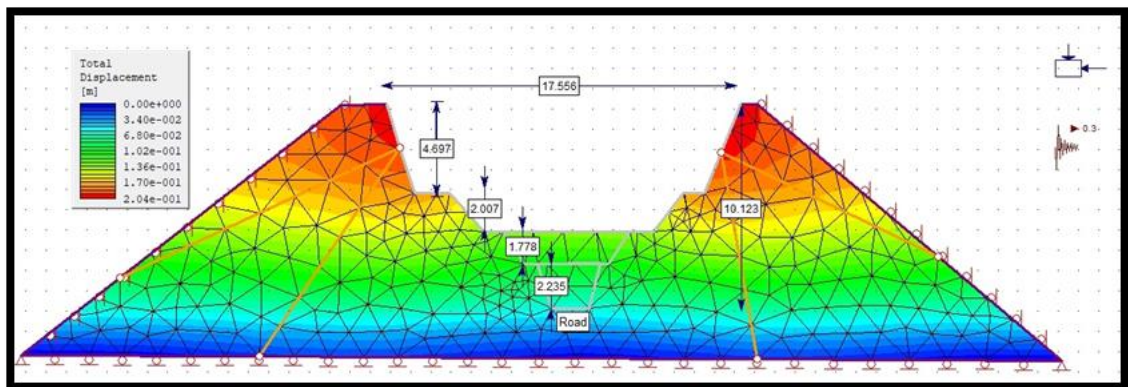
Figure 6.15 Total displacement simulated at stage 2 of road construction
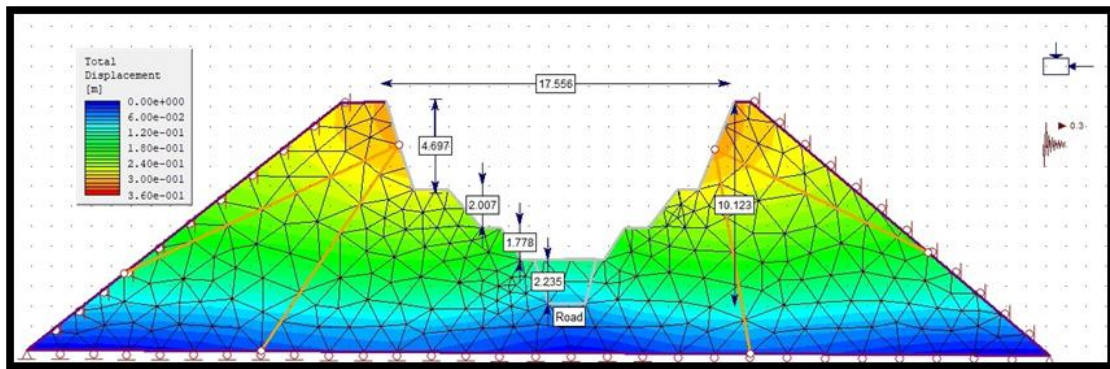
Figure 6.16 Total displacements simulated at stage 3 of road construction
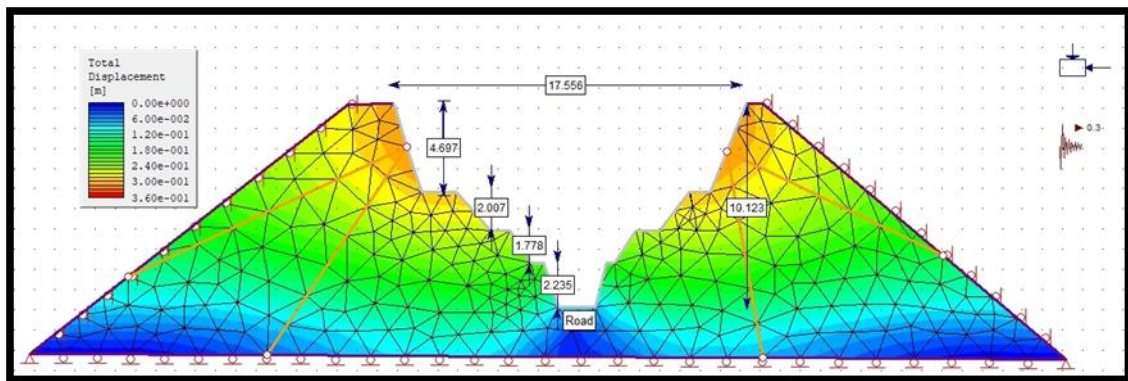
Figure 6.17 Total displacements simulated at stage 4 of road construction

The results of the simulation indicate much redistribution of the displacement field across the rockmass and through the construction stages. It can be seen that displacement rapidly increases as road construction progresses. The increased deformation relative to Figures 6.14 – 6.17 demonstrates that the development of the road has altered the morphology of the rockmass and subsequently contributed to unstable slopes in the area.

6.5.3   Influence of joints on slope stability

The effect of joints on slope stability is considered in this section. The idea is to look at the displacement generated by each joint separately as road construction progresses.

The results of the simulation show a maximum relative displacement of 0.0011 for joint #4 at the fourth or final stage of road construction. Such displacement is noted specifically along the road sidewall. The magnitude of the displacement was therefore tracked along the rockface at all four stages of road construction. It can be seen that displacement sharply increases within the few first meters and then slowly reduce the distance of the solid mass to the feature increases (see Figure 6.18).
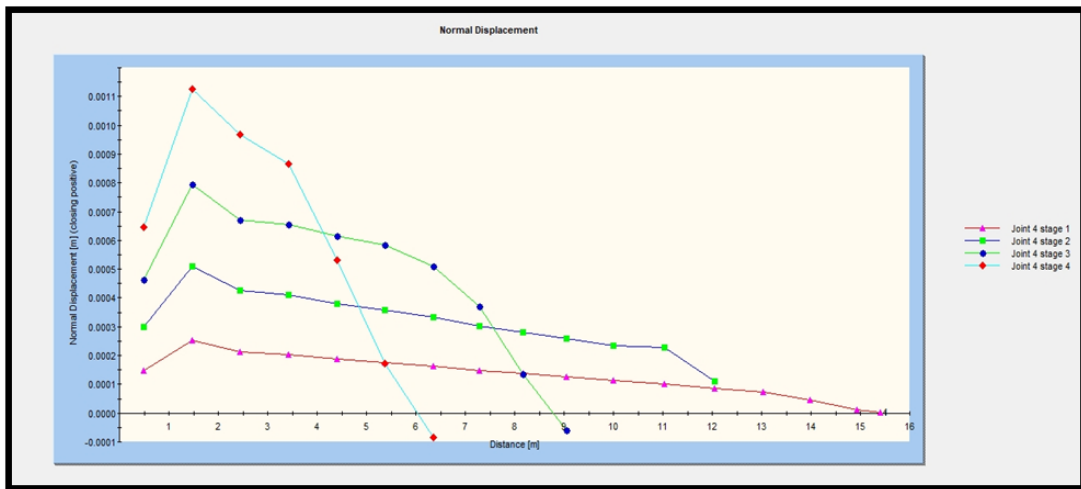
Figure 6.18 Normal displacements caused by joint 4 along the slope

From Figure 6.18, one can see that the displacement generated by joint #4 gradually increases as construction progresses. This implies that the slope angle of the road wall changes also with the depth of the road. Similar predictions were made for joints #1 through joint #3 as shown in Figures 6.19 – 6.21 also of lower magnitude. But for all 4 joints, the general observation is that both tension and compressive displacement are present. The tension displacement is shown as a positive value while the compressive displacement is negative.
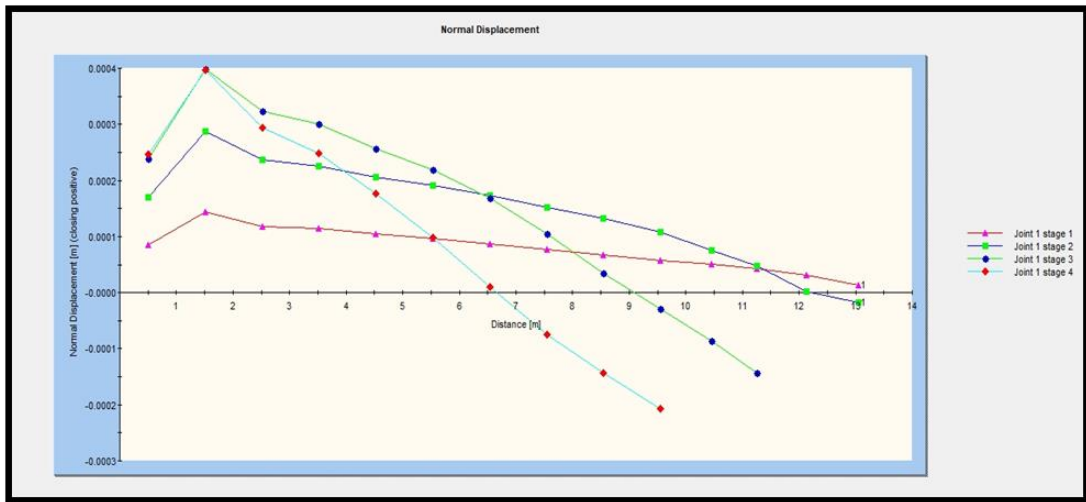
Figure 6.19 Normal displacements caused by Joint 1 along the slope
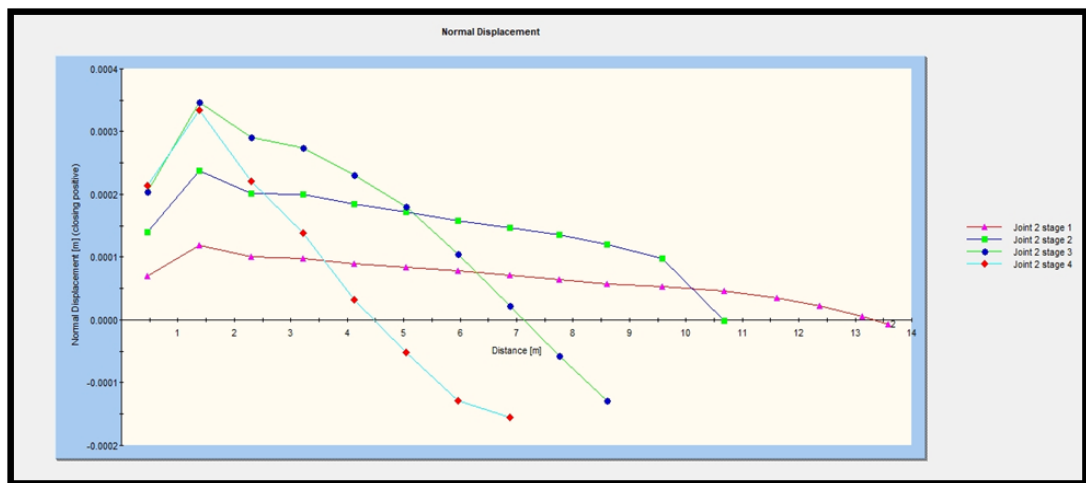
Figure 6.20 Normal displacements caused by Joint 2 along the slope

193
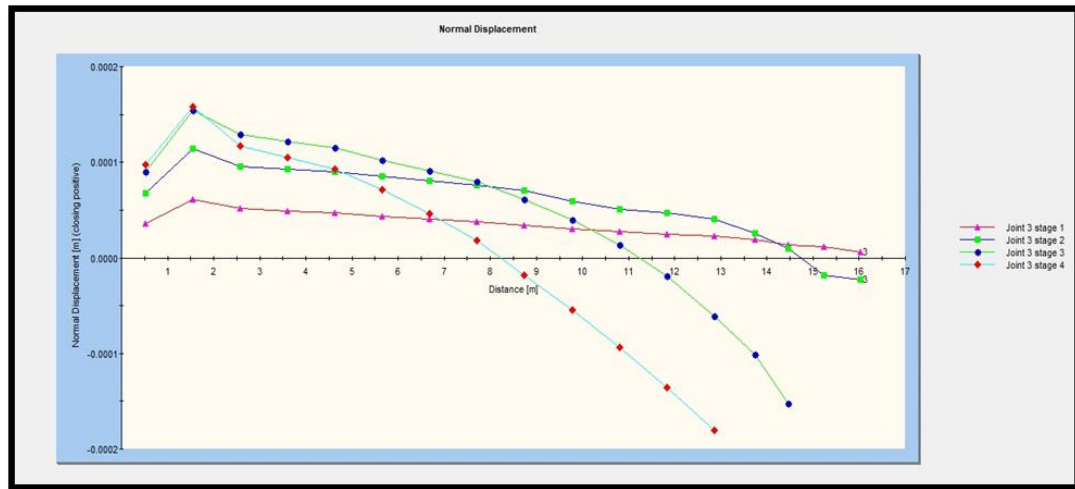
Figure 6.21 Normal displacements caused by Joint 3 along the slope

In summary, Figures 6.18 – 6.21 show how geological features within the rock mass can affect slope stability. All four line charts display similar characteristics irrespective of joint orientation. Finally, displacement was much noted within the solid material closer to the joint than otherwise.

6.6   Development of the slope stability chart for unsaturated soil

Based on the remote sensing and geotechnical analysis, a slope stability chart describing the occurrence, conditions and hazard rating of the studied slopes along the R518 and R523 roads was developed. The chart integrates the following causative factors identified in previous analyses: the slope angle, the geographical elevation, and the distance between the location and known geological features as well as water streams. The slope stability chart is illustrated in Figure 6.22 and should be noted to be suitable for clay soil.
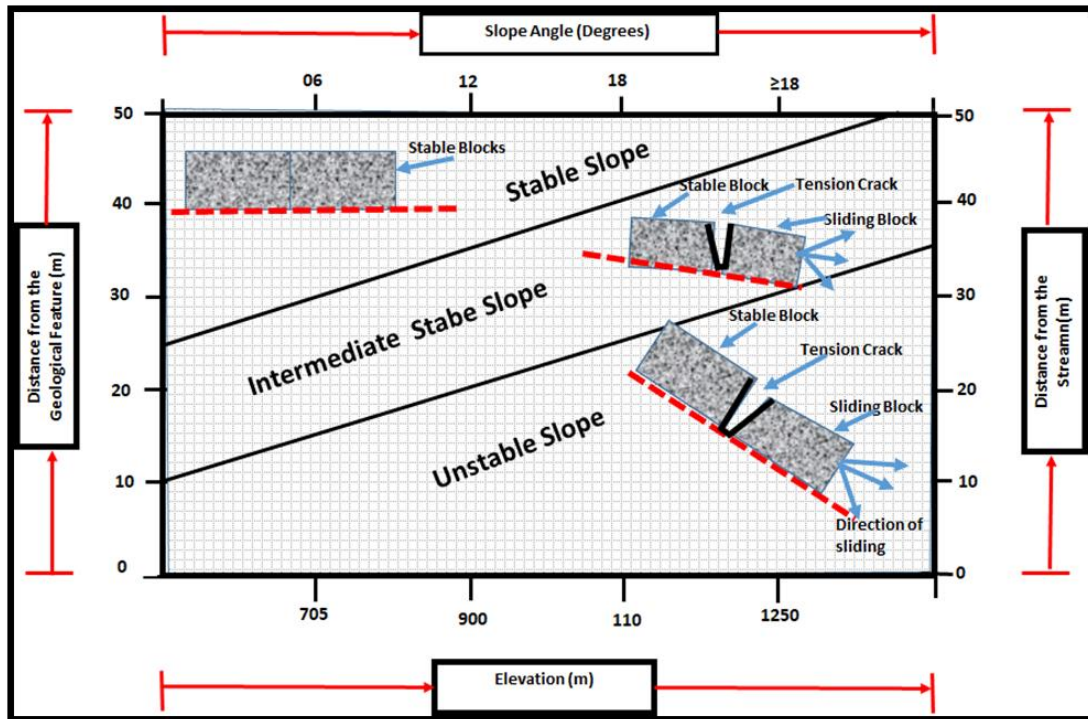
Figure 6.22 Slope stability chart for sensitive unsaturated clay soil

It can be seen from Figure 6.22 that slopes close to or located between the boundaries of two geological features or water streams can fail. The effects of slope angle and geographical elevation are also allowed in the slope stability chart.

It is recalled from Sections 5.5.4 and 6.5 that the influence of geological features on total displacement and strength factor is significant. Indeed, geological features reduce the strength of the solid mass. Using that as the point of departure, one can see that the chart in Figure 6.22 is easy to use and interpret. The chart can also categorize slopes into several hazard prediction subsections. Moreover, the chart indicates that most slope failure is due to sliding that in turn is dependent on the presence of tension cracks. Finally, the displacement taking place along the tension cracks is influenced by the water stream, rainfall and the movement of geological features. Much displacement is expected closer to or along the features and reduces as distance increases

towards the slope. This limits the capability of the chart since at several meters from a joint for example the chart will probably predict a stable slope.

In closing, the developed chart is not meant to solve all problems related to slope instability. It is rather purposed to predict the recurrence of landslides based on the input parameters stated on the boundaries of the chart.

6.7   Application of slope stability charts to past work

In attempting to validate the chart in Figure 6.22, recent studies on slope stability using remote sensing techniques were considered. Their results were studied and the reported parameters were used to plot their corresponding slope stability chart. The focus was on areas of high landslide susceptibility that include the following: Roy et al. (2019), Arebemeri et al. (2019 & 2020) and Dou et al. (2019). Their results were plotted and found to fall within the unstable slope region as evidenced in Figure 6.23. The consistent findings consolidate the position of the slope stability chart as an easy alternative tool for the assessment of slope stability.
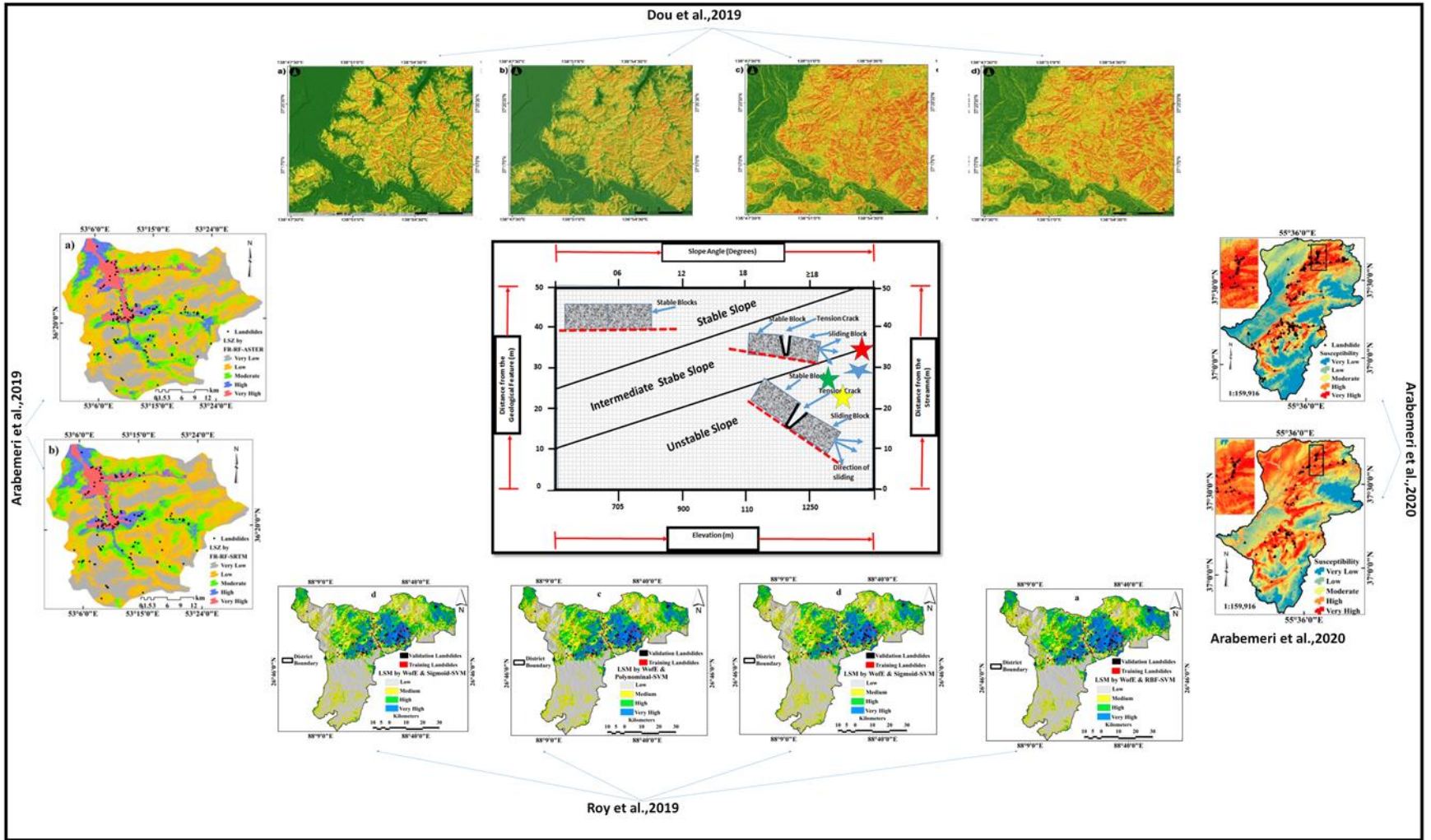
Figure 6.23 Validating the chart using previous published work landslide susceptibility

6.8   Conclusion of the chapter

The present chapter was aimed at applying both remote sensing and geotechnical techniques to develop a hazard rating system for use along the R518 and R523 roads in Limpopo.

Results showed that the selected study area consists of very steep slopes cut across by several geological features and multiple periodical streams. Numerical simulations of the occurrence of slope instability enabled the identification of two joint sets responsible for slope instability in the area. The two joint sets also generate unanchored boundaries along the slope and tension cracks that can initiate failure when exposed to water or rainfall.

Advanced numerical simulation was also performed and looked into the influence of road construction on the strength and total displacement of the solid mass. Simulation outputs revealed that the strength factor of the slope gradually reduces as road construction progresses. Furthermore, results indicated that the presence of joints along the road slope plays a major role in reducing the strength of the material thereby weakening the solid mass. The total displacement of the material, on the other hand, was shown to increase as road construction progresses.

Lastly, a simple slope stability chart for unsaturated soil was developed based on the above results. The chart used several factors that were characterized by remote sensing and geotechnical techniques. The chart was tested on existing data and demonstrated to be appropriate for mountainous areas. Perhaps the most important point is that from the developed chart, all active slope instabilities of the Thulamela Municipality were found to be unstable in line with actual field observation.

Chapter 7   Rockfall stability analysis for hazard assessment and prediction of recurrence

The purpose of the study covered in this chapter was to perform rockfall stability analysis and develop a new rockfall hazard matrix chart using the R518 road in Limpopo as the case study.

The study entailed structural mapping, wedge simulation using stereonet plots. The RocFall software was then used to identify the parameters that influence the occurrence of rockfall. The software was also used to monitor the variations in the kinetic energy of rolling, bouncing, or falling rocks. The effects of the initial height and velocity of falling rocks on the final destination of fragments were also explored.

Results showed that the selected area along the R518 road consists of joints and bedding planes. These features weaken the rock mass and create wedges that can potentially fall. Simulations with RocFall, on the other hand, indicated that slope height, vegetation density, the velocity of the falling rock largely contribute to the extent that the broken rock could reach. From the empirical and numerical findings, a new rockfall hazard rating chart was proposed. The chart was found to be suitable for the rating of the level of rockfall hazard along highways and roads.[6]

---

[6] There are two papers which has used some of the data presented in this chapter, the first paper is in review in the journal of Environmental Earth Sciences Journal with the following tittle: New hazard assessment for rock falls in near vertical blocky rock environments. While the second paper is under review at the Journal Tranport Getchnics and only visual observations were presented in the second paper while the other data were developed using extract data which is not presented in this thesis, such data include the use of SENTINEL, FLACSlope, SLIDES and detailed Kinematic analysis. The tittle of the second paper is as follows: Advanced Reliability Analysis of Rock-Slope Stability in a Geologic-Structural Control Terrain by Several Techniques.

7.1   Introduction

The assessment of rockfall hazards is continuously performed because of the unpredictable nature of rockfall events. Analytical tools are a significant part of the assessment routine of rockfalls as they provide relevant information for numerical simulations. They are however anchored on the determination of the properties of rock mass such as rock strength, water pressure, and joint orientation among others.

In this chapter, rockfall analysis is performed using both analytical and numerical approaches. The two approaches are applied to the locations along the R518 and R523 roads in Limpopo that are exemplified in Figure 7.1.
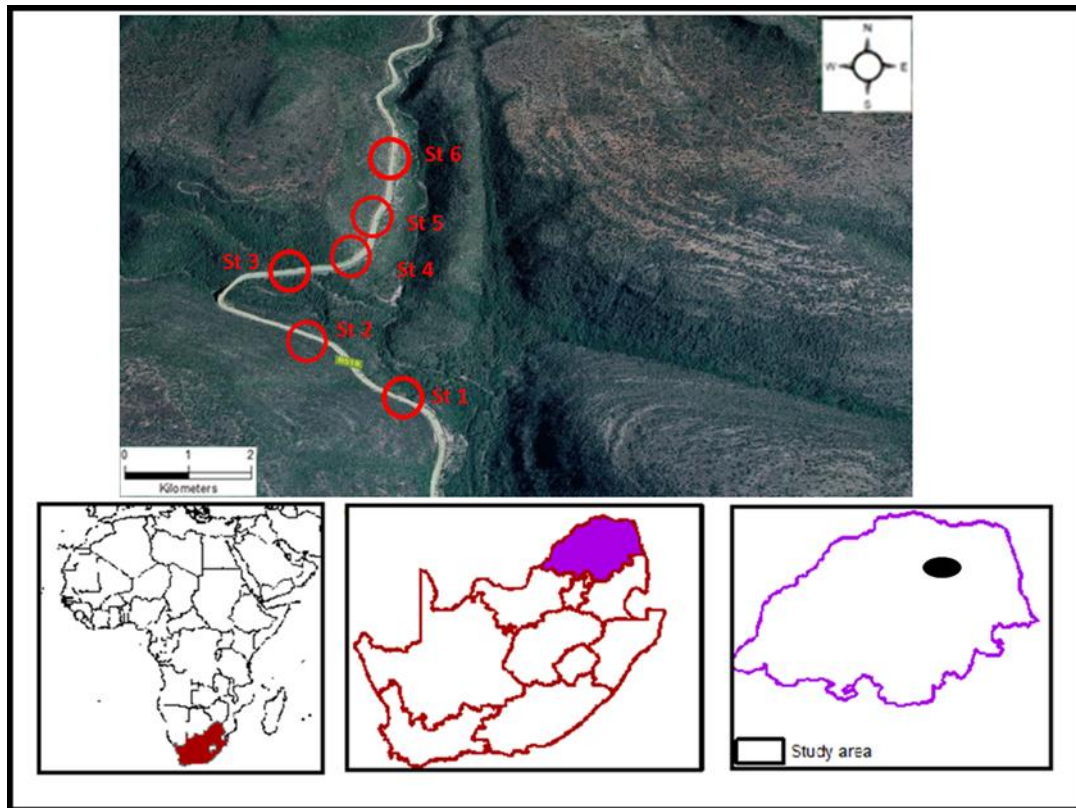
Figure 7.1 Locality of the selected area along R518 road in Limpopo Province, Republic of South Africa

The combination of analytical and numerical approaches is aimed at developing another hazard rating chart, this time, for rockfalls. Here also, the proposed chart is tested to the study area and to other roads in the mountainous environment. Finally, prediction results obtained from the proposed chart are benchmarked against established charts.

The study commences with field observations along areas believed to be prone to rockfalls or reported to have experienced rockfalls. The observations strictly focused on identifying geological features that might cause the occurrence of the rockfall. The orientations of these features were measured together with parameters such as slope height while loose rocks were identified. The density of the vegetation along the slopes was also estimated as it controls the rolling and falling of rocks down the hill (or the slope). The geological mapping information was inputted into the DIPS simulator; then, stereonets of each identified area created while possible rock detachments were estimated. Finally, the RocFall simulator was used to generate the falling/rolling trajectories of the individual or multiple rocks upon detachment.

7.2   Field observations

Field observations are primarily used to provide a broad view of what is happening on the ground. The information collected on the site guides the methods that can be implemented to assess the problem at hand.

Six sites prone to rockfall were identified as shown in Figure 7.1 above. From an observational point of view, site 1 was dominated with blocky rock mass dominated by bedding planes as shown in Figure 7.2. The planes are dipping and striking at the same pattern. Furthermore, the common rock type identified is partial metamorphic sandstone with minor beds of the conglomerate between sandstone layers. Owing to that, the overall rock mass is dominated by small and large joints that can create

wedges along the sedimentary layers. This complex structural geology influences the generation of a blocky and fractured rock mass. It was also observed that most boulders were loose and could fall anytime. This makes rockfall monitoring along the road a challenging exercise. This state of affairs is worsened since broken rocks are generally cleared from the road before evidence collection is conducted.

Figure 7.2 Poor quality rock mass in site 1 with loose rock at the upper part of the road slope and very steep slope

It should be indicated that all selected sites are not supported by roof bolts, wire mesh, or any other support. As such, the rock mass is not glued together to the point that a small movement can initiate rockfall. Weathering and erosion are noted to be taking place at a rapid pace across the municipality. The stability of the rock mass is therefore expected to deteriorate with time.

In sites 2 to 6, the rock mass is similar to that found in the first site with slight differences noted for the density of fracturing, slope height, and bedding planes.

Similar to the observations from site 1, sandy red soil dominates the top layers of the strata. Low density and far spread vegetation coverage are associated with the sites (see Figures 7.3 – 7.7).

Figure 7.3 General view of site 2 with associated geological features

Figure 7.4 General view of site 3 with associated geological features
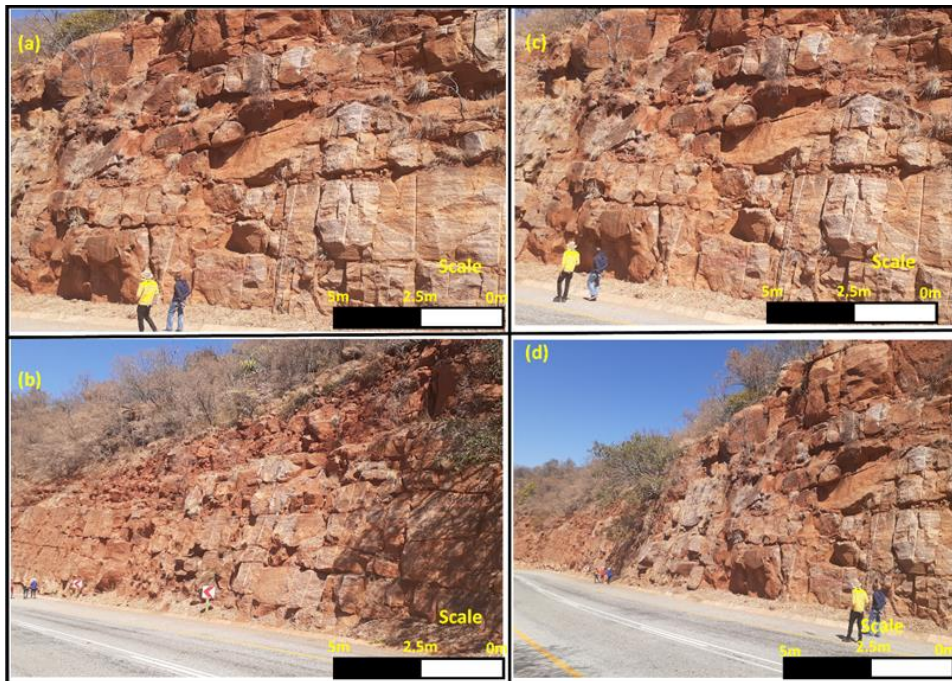
Figure 7.5 General view of site 4 with associated geological features
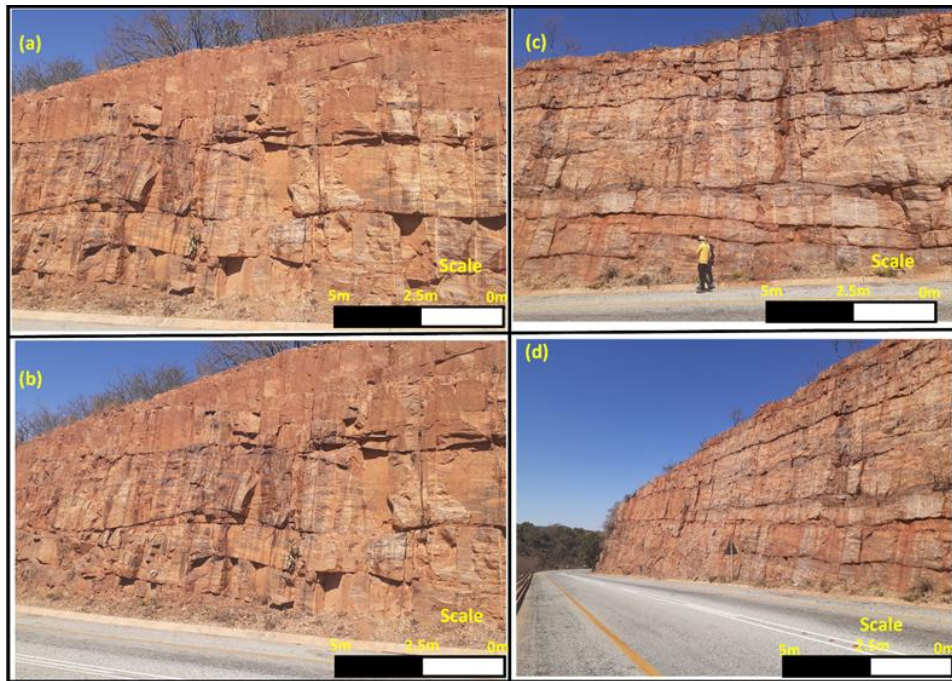
Figure 7.6 General view of site 5 with associated geological features

Figure 7.7 General view of site 6 with associated geological features

Slope height was found to range between 12 m and 19 m across the six sites. Some small rock fragments have been observed to spread at the slope toes. It is believed that rockfall has been continuously occurring but due to road maintenance the evidence is regularly removed from the road.

Lastly, vegetation and trees growing in the perimeter of the slopes were observed in some sections to rapidly disintegrate the rock mass (see for example Figure 7.4). This weakens the rock mass and leads to rock sliding down the slope.

7.3   Kinematic analysis of the rock mass along the R518 road

Rock mass rating or rock mass classification is a technique recommended by ISRM (1978 & 2007) for assessing the geomechanical conditions of a slope.

The six sites were assessed following the rock mass rating. The assessment was done only in-accessible areas while mapping was conducted along exposed slopes along the road. Several parameters were considered; they include joint persistence, spacing, opening, in-filling, roughness, uniaxial compressive strength (UCS), dip-immersion and hydraulic conditions. All parameters were measured and analyzed along the scanlines for each discontinuity. The orientation of discontinuities was also analyzed and plotted for the sets of joints and bedding. The Fisher distribution method was used for this purpose (Mineo et al. 2018).

Based on the rock mass rating obtained, the overall rock mass was classified as a fair rock mass (see Table B1). To be more precise, the rock mass in the region was found to range from class 54 III fair rock to class 56 III fair rock. This simply means from a kinematic point of view that several weak zones or wedges that can fail exist within the rock mass (see Figure 7.8 – 7.13). And from the steorenets, the

unfavorable kinematic orientation of discontinuities leads to the state that the most likely failure would be planar sliding.
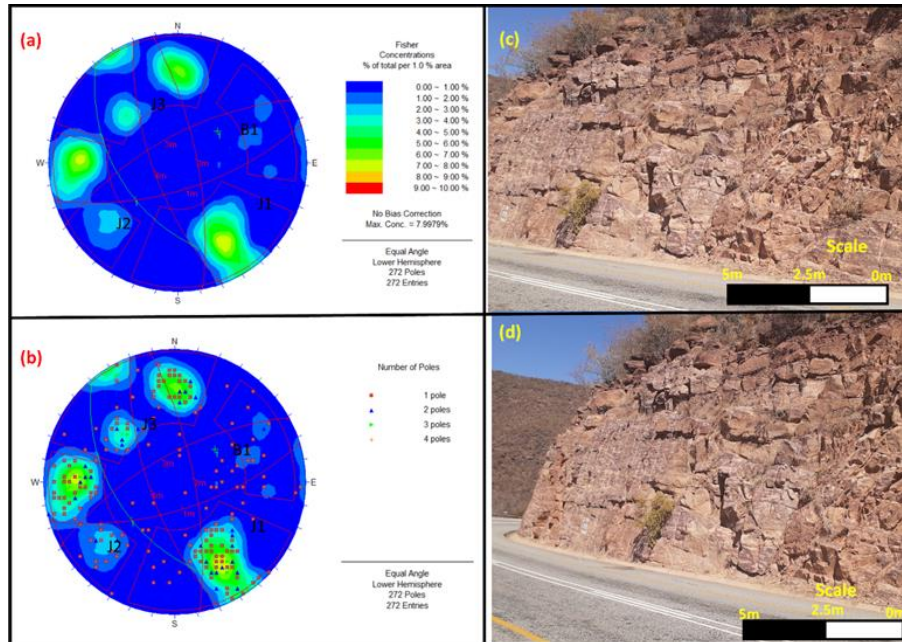
Figure 7.8 Stereonets showing the contour plots of the common discontinuities and the unstable kinematic patterns in site 1
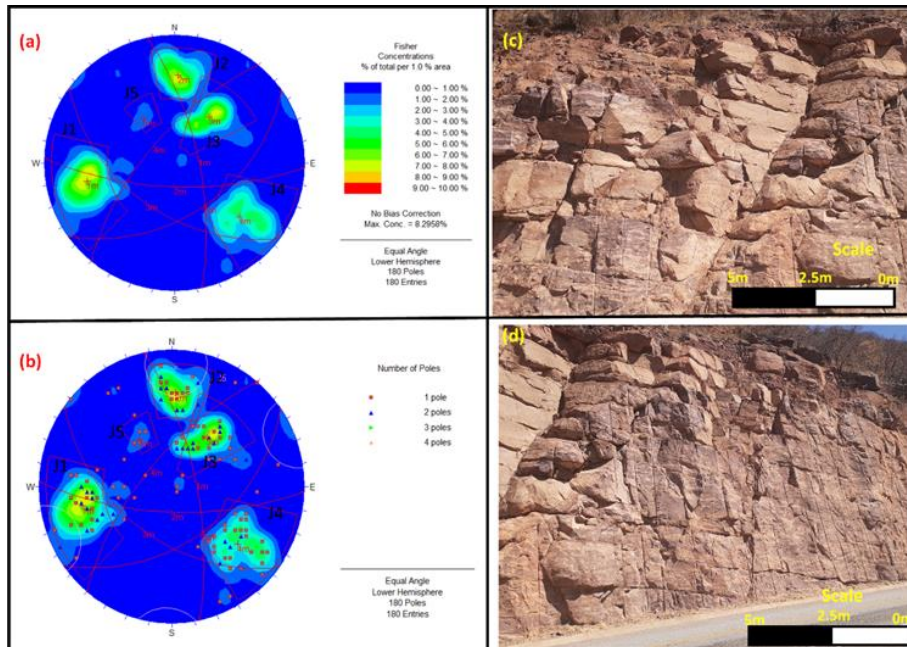
Figure 7.9 Stereonets showing the contour plots of the common discontinuities and the unstable kinematic patterns in Site 2
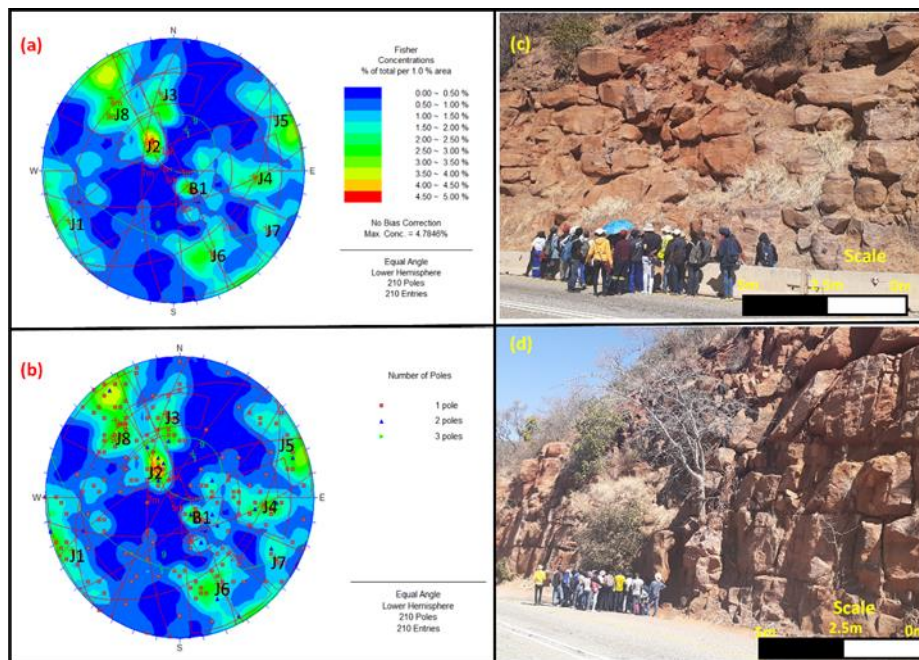
Figure 7.10 Stereonets showing the contour plots of the common discontinuities and the unstable kinematic patterns in Site 2
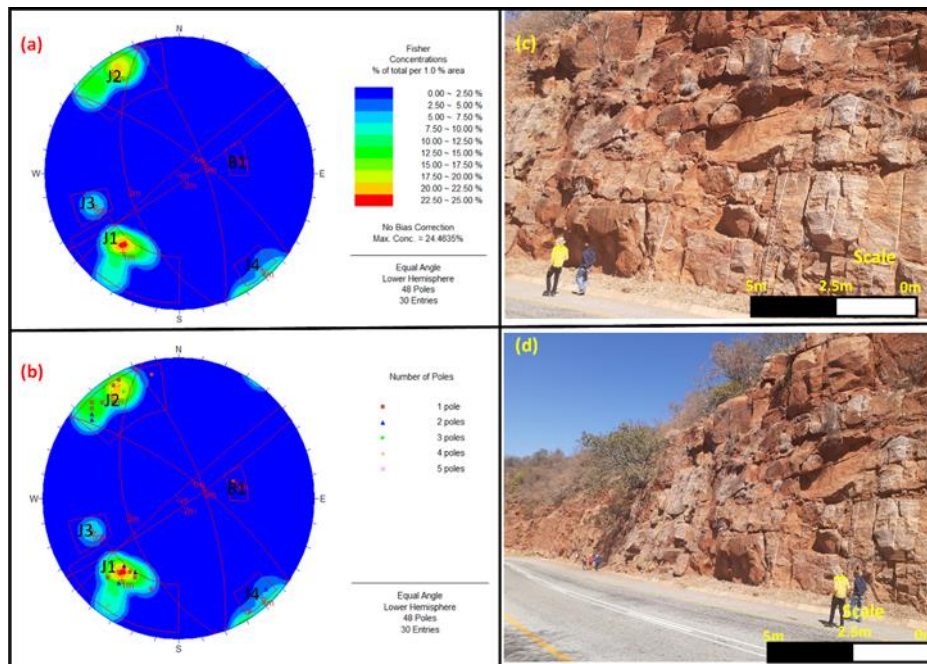
Figure 7.11 Stereonets showing the contour plots of the common discontinuities and the unstable kinematic patterns in Site 4
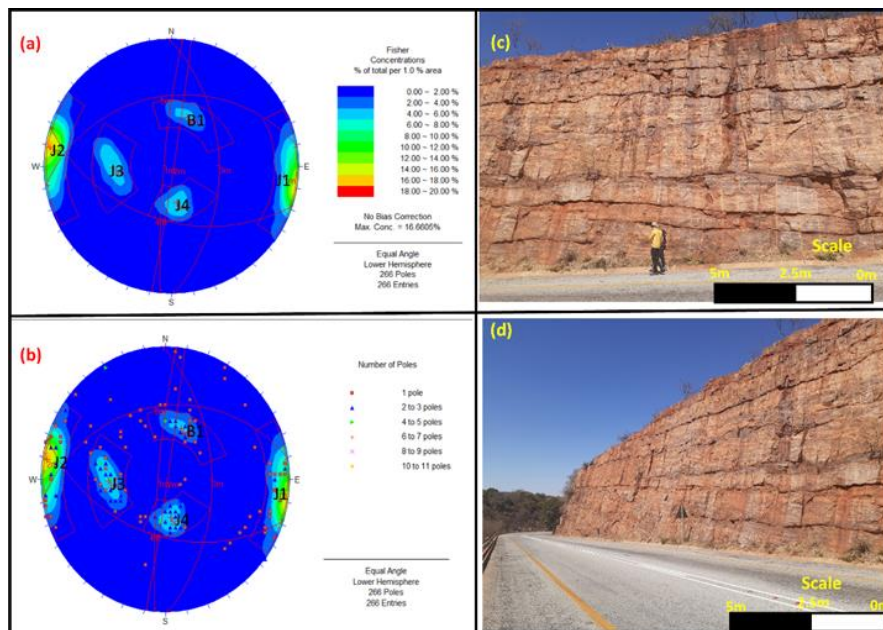
Figure 7.12 Stereonets showing the contour plots of the common discontinuities and the unstable kinematic patterns in Site 5
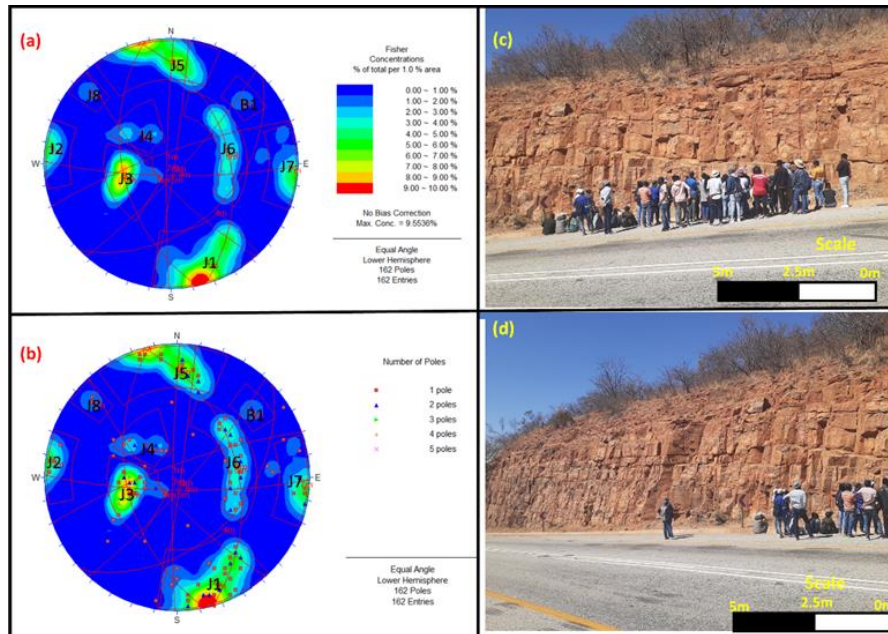
Figure 7.13 Stereonets showing the contour plots of the common discontinuities and the unstable kinematic patterns in Site 6

These results support the visual evidence collected on-site where wedges have been noted to develop due to multiple discontinuities with irregular orientations. It can also be argued that toppling is another possible mode of failure that can occur in the study area. This is because some discontinuities dip into the facing slope. Small and large wedges were also plotted from the stereonets presented in all sites (see for example Figure 7.8). In addition to this, similar bedding planes were identified in all the sites (see Figures 7.8 – 7.13 for comparison).

In conclusion, the area of study is weak to moderate rock mass with dip-dominated bedding and multiple major and small joints. This makes the rock mass unstable and creates several wedges. It is therefore likely that rock failure in the six sites occurs through planar sliding and toppling.

7.4 Analysis of the final deposit of the rockfall

It is always important for the final deposit of the rockfall to be estimated. This ensures that remedial action is taken based on the extent of the hazard.

There exists at the moment no analytical method that can accurately predict the final deposit of the rockfall. However, numerical tools such as the RocFall simulator provide an approximate solution to the rockfall deposit problem.

In this thesis, the RocFall simulator was used to estimate the final rockfall deposit based on the trajectories of blocks generated. Input parameters such as rock mass properties, slope geometry, block size among others were taken into consideration.

The scenarios that were considered included the estimation of the final deposit at constant slope height; however, falling rocks were subjected to different slope heights and different initial velocities. A detailed analysis of the variation in kinetic energy was done throughout the journey of falling rocks.

7.4.1 Impact of slope height on the final deposit of the rockfall

The RocFall simulator was used to compute the various trajectories of rocks falling down the slope as a function of slope height. The locus of these trajectories was to give insight into the final deposit of the broken rock.

Based on the simulation results, slope height contributes substantially to the rolling distance of falling blocks and therefore to the extent of the deposit. See Figure 7.14 for instance that when the height is about 5.5 m from the road, the falling rock spreads out at the vicinity of the road. Some rock fragments are expected to bounce less than 2.5 m while others settle immediately after hitting the road (see Figure 7.14a). It is crucial to indicate that the road width also plays a major role in the rolling

motion of fragments. Simply put, with an 8 to 10 m wide road as is the case here, most of the falling fragments are expected to end their rolling motion in the middle of the road. By increasing the slope height to 9.8 m while keeping all other input parameters unchanged, the picture changes as shown in Figure 7.14b. For one, fragments are predicted to roll over the entire road length into the river; and two, a large deposit of fragments can be potentially formed farther away from the toe.
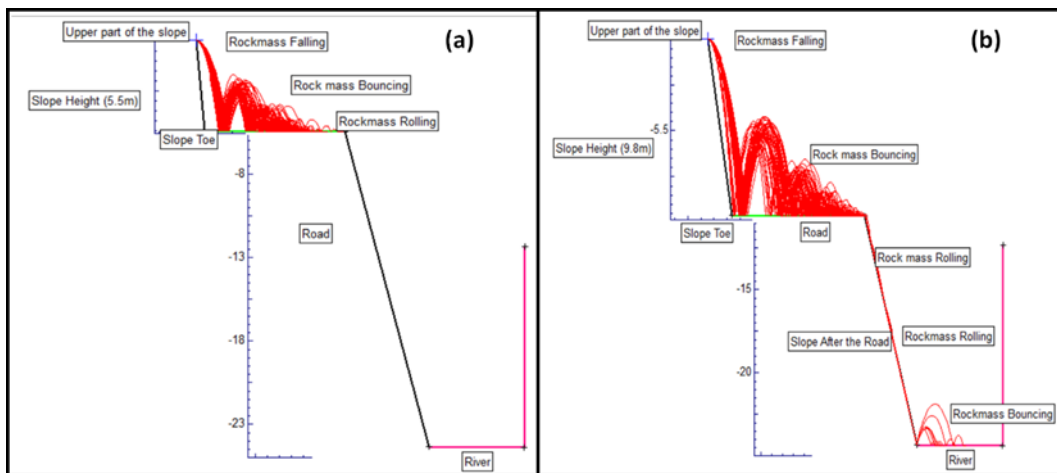
Figure 7.14 Rockfall trajectory of the designed slope (a) with a height of 5.5 m and (b) with a height of 9.8 m

Additional simulations were performed in order to get a better understanding of the effect of slope height. Various heights were considered in line with the observation reported in Section 7.2 as follows: 12.5 m, 14.5 m, and 19 m.

As can be noted in Figure 7.15, most fragments experienced bouncing at wide spacing and subsequently roll over into the river floor. It also appears that the final deposit of rolling fragments is controlled by the kinetic and potential energy rather than the kinetic energy alone. Indeed, slope height controls the velocity of the falling rock; at the toe, this energy is converted into a rolling motion that then defines the extent of the final deposit.

When comparing slope heights of 12.5 m and 14.5 m, simulation results show that the bouncing and rolling of fragments increase rapidly with height. Furthermore, a large quantity (50kg, 0.5x0.5m x0.2m) of rolling rock is estimated to be deposited away from the road. This large fraction of material also generates sharp curves after hitting the river floor (see Figure 7.15b). It may therefore be argued that the height of a slope has an impact on the final destination as well as the spread of rolling fragments.
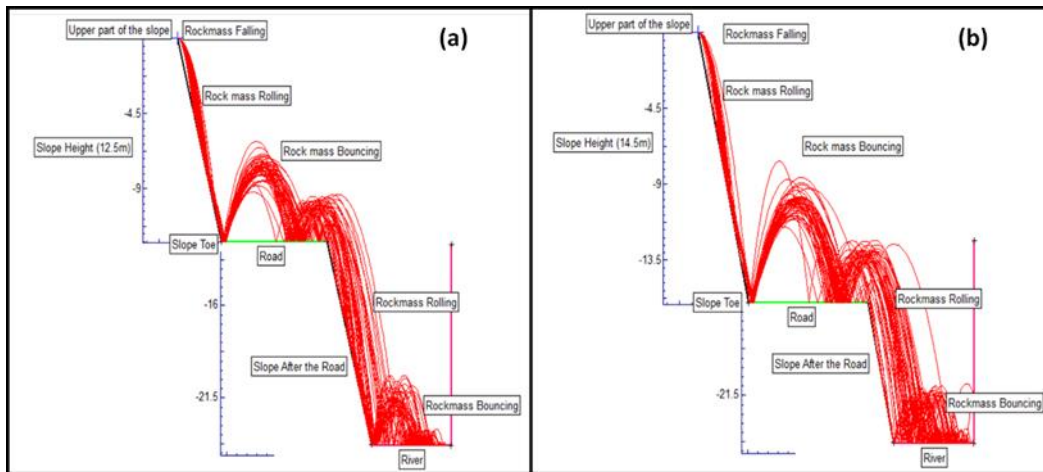
Figure 7.15 Rockfall trajectory of the designed slope (a) with a height of 12.5 m and (b) with a height of 14.5 m

To confirm these findings, let us look at the simulation for the slope height of 19.0 m in Figure 7.16. Similarly to the 14.5 m high case, it is noted that the falling fragments are predicted to all deposit into the river after rolling, bouncing through the slope and the road.

The other observation is that the simulated bouncing height at the final deposit was great since blocks hit the road aggressively. Unfortunately, in this case, RocFall does not model the fragmentation of rock due to its impact. That is why the use of the simulator is generally limited to qualitative analysis.

Finally, in terms of the kinetic energy, it can be seen that the slope height is a determining factor for the rolling velocity and the final deposit of broken rock. So, in a sense, high slopes are more dangerous than small ones. This is indeed supported by Figure 7.16 where the fraction of fragments bouncing off higher has risen.
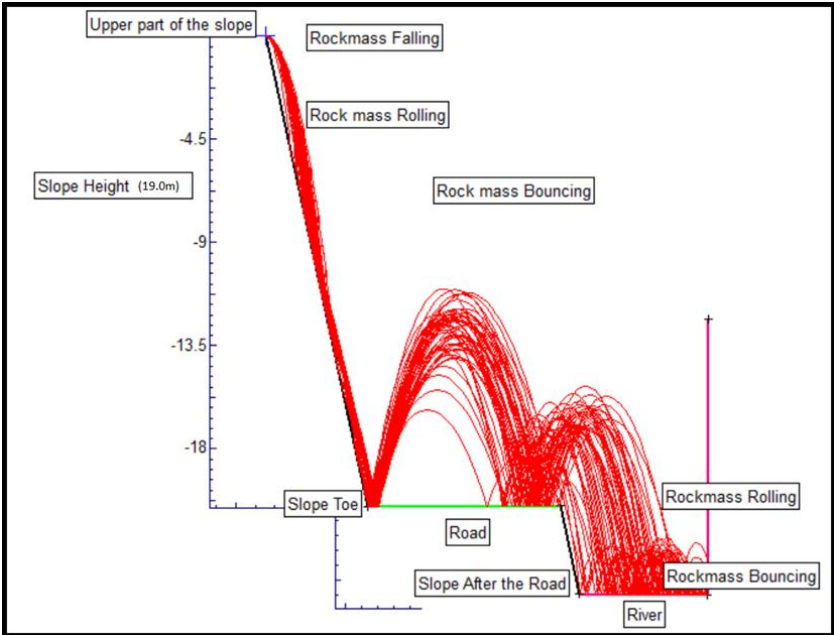
Figure 7.16 Rockfall trajectory of the designed slope with a height of 19.0 m

7.4.2   Distribution of the total kinetic energy during a rockfall

The distribution of kinetic energy during rockfall can be extracted from the RocFall simulation model. The outcome of that study is presented in this section with the aim of getting insight into the rockfall process from an energetic point of view. However, only the kinetic energy along the slope, the road, and the slope leading into the river were considered in the analysis.

Figure 7.17 is an example of the outcome of the analysis; it shows that kinetic energy is rapidly lost when the rock bounces off or hits back the road. The other observation

is that kinetic energy associated with the different legs of the full trajectory all range between 0 kJ and 100 kJ.
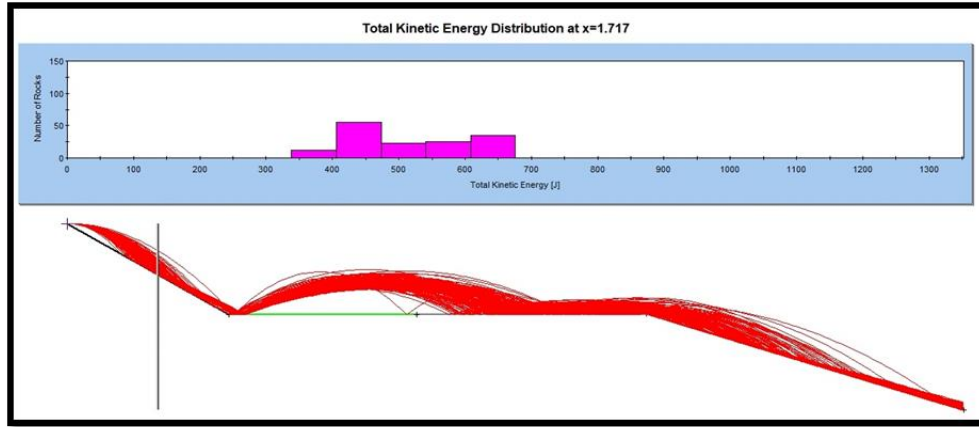
Figure 7.17 Total kinetic energy distributed in the upper section on the slope

The frequency distribution of kinetic energy is provided along in Figure 7.17 and in other cases as shown in Figures 7.18 – 7.23. Arguably, the kinetic energy is observed in all cases to rapidly increase when a fragment hits the road. This is because the velocity of the projectile is at its highest before it slows down and recovers with a bounce. Subsequent to this, the predicted kinetic energy along the trajectory of a rock fragment upon hitting the road the second time is not high. This is captured in the energy distribution coming with each pair of plots in Figure 7.18 – 7.23.
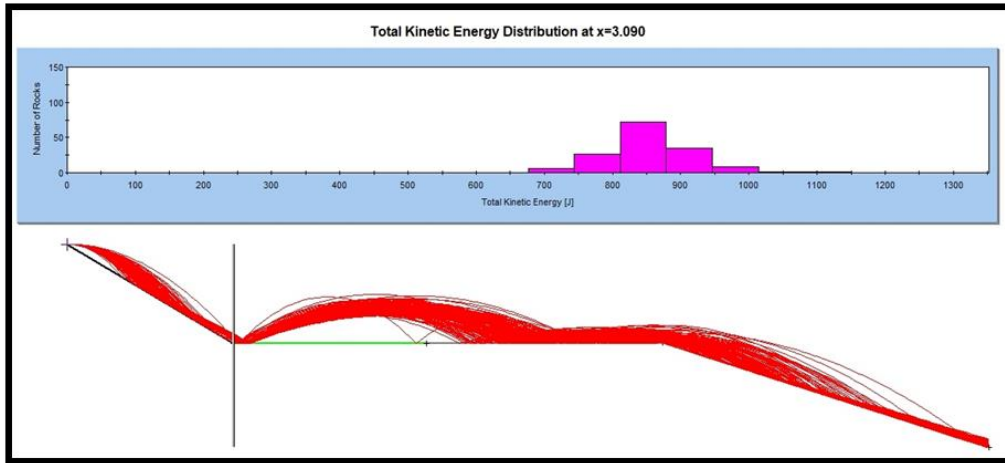
Figure 7.18 Total kinetic energy distribution at the slope toe

The loss of kinetic energy that can be inferred from first principles as far as physical sciences are concerned is reproduced in the simulation outputs. Indeed, a comparative look at the energy distributions in Figures 7.19 to 7.23 for example shows that energy is spread at the second hit. While the distribution is skewed to the left in Figure 7.19 indicating a high energy level, that in Figure 7.20 is right-skewed. Impact events in Figure 7.23 are captured by the right tail of the distribution.
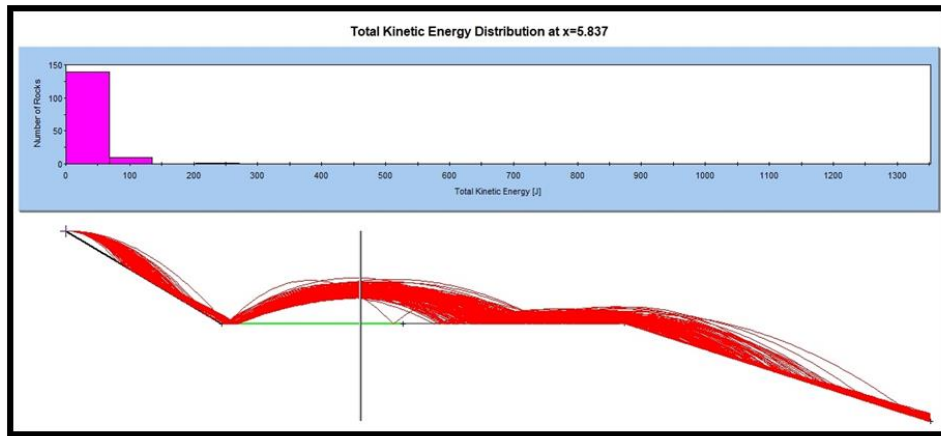
Figure 7.19 Total kinetic energy distribution at the bouncing shadow
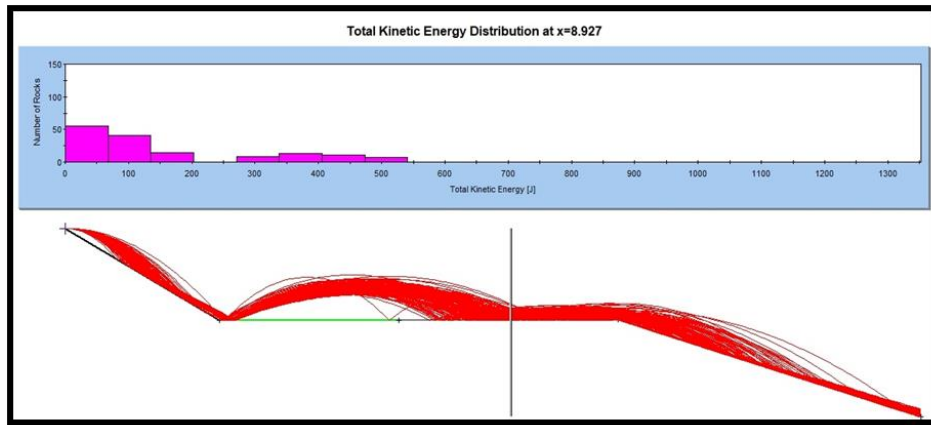
Figure 7.20 Total kinetic energy distribution when hitting the ground for the second time
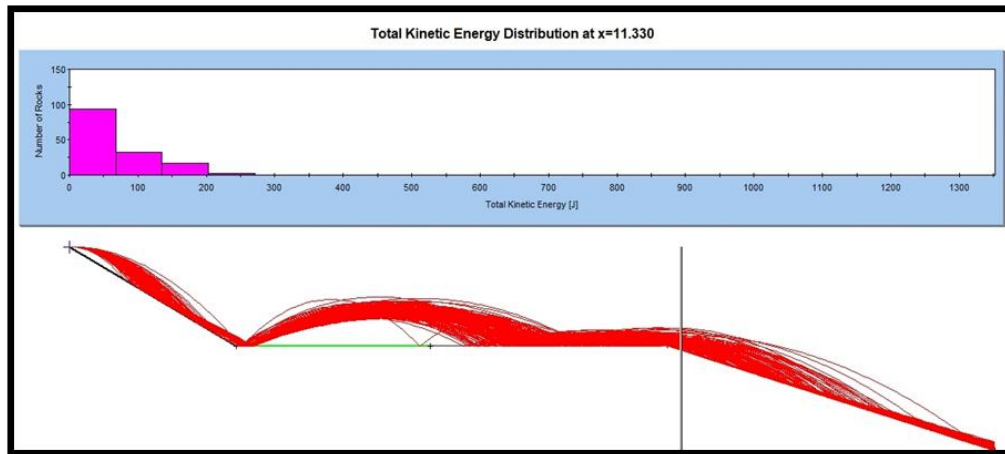
Figure 7.21 Total kinetic energy distribution as fragments start to roll from the rebounce
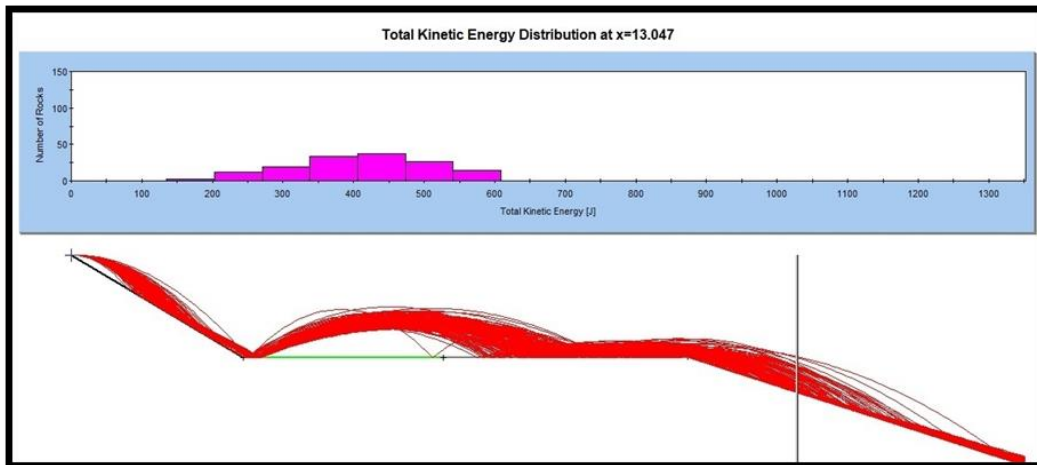
Figure 7.22 Total kinetic energy distribution at the upper section of the slope after the road
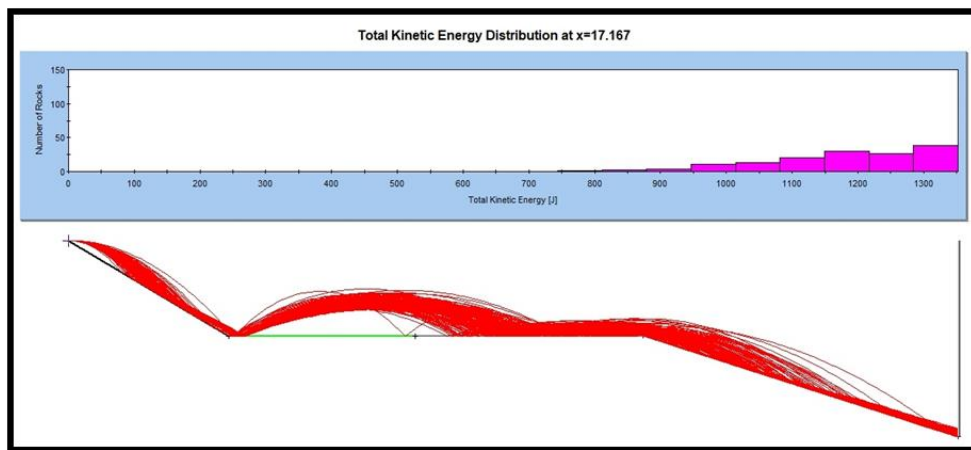
Figure 7.23 Total kinetic energy distribution on the river floor

A summarised understating of the simulation outputs in Figure 7.19 – 7.23 is that the kinetic energy distribution is dependent on the height of the fall of the rock. In the next section, an attempt is made to explore the effects of the initial velocity of the falling rock. In doing so, a richer picture of the contribution of the potential and kinetic energies on the final rock deposition can be drawn.

7.4.3   Effects of initial rockfall velocity on the final deposit

In this section, simulation results are reported on the contribution of the starting velocity as part of the rockfall. Initial velocities of various fragments making up the slide were allocated between 1.5 and 3 m/s (note that this is not the initial velocity of the rock at stationary but the velocity when rockmass starts to move). The idea is to mimic the ejection of blocks as a result of water pressure, superficial torrent, or internal stress for example.

Figure 7.24 shows how significant the effect of the initial falling velocity is on the trajectories assumed by rock fragments. Indeed, fragments roll and spread out differently between 1.5 and 2.0 m/s. The significant input that the initial velocity has on the final deposition should also be noted.
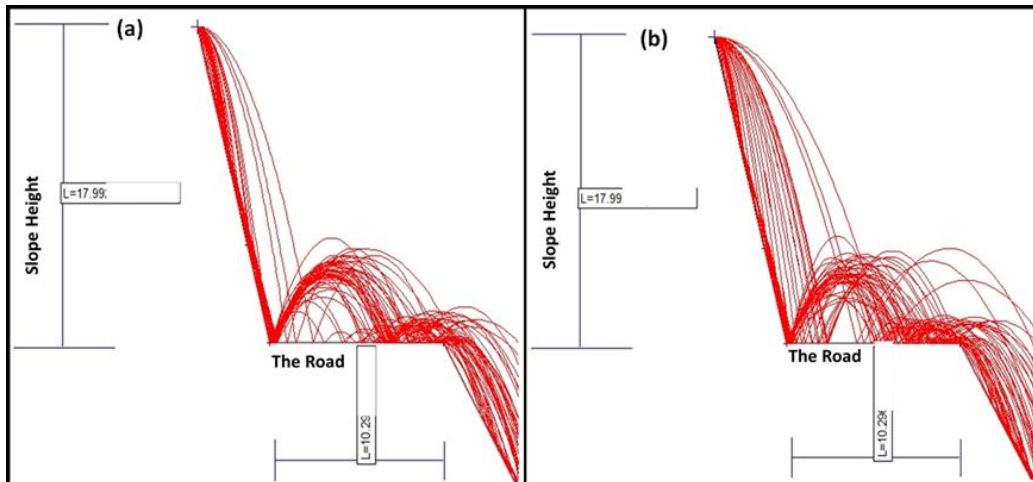
Figure 7.24 Simulation of distribution of rockfall trajectories (a) at 1.5 m/s and (b) 2.0 m/s total velocity

Further evidence is rendered in Figure 5.25 where the initial velocity has increased from 2.0 to 2.5 and 3.0 m/s. Here also, the final deposit is seen to be strongly dependent on the initial velocity of blocks.
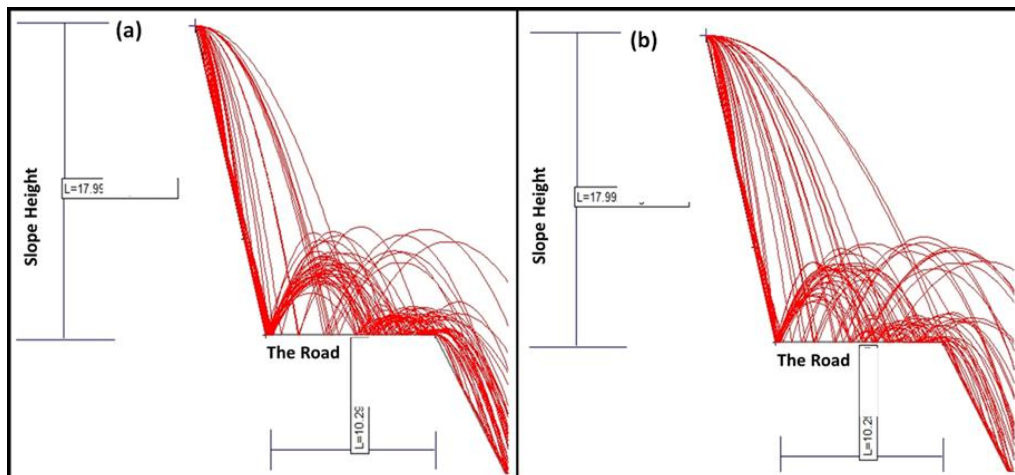
Figure 7.25 Simulation of distribution of rockfall trajectories (a) at 2.5 m/s and (b) 3.0 m/s total velocity

What seems evident from Figures 7.24 and 7.25 is that the extent of the final deposition is governed by the initial velocities of falling rock fragments. One may argue, as a first approximation, that the final distance reached by rolling, tumbling, and falling rocks is directly proportional to velocity. The simulation results presented in this section open the possibility for further inquiry around rockfall deposition. It is also suggested that the recurrence of rockfall around any of the six sites from high grounds is possible. This is because lots of loose boulders are observed in the upper part of the slopes. While the area has some vegetation that could help slow down tumbling rocks, the great falling height is concerning. As such, even a relatively small rock fragment can cause great damage and should therefore be regarded as a serious hazard along the road. Multiple geological features within the slopes should also be equally treated as a hazard. And although the simulation illustrated in Figures 7.24 and 7.25 provides some insight on rockfall dynamics and deposition, the absence of actual data for validation is limiting the analysis. Empirical models become the best available alternative. It is in this light that the next section proposes a hazard matrix for rockfalls and applies it to the six sites located in the Thulamela area (refer to Figure 7.1).

7.5 Development of the rockfall hazard assessment chart

A number of procedures exist for assessing rockfall hazards worldwide with the most recent being the Evolving Rockfall Hazard Assessment. Known as ERHA, the procedure has been developed as a hazard matrix chart for rockfall (Lateltin et al., 2005; Ferrari et al., 2017).

Figure 7.26 illustrates the principle used in the ERHA chart to identify the most hazardous areas along a slope. The chart consists of matrix cells labeled column-wise as low, medium and high according to the state of activity. The latter grows proportionally with the probability of occurrence and intensity of events (Lateltin et al., 2005; Ferrari et al., 2017). Based on the energy level of the rockfall process, the hazard level can now be estimated.
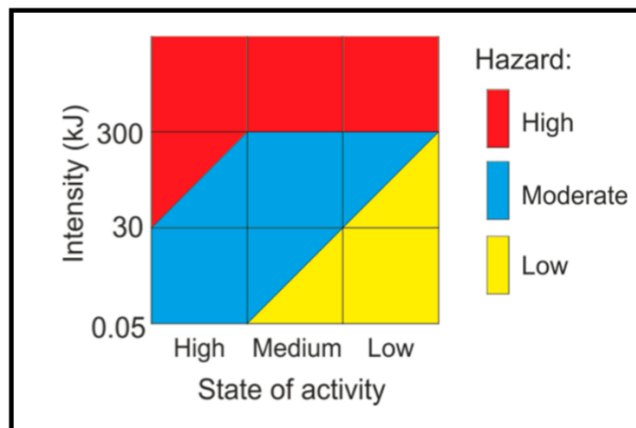
Figure 7.26 Hazard matrix (after Lateltin et al., 2005; Ferrari et al., 2017)

In a sense, the matrix chart rates hazards based on the kinetic energy of the rock mass. It does not take into account the starting height of rocks and the existing vegetation coverage over the slope. Furthermore, the matrix itself does not provide some indication of slope parameters and rockfall conditions. Due to such limitations, the chart cannot be used to compare the six sites in Figure 7.1. It is therefore

proposed to repurpose the hazard matrix chart in Figure 7.26 with the inclusion of components such as vegetation density, rock size, and slope height. This is based on the findings from the structural mapping, the stereonet plots, and the rockfall simulations discussed in the early section of the thesis. The proposed chart is to capture aspects of the kinetic energy and the potential energy with the latter being an indicator of slope height. Rock size is the next parameter included as part of the proposed chart; this is because the hazard level of a rockfall increases with the size of the rock involved. Talking about vegetation coverage, it can be seen that this factor has been disregarded in the hazard rating of rockfalls along the road (see Figure 7.26). In this study, it was found that the density of vegetation contributes positively to the hazard rating of the rockfall along the roads. Based on this, the influence of vegetation density has also been incorporated. Lastly, the hazard matrix was divided into three zones: low-risk, moderate risk, and high-risk zones. In the end, all the above were integrated in a compact manner in the proposed hazard matrix chart given in Figure 7.27.
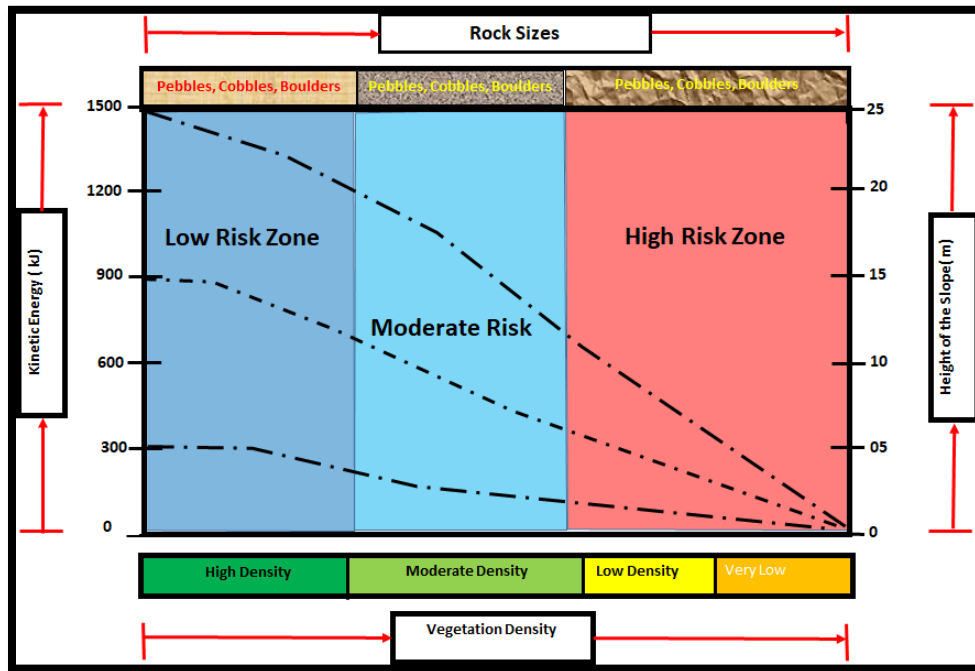
Figure 7.27 Newly developed hazard matrix for rockfalls in highways (roads)

The newly developed chart consisted of kinetic energy, potential energy (height), vegetation density and rock mass size. The chart attempts to closely reproduce the reality of what is observed on the ground. However, the chart differs from its predecessors as it gives the user the ability to assess the rockfall hazards at different slope heights. This is important when a comparison of sites is needed especially when other factors remain substantially unchanged. The other aspect of the proposed chart is that the impact of vegetation coverage on the rockfall rate can be explored.

The use of the new hazard matrix chart to rockfall problems is discussed next to ascertain its performance. Consider the real-life case studies that the present thesis is based upon. It makes sense to start off by assuming for example a rock mass of 1200 kJ in kinetic energy detached from a slope of maximum height of 20 m. Three scenarios can be considered in the area of study: low to very low vegetation density, moderate vegetation density, and high-density vegetation.

The new hazard matrix chart shows that rockfalls are rated as high-risk when the area is covered in low to very low-density vegetation. However, as the vegetation increases to moderate density, the rockfall hazard rating falls under the moderate risk zone. Further vegetation coverage upgrades the rating to that of a low-risk zone as shown in Figure 7.28.
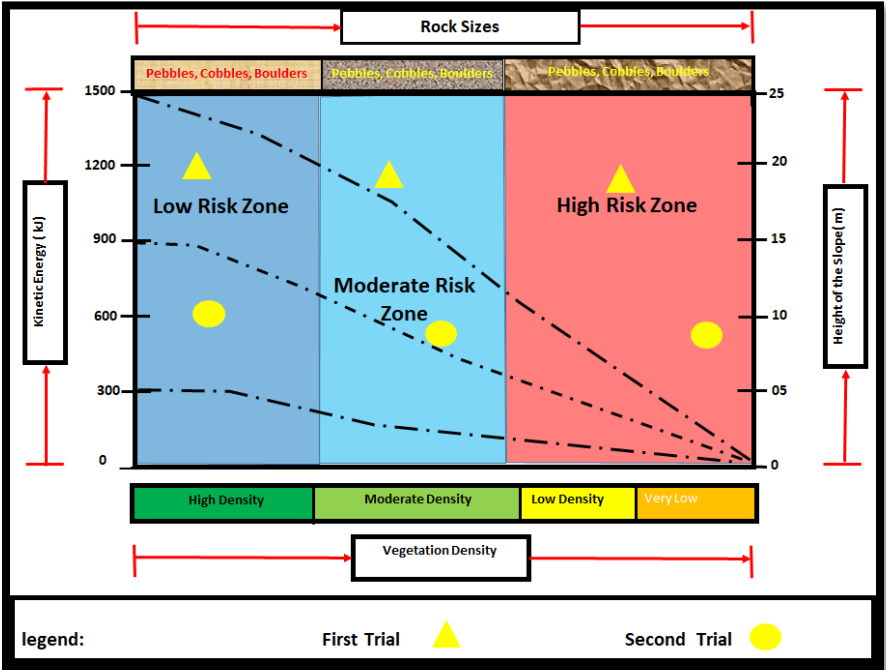
Figure 7.28 Application of the newly developed hazard matrix for rockfall in highways (roads)

The second trial also revealed similar results as the first. Indeed, vegetation coverage helps reduce the hazard rating of rockfalls while acting as a blockage to rolling. Finally, one should note that the developed chart can be read from a rock size scale instead of vegetation density and vice-versa.

224

7.6   Conclusion

The aim of this chapter was to assess the hazard level of six sites identified along the R518 and R523 roads in the Thulamela Municipality.

First, based on the in situ mapping, the study area was deemed a fair rock mass according to the rock mass rating system. In addition to this, the area is dominated by multiple geological features that create instability. The situation is further exacerbated by the low-density vegetation and loose boulders in the area. It is anticipated that if no further remedial action is contemplated, the area should be considered as a high-risk zone area.

Second, the distribution and orientation of geological features were analyzed using a stereonet plot so as to identify potential wedges. The results showed that the study area consists of multiple wedges that could fall at any given time. Simulations were performed using the RocFall software to identify the factors that influence the final deposition of rock fragments. Slope height, vegetation density, and rockfall velocity were shortlisted as a result. This was later used to develop a new hazard matrix chart for rockfalls along highways and roads. The combination of surface measurement and numerical simulation was intended to bridge the gap in the analysis of rockfall and its hazards prediction. The outcome of the endeavor was the development of a new hazard rating chart that is inclusive of factors such as rock size or vegetation coverage. The proposed chart is expected to add new knowledge when used as a complementary tool to existing and established tools such as the ERHA chart.

The next level of effort should be to perform a detailed analysis of cases with the new hazard rating chart. Equally important should be the development of techniques for the prediction of the time to failure.

Chapter 8   Influence of rainfall intensity on the stability of unsaturated soil slope

The purpose of this chapter was to analyze the impact of extreme rainfall on the recurrence of the landslide or slope instability using the Thulamela Municipality roads (R523) as a case study.

To this end, the historical rainfall data of the area of study was analyzed between 1988 and 2018. This resulted in showing that a significant increase in rainfall is usually experienced in the summer months of December and January. Following this, FoS of slopes of silt clay, clay and clay loam soils were estimated using the SLIDE simulator under rainfalls typical of the area.

Simulation results show that extreme rainfall has the ability to reduce the shear strength and resistance of the soil slope material. This may explain the recurrent landslides noted in the area.

Finally, the study area has also been observed to have tension cracks as a result of post landslides. These tension cracks weaken the material by letting water in the rockmass. Extreme rainfall alters the phase of the material solid in a manner that may require further research for a better understanding. The numerical simulation results presented in this chapter are one step in that direction. [7]

---

[7] Part of this chapter has been published the tittle of the article is as follows: Sengani, F.; Mulenga, F. Influence of rainfall intensity on the stability of unsaturated soil slope: Case Study of R523 road in Thulamela Municipality, Limpopo Province, South Africa. Applied Sciences 2020, 10, applsci-982838.

8.1 Introduction

Almost all reported high or large landslides are associated with predisposing conditions (Guzzetti, 2006; Lazzari and Gioia, 2018). These include prevailing clay material, the morphological setting of the slope, extreme rainfall events, and human activities such as road construction. Extreme rainfall and snowmelt are however the greatest triggers of landslides (Naudet et al., 2008; Manconi et al., 2013). Nonetheless, understanding the impact of extreme rainfall on slope stability in unsaturated soil is still to be improved. To this end, this chapter aims at evaluating the influence of extreme rainfall on the stability of unsaturated soil slope. The Thohoyandou area in the Thulamela Municipality in the Limpopo Province served as a case study. The area was reported in the previous chapter to experience regular slope instability events mostly in summer. However, the mechanism associated with the recurrence of these slope instability events is not well defined.

In order to pave the way forward, monthly rainfall statistics between 1988 and 2018 were sourced from the South African Weather Service (SAWS) as indicated in Chapter 3. Then, a statistical analysis of rainfall was performed to extract meaningful properties for the study area. These were used as input parameters in the numerical modeling of the slopes so that associated FoS values are estimated. Methodologies followed in Chapters 4 and 5 were also implemented in this chapter.

8.2 Rainfall in the Thulamela Municipality

The analysis of rainfall patterns was intended to determine the months during which slope failure is more likely to occur.

The monthly rainfall over a period spanning from 1988 and 2018 in the Thohoyandou area varied between 20 mm and 1100 mm. As reported in Figure 8.1, most of the

annual rainfall is received in the summer months, that is, between November and February. The rainfall departure of the study area was also constructed as shown in Figure 8.2; this was to verify whether extreme rainfall had occurred within specific months.
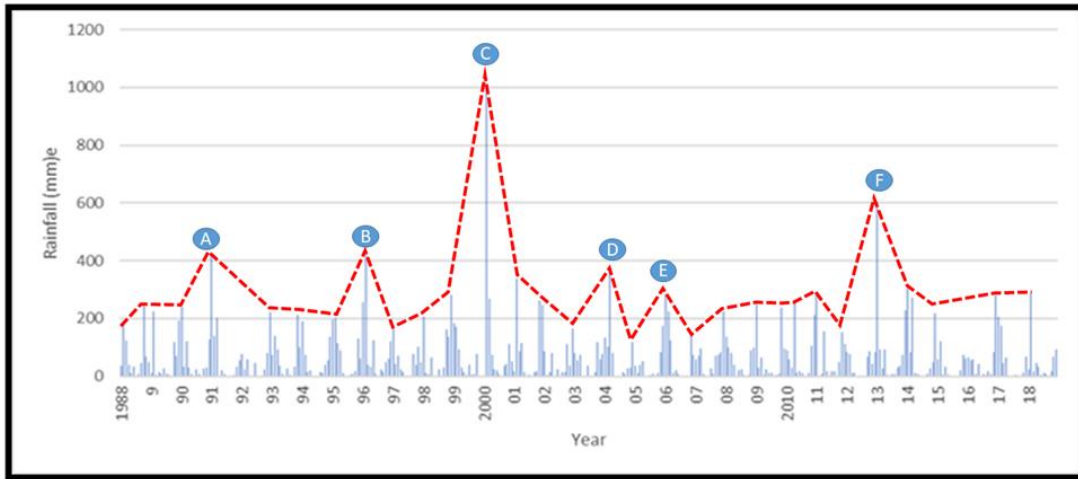
Figure 8.1 Monthly rainfalls in the Thohoyandou area from 1988 to 2018
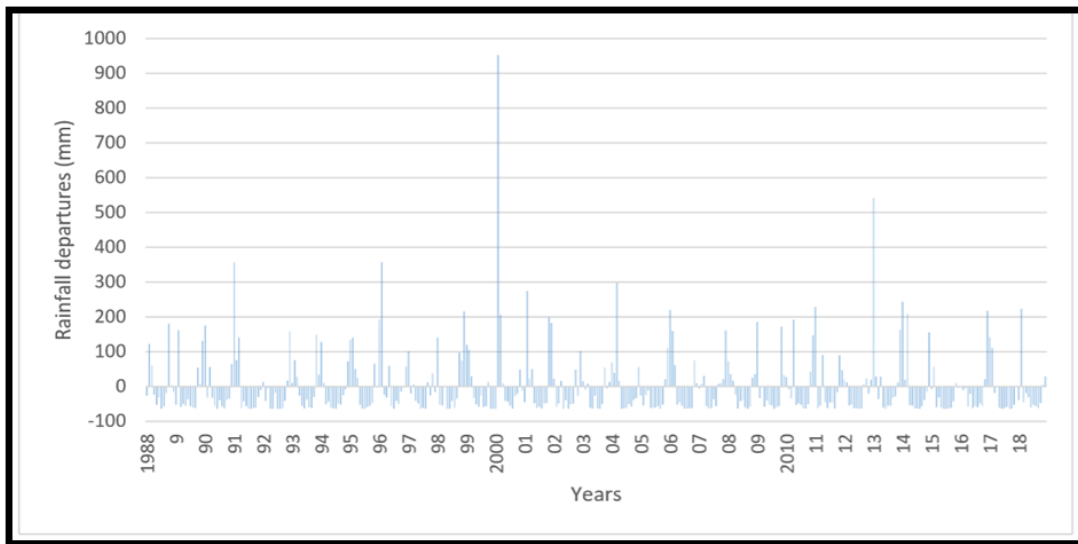
Figure 8.2 Rainfall departures of the Thohoyandou area from 1988 to 2018

The general pattern is that extreme rains happen during the summer months with rainfalls ranging between 150 mm to 1100 mm. The extreme rainfall experienced in the year 2000 is also noted in Figure 8.2 as an outlier. This abnormal event was reported with floodings that had been experienced in most African countries that year. The abnormal event and any other extreme rainfall recorded in the area of study to date all happened between December and January.

The study area itself does also has a number of streams cutting across. These streams are constantly fed by the rains; they in turn compromise the stability of slopes in the area. In short, the weather of the study area is very humid in a typical mountainous region covered with vegetation as evidenced in Figure 8.3.
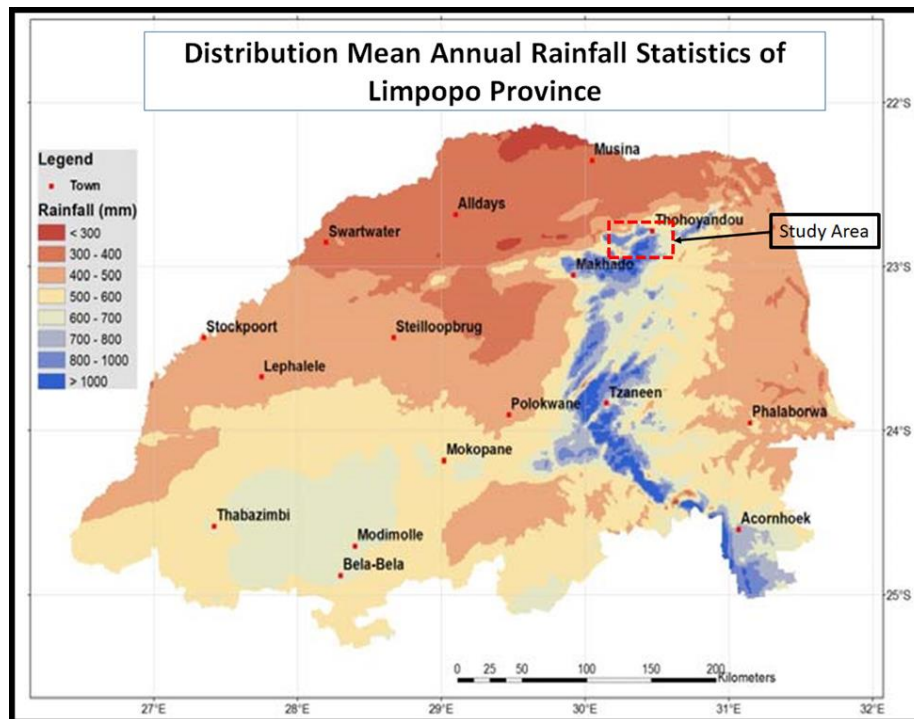
Figure 8.3 Mean annual rainfall statistics of the Limpopo province (modified after ARC-ISCW, 2014)

Early rains are usually absorbed into the soil through the pores that get filled with water very quickly. Therefore, extreme rainfall in the study area can easily trigger

landslides. Although some of the road sidewalls have been supported using gabions, these are usually washed away during mass movement. Note that mass movement is commonly triggered by extreme rainfalls.

It can be argued that heavy rainfalls create significant positive pore pressure; this then reduces the frictional shear resistance of the material and results in slope instability across the study area. The underground water also receives a constant supply of rain to form periodical streams meandering across steep slopes. This further contributes to widespread slope instability in the area.

In the next section, numerical modeling was resorted to with the view to explore the impact of extreme rainfall on the rock slope instability. To align the analysis with the study area, the soil properties obtained within the study area and reported in Tables 3.3, 4.1 and 4.2 were used. The study area was assumed to experience drained conditions, but undrained conditions were also simulated to obtain a full view of the impact of rainfall within the simulation. The results of the simulations are discussed below.

8.3   Simulation of the effects of rainfall intensity on slope stability

This section is devoted to the numerical simulation of the contribution of rainfall to the stability of soils of different compositions. The soils under consideration are characteristic of the localities along the R518 and R523 roads in the Thulamela Municipality. Simulations entail the estimation of FoS values of the different slope compositions subjected to sunny and rainy conditions. The effects of rainfall intensity are tested on silt clay soil, clay soil, and loam soil slopes.

8.3.1   Simulation case of a silt clay soil

From Section 8.2, it was conjectured that extreme rainfall has been influencing the recurrence of slope instability within the study area. To test this, numerical simulations were used to estimate the safety factors of various soil slopes of the area under drained and undrained conditions.

Simulation work presented in Chapter 5 is considered as the baseline since rainfall was not included in the analysis. Following the same approach presented in Chapter 5, simulation models included the following: Bishop's simplified, Janbu's Simplified, Janbu's corrected, Spencer's, Corp of Engineers' Number One and Number Two, Lower Karafiath and Gle/ Morgenstern Price. All these computational methods were filtered in the SLIDE model to produce representative safety factors.

Figures 8.4 – 8.7 give a summary of the simulated scenarios as well as the associated FoS for the silt clay soil. It can be seen that FoS values range from 0.264 to 0.350. So, regardless of the computational methods used, the slope in this silt clay soil is deemed unstable. This confirms that the selected type of slope is highly prone to landslides in the area. Furthermore, it was also noted that Spencer's and Corp of Engineers' methods produced closely comparable FoS values. In general, FoS estimates are similar to within $\pm$ 0.2 units (i.e. 0.264 < FoS < 0.350).
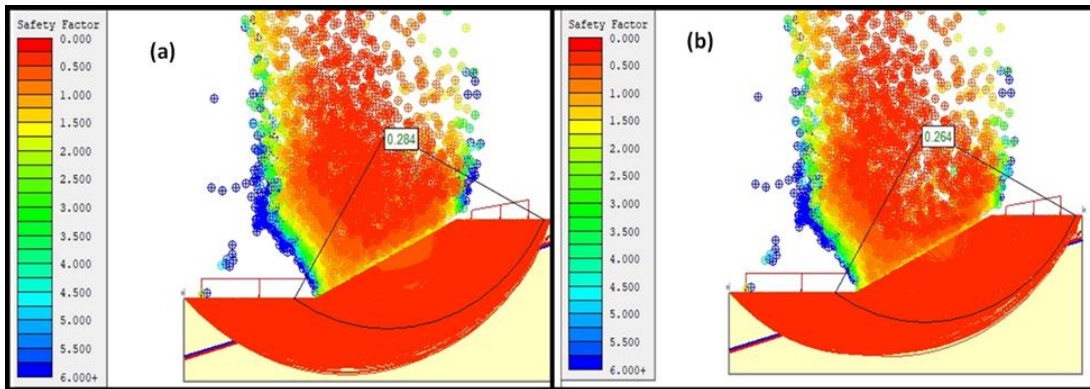
Figure 8.4   Safety factor simulated for rainy conditions in silt clay soil slope using (a) Bishop's simplified method and (b) Janbu's simplified method
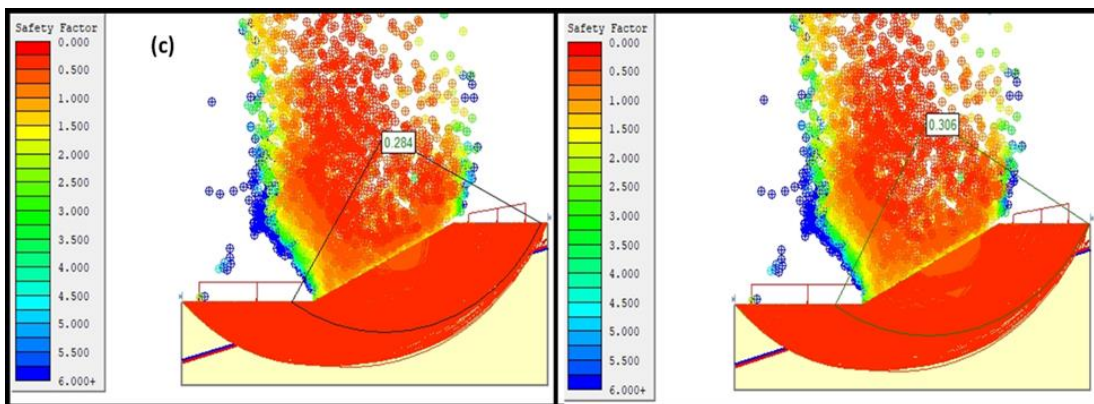
Figure 8.5 Safety factor simulated for rainy conditions in silt clay soil slope using (c) Spencer's method and (d) Corp of Engineers' Number One method
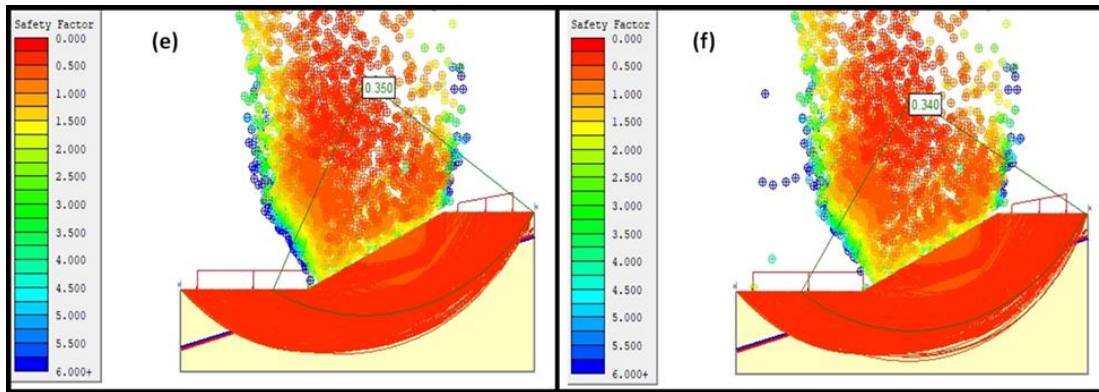
Figure 8.6 Safety factor simulated for rainy conditions in silt clay soil slope using (e) Corp of Engineers' Number Two method and (f) Lower Karafiath method
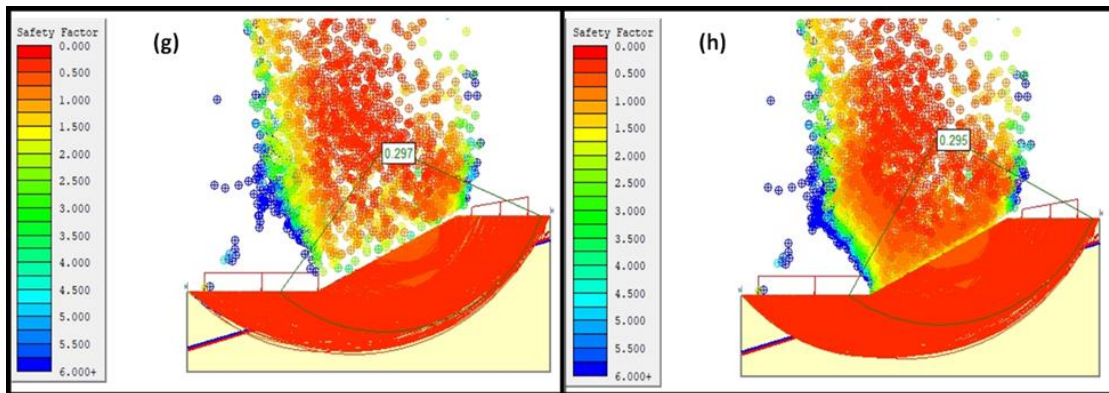
Figure 8.7 Safety factor simulated for rainy conditions in silt clay soil slope using (g) Lower Karafiath method and (h) Gle/Morgenstern Price method

The simulation results in Figures 8.4 – 8.7 show a rapid drop in FoS compared to those in Figures 5.27 – 5.28 irrespective of the computational method used. This is indicative of the contribution of rainfall to the FoS which basically leads to a less stable slope. To put it another way, landslides are more likely to occur in this material when extremely wet.

In summary, historical rainfall data and visual observations corroborate the simulation results. It is posited that the soil phase quickly changes during heavy rains. This turns the soil into a liquid-like material. At this stage, the shear strength

rapidly drops and weakens the bond between particles. Finally, deformation ensues in the form of a landslide.

8.3.2 Simulation case of a clay soil

Simulation scenarios similar in conditions to those in the previous section were set up. The difference is that this time, the clay soil typical to the Thulamela area was tested. The outcome of the simulation work is summarised in Figure 8.8 – 8.11.
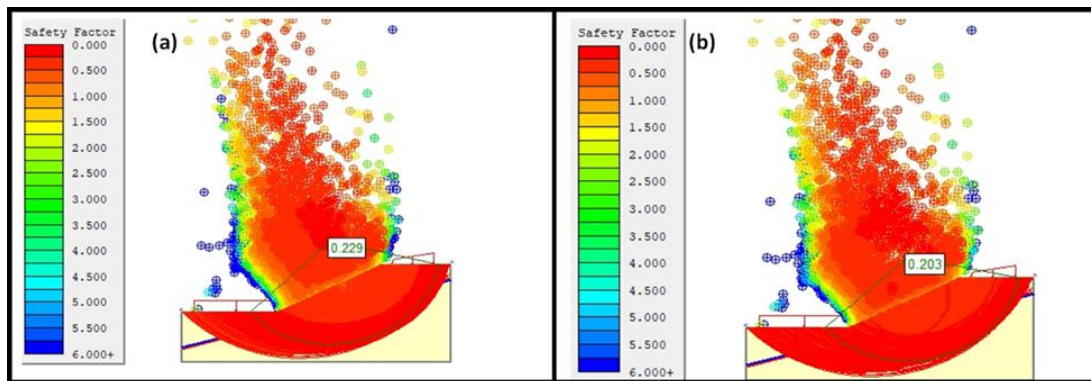
Figure 8.8 Safety factor simulated for rainy conditions in clay soil slope using (a) Bishop's simplified method and (b) Janbu's simplified method
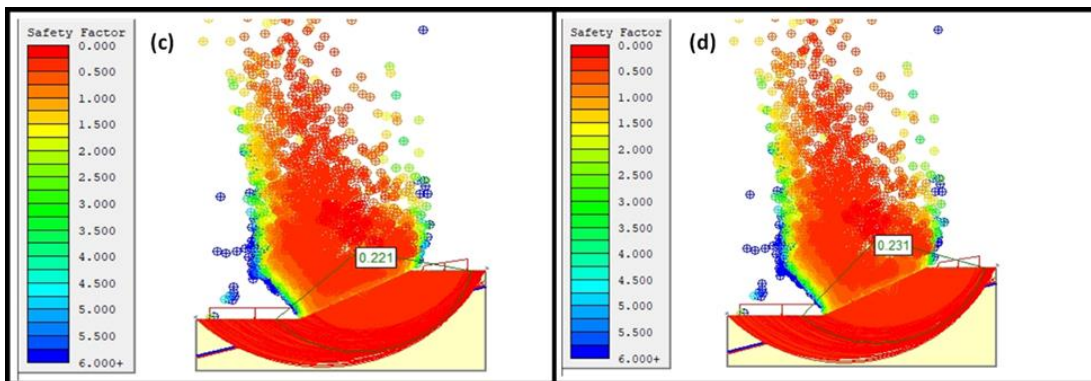
Figure 8.9 Safety factor simulated for rainy conditions in clay soil slope using (c) Spencer's method and (d) Corp of Engineers' Number One
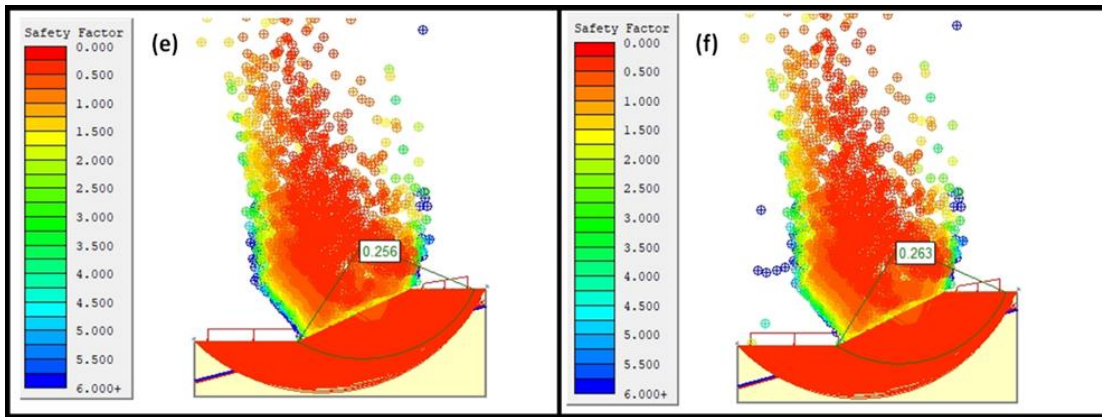
Figure 8.10 Safety factor simulated for rainy conditions in clay soil slope using (e) Corp of Engineers' Number Two method and (f) the Lower Karafiath method
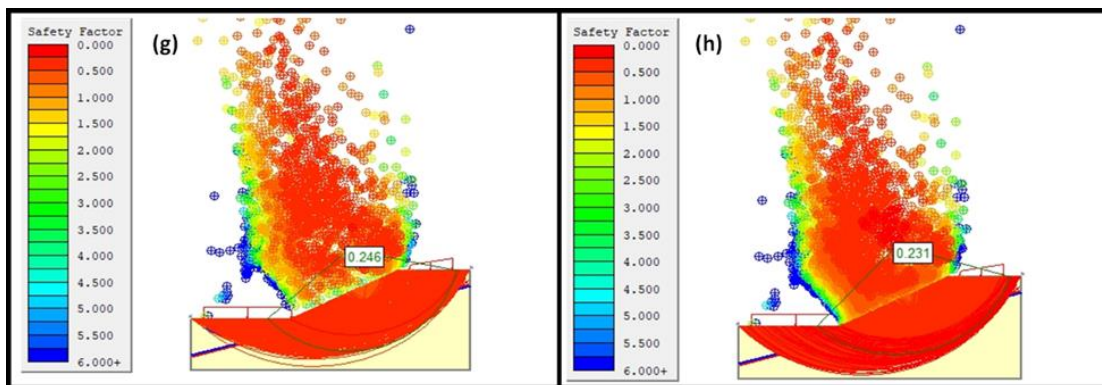
Figure 8.11 Safety factor simulated for rainy conditions in clay soil slope using (g) Lower Karafiath method and (h) the Gle/Morgenstern Price method

For all computational methods used, it can be seen that FoS values are all below 0.3 and range between 0.203 and 0.263. This means that the soil type is also prone to failure even under moderate raining conditions. Insitu observations support the simulation outcomes with evidence of multiple tension cracks around the area. In simple terms, clay soil slopes in the area do not require a lot of water pressure in order to collapse.

Finally, Lazzari and Piccarreta (2018) argued that hydrometric streams usually play a major role in triggering landslides in most sensitive clay soil. Although in some places, the increase in rainfall may not necessarily mean a landslide will occur. The understanding is that the soil phase changes with time but depends on the amount of rainfall filling the pore spaces. The latter is also controlled by the existence of water streams cutting across certain lithologies in the area.

8.3.3 Simulation case of a clay loam soil

The last simulations were undertaken to verify the performance of the typical clay loam soil. The results of the simulation, in this case, also suggest an unstable slope under heavy raining conditions. Low FoS values were estimated using different methods as illustrated in Figures 8.12 through 8.15. This means that clay loam slopes in the Thulamela area are prone to failure when exposed to typical local heavy rainfalls.
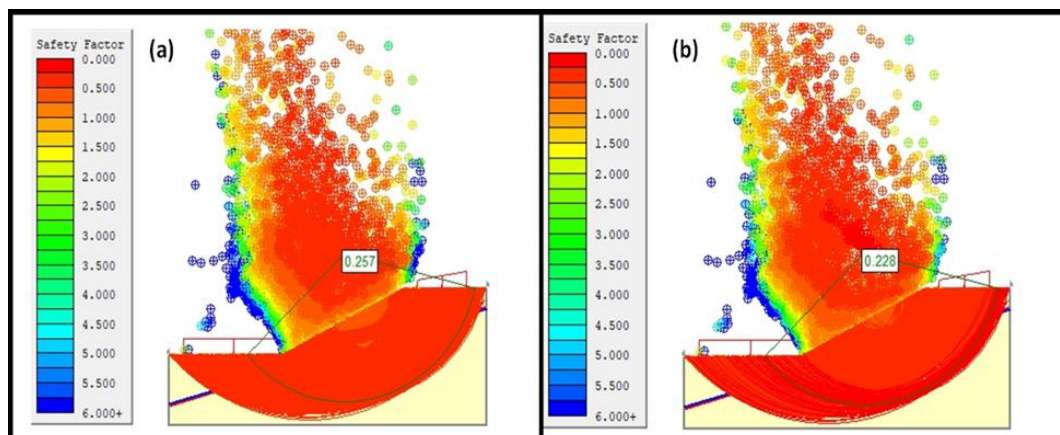
Figure 8.12 Safety factor simulated for rainy conditions in clay loam soil slope using (a) Bishop's simplified method and (b) Janbu's simplified method
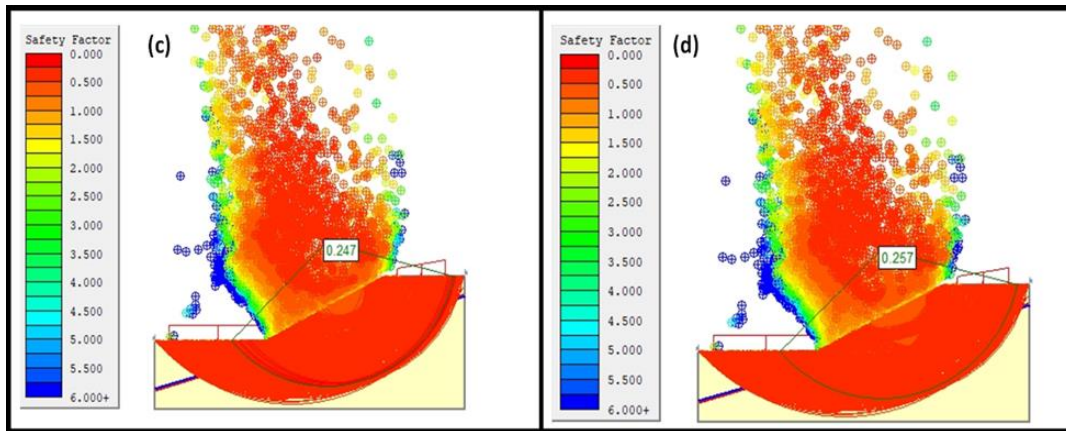
Figure 8.13 Safety factor simulated for rainy conditions in clay loam soil slope using (c) Spencer's method and (d) Corp of Engineers' Number One method
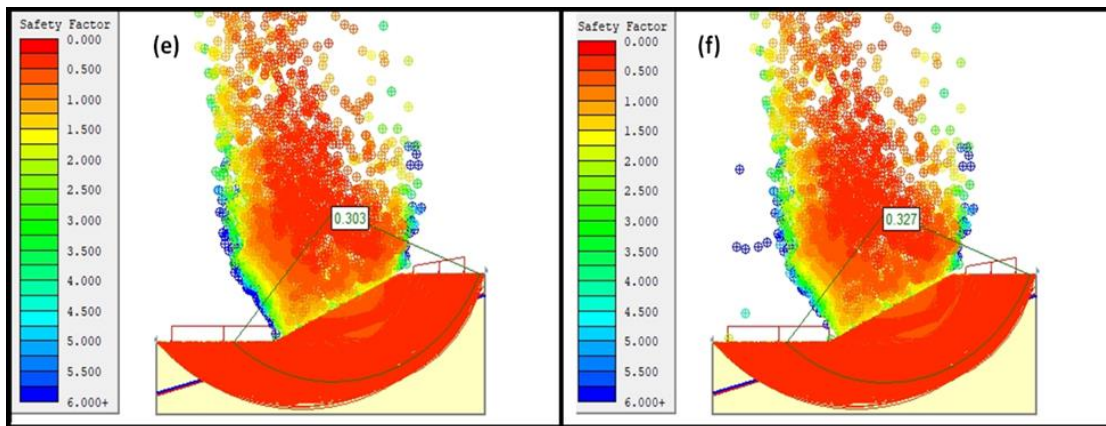
Figure 8.14 Safety factor simulated for rainy conditions in clay loam soil slope using (e) Corp of Engineers' Number Two method and (f) the Lower Karafiath method

237
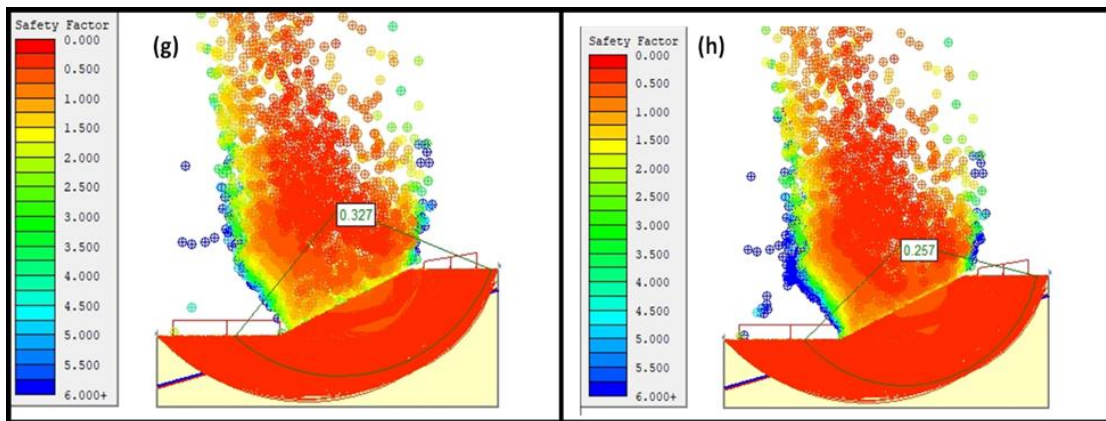
Figure 8.15 Safety factor simulated for rainy conditions in clay loam soil slope using (g) the Lower Karafiath method and (h) the Gle/Morgenstern Price method

Based on observations, it was noted that post landslides create land fractures as long as 10 m. The uncontrolled surface drainage water gets channeled toward these fractures resulting in more unstable slopes. Although some slopes have been supported, the support system has been observed to fail dramatically. Perhaps the most important point to make is that further research is needed to probe the ineffective support systems.

8.4   Significance of the simulation findings

Several scholars have examined the application of physical or empirical models to the impact of rainfall on slope stability (e.g. Aleotti, 2004; Brunetti et al., 2010; Caine, 1980; Cannon et al., 2008; Cevasco et al., 2010; Chleborad et al., 2006; Corominas et al., 2002; Guzzetti et al., 2005; Iverson, 2000; Luino, 2008; Zezere et al., 2008). Most have argued that the effects of meteorological, morphological and geological characteristics have been mixed. Indeed, different geographical locations have yielded different results with regard to rainfall thresholds for a landslide.

In terms of the results reported in this thesis, they follow the same pattern as those of past work. For example, Lazzari et al. (2013) were able to demonstrate that extreme rainfall impact the recurrence and occurrence of landslides. This is especially true in steep and clay soil areas as has also been interestingly found in the present thesis. It may therefore be said that rainfall and other factors still unknown have much influence on the occurrence of slope instability within the Thohoyandou areas.

The findings reported in this chapter provide a broad view of the common mechanisms associated with the recurrence of slope instability in the Thulamela area. In line with the aforesaid, several scholars have conceded that extreme rainfall, active tectonics, and weathering strongly influence rock slope instability (Terzaghi, 1950 & 1962; Bieniawski, 1976; Selby, 1982; Willie and Mah, 2004; Jaboyedoff and Derron, 2005). This thesis is no different with results that compare with previous studies conducted in other areas.

On another note, numerical simulation has been resorted to in this chapter in an attempt to understand the overall behavior of slopes. Nevertheless, it is crucial to indicate that numerical software does not replace critical thinking and visual observation. That is why actual data collected from a controlled environment such as in a laboratory or on the field is required for validation. It is anticipated that the simulation findings presented in this thesis may guide the compilation of meaningful data for the purpose.

8.5   Conclusion

The findings of this chapter suggest that extreme rainfall that usually occurs between December and January is a triggering factor for landslides along the R518 and R523 roads in Thohoyandou. Such rainfall can compromise the stability of the road slopes

and worsen the high landslide-prone area. Besides the post landslide reported, the area has been observed to be dominated by tension cracks as a result of post landslides. These tension cracks are amenable to weakening the material with water infilling. The material behavior changes from that of a solid phase to a liquid one. Soil particles lose their bond under extreme rainfall and give way to landslides.

The core of the work was the simulation of slopes of different soil types that have provided results in support of physical observation. Three soil types were simulated: silt clay, clay, and clay loam slopes. In all three cases, FoS values were estimated to be 0.200 to 0.363 signifying a high likelihood for slope failure, it is expected that the stable slope will present a Safety Factor of 1.5. Therefore, it is concluded that the slopes along the R518 and R523 roads are of high risk when exposed to heavy rainfall. However, mitigation can be implemented to stabilize slopes including channeling natural water streams around the area. Road walls may be the other mitigating solution, but further research is needed to ascertain their efficacy.

Chapter 9   Conclusion and recommendations for future work

The main objective of this thesis was to apply advanced geotechnical methods and ASTER images to investigate rockfall and slope instability. Selected sites along the R523 and R518 roads in Limpopo province were used as a case study. This chapter presents the summarised findings of the thesis, the overall conclusion and recommendations for future work.

9.1   Summary of the thesis

Rockfalls, and more generically landslides, have enjoyed a lot of attention in the field of geotechnical engineering and specifically in rock mechanics. Several methods have been implemented to describe the mechanisms behind rockfalls with various degrees of success. Most common analysis methods have been centered on the traditional Lagrangian Finite Element Method (FEM). However, the literature (Zhang, 2014; Zhang et al. 2017-2019) reveals that the traditional Lagrangian FEM falls short when large strains emerge and result in limit loads that trigger failure.

It should be acknowledged that FEM has enabled the development of numerical simulation tools for a better description of rockfalls. However, aspects of landslides pertaining to the material deposition and the effects of water have remained unanswered. In that respect, it was proposed in this thesis to combine advanced geotechnical analysis and remote sensing techniques. Advanced geotechnical analysis techniques basically revolved around the FEM framework. Advanced remote sensing, on the other hand, was built on data collected using Advanced Space-borne Thermal Emission and Reflection Radiometer (ASTER) imagery. The

idea was to gain a better understanding of landslides in an attempt to bridge that gap.

The main objective of this thesis was to use FEM-ASTER and study the mechanisms behind the slope instability along the R518 and R523 roads in Limpopo. It was anticipated that rockfall hazard rating matrix charts could be developed for the typical unsaturated sensitive clay soil of mountainous areas found in the Thulamela Municipality of the Limpopo province. Lastly, the influence of extreme rainfall on the stability of slopes was characterized for the area of study.

To achieve the objectives of the study, the following methods were employed: field observations and measurements, laboratory tests, kinematic analysis, limit equilibrium analysis, numerical simulations including FEM, and ASTER image analysis for landslide susceptibility.

Results showed that the common mechanism associated with the recurrence of slope instability is extreme rainfall received in the Thulamela Municipality. The steepness of the slope, geological features, and streams cutting across the study area were also found to weaken the solid mass.

Furthermore, the rockfall hazard rating matrix chart was developed based on field observation, laboratory analysis, and numerical simulations. Indeed, previous charts rate the rockfall hazard by incorporating kinetic energy as the only defining factor. However, the findings of this thesis demonstrate that several factors are equally important. These include potential energy, vegetation density, and slope angle amongst others. The rockfall hazard matrix chart proposed in this thesis allows for these factors to a certain extent. The proposed chart was then applied to selected locations in the study area and proved to be suitable for characterizing rockfall hazards.

Details on the findings brought about in this thesis are presented in the subsequent sections in a logical order.

9.2   Mechanism associated with slope instability

In order to study the mechanisms associated with slope instability in the study area, several approaches were implemented. The results and associated findings of each approach are outlined in the sections below.

9.2.1   Visual observations and laboratory tests

Field mapping of the study area was done while soil samples were collected for subsequent laboratory testing.

From the field mapping work, it was noted that multiple geological features and water streams cut across the study area. Some of these geological features were observed to create wedges where they intersect. Such wedges create weak zones along slopes while a number of tension cracks were observed in the upper section of the slope. Tension cracks resulted in the weakening of the strength of the solid mass. The amount of rainfall in the province (i.e. more than 100 mm/h in summer) was established to be the triggering source of the tension cracks. The correlation between extreme rainfall and slope instability events was posited; this was subsequently confirmed with landslides occurring primarily during the heavy rainfall season.

Finally, it was observed that natural slopes were disturbed during road construction since the natural drainage pattern was altered. As a result of this, steep and unstable slopes were excavated. This may also have played a role in the recurrence of

landslides although gabion meshes have been installed as a mitigating solution. Additionally, laboratory analyses have been carried to show that the study area consists mostly of clay soil. This soil is known for the high possibility of sliding and shrinkage. It was concluded that clay soil plays a major role in slope failures in the study area.

9.2.2   Kinematic analysis

The kinematic analysis was performed as part of this research using the SWEDGE numerical software. Slope angles spanning from 40° to 90° were considered while corresponding factors of safety (FoS) were estimated. This set of simulations was to ascertain the relationship between relative frequency and FoS. Relative frequency should be understood to signify the number of valid wedges formed by Monte Carlo sampling input parameters. Next, the kinematic analysis program was pursued in an attempt to evaluate the effect of friction angle on slope stability. This was aimed at reproducing the contribution of geological features present in the area of study and within the slope mass. Geological features here refer specifically to joints and soil type making up the various slopes in the region. Finally, the type of soil was modeled by altering the shear stress of the soil relative to its minor stress acting along the slope.

In terms of results and findings, SWEDGE helped to show that the increase in slope angle results in a rapid decrease in simulated FoS. Graphical techniques involving stereonet plots were resorted to. The endeavor led to prove that some wedges in the slope mass are stable initially but become unstable as the slope angle increase. This means that the increase in slope steepness has much influence on the recurrence of the slope instability. The simulation work also suggested that slope failure in the study area is governed by the presence of geological features

responsible for the creation of wedges. This was supported by on-site observations that evidenced the creation of boundaries of weak zones across the slope and the development of tension cracks along the upper sections of the slopes. Results further showed that joints can activate slope instability when the friction angle is very low. The underlying model simulated that as the friction angle increases, it is expected that the slope becomes more stable. In addition to this, FoS values as low as 1.0 to 1.3 were estimated which is indicative of an unstable slope. With this, the studied slope was deemed unstable due to the influence of the friction angle of the geological features recorded in the field. It is important to indicate that the majority of the simulation output renderings have shown a positive relation between friction angle and FoS. But these relationships have less to do with the stability of the slope but more with the fact that the joint friction angle was found to be directly proportional to FoS.

Finally, water pressure is known to be ascribed to the extreme rainfall in the region. Simulation results showed that extreme rainfall may be a key factor responsible for slope instabilities. Indeed, extreme rainfall reduces the resistance of the material. The shear strength of the material drops as a result and leads to the initiation of slope instability.

9.2.3   Limit equilibrium

The concepts of toppling and sliding of blocks have been utilized in this study to identify the mechanisms behind the slope failure in the area of study. To this end, rotational and translational analyses were performed on selected slopes. The rotational analysis was performed using classical theoretical equations while transitional analysis relied on the RocPlane numerical software.

It was found that the failure mechanism of all the selected areas conforms to sliding rather than toppling. In other words, the selected areas appear to be dominated by sliding failure due to the fact that the slope material is mainly clay soil. Tension cracks were also found to be responsible for the initiation of the sliding motion of blocks. However, the initiation was noted to be controlled by the amount of rainfall which reduces the resistance of the material against sliding. Slope failure occurred for two reasons: first, wedges fail to anchor the ground due to the lubricating effect of rainwater and second, tension cracks develop and eventually sliding takes place.

The rotational analysis was also performed in three different types of soil: clay, silt clay, and loam clay. The purpose was to confirm the mechanism behind the slope instability. The first simulation using clay soil slope yielded FoS values ranging from 0.612 to 0.894. The second set of simulations on silt clay produced $1.424 < FoS < 1.717$. Similar results were produced with the third set of simulations. The extent of slope failure is expected to be moderate in silty clay areas as compared to purely clay soils. From the outputs, it can be said that the slopes appear to be less stable in normal conditions but when extreme rainfall occurs, their stability gets compromised further.

Finally, the results of the transitional analysis using RocPlane indicate a more unstable ground with an increase in slope angle. This basically means that as the slope gets steeper, FoS drops. The other finding from the RocPlane simulations was that the slope angle and the driving force of the water pressure are the common factors that can initiate sliding. In conclusion, the transitional analysis also concurs with other methods. This is because here also joints, heavy rainfall, slope steepness, and material properties were found to be the main contributors to slope instability along the study area.

9.2.4   Advanced numerical simulation

To complement the theory-based analysis summarised above, the advanced simulation was initiated as part of the research. Phase 2 simulator was first used to understand the mechanism of the slope instability of the study area. Here, various stages of road construction were set and simulated along the mountain through which the R513 and R528 roads were carved. Volumetric strain, shear stress, shear strain, total displacement, as well as minor and major principal stresses are the factors that were evaluated.

Looking into the volumetric analysis of the slope, results showed that some minimal instability is to be expected during the first stage of road construction. The situation gradually worsens as road construction progresses while much deformation is expected to occur on the sides of road walls. These simulated results were noted to agree with the other techniques such as rock fracturing on the sidewall of the excavation and other numerical simulations.

The maximum shear strain was also constructed using the Phase 2 modeling tool. A gradual increase of shear strain from the first stage to the final stage of road construction was noted. Similar conclusions were reached with shear stress as well as minor and major principal stresses. This result implies that the resistance and integrity of the material were gradually reduced with each stage of road construction thereby affecting the shear strength of the material.

An additional set of the simulation was to look into the effects of road construction on the strength of the solid mass and total displacement caused by road construction in the presence of joints across the slopes. The findings suggest that the strength factor of the slope should drop as road construction progresses. The results also indicate that the presence of joints along the road slope plays a major role in reducing the strength of the material. This is because joints create weaknesses across the solid mass.

Finally, the influence of a joint set was studied using Phase 2. It was noted that the tensioned and compressive displacement of the solid mass were both present. However, there was a common trend in which the displacement was simulated to increase with road construction and far away from the joint.

9.2.5   ASTER image processing

Remote sensing techniques were used to simulate landslides susceptibility maps of the study area. This required several input parameters such as slope angle, geological features, rock types, etc.

ASTER imagery was used for this purpose and enabled to show that the study area is situated along the steepness zones of the Limpopo province. In addition to this, the area was found to be dominated by large geological features that had not been mapped before. Most importantly, almost all slope instabilities were found to be located along these geological features. ASTER images also revealed that these slope instabilities were located very close to most of the perennial water streams cutting across the area.

The vegetation cover was the second indicator characterized by ASTER imagery. Change in vegetation was evidenced by monitoring images taken between 2004 and 2017. This strongly suggests a certain activity, possibly of the human type, that reduces the vegetation cover of the study area.

Lastly, landslides susceptibility maps were constructed for the area. Results show that all selected areas, as well as the post landslide areas, are highly prone to the occurrence of the landslide. These results correlate very with geotechnical analysis in which it was simulated that the selected area is prone to landslides. What transpires from the above is that both geotechnical techniques as well as remote sensing can identify mechanisms associated with the recurrence of landslides along

the Thulamela municipality roads. Finally, from landslide susceptibility maps, there is some indication of highly prone landslides in the area.

9.3   Mechanisms associated with rockfall

Visual observations on the field have highlighted that the rock mass was dominated by bedding planes dipping and striking at the angle. The common rock type identified from the study area was a partial metamorphic sandstone. The sandstone has minor beds of the conglomerate in between sandstone layers while the country-rock mass was dominated by small and large joints. These joints appear to create wedges along with the sedimentary layers. It was also observed that the upper part of the stratigraphy was dominated by the disseminated boulder of both sandstone and conglomerate with small pebbles and cobbles spread around the area. Furthermore, sandy red soil was observed on top layers throughout the strata, with few vegetation coverages or far spread vegetation (moderately low to low density).

The orientation of the small and large joints was not similar at all; however, it was thought that the varying structural orientation has much influence on the generation of the blocky and fractured rock mass. Most boulders and fractured rock mass were loosening and could fall anytime. Monitoring the frequency of rockfalls along the road because is also difficult because whenever there is a rockfall, broken rocks are quickly removed from the road to clear the road and avoid traffic blockage.

The stereonet analysis was performed based on geological input parameters mapped within the study area. The results of the analysis indicated that the overall rock mass can be classified as a fair rock mass. The rock mass was found to range from class 54 III fair rock to 56 III fair rock. The kinematic analysis was then done where it was noted that the rock mass consisted of several weak zones or wedges that can fail. As a result, the rock mass was deemed unstable due to the unfavorable

orientation of the discontinuities. Furthermore, the kinematic analysis identified planar sliding as a likely failure. Toppling cannot also be excluded especially with the discontinuities dipping into the facing slope. But eventually, stereonet plots indicated that the common mechanism associated with rockfall could be slope angle and multiple geological features that create wedges throughout the rock mass.

Finally, further confirmation using the RocFall model was performed. It was found that the height of the slope has extensive contributions to the distance in which the falling rock mass can be deposited. When the height was about 5.5 m from the road, the falling rock mass is expected to spread out in the vicinity of the road. In this case, falling rock mass is also expected to bounce less than 2.5 m high from the road, while some fragments are expected to just settle immediately after hitting the road. Nevertheless, when the height of the slope increases the final deposit of the rock fragment was different. Most fragments were noted to be finally deposited on the other side of the road.

9.4   Influence of extreme rainfall of slope instability

The historical rainfall data of the study area was evaluated. From the endeavor, a significant increase in rainfall was noted in the summer months running between December and January. As a result, such extreme rainfall can reduce the stability of the road slope. This may explain why the area has been identified as a high landslide-prone area. Also, the area of study is dominated by tension cracks as a result of post landslides that weaken the material from time to time.

It was established that extreme rainfall usually changes the material phase from the solid phase to the liquid phase. Indeed, soil particles usually lose their binding properties when exposed to extreme rainfall. Slope instability then ensues especially during the heavy rain season, i.e. between December and January. In supporting

the physical observation, slopes of different soil types were simulated and shown to be unstable under extreme rainfall. This is because FoS values between 0.200 and 0.363 were found irrespective of the soil type simulated. Such values imply that a high likelihood of failure and collapse of slopes. It was concluded that the numerical simulation tools provided reasonable results when compared with the actual behavior of slopes under heavy rainy conditions.

9.5   Development of rockfall hazard rating matrix

The hazards matrix chart developed by Lateltin et al. (2005) and improved by Ferrari et al. (2017) rates hazards based on the kinetic energy of the rock mass. This is done regardless of the initial height that the rock mass is detached from. Furthermore, the chart itself does not consider the effect of vegetation coverage on rating the hazard around slopes. And, the matrix behind the chart does not allow for some slope parameters deemed important such as slope height. Due to such limitations, the chart cannot be used for or applied to mountainous areas such as the Thulamela Municipality that the thesis is based on. To identify factors for integration into the map, an improved version of the hazard map was explored.

The newly developed chart consisted of kinetic energy, potential energy (height), vegetation density and the rock mass sizes. The proposed chart is simply to use and based on the reality that has been observed on the ground. Nevertheless, this chart differs completely from the previous charts. Indeed, the developed chart gives the user the ability to assess the rockfall hazards at different slope heights. Evidently, other factors remain constant while the rockfall can also be assessed with other factors changing. The impact of vegetation coverage on the rate at which the rockfall occurred is one such case that can be rated with the proposed chart. Two examples of the application of the new chart were finally given; it was demonstrated that the

chart can give sensible results. Indeed, a close look at the results showed consistency with reality.

9.6   Development of slope stability prediction chart

Based on findings from both ASTER images and geotechnical analysis, a slope stability chart was described. The intention of the chart was to describe the occurrence, conditions and hazard rating of the studied slopes.

The chart was based on several factors that were validated statistically, numerically and remote sensing. The selected factors underpinned the idea that slope stability is a function of the distance from a known geological feature, water streams, as well as slope angle and elevation. The chart is suitable for sensitive clay soil or clay soil. The other observation supporting this chart is that slope failure is influenced by the angle and elevation of the slope.

Indeed, from numerical simulations, it is clear that geological features affect the total displacement and the strength factor of the solid mass. It was observed that geological features/ structures reduce the strength of the solid mass wherein the solid mass is well intact or at the boundary or sidewall of the excavated road or slope cuts. Therefore, it was concluded the proposed chart can be used to rate the stability of the slope.

Following the above, a simple criterion was suggested as a way of defining slope instability. The criterion states that much displacement is expected closer or along with the geological features. Displacement reduces as the distance from the geological increases towards the slope. In this criterion, the size of the geological features and their interaction with the solid mass will also limit the damage or slope instability. In the case of predicting slope failure that is located several meters from

the features, the chart will probably indicate that the slope is stable. This is because the influence of geological features will be less. In supporting the above discussion, all active slope instability was located closer to the geological features and the rest of the affected slopes were far from geological features. The conclusion is that the presence of geological features has much impact on the occurrence of slope instability.

9.7   Overall conclusion of the thesis

The purpose of this study was to apply both ASTER images and geotechnical techniques to investigate rockfall and slope stability using Limpopo road (R518 and R523). Based on the results and findings, it was noted that several mechanisms are associated with the recurrence of slope instability along Thulamela Municipality roads. The identified mechanism includes heavy rainfall, material properties, multiple geological features cutting across the study area, the topography of the study area and improper road construction. It was noted that the rainfall tends to trigger slope failure due to the increase in water pressure within the soil pores. Indeed, SWEDGE analysis has confirmed that the developed wedges along the selected slopes usually slide downwards as the rainfall quantity increases. In terms of material properties, clay soil is well known for its swelling behavior. During this behavior, clay soil changes from the soil phase to the liquid phase which may induce the movement of soil particles at that time. In contrast, if the phase remains similar; then, the movement will occur until the soil phase changes.

Lastly, a simple slope stability chart for unsaturated soil was developed based on the above results. The chart used several factors that were simulated by either remote sensing or geotechnical techniques. From the chart developed, all selected active slopes in the study area were found to be unstable as observed in the field.

Furthermore, a rockfall hazard predictive chart was also developed and few examples were performed to identify the suitability of the chart, indeed the chart was found very useful and relevant to rockfall prediction. Therefore, the chart should have used for the analysis of landslides and rockfalls.

9.8   Recommended future studies

Based on the scope of the work covered in this thesis, the following items are suggested for future studies:

➢ The use of more sophisticated methods (Fuzzy Mathematics Theory and Machine Learning) so as to develop improved slope and rockfall hazard matrix rating charts

➢ The use of specialized instrumentation such as geophones and extensometers among others for the collection of field data pertaining to rock deformation and displacement

➢ The application of the novel Particle Finite Element Method (PFEM) under drained and undrained slope conditions. The comparative work may lead to developing a clear view of the current limitation of the framework

➢ The combined use of remote sensing techniques and advanced numerical analysis implemented in this thesis can be revisited, this time, using PFEM instead of the traditional FEM. This may potentially lead to improved description and prediction of landslides and rockfalls.

List of references

Abbott, P.L., 2002. Natural disasters. Mc-Graw-Hill, Boston

Abolmasov, B., Milenković, S., Marjanović, M., Durić, U., Jelisavac, B., 2015. A geotechnical model of the Umka landslide with reference to landslides in weathered Neogene marls in Serbia. Landslides, vol. 12, pp. 689 – 702

Abramson, L.W., Lee, T.S., Sharma, S., Boyce, G., 2002. Slope stability concepts. Slope stabilisation and stabilisation methods, Second edition. John Willey & Sons, Inc.

Adoko, A.C., Wu, L., 2011. Fuzzy inference systems-based approaches in geotechnical engineering – a review. Electron Journal of Geotechnical Engineering, vol. 16, pp.1543 – 1558

Adoko, A.C., Zuo, Q.J., Wu, L., 2011. A fuzzy model for high-speed railway tunnel convergence prediction in weak rock. Electronic Journal Geotechnical Engineering, vol. 16, pp.1275 – 1295

Adoko, A.C., Gokceoglu, C., Wu, L., Zuo, Q.J., 2013. Knowledge based and data-driven fuzzy modeling for rockburst prediction. International Journal of Rock Mechanic Mining Science, vol. 61, pp. 86 – 95

Adoko, A.C., Gokceoglu, C., Yagiz, S., 2017. Bayesian prediction of TBM penetration rate in rock mass. Engineering Geology, vol. 226, pp. 245 – 256

Agah-Tehrani, A., Lee, E.H., Mallet, R.L., Oñate, E.T., 1986. The theory of elastic-plastic deformation at finite strain with induced anisotropy modeled as combined isotropic-kinematic hardening. Metal Forming Report, Rensselaer Polytechnic Institute, Troy, N.Y., June 1986

Ansari, M.K., Ahmad, M., Singh, R., Singh, T.N., 2014. Rockfall hazard assessment at Ajanta Cave Aurangabad, Maharashtra, India. Arabian Journal of Geoscience, vol. 7, pp.1773 – 1780

Antolini, F., Tofani, V., Del Ventisette, C., Luzi, G., Casagli, N., Moretti, S., 2013. SAR interferometry for landslides risk assessment at local scale: the case study of Castagnola (Northern Apennines, Italy). In Margottini, C., et al. (Eds.), Landslide Science and Practice, vol. 2: Early Warning, Instrumentation and Monitoring. Springer, Berlin, pp. 407 – 414

Antronico, L., Borrelli, L., Peduto, D., Fornaro, G., Gullà, G., Paglia, L., Zeni, G., 2013. Conventional and innovative techniques for the monitoring of displacements in landslide affected area. In Margottini, C., et al. (Eds.), Landslide Science and Practice, vol. 2: Early Warning, Instrumentation and Monitoring. Springer, Berlin, pp 125 – 131

Antronico, L., Borrelli, L., Coscarelli, R., Gullà, G., 2015. Time evolution of landslide damages to buildings: the case study of Lungro (Calabria, Southern Italy). Bulletin Engineering Geology and Environment, vol. 74, pp.47 – 59

Alcaraz-Segura, D., Cabello, J., Paruelo, J., 2009. Baseline characterization of major Iberian vegetation types based on the NDVI dynamics. Plant Ecology, vol. 202, pp.13 – 29

Aldrich, J., Nelson, F., 1984. Linear probability, logit, and probit models. SAGE Publications, United States of America

Arabameri, A., Saha, S., Roy, J., Chen, W., Blaschke, T., Bui, D.T.,2019. Landslide Susceptibility Evaluation and Management Using Different Machine Learning Methods in The Gallicash River Watershed, Iran. Remote Sensing, vol.12 (475), pp.1-29.

ARC-ISCW. 2014. Agricultural Research Council – Institute for Soil, Climate and Water, South Africa

Arnone, E., Francipane, A., Noto, L.V., Scarbaci, A., La Loggia, G., 2014. Strategies investigation in using artificial neural network for landslide susceptibility mapping: Application to a Sicilian catchment. Journal of Hydroinformation, vol. 16, pp. 502 – 515

Asaro, R.J., Rice, J.R., 1977. Strain localization in ductile single crystals. Journal of Mechanics and Physics of Solids, vol. 25, pp. 309 – 338

Aubry, R., Idelsohn, S.R., Onate, E., 2005. Particle finite element method in fluid mechanics including thermal convection-diffusion. Computer and Structures, vol. 83, pp.1459 – 1475

Azimi, A., Osanloo, Y.M., Aakbarpour-Shirazi, M., Aghajani, B.A., 2010. Prediction of the blastability designation of rock masses using fuzzy sets. International Journal of Rock Mechanics Mining Science, vol. 47, no. 7, pp 1126 – 1140

Baba, K., Bahi, L., Ouadif, L., Akhssas, A., 2012. Slope stability evaluations by limit equilibrium and finite element methods applied to a railway in the Moroccan Rif. Open Journal of Civil Engineering, vol. 2, pp. 27 – 32

Babuska, I., 1971. Error-bounds for finite element method. Numerische Mathematik, vol. 16, no. 4, pp. 322 – 333

Baiges, J., Codina R., 2010. The fixed-mesh ALE approach applied to solid mechanics and fluid-structure interaction problems. International Journal of Numerical Methods and Energy, vol. 81, pp.1529 – 1557

Baillifard, F., Jaboyedoff, M., Sartori, M., 2003. Rockfall hazard mapping along a mountainous road in Switzerland using a GIS-based parameter rating approach. Natural Hazards Earth System Science, vol. 3, pp. 435 – 442

Bathe, K.J., 2001. The inf–sup condition and its evaluation for mixed finite element methods. Computers and Structures, vol. 79, no. 2, pp. 243 – 252

Barla, G., Antolini, F., Barla, M., Mensi, E., Piovano, G., 2010. Monitoring of the Beauregard landslide (Aosta Valley, Italy) using advanced and conventional techniques. Engineering Geology, vol. 116, pp. 218 – 235

Barker, O.B., 1979. A contribution to the geology of the Soutpansberg Group, Waterberg Supergroup, Northern Transvaal. PhD thesis, University of the Witwatersrand, Johannesburg

Barker, O.B, Brandl, G, Callaghan, C.C, Erikson, P.G, van der Neut, M., 2006. The Soutpansberg and Waterburg Groups and the Blouberg formation. In: Anhaeusser, M.R., Thomas, C.R., Johnson, R.J. (Eds.), The Geology of South Africa,. Council for Geosciences, Geological Society of South Africa, Pretoria, pp. 301 – 324

Bazilevs, Y., Hsu, M.C., Zhang, Y., Wang, W., Liang, X., Kvamsdal, T., Brekken, R., Isaksen, J., 2010. A fully coupled fluid-structure interaction simulation of cerebral aneurysms. Computational Mechanics, vol. 46, pp. 3 – 16

Bennett, M.R., Doyle, P., 1997. Environmental geology: Geology and the human environment. John Wiley & Sons, Chisester, U.K.

Bieniawski, Z.T., 1976. Rock mass classification in rock engineering. In: Proceeding of the Symposium on Exploration for Rock Engineering, vol. 1, Bieniawski, Z.T. (Eds.), Johannesburg, South Africa, 1 – 5 November, pp. 97 – 106

Biondi, E., Casavecchia, S., Pesaresi, S., 2011. Phytosociological synrelevés and plant landscape mapping: From theory to practice. Plant Biosystem, vol. 145, pp. 261 – 273

Bishop, A.W., 1955. The use of slip circles in stability analysis of slopes. Geotechnique, vol. 5, no. 1, pp. 7 – 17

Bochev, P.B., Dohrmann, C.R., Gunzburger, M.D., 2006. Stabilization of low-order mixed finite elements for the Stokes equations. SIAM Journal of Numerical Analysis, vol. 44, no. 1, pp. 82 – 101

Böhner, J., Antonic, O., 2009. Land-surface parameters specific to topo-climatology. In: Hengl, T., Reuter, H.I. (Eds.), Developments in Soil Science, Chap. 8, Elsevier, Amsterdam, The Netherlands, pp. 195 – 226

Borrelli, L., Antronico, L., Gullà, G., Sorriso-Valvo, G.M., 2014.Geology, geomorphology and dynamics of the 15 February 2010 Maierato landslide (Calabria, Italy). Geomorphology, vol. 208, pp. 50 – 73

Bovenga, F., Nitti, D.O.,Fornaro, G., Radicioni, F., Stoppini, A., Brigante, R., 2013. Using C/X-band SAR interferometry and GNSS measurements for the Assisi landslide analysis. International Journal of Remote Sensing, vol. 34, pp. 4083 – 4104

Blakemore, L.C.; Swindale, L. D. 1958: The Chemistry and Clay Mineralogy of a Soil Sample from Antarctica. Nature (Land.) 182: 47-8.

Brandl, G., 1981. The geology of the Messina area, Explain, Sheet 2230 (Messina). Geology Survey of South Africa, Report number, 35

Brandl, G., 1986. The geology of Pieterburg area, Explain, Sheet 2230 (Pietersburg). Geology Survey of South Africa, Report number, 43

Brezzi, F., 1974. On the existence, uniqueness and approximation of saddle-point problems arising from Lagrangian multipliers. Revue francaise d'Automatique, Informatique, Recherche Operationnelle. Analyse Numérique, vol. 8, no. 2, pp. 129 – 151

Brunetti, M.T., Peruccacci, S., Rossi, M., Luciano, S., Valigi, D., Guzzetti, F., 2010. Rainfall thresholds for the possible occurrence of landslides in Italy. Natural Hazards Earth System Science, vol. 10, pp. 447 – 458

Budetta, P., 2004. Assessment of rockfall risk along roads. Natural Hazards Earth System Science, vol. 4, pp. 71 – 81

Budetta, P.,Nappi, M., 2015. Comparison between qualitative and quantitative rockfall risk methods for a hazardous road stretch. Advances in Environmental and Agricultural Science, pp. 13 – 17

Caine, N., 1980. The rainfall intensity-duration control of shallow landslides and debris flows. Geography Annual 62A:23–27

Cannon, S.H., Gartner, J.E., Wilson, R.C., Bowers, J.C., Laber, J.L., 2008. Storm rainfall conditions for floods and debris flows from recently areas in Southwestern Colorado and southern California. Geomorphology, vol. 96, pp. 250 – 269

Carbonell, J.M., Oñate, E., Suárez, B., 2010. Modeling of ground excavation with the particle finite-element method. ASCE Journal of Engineering Mechanics, vol. 136, no. 4, pp. 455 – 463

Carbonell, J.M., Oñate, E., Suárez, B., 2013. Modelling of tunnelling processes and rock cutting tool wear with the particle finite element method. Computer Mechanics Journal, vol. 52, no. 3, pp. 607 – 629

Carter, A., Ramsey, M., 2010. Long-term volcanic activity at Shiveluch volcano: Nine years of ASTER spaceborne thermal infrared observations. Remote Sensing, vol. 2, pp. 2571 – 2583

Carter, M., Bentley, S.P., 1985. The geometry of slip surfaces beneath landslides: predictions from surface measurements. Canadian Geotechnical Journal, vol. 22, pp. 234 – 238

Carter, B.J., Lajtai, E.Z., 1992. Rock slope stability and distributed joint systems. Canadian Geotechnical Journal, vol. 29, pp. 53 – 60

Cevasco, A., Sacchini, A., Robbiano, A., Vincenzi, E., 2010. Evaluation of rainfall thresholds for triggering shallow landslides on the Genoa municipality area (Italy): the case study of the Bisagno Valley. Italian Journal Engineering Geology and Environment, vol. 1, pp. 35 – 50

Chau, K.T., Wong, R.C.H., Liu, J., Lee, C.F., 2003. Rockfall hazard analysis for Hong Kong based on rockfall inventory. Rock Mechanic Rock Engineering, vol. 36, pp. 383 – 408

Chen, W., Li, X., Wang, Y., Liu, S., 2013. Landslide susceptibility mapping using LiDAR and DMC data: a case study in the Three Gorges area, China. Environment Earth Science, vol. 70, pp. 673 – 685

Chen, W., Pourghasemi, H.R., Naghibi, S.A., 2018.Prioritization of landslide conditioning factors and its spatial modeling in Shangnan County, China using GIS-based data mining algorithms. Bulletin Engineering Geology Environment, vol. 77, pp. 611 – 615

Cheng, J.H., Kikuchi, N., 1986. A mesh rezoning technique for finite element simulations of metal forming processes. International Journal for Numerical Methods in Engineering, vol. 23, pp. 219 – 228

Chowdhury, R. N., Xu, D.W., 1992. Reliability index for slope stability assessment – two methods compared. Reliabilty Engineering and System Safety, vol. 37, pp. 99 – 108

Chowdhury, R.N., Tang, W.H., Sidi, I., 1988. Reliability model of progressive failure. Geotechnique, vol. 37, no. 4, pp. 467 – 481

Coggan, J.S., Stead, D., Eyre, J.M., 1998. Evaluation of techniques for quarry slope stability assessment. Transactions of the Institution of Mining and Metallurgy, Section B, vol. 107, pp. B139 – B147

Collin, J.C, Loehr, J.E., Hung, C.J., 2008. References slope maintenance and slide restoration. Federal Highway Administration, National Highway Institute, pp. 58 – 122

Conte, E., Donato, A., Troncone, A., 2014. A finite element approach for the analysis of active slow-moving landslides. Landslide, vol. 11, pp. 723 – 731

Corominas, J., Mavrouli, O., Ruiz-Carulla, R., 2017. Rockfall occurrence and fragmentation. In: Sassa K. et al. (Eds.), Advancing Culture of Living with Landslides, DOI 10.1007/978-3-319-59469-9_4

Corominas, J., van Westen, C., Frattini, P., Cascini, L., Malet, J.P., Fotopoulou, S., Catani F., Van Den Eeckhaut, M., Mavrouli, O., Agliardi, F., Pitilakis, K., Winter, M.G., Pastor, M., Ferlisi, S., Tofani, V., Hervás, J., Smith, J.T., 2014. Recommendations for the quantitative analysis of landslide risk. Bulletin Engineering Geology Environment, vol. 73, pp. 209 – 226

Corominas, J., Mavrouli, O., 2011. Rockfall quantitative risk assessment. In Lambert, S., Nicot, F. (Eds.), Rockfall Engineering, ISTE Ltd. & Wiley, pp. 255 – 301

Corominas, J., Moya, J., 2008. A review of assessing landslide frequency for hazard zoning purposes. Engineering Geology, vol. 102, pp. 193 – 213

Corominas, J., Copons, R., Moya, J., Vilaplana, J.M., Altimir, J., Amigó, J., 2005. Quantitative assessment of the residual risk in a rock fall protected area. Landslides, vol. 2, pp. 343 – 357

Corps of Engineers, 1970. Slope Stability manual, EM 1110-21902. Department of the Army, Office of the Chief Engineers, Washington, DC

Cremonesi, M., Frangi, A., Perego, U., 2010. A Lagrangian finite element approach for the analysis of fluid-structure interaction problems. International Journal for Numerical Methods in Engineering, vol. 84, pp. 610 – 630

Crosta, G.B., Agliardi, F., 2003. A methodology for physically based rockfall hazard assessment. Natural Hazards Earth System Science, vol. 3, pp. 407 – 422

Crowley, J., Hubbard, B., Mars, J., 2003. Analysis of potential debris flow source areas on Mountain Shasta, California, by using airborne and satellite remote sensing data. Remote Sensing of Environment, vol.87, pp.345–358

Cruden, D.M., Varnes, D.J., 1996. Landslide types and processes. In Turner A.K., Schuster R.L. (Eds.), Landslides investigation and mitigation, National Research Council, Transportation Research Board, Special Report, vol. 247, pp. 36 – 75

Dai, X., Hadjipantelis, P.Z., Han, K., Ji, H., 2020. fdapace: Functional Data Analysis and Empirical Dynamics, R Package version 0.4.0. Available online: https://cran.r-project.org/package=fdapace (accessed on 8 April 2020)

Dai, T., Xie, D., Yao, H., Li, G., 2011. Establishment of grey system model about tunnel surrounding rock convergence and information renewal GM(1,1) model forecasting. Proceedings of the International Conference on Remote Sensing, Environment and Transportation Engineering (RSETE 2011). Springer, Berlin, pp. 310 – 314

Das, B.M., 2010. Principles of geotechnical engineering, 7th Edition.United State of America

De Borst, R., Vermeer, P.A., 1984. Possibilities and limitations of finite elements for limit analysis. Geotechnique, vol. 34, pp. 199 – 210

Deb, D., Choi, S.O., 2006. Analysis of sinkhole occurrences over abandoned mines using fuzzy reasoning: a case study. Geotechnical and Geological Engineering, vol. 24, no. 5, pp. 1243 – 1253

Dehnavi, A., Aghdam, I.N., Pradhan, B., Morshed, V.M.H., 2015. A new hybrid model using step-wise weight assessment ratio analysis (SWARA) technique and adaptive

neuro-fuzzy inference system (ANFIS) for regional landslide hazard assessment in Iran. Catena, vol. 135, pp. 122 – 148

Diko, M.L., Banyini, S.C., Monareng, B.F., 2014. Landslide susceptibility on selected slopes in Dzanani, Limpopo Province, South Africa. Journal of Disaster Risk Studies, vol. 6, no. 1, pp. 1 – 7

Dodagoudar, G.R., Venkatachalam, G., 2000. Reliability analysis of slopes using fuzzy sets theory. Computers and Geotechnics, vol. 27, no. 3, pp. 101 – 115

Dohrmann, C.R., Bochev, P.B., 2004. A stabilized finite element method for the Stokes problem based on polynomial pressure projections. International Journal of Numerical Methods Fluids, vol. 46, no. 2, pp. 183 – 201

Dou, J., Yunus, A.P., Bui, D.T., Sahana, M., Chen, C.W., Zhu, Z., Wang, W., Pham, B.T., 2019. Evaluating GIS-based multiple statistical models and data mining for earthquake and rainfall-induced landslide susceptibility using the LiDAR DEM, Remote Sensing, vol. 11, pp. 1 – 30

Dow, J.O., 2015. A concise overview of the finite element method. Momentum Press Engineering, New York

Dubois, D., Prade, H., 2010. Gradualness, uncertainty and bipolarity: making sense of fuzzy sets, fuzzy sets and systems. Fuzzy Sets and Systems, doi: 10.1016/j.fss.2010.11.007

Dubeau, P., King, D.J., Unbushe, D.G., Rebelo, L.M., 2017. Mapping the Dabus Wetlands, Ethiopia, using random forest classification of Landsat, PALSAR and topographic data. Remote Sensing, vol. 9, pp. 1056 – 1058

Duncan, J.M., Wright, S.G., 2005. Soil strength and slope stability. John Wiley & Sons, Inc., Hoboken

Duncan, J.M., 1996. State of the art: limit equilibrium and finite-element analysis of slopes. Journal of Geotechnical Engineering (ASCE), vol. 122, pp. 577 – 596

Dussauge-Peisser, A., Helmstetter, A., Grasso, J.R., Hanz, D., Desvarreux, P., Jeannin, M., Giraud, A., 2002. Probabilistic approach to rockfall hazard assessment: potential of historical data analysis. Natural Hazards Earth System Science, vol. 2, pp. 15 – 26

Eberhardt, E., Stead, D., Coggan, J.S., 2004. Numerical analysis of initiation and progressive failure in natural rock slopes – the 1991 Randa rockslide. International Journal of Rock Mechanics Mining Science, vol. 41, pp. 69 – 87

Eberhardt, E., 2003. Rock slope stability analysis – Utilization of advanced numerical techniques. Research report, University British Columbia, Vancouver, Canada, pp. 4 – 38

Edelsbrunner, H., Mucke, E.P., 1994. Three dimensional alpha shapes. ACM Transactions on Graphics, vol. 13, pp. 43 – 72

Einstein, H.H. 1996. Risk and risk analysis in rock engineering. Tunnelling and Underground Space Technology, vol. 11, no. 2, pp. 141 – 155

Ellison, R.D., 1978. Underground mine hazard analysis technique. Proceedings of the First Internaltional of the Symposium on Stability in Coal Mining, pp. 299 – 318, Vancouver

Ellenberger, J.L., 1981. Hazard prediction model development: the multiple overlay technique. SME-AIME Annual Meeting, Preprint no. 81 – 16, Chicago

Fawaz, A., Farah, E., Hagechehade, F., 2014. Slope stability analysis using numerical modelling. American Journal of Civil Engineering, vol. 2, pp. 60 – 67

Fell, R., Ho, K.K.S., Lacasse, S., Leroi, E., 2005. A framework for landslide risk assessment and management. In Hungr, O., Fell, R., Couture, R., Eberthardt, E. (Eds.), Landslide risk management, Taylor and Francis, London, pp. 3 – 25

Feret, J.B., Corbane, C., Alleaume, S., 2015. Detecting the phenology and discriminating mediterranean natural habitats with multispectral sensors – An analysis based on multiseasonal field spectra. IEEE Journal of Selected Topics in Applied Earth Observations and Remote Sensing, vol. 8, pp. 2294 – 2305

Frattini, P., Crosta, G., Carrara, A., Agliardi, F., 2008. Assessment of rockfall susceptibility by integrating statistical and physically based approaches. Geomorphology, vol. 94, pp. 419 – 437

Ferrari, F., Giacomini, A., Thoeni, K., Lambert, C., 2017. Qualitative evolving rockfall hazard assessment for highwalls. International Journal Rock Mechanics Mining Science, vol. 98, pp. 88 – 101

Gadala, M.S., Oravas, G.A.E., Dokainish, M.A., 1983. A consistent Eulerian formulation of large deformation problems in statics and dynamics. International Journal of Non-linear Mechanics, vol. 18, pp. 21 – 35

Gariano, S.L., Guzzetti, F., 2016. Landslides in a changing climate. Earth-Science Reviews, vol. 162, pp. 227 – 252

Ghosh, K., Bandyopadhyay, S., De, S.K., 2017. A comparative evaluation of weight-rating and analytical hierarchical (AHP) for landslide susceptibility mapping in Dhalai District, Tripura. In Hazra, S., Mukhopadhyay, A., Ghosh, A., Mitra, D. and Dadhwal, V. (Eds.), Environment and Earth Observation, Remote Sensing/Photogrammetry, Springer, pp. 175 – 193

Gökceoğlu, C., 2002. A fuzzy triangular chart to predict the uniaxial compressive strength of the Ankara agglomerates from their petrographic composition. Engineering Geology, vol. 66, no. 2, pp. 39 – 51

Gokceoglu, C., Sonmez, H., Ercanoglu, M., 2000. Discontinuity controlled probabilistic slope failure risk maps of the Altindag (settlement) region in Turkey. Engineering Geology, vol. 55, pp. 277 – 296

Gökceoğlu, C., Zorlu, K., 2004. A fuzzy model to predict the uniaxial compressive strength and the modulus of elasticity of a problematic rock. Engineering Applications of Artificial Intelligence, vol. 17, no. 1, pp. 61 – 72

Goktepe, A.B., Lav, A., Altun, S., Altintas, G., 2008. Fuzzy decision support system to determine swell/shrink factor affecting earthwork optimization of highways. Mathematical and Computational Applications, vol. 13, no. 1, pp. 61 – 70

Göktepe, I., Keskin, F., 2018. A comparison study between traditional and finite element methods for slope stability evaluations. Journal Geological Society of India, vol. 91, pp. 373 – 379

Grana, V., Tommasi, P., 2014. A deep-seated slow movement controlled by structural setting in marly formations of Central Italy. Landslides, vol.11, pp.195 – 212

Grignetti, A., Salvatori, R., Casacchia, R., Manes, F., 1997. Mediterranean vegetation analysis by multi-temporal satellite sensor data. Internatioanl Journal of Remote Sensing, vol. 18, pp.1307 – 1318

Gullà, G., 2014. Field monitoring in sample sites: hydrological response of slopes with reference to widespread landslide events. Procedia Earth and Planetary Science, vol. 9, pp. 44 – 53

Gullà, G., Niceforo, D., Bonci, L., Calcaterra, S., Cesi, C., Gambino, P., 2004. Surface movements of a landslide involving weathered and degraded rocks. Proceedings of the 15th Southeast Asian Geotechnical Conference, November 22 – 26, 2004 (15th SEAGC), Bangkok, Thailand, vol. 1, pp. 375 – 378

Gupta, S.K., Shukla, D.P., Thakur, M., 2018. Selection of weightages for causative factors used in preparation of landslide susceptibility zonation (LSZ). Geomatics, Natural Hazards and Risk, vol. 9, no. 1, pp. 471 – 487

Guthrie, R.H., Evans, S.G., 2004. Analaysis of landslide frequencies and characteristics in a natural system, coastal British Columbia. Earth Surface Processes and Landforms, vol. 29, pp. 1321 – 1339

Guzzetti, F., Mondini, A.C., Cardinali, M., Fiorucci, F., Santangelo, M., Chang, K.T., 2012. Landslide inventory maps: new tools for an old problem. Earth Science Reviews, vol. 112, pp. 42 – 66

Guzzetti, F., 2006. Landslide fatalities and the evaluation of landslide risk in Italy. Engineering Geology, vol. 58, pp. 89 – 107

Guzzetti, F., Stark, C.P, Salvati P., 2005. Evaluation of flood and landslide risk to the opulation in Italy. Environmental Management, vol. 36, no. 1, pp. 15 – 36

Guzzetti, F., Reichenbach, P., Wieczorek, G.F., 2003. Rockfall hazard and risk assessment in the Yosemite Valley, California, USA. Natural Hazards Earth System Science, vol. 3, pp. 491 – 503

Guzzetti, F, Malamud, B.D, Turcotte, D.L, Reichenbach, P., 2002. Power-law correlations of landslide areas in Central Italy. Earth and Planetary Science Letters, vol. 195, pp. 169 – 170

Guzzetti, F., Carrara, A., Cardinali, M., Reichenbach, P., 1999. Landslide hazard evaluation: a review of current techniques and their application in a multi-scale study, Central Italy. Geomorphology, vol. 31, pp. 181 – 216

Haque, U., Blum, P., da Silva, P.F., Andersen, P., Pilz, J., Chalov, S.R., Malet, J.P., Auflic, M.J., Andres, N., Poyiadji, E., Lamas, P.C., Zhang, W., Peshevski, I., Pétursson, H.G., Kurt, T., Dobrev, N., Garcia-Davalillo, J.C., Halkia, M., Ferri, S., Gaprindashvili, G., Engström, J., Keellings, D., 2016. Fatal landslides in Europe. Landslides 1–10. doi:10.1007/s10346-016-0689-3

Heim, A., 1932. Bergsturz und Menschenleben. Fretz and Wasmuth Verlag, Zurich

Hill, R., 1966. Generalized constitutive relations for incremental deformation of metal crystals by multislip. Journal of Mechanics and Physics of Solids, vol. 14, pp. 95 – 102

Hill, R., Rice, J.R., 1972. Constitutive analysis of elastic-plastic crystals at arbitrary strain. Journal of Mechanics and Physics of Solids, vol. 20, pp. 401 – 413

Hoek, E., 1991. When is design in rock engineering acceptable? In Wittke (Eds.), Proceedings of the 7th International Congress on Rock Mechanics, Aachen, A.A. Balkema, Rotterdam, pp. 1485 – 1497

Hoek, E., Bray, J.W., 1991. Rock Slope Engineering. Elsevier Science Publishing, New York

Hoek, E., Bray, J.W., 1981. Rock Slope Engineering, 3rd Edition. Institution of Mining and Metallurgy, London

Hong, H., Liu, J., Bui, D.T., Pradhan, B., Acharya, T.D., Pham, B.T., Zhu, A.X., Chen, W., Ahmad, B.B., 2018. Landslide susceptibility mapping using J48 Decision Tree with AdaBoost, Bagging and Rotation Forest ensembles in the Guangchang area (China). Catena, vol. 163, pp. 399 – 413

Hong, H., Chen, W., Xu, C., Youssef, A.M., Pradhan, B., Tien Bui, D., 2017. Rainfall induced landslide susceptibility assessment at the Chongren area (China) using frequency ratio, certainty factor, and index of entropy. Geocarto International, vol. 32, pp. 139 – 154.

Hong, Y., Adler, R., Huffman, G., 2007. Use of satellite remote sensing data in the mapping of global landslide susceptibility. Natural Hazards, vol. 43, pp. 245 – 256

Hu, Y., Randolph, M.F., 1998. A practical numerical approach for large deformation problems in soil. International Journal for Numerical and Analytical Methods in Geomechanics, vol. 22, pp. 327 – 350

Hudson, J.A., Harrison, J.P., 1997. Engineering rock mechanics: an introduction to the principles. Elsevier Science, Oxford

Hungr, O., 2016. A review of landslide hazard and risk methodology. In Aversa, S., Cascini, L., Picarelli, L., Scavia, C. (Eds.), Landslides and engineered slopes: experience, theory and practice, CRC press, vol. 1, pp. 3 – 27

Hungr, O, Leroueil, S., Picarelli, L., 2014. The Varnes classification of landslides types, an update. Landslides, vol. 11, pp. 167 – 194

Hungr, O., McDougall, S., Wise, M., Cullen, M., 2008. Magnitude-frequency relationships of debris flows and debris avalanches in relation to slope relief. Geomorphology, vol. 96, pp. 355 – 365

Hungr, O., Corominas, J., Eberhardt, E., 2005. Estimating landslide motion mechanisms, travel distance and velocity. In Hungr, O., Fell, R., Couture, R., Eberthardt, E. (Eds.), Landslide risk management, Taylor and Francis, London, pp. 99 – 128

Hungr, O., Evans, S.G., Hazzard, J., 1999. Magnitude and frequency of rock falls and rock slides along the main transportation corridors of southwestern British Columbia. Canadian Geotechnical Journal, vol. 36, pp. 224 – 238

Idelsohn, S.R., Onate, E., Calvo, N., Pin, F., 2003a. The meshless finite element method. International Journal of Numerical Methods Engineering, vol. 58, pp. 893 – 912

Idelsohn, S., Onate, E., Del Pin, F.D., 2003b. A Lagrangian meshless finite element method applied to fluid structure interaction problems. Computer and Structures, vol. 81, pp. 655 – 671

Idelsohn, S.R., Onate, E., Pin, F.D., 2004. The particle finite element method: a powerful tool to solve incompressible flows with free surfaces and breaking waves. International Journal for Numerical Methods in Engineering, vol. 61, 964 – 989

International Society for Rock Mechanics (ISRM), 1978. Suggested methods for the quantitative description of discontinuities in rock masses. International Journal of Rock Mechanic Mining Science, vol. 15, pp. 319 – 368

International Society for Rock Mechanics (ISRM), 2007. The complete ISRM suggested methods for rock characterization, testing and monitoring: 1974–2006. In Ulusay, R., Hudson, J.A. (Eds.), Suggested Methods Prepared by the Commission on Testing Methods, Compilation arranged by the ISRM Turkish National Group, International Society for Rock Mechanics, Ankara, Turkey

Ishii, Y., Ota, K., Kuraoka, S., Tsunaki, R., 2012. Evaluation of slope stability by finite element method using observed displacement of landslide. Landslides, vol. 9, pp. 335 – 348

Iverson, R.M., 2000. Landslide triggering by rain infiltration. Water Resources Research, vol. 36, pp. 1897 – 1910

Jaboyedoff, M., Labiouse, V., 2003. Preliminary assessment of rockfall hazard based on GIS data. Proceedings of the 10th International Congress on Rock Mechanics ISRM 2003 – Technology roadmap for rock mechanics, South African Institute of Mining and Metallurgy, Johannesburg, South Africa, 8 – 12 September 2003, pp. 575 – 778

Jaboyedoff, M., Derron, M.H., 2005. Integrated risk assessment process for landslides. In Hungr, O., Fell, R., Couture, R., Eberhardt, E. (Eds.), Landslide risk management,Taylor and Francis

Jaboyedoff, M., Baillifard, F.J., Marro, C., Philippossian, F., Rouiller, J.D., 1999. Detection of rock instabilities: Matterock Methodology. Joint Japan-Swiss Scientific on Impact Load by Rock Falls and Design of Protection Structures, Kanazawa, Japan, 4 – 7 October 1999, pp. 37 – 43

Janbu, N., 1954. Stability analysis of slopes with dimensionless parameters. Doctor of Science Thesis, Harvard University

Janbu, N., 1973. Slope stability computations. Embankment- Dam Engineering Casagrande, Volume, John Wiley & Sons, Inc., New York, pp. 47 – 86

Jensen, J.R., 2005. Introductory Digital Image Processing: A Remote Sensing Perspective. New Jersey: Pearson Education.

Kang, Y., Wang, J., 2010. A support-vector-machine-based method for predicting large-deformation in rock mass. Proceedings of the 7th International Conference on Fuzzy Systems and Knowledge Discovery, FSKD 2010, IEEE Computer Society, Yantai, Shandong, China, pp. 1176 – 1180

Kayadelen, C., Taşkiran, T., Günaydın, O., Fener M., 2009. Adaptive neuro-fuzzy modeling for the swelling potential of compacted soils. Environmental Earth Science, vol. 59, no. 1, pp. 109 – 115

Kelly, W. C.; Zumberge,J. H. 1961: Weathering of a Quartz Diorite at Marble Point, McMurdo Sound, Antarctica. J. Geol. 69: 433-46.

Khoa, H.D.V., Jostad, H.P., 2010. Finite element modeling of the Las Colinas landslide under earthquake shaking. Proceedings of the International Conferences on Recent Advances in Geotechnical Earthquake Engineering and Soil Dynamics, Symposium in honor of Professor I.M. Idriss, San Diego, California, paper no. 4

Kirschbaum, D.B., Adler, R., Hong, Y., Lerner-Lam, A., 2009. Evaluation of a preliminary satellite-based landslide hazard algorithm using global landslide inventories. Natural Hazards Earth System. Science, vol. 9, pp. 673 – 686

Kirschbaum, D.B., Adler, R., Hong, Y., Hill, S., Lerner-Lam, A., 2010. A global landslide catalog for hazard applications: method, results, and limitations. Natural Hazards, vol. 52, pp. 561 – 575

Kirschbaum, D., Stanley, T., Zhou, Y., 2015. Spatial and temporal analysis of a global landslide catalog. Geomorphology, vol. 249, pp. 4 – 15

Kjekstad, O., Highland, L., 2009. Economic and social impacts of landslides. In Landslides-Disaster Risk Reduction, Springer, Berlin, Heidelberg, pp. 573 – 587

Kleinbaum, D., Klein, M., 2010. Survival analysis: a self-learning text, 3rd Edition. Springer, New York Dordrecht Heidelberg London

Krahn, J., 2004. Stability modelling with SLOPE/W. An engineering methodology. GeoSlope International

Kratochvil, J., 1973. On a finite strain theory of elastic-inelastic materials. Acta Mechanica, vol. 16, pp. 127 – 142

Kroner, E., Teodosiu, C., 1972. Lattice defect approach to plasticity and viscoplasticity. In Sawczuk, A. (Eds.), Problems of plasticity, Noordhoff

Lang, H., Welch, R., 1999. Algorithm theoretical basis document for ASTER digital elevation models, version 3.0. Jet Propulsion Laboratory, Pasadena, CA

Lateltin, O., Haemmig, C., Raetzo, H., Bonnard, C., 2005. Landslide risk management in Switzerland. Landslides, vol. 2, pp. 313 – 320

Larese, R., Rossi, E., Oñate, S.R., Idelsohn, S., 2008. Validation of the Particle Finite Element Method (PFEM) for simulation of free surface flows. Engineering Computations, vol. 25, pp. 385 – 425

Laribi, A., Walstra, J., Ougrine, M., Seridi, A., Dechemi, N., 2015. Use of digital photogrammetry for the study of unstable slopes in urban areas: case study of the El Biar landslide, Algiers. Engineering Geology, vol. 187, pp. 73 – 83

Lazzari, M., Geraldi, E., Lapenna, V., Loperte, A., 2006. Natural hazards vs human impact: An integrated methodological approaching eomorphological risk assessing on Tursi historical site, southern Italy. Landslides, vol. 3, pp. 275 – 287

Lazzari, M., 2009. The Bosco Piccolo snow-melt triggered-landslide (southern Italy): A natural laboratory to apply integrated techniques to mapping, monitoring and damage assessment. Proceedings of the Conference on Landslide Processes: From Geomorphologic Mapping to Dynamic Modelling, Strasbourg, France, 6 – 7 February 2009; pp. 163 – 168

Lazzari, M., Piccarreta, M., Capolongo, D., 2011. Landslide triggering and local rainfall thresholds in bradanic foredeep, Basilicata region (Southern Italy). In Margottini, C., Canuti, P., Sassa, K. (Eds.), Landslide Science and Practice, vol. 2: Early warning, instrumentation and modeling, Springer: Heidelberg, Germany, pp. 671 – 678

Lazzari, M., Gioia, D., 2015. Regional-scale landslide inventory, central-western sector of the Basilicata region (Southern Apennines, Italy). Journal of Maps, vol. 12, pp. 852 – 859

Lazzari, M., Gioia, D., Anzidei, B., 2018. Landslide inventory of the Basilicata region (Southern Italy). Journal of Maps, vol. 14, pp. 348 – 356

Lee, E.H., Liu, D.T., 1967. Finite strain elastic-plastic theory particularly for plane wave analysis. Journal of Applied Physics, vol. 38, pp. 19 – 27

Lee, R.L., Gresho, P.M., Sani, R.L., 1979. Smoothing techniques for certain primitive variable solutions of the Navier-Stokes equations. International Journal for Numerical Methods in Engineering, vol. 14, pp. 1785 – 1804

Lee, J., Akutagawa, S., 2009. Quick prediction of tunnel displacements using artificial neural network and field measurement results. International Journal of the JCRM, vol. 5, no. 2, pp. 53 – 62

Lee, E.M, Jones, D.K.C., 2004. Landslide risk assessment. Thomas Telford, London

Lee, S., Choi, J., Min, K., 2002. Landslide susceptibility analysis and verification using the Bayesian probability model. Environmental Geology. vol. 43, pp. 120 – 131

Li, X., He, S., Luo, Y., Wu, Y., 2012. Simulation of the sliding process of Donghekou landslide triggered by the Wenchuan earthquake using a distinct element method. Environmental Earth Sciences, vol. 65, pp. 1049 – 1054

Li, Y., Li, X., Zhang, C., 2006. Displacement prediction method of surrounding rock in tunnel based on BP neural network. Chinese Journal of Rock Mechanics and Engineering, vol. 25, no. 1, pp. 969 – 973

Liang, R.Y., 2006. Landslide hazard rating matrix and database. A Draft Preliminary Interim Report to Ohio Department of Transportation Office of Research and Development, vol. 1, pp. 100 – 122

Locat, A., 2017. The Saint-Jude landslide of 10 May 2010, Quebec, Canada: investigation and characterization of the landslide and its failure mechanism. Canadian Geotechnical Journal, vol. 54, no. 10, pp. 1357 – 1374

Locat, J., Leroueil, S., Picarelli, L., 2000. Some considerations on the role of geological history on slope stability and estimation of minimum apparent cohesion of a rock mass. In Bromhead, E., Dixon, N., Ibsen, M.L. (Eds.), Landslides in research, theory and practice, the 8th International Symposium on Landslides in Cardiff, Wales, 26 – 30 June, pp. 935 – 942

Lohner, R., 2008. Applied Computational Fluid Dynamics Techniques. John Wiley, United South Africa

Lowe, J., Karafiath, R.V., 1960. Stability of earth dam upon drawdown. Proceedings of the First Pan American Conference on Soil Mechanics and Foundation Engineering, Mexico City, pp. 537 – 542

Lubliner, J., 1984. A maximum-dissipation principle in generalized plasticity. Acta Mechanica, vol. 52, pp. 225 – 237

Lubliner, J., 1986. Normality rules in large-deformation plasticity. Mechanics of Materials, vol. 5, pp. 29 – 34

Liu, J.G., Masona, P.J., Clericia, N., Chena, S., Davisa, A., Miaob, F., Dengb, H.,Liangb, L., 2004. Landslide hazard assessment in the Three Gorges area of the Yangtze river using ASTER imagery: Zigui–Badong. Geomorphology, vol. 61,pp.171–187.

Luino, F., 2008. Definizione delle soglie pluviometriche d'innesco di frane superficiali e colate torrentizie: accorpamento per aree omogenee. Istituto Regionale di Ricerca della Lombardia. Rapporto finale, Milano

Maerz, N.H., Youssef, A., Fennessey, F., 2005. New risk-consequence rockfall hazard rating system for Missouri highways using digital image analysis. Environmental and Engineering Geoscience, Vol. XI, No. 3, pp. 229 – 249

Maiorano, S.C, Borrelli, L, Moraci, N, Gullà, G., 2015. Numerical modelling to calibrate the geotechnical model of a deep-seated landslide in weathered crystalline rocks: Acri (Calabria, Italy). Lollino, G., et al. (Eds.), Engineering Geology for Society and Territory, vol. 2, pp. 1271 – 1274

Maji, V.B., 2017. An insight into slope stability using strength reduction technique. Journal of the Geology Society of India, vol. 89, pp. 77 – 81

Manconi, A., Casu, F.; Ardizzone, F., Bonano, M., Cardinali, M., De Luca, C., Gueguen, E.; Marchesini, I., Parise, M., Vennari, C., 2014. Rapid mapping of event landslides: The 3 December 2013 Montescaglioso landslide (Italy). Natural. Hazards Earth System Science, vol. 2, pp. 1465 – 1479

Mandel, J., 1964. Contribution théorique à l'étude de l'écrouissage et des lois de l'écoulement plastique. Proceedings of the 11th International Congress on Applied Mechanics, pp. 502 – 509

Mandel, J., 1974. Thermodynamics and plasticity. In Delgado, J.J., et al. (Eds.), Foundations of continuum thermodynamics, Macmillan, New York

Marcinkowska-Ochtyra, A., Gryguc, K., Ochtyra, A., Kopec, D., Jarocinska, A., Sławik, Ł., 2019. Multitemporal hyperspectral data fusion with topographic indices – Improving classification of Natura 2000 grassland habitats. Remote Sensing, vol. 11, pp. 2264 – 2265

Mazzocola, D.F., Hudson, J.A., 1996. A comprehensive method of rock mass characterization for indicating natural slope instability. Quarterly Journal of Engineering Geology, vol. 29, pp. 37 – 56

McCullagh, P., Nelder, J., 1982. Generalized linear models. Chapman & Hall, Inc., Routledge

Meyer, N.K., Schwanghart, W., Korup, O., Romstad, B.A., Etzelmüller, B., 2013. Estimating the topographic predictability of debris flows. Geomorphology, vol. 207, pp. 114 – 125

Michoud. C., Derron, M.H., Horton, P., Jaboyedoff, M., Baillifard, F.J., Loye, A., Nicolet, P., Pedrazzini, A., Queyrel, A., 2012. Rockfall hazard and risk assessments along roads at a regional scale: example in Swiss Alps. Natural Hazards Earth System Science, vol. 12, pp. 615 – 629

Min, T.K., Phan T.H., 2010. A soil-water hysteresis model for unsaturated sands based on fuzzy set plasticity theory. KSCE Journal of Civil Engineering, vol. 14, no. 2, pp. 165 – 172

Mineo, S., Pappalardo, G., Mangiameli, M., Campolo, S., Mussumeci, G., 2018. Rockfall Analysis for Preliminary Hazard Assessment of the Cliff of Taormina Saracen Castle (Sicily). Sustainability, vol.10, 417;pp. 1-18

Mineo, S., Pappalardo, G., D'Urso, A., Calcaterra, D., 2017. Event tree analysis for rockfall risk assessment along a strategic mountainous transportation route. Environmental Earth Science, vol. 76, pp. 620 – 625

Mishnaevsky Jr, L.L., Schmauder, S., 1996. Analysis of rock fragmentation with the use of the theory of fuzzy sets. Proceedings of the ISRM International Conference EUROCK '96, Turin, pp. 735 – 740

Mohammady, M., Pourghasemi, H.R., Pradhan, B., 2012. Landslide susceptibility mapping at Golestan Province, Iran: a comparison between frequency ratio, Dempster-Shafer, and weights-of-evidence models. Journal Asian Earth Science, vol. 61, pp. 221 – 236

Monforte, L., Arroyo, M., Carbonell, J.M., Gens, A., 2017. Numerical simulation of undrained insertion problems in geotechnical engineering with the particle finite element method (PFEM). Computer Geotechnical, vol. 82, pp.144 – 156

Monforte, L., Arroyo, M., Carbonell, J.M., Gens, A., 2018c. Coupled effective stress analysis of insertion problems in geotechnics with the particle finite element method. Computer Geotechnical, vol. 101, pp. 114 – 129

Monforte, L., Arroyo, M., Gens, A., Parolini, C. 2018a. Permeability estimates from CPTu: a numerical study. The 4th International Symposium on Cone Penetration Testing, CPT18

Monforte, L., Arroyo, M., Gens, A., Carbonell, J.M., 2018b. Three-dimensional analysis of penetration problems using G-PFEM. The 9th European Conference on Numerical Methods in Geotechnical Engineering, NUMGE-18

Monjezi, M., Rezaei, M., 2011. Developing a new fuzzy model to predict burden from rock geomechanical properties, Expert Syst. Appl., vol. 38, (8), pp 9266-9273.

Monjezi, M., Rezaei, M., Yazdian Varjani, A., 2009. Prediction of rock fragmentation due to blasting in Gol-E-Gohar iron mine using fuzzy logic," International Journal of Rock Mechanics and Mining Sciences, vol. 46, (8), pp 1273-1280.

Morgenstern, N. R., Price, V. E.,1965. The Analysis of the Stability of General Slip Surfaces. Geotechnique, vol. 15, No. 1 pp. 77-93.

Muhammad, I (2017) Geotechnical Engineering–I [CE-221] BSc Civil Engineering – 4th Semester. Civil Engg. Dept. – UET Lahore, pp1.

Mutanamba, M., 2013. Analyze the stability of cut slopes along the R523 road between Thathe Vondo and Khalavha area and to find the most appropriate stabilization methods to prevent future slope failure along the road R523. Master of Science Mini-dissertation, University of Venda

Murthy, V.N.S., 2002. Geotechnical Engineering: Principles and Practices of Soil Mechanics and Foundation Engineering. (Civil and Environmental Engineering). CRC Press, New Delhi. ISBN 10:0824708733.

Nadim, F., Kjekstad, O., Peduzzi, P., Herold, C., Jaedicke, C., 2006. Global landslide and avalanche hotspots. Landslides, vol.3, pp.159–173.

Nash, D.,1987. Comprehensive Review of Limit Equilibrium Methods of Stability Analysis. Slope Stability, Chapter 2. M. G. Andersen and K. S. Richards, Eds. New York: Wiley, pp. 11-75.

Naudet, V., Lazzari, M., Perrone, A., Loperte, A., Piscitelli, S., Lapenna, V., 2008. Integrated geophysical techniques and geomorphological approach to investigate the snowmelt-triggered landslide of Bosco Piccolo village (Basilicata, southern Italy). Engineering Geology, vol.98, pp.156–167

Nazem, M. Sheng, D.C., Carter, J.P., 2006. Stress integration and mesh refinement for large deformation in geomechanics. International Journal for Numerical Methods in Engineering, vol. 65, pp. 1002 – 1027

Nemat-Nasser, S., 1982. On finite deformation elasto-plasticity. International Journal of Solids Structures, vol. 18, pp. 857 – 872

Nguyen, V.U., 1985. Some fuzzy set applications in mining geomechanics," International Journal of Rock Mechanics and Mining Sciences & Geomechanics Abstracts, Vol. 22, No. 6, pp 369-379.

Nguyen, V.U., Ashworth, E.A., 1985. Rock mass classification by fuzzy sets," In: 26th US Symposium on Rock Mechanics, Rapid City, SD, pp. 937- 945.

Nguyen, V.P., Rabczuk, T., Bordas, S., Duflot, M., 2008. Meshless methods: a review and computer implementation aspects. Mathematics and Computers in Simulation, vol. 79, pp. 763 – 813

Nico, G., Borrelli, L., Di Pasquale, A., Antronico, L., Gullà, G., 2015. Monitoring of an ancient landslide phenomenon by GBSAR technique in the Maierato town (Calabria, Italy). G. Lollino et al. (eds.). Engineering Geology for Society and Territory, vol.2, pp.129–13

Oka, Y., Wu, T.H., 1990, System reliability of slope stability. Journal of Geotechnical Engineering, ASCE, vol.116 (8), pp.1185-1189.

Oliver, J., Cante, J.C., Weyler, R., Gonzalez, C., Hernandez, J., 2007. Particle finite element methods in solid mechanics problems. In E. Onate & D.R.J. Owen (Eds.), Computational Plasticity, pp. 87 – 103

Onate, E., Garcia, J., 2001. A finite element method for fluid-structure interaction with surface waves using a finite calculus formulation, Comput. Meth. Appl. Mech. Engrg. vol.191, pp.635–660.

Onate, E., Idelsohn, S.R., Del Pin, F. 2003. Lagrangian formulation for incompressible fluids using finite calculus and the finite element method. In Numerical Methods for Scientific Computing Variational Problems and Applications, Y. Kuznetsov, P. Neittanmaki and O. Pironneau (Eds.), CIMNE, Barcelona

Onate, E., Idelsohn, S.R., Del Pin, F., Aubry, R., 2004. The particle finite element method: an overview. International Journal of Computational Methods, vol. 2, pp. 267 – 307

Onate, E., Idelsohn, S.R., Celigueta, M.A., Rossi, R., 2008. Advances in the particle finite element method for the analysis of fluid multibody interaction and bed erosion in free surface flows. Computer Methods in Applied Mechanics and Engineering, vol. 197, pp. 1777 – 1800

Onate, E., Idelsohn, S.R., Celigueta, M.A., Rossi, R., Marti, J., Carbonell, J.M., Ryzhakov, P., Suarez, B., 2011. Advances in the particle finite element method (PFEM) for solving coupled problems in engineering. Computational Methods in Applied Sciences, vol. 25, pp. 47 – 54

Othman, A., Gloaguen, R., 2013. River courses affected by landslides and implications for hazard assessment: a high resolution remote sensing case study in NE Iraq–W Iran, Remote Sensing, vol.5, pp.1024–1044,

Oppikofer, T., Jaboyedoff, M., Coe, J. A., 2007. Rockfall hazard at Little Mill Campground, Uinta National Forest: Part 2. DEM analysis, in: First North American Landslide Conference – Landslides and Society: Integrated Science, Engineering, Management, and Mitigation, Vail, USA, 3–8 June 2007, pp.1351–1361.

Ozdemir, A., Altural, T., 2012. A comparative study of frequency ratio, weights of evidence and logistic regression methods for landslide susceptibility mapping: Sultan Mountains, SW Turkey Journal Asian Earth Science, vol.64,pp.180–197

Pan, N.F., 2009. Selecting an appropriate excavation construction method based on qualitative assessments," Expert Systems with Applications, vol. 36, (3) pp 5481-5490.

Pandian, N. S., 2004. Fly ash characterization with reference to geotechnical applications. J. Indian Inst. Sci., Nov.–Dec. 2004, vol.84, pp.189–216

Pappalardo, G., Mineo, S., Rapisarda, F., 2014. Rockfall hazard assessment along a road on the Peloritani Mountains (northeastern Sicily, Italy). Nat. Hazards Earth Syst. Sci., vol.14, pp.2735–2748

Pradhan, B., Abokharima, M.H., Jebur, M.N., Tehrany, M.S., 2014. Land subsidence susceptibility mapping at Kinta Valley (Malaysia) using the evidential belief function model in GIS. Nat. Hazards, vol.73, pp.1019–1042

Pelletier, F. J., 1994. Fuzzy Logic, a Misplaced Appeal," IEEE Expert, vol. 9, (4), pp 29-31

Petley, D., 2012. Global patterns of loss of life from landslides. Geology vol.40, pp.927–930. http://dx.doi.org/10.1130/G33217.1.

Petley, D.N., 2004. The evolution of slope failures: mechanisms of rupture propagation. Natural Hazards Earth System Science, vol.4,pp.147–152

Petley, D.N, Bulmer, M.H.K, Murphy W., 2002. Patterns of movement in rotational and translational landslides. Geology, vol.30, pp.719–722

Peric, D., Hochard, C., Dutko, M., Owen, D.R.J., 1996. Transfer operators for evolving meshes in small strain elasto-plasticity. Computer Methods in Applied Mechanics and Engineering, vol.137, pp.331–344.

Pérez-Foguet A., Armero F., 2002. On the formulation of closest-point projection algorithms in elastoplasticity – Part II: globally convergent schemes. International Journal of Numerical Methods in Engineering, vol. 53, (2), pp.331–74

Phua, M.H., Conrad, O., Kamlisa, U.K., Fischer, M., Bohner, J., 2008. Multitemporal fragmentation analysis of peat swamp forest in the Klias peninsular, Sabah, Malaysia Using GIS and Remote Sensing Techniques.SAGA-Seconds Out, Hamburger Beitrage Zur Physischen Geographie Und Landschaftsokologie, Univ. Hamburg, Inst. Fur Geographie, pp.81-90.

Piccarreta, M.; Capolongo, D.; Boenzi, F., 2004. Trend analysis of precipitation and drought in Basilicata from 1923 to 2000 within a southern Italy context. Internation Journal Climatology, vol.24, pp.907–922.

Pieri, D., Abrams, M., 2004. ASTER Watches the World's Volcanoes: A New Paradigm for Volcanological Observations from Orbit. Journal of Volcanology and Geothermal Research,vol.135,pp.13–28

Pilot, G.,1984. Instrumentation and warning system for research and complex slope stability problems. Proc. 4th Int. Symp. on Landslides, Toronto, I:pp.275–306

Preisig, M., Prévost, J.H., 2011. Stabilization procedures in coupled poromechanics problems: a critical assessment. International Journal of Numerical Analysis of Methematics and Geomechanics, vol. 35, no. 11, pp. 1207 – 1225

Quan, H.C., Lee, B.G. 2012. GIS-Based Landslide Susceptibility Mapping Using Analytic Hierarchy Process and Artificial Neural Network in Jeju (Korea). Journal of Civil Engineering, vol.16(7), pp.1258-1266.

Rabie. M., 2014. Comparison study between traditional and finite element methods for slopes under heavy rainfall." Journal of Housing and Building National Research Center, vol.10, pp.160-168

Ramesh, V., Mani, S., Baskar, M., Kavitha, G., Anbazhagan, S., 2017. Landslide hazard zonation mapping and cut slope stability analyses along Yercaud ghat road (Kuppanur–Yercaud) section, Tamil Nadu, India. International Journal of Geotechnical Engineering, vol.8:pp.2.

Ramos-Bernal, R.N., Vázquez-Jiménez, R., Romero-Rojas, W., 2018. Modeling the Susceptibility to Landslides by Remote Sensing Techniques. Case Study: Central Area of the State of Guerrero in México, Havana, Cuba, Ministerio de Comunicaciones: Havana, Cuba, pp. 1–8.

Ramsey, M. S., Wessels, R. L., Anderson, S. W., 2012.Surface Textures and Dynamics of the 2005 Lava Dome at Shiveluch Volcano, Kamchatka. Bulletin of Geological Society. Am., vol.124 (5–6), pp.678–689. https: //doi.org/10.1130/B30580.1.

Raviart, P. A., Thomas, J. M., 1977. A mixed finite element method for 2-nd order elliptic problems. In Mathematical aspects of finite element methods, pp. 292–315. Springer.

Rawat, M.S., Uniyal, D.P., Dobhal, R., Joshi, V., Rawat, B.S., Bartwal, A., Singh, D., Aswal, A., 2015. Study of landslide hazard zonation in Mandakini Valley, Rudraprayag district, Uttarakhand using remote sensing and GIS. Current Science, vol.109, pp. 158–170.

Reichenbach, P., Rossi, M., Malamud, B., Mihir, M., Guzzetti, F., 2018. A Review of Statistically-Based Landslide Susceptibility Models. Earth Science Reviews, vol.180, pp.60 –91. http://dx.doi.org/10.1016/j.earscirev.2018.03.001.

Regmi, N. R., Giardino, J. R., Vitek, J. D.,2010. Assessing susceptibility to landslides: using 10 models to understand observed changes in slopes, Geomorphology, vol.122,pp.25–38

Ren, F., Wu, X., Zhang, K., Niu, R. 2015. Application of wavelet analysis and a particle swarm-optimized support vector machine to predict the displacement of the Shuping landslide in the Three Gorges, China. Environment Earth Science vol.73, pp.4791–4804

Rocscience., 2001a. DIPS - Graphical and Statistical Analysis of Orientation Data (Version 5.0). Rocscience Inc., Toronto

Rocscience., 2001b. SWEDGE - 3D Surface Wedge Analysis for Slopes (Version 4.0). Rocscience Inc., Toronto.

Rocscience., 2001c. SLIDE - 2D Limit Equilibrium Analysis of Slope Stability (Version 3.0). Rocscience Inc., Toronto

Rocscience., 2004. A New Era in Slope Stability Analysis: Shear Strength Reduction Finite Element Technique,

Rose, N.D, Hungr, O., 2007. Forecasting potential rock slope failure in open pit mines using the inverse-velocity method. International Journal Rock Mech Mining Science, vol.44, pp.308–320

Roy, J., Saha, S., Arabameri, A., Blaschke, T., Bui, D,T., 2019. A Novel Ensemble Approach for Landslide Susceptibility Mapping (LSM) in Darjeeling and Kalimpong Districts, West Bengal, India. Remote Sensing, vol.11,pp.1-28

Rubio, R. H., Florez, J. H., Zingano A. C., 2016. Slope stability analysis at highway BR-153 using numerical models. REM: R. Esc. Minas, Ouro Preto, vol.69,(2),pp.185-191

Rouainia, M., Wood, D.M., 2006. Computational aspects in finite strain plasticity analysis of geotechnical materials. Mechanic Research Communications, vol. 33, pp. 123 – 133

Salazar, F., Irazabal, J., Larese, A., Onate, E., 2016. Numerical modelling of landslide-generated waves with the particle finite element method (PFEM) and a non-Newtonian flow model. International Journal of Numerical Analysis Methods and Geomechanics, vol. 40, pp. 809 – 836

Santini, M., Grimaldi, S., Nardi, F., Petroselli, A., Rulli, M.C., 2009. Pre-processing algorithms and landslide modelling on remotely sensed DEMs. Geomorphology, vol.113 (1–2), pp.110–125

Sarkar, S., Kanungo, D.P., 2004. An integrated approach for landslide susceptibility mapping using remote sensing and GIS. Photogrammetric Engineering & Remote Sensing, vol.70 (5), pp. 617- 625.

Sarma, S. K.,1973. Stability Analysis of Embankment and Slopes. Geotechnique, Vol.23 (3), pp. 423-33

Sassa, K., Canuti, P. (Eds.), 2009. Landslides-Disaster Risk Reduction. Springer Berlin Heidelberg

Scavia, C., Barla, G., Vai. L., 1988. Analisi di tipo probabilistico. Pendii Naturali e Fronti di Scavo, Atti del Secondo Ciclo di Conferenze di Meccanica ed Ingegneria delle Rocce, MIR. Politecnico de Torino, vol.12, pp.1-12.27.

Schuster, R.L. 1996. Socioeconomic significance of landslides, AK Turner, RL Schuster (Eds.) Landslides:. Washington DC: Transportation Research Board National Research Council National Academy Press, pp.12–35.

Seegmiller, B. L., 1983. Geotechnical and stability requirements for future coal mines. Proc. 1st Int. Syrup. on Stabili O' in Coal Mining, pp. 223 246. Vancouver

Sengani, F., Zvarivadza, T., 2019. Evaluation of factors influencing slope instability: case study of the R523 Road between Thathe Vondo and khalavha area in South Africa. Symposium of Environmental Issues and Waste Management in Energy and Mineral Production, Springer, Cham, pp. 81 – 89

Selby, M.J., 1982. Hillslope materials and processes. Oxford University Press, New York

Shahabi, H., Khezri, S., Ahmad, B.B., Hasim, M., 2014. Landslide susceptibility mapping at central Zab basin, Iran: A comparison between analytical hierarchy process, frequency ratio and logistic regression models. CATENA, vol.155, pp. 55–70

Shahabi, H., Khezri, S., Ahmad, B. B., Hashim, M.,2013. Landslide susceptibility mapping at central Zab basin, Iran: a comparison between analytical hierarchy process, frequency ra-25 tio and logistic regression models, Catena, vol.115, pp.55–70,

Sharma, S., Raghuvanshi, T.K., Anbalagan, R., 1995. Plane failure analysis of rock slopes. Geotechnical and Geological Engineering 13 (2), pp.105-111

Shepard, D., 1968. A two-dimensional interpolation function for irregularly-spaced data. In Proceedings of the 23rd ACM National Conference, pp. 517 – 524

Shewchuk, J.R., 1996. Triangle: engineering a 2D quality mesh generator and delaunay triangulator. In M.C. Lin & D. Manocha (Eds.), Applied Computational Geometry: Towards Geometric Engineering, vol. 1148, pp. 203 – 222

Shewchuk, J.R., 2002. Delaunay refinement algorithms for triangular mesh generation. Computational Geometry: Theory and Applications, pp. 21 – 74

Sidoroff, F., 1974. Un modèle viscoélastique non lineaire avec configuration intermediaire. Journal de Mécanique, vol. 13, pp. 679 – 713

Simeoni, L., Mongiovì, L., 2007. Inclinometer monitoring of the Castelrotto landslide in Italy. Journal Geotechnical Geoenvironment Engineering, vol.133, pp.653–666

Simo, J.C., Ortiz, M., 1985. A unified approach to finite deformation elastoplasticity based on the use of hyperelastic constitutive equations. Computer Methods in Applied Mechanics and Engineering, vol. 49, pp. 221 – 245

Simo, J.C., 1998. Numerical analysis and simulation of plasticity. Handbook of Numerical Analysis., vol. 6, pp.183 – 499

Simo, J.C., Hughes, T.J.R., 2006. Computational inelasticity. Springer Science & Business Media

Sin, K.S., Thornton, C.I., Cox, A.L., Abt, S.R., 2012. Methodology for calculating shear stress in a meandering channe. Colorado State University

Singh, R., Forbes, C., Diop S., Musekiwa, C., Claasen, D., 2011. Landslide geohazards in South Africa. Landslide susceptibility mapping, socio-economic impacts, mitigation and remediation measure. Pretoria: Council for Geoscience, pp.58.

Singh, P.K., Wasnik, A.B., Kainthola, A., Sazid, M., Singh, T.N., 2013. The stability of road cut cliff face along SH-121: a case study. Natural Hazards, vol.68, pp. 497-507.

Skinner, B.J., Porter, S.C., 1987. Physical Geology, John Wiley & Sons, New York, pp 205-237

Sowers., 1979. Introductory Soil Mechanics and Foundations: Geotechnical Engineering, 4th Ed., Macmillan, New York.

Spang, R.M., Rautenstrauch, R.W., 1988. Empirical and mathematical approaches to rock fall protection and their practical application. In: Bonnard C (ed) 5th International Congress on Landslides, vol 2. Lausanne. Balkema, Rotterdam, pp 1237–1243. ISBN 90-6191-838-3

Spencer, E.,1967. A method of Analysis of the Stability of Embankments, Assuming Parallel Interslice Forces. Geotechnique, vol. 17, pp. 11-26.

Stanley, T., Kirschbaum, D.B., 2017. A heuristic approach to global landslide susceptibility mapping. Natural Hazards. http://dx.doi.org/10.1007/s11069-017-2757-y.

Stead, D., Eberhardt, E., Coggan, J.S., 2006. Developments in the characterization of complex rock slope deformation and failure using numerical modelling techniques. Engineering Geology, vol.83, pp.217–235

Stock, G.M., Martel, S.J., Collins, B.D., Harp, E.L., 2012. Progressive failure of sheeted rock slopes: the 2009–2010 Rhombus Wall rock falls in Yosemite Valley, California, USA. Earth Surface Proccess Land, vol.37, pp.546– 561

Takizawa, K., Tezduyar, T.E., 2011. Multiscale space time fluid-structure interaction techniques. Computational Mechanics, Published online, DOI:10.1007/s00466011-0571-z

Tyado, Z., 2013. Landslide Susceptibility Mapping: Remote Sensing and GIS Approach. MSc. University of Stellenbosch.

Taylor, G.I., 1938. Analysis of plastic strain in a cubic crystal. In Lessels, J.M. (Eds.), Stephen Timoshenko 60th Anniversary Volume, Macmillan, New York

Terzaghi, K., 1962. Mechanism of landslides. Engineering Geology, pp. 83 – 123

Terzaghi, K., 1950. Stability of steep slopes on hard unweathered rock. Géotechnique, vol. 12, pp. 251 – 270

Thulamela Municipality, 2019. Background of Thulamela Municipality. Thulamela Municipality Limpopo Province.

Tian, Y., Cassidy, M.J., Randolph, M.F., Wang, D., Gaudin, C., 2014. A simple implementation of RITSS and its application in large deformation analysis. Computers and Geotechnics, vol. 56, pp.160 – 167

Toppe, R., 1987. Terrain models – a tool for natural hazard mapping. IAHS, vol. 162, pp. 629 – 638

Turner, A.K., Jayaprakash, G.P., 2012. Introduction. In Turner, A.K., Schuster, R.L. (Eds.), Rockfall characterization and control, Transportation Research Board, National Academy of Sciences, Washington D.C., pp. 3 – 20

Tutmez, B., Kahraman, S., Günaydin, O., 2007. Multifactorial fuzzy approach to the sawability classification of building stones. Construction and Building Materials, vol. 21, no. 8, pp. 1672 – 1679

Urai, M., 2004. Sulfur Dioxide Flux Estimation from Volcanoes Using Advanced Space borne Thermal Emissionand Reflection Radiometer—A Case Study of Miyakejima Volcano, Japan. Journal of Volcanology and Geothermal Research, vol. 2004, 134, 1–13

U.S. Army Corps of Engineers., 1970. Engineering and Design - Stability of Earth and Rockfill Dams. Engineer Manual EM 1110-2-1902, Department of the Army, Corps of Engineers, Washington, DC.

Uzielli, M., Catani, F., Tofani, V., Casagli, N., 2015. Risk analysis for the Ancona landslide – I: Characterization of landslide kinematics. Landslides, vol. 12, pp. 69 – 82

Van Den Eeckhaut, M., Moeyersons, J., Nyssen, J., Abraha, A., Poesen, J., Haile, M., Deckers, J., 2008. Spatial patterns of old, deep-seated landslides: a case-study in the northern Ethiopian highlands. Geomorphology, vol. 105, pp. 239 – 252

Vaunat, J., Leroueil, S., 2002. Analysis of post-failure slope movements within the framework of hazard and risk analysis. Natural Hazards, vol. 26, pp. 83 – 109

Wagner, A., Leite, E., Olivier, R., 1988. Rock and debris-slides risk mapping in Nepal – A user-friendly PC system for risk mapping. Proceedings of the Ffth International Symposium on Landslides, Lausanne, Switzerland, 10 – 15 July 1988, pp.1251 – 1258

Wang, L., Zhang, X., Tinti, S. 2019. Shallow landslides modeling using a particle finite element model with emphasis on landslide evolution. Journal Earth Surface Dynamics, https://doi.org/10.5194/esurf-2019-17. 1-19

Wang, D., Bienen, B., Nazem, M., Tian, Y., Zheng, J., Pucker, T., 2015. Large deformation finite element analyses in geotechnical engineering. Computer Geotechnical, vol. 65, pp. 104 – 114

Wang, J.J., Liang, I.Y., Zhang, H.P., Wu, W.Y., Lin, X., 2014. Aloess landslide induced by excavation and rainfall. Landslides, vol. 11, pp. 141 – 152

Wang, G., 2012. Kinematics of the Cerca del Cielo, PuertoRico landslide derived from GPS observations. Landslides, vol. 9, pp. 117 – 130

Wang, G., Ming-Wu, Y., Chen, G.Y., Jin, J.L., 2011. Risk evaluation of surrounding rock stability based on stochastic simulation of multi-element connection number and triangular fuzzy numbers. Chinese Journal of Geotechnical Engineering, vol. 33, no. 4, pp. 643 – 647

Wang, J., Rich, P.M., Price, K.P., 2003. Temporal responses of NDVI to precipitation and temperature in the central Great Plains, USA. Int. J. Remote Sens., vol.24, pp.2345-2364.

Welch, R. Marko, W., 1981, Cartographic potential of spacecraft line-array camera system: stereos at. Photogrammetric Engineering and Remote Sensing, vol. 47, pp. 1173 – 1185

Whalley, W.B., 1984. Rockfalls. In Brunsden, D., Prior, D.B. (Eds.), Slope instability, Wiley, New York, pp. 217 – 256

White, M.A., Hoffman, F., Hargrove, W.W., Nemani, R.R., 2005. A global framework for monitoring phenological responses to climate change. Geophysical. Research Letter, vol. 32, pp. 1 – 5

Wills, C.J, Manson, K.D, Brown, C.W, Daveport, Domrose, C.J, 2008. Landslides in the highway 1 corridor: geology and slope stability along the big sur coast between point lobos and san carposoro creek, montery and san luis Obispo counties,

California. Special report, Department of conservation, California Geological Survey, USA

Wriggers, P., 1995. Finite element algorithms for contact problems. Archives of Computational Methods in Engineering, vol. 2, no. 4, 1 – 49

Wu, Z.Z., 2010. Stochastic medium predicting model of ground movement tunneling based on non-uniform convergence mode. Zhongnan Daxue Xuebao (Ziran Kexue Ban)/ Journal of Central South University (Science and Technology), vol. 41, pp. 2005 – 2010

Wyllie, D.C., Mah, C.W., 2004. Rock slope engineering, civil and mining, Fourth Edition. Taylor & Francis, London and New-York

Yao, F., Müller, H.G., Wang, J.L., 2005. Functional data analysis for sparse

Yamaguchi, Y., Kahle, A.B., Tsu, H., Kawakami, T., Pniel, M., 1998. Overview of Advanced Spaceborne Thermal Emission and Reflection Radiometer (ASTER). IEEE Geoscience and Remote Sensing Society, vol. 36, 1062 – 1071

Yin, Y., Zheng, W., Liu, Y., Zhang, J., Li, X., 2010. Integration of GPS with In SAR to monitoring of the Jiaju landslide in Sichuan, China. Landslides, vol. 7, pp. 359 – 365

Youssef, A.M., Al-Kathery, M., Pradhan, B., 2015. Landslide susceptibility mapping at Al-Hasher Area, Jizan (Saudi Arabia) using GIS-based frequency ratio and index of entropy models. Geoscience Journal, vol. 19, pp. 113 – 134

Yu, L., Hu, Y.X., Liu, J., Randolph, M.F., Kong, X.J., 2012. Numerical study of spudcan penetration in loose sand overlying clay. Computers and Geotechnics, vol. 46, pp. 1 – 12

Yu, H.S., Mitchell, J.K., 1998. Analysis of cone resistance: review of methods. Journal of Geotechnical Geoenviron Engineering, vol. 124, pp. 140 – 149

Yuan, W. H., Zhang, W., Dai, B. B., Wang, Y., 2019a. Application of the particle finite element method for large deformation consolidation analysis. Engineering Computer, in press

Yuan, W. H., Liu, K., Zhang, W., Dai, B., Wang, Y., 2020. Dynamic modeling of large deformation slope failure using smoothed particle finite element method. Landslides: DOI 10.1007/s10346-020-01375-w

Zezere, J.L., Trigo, R.M., Fragoso, M., Oliveira, S.C., Garcia, A.C., 2008. Rainfall-triggered landslides in the Lisbon region over 2006 and relationships with the North Atlantic Oscillation. Natural Hazards Earth System Science, vol. 8, 483 – 499

Zhang, G., Cai, Y., Zheng, Z., Zhen, J., Liu, Y., Huang, K., 2016. Integration of the statistical index method and the analytic hierarchy process technique for the assessment of landslide susceptibility in Huizhou, China. CATENA, vol. 142, pp. 233 – 244

Zhang, W.G., Goh, A.T.C., 2013. Multivariate adaptive regression splines for analysis of geotechnical engineering systems. Computer Geotechnical, vol.48, 82– 95.

Zhang, X., Krabbenhoft, K., Pedroso, D.M.., Lyamin, A.V., Sheng, D., Da Silva M.V., 2013. Particle finite element analysis of large deformation and granular flow problems. Computer Geotechnical, vol.54, pp.133 – 142.

Zhang, X., 2014. Particle finite element method in geomechanics. PhD thesis, University of Newcastle, Australia

Zhang, X., Krabbenhoft, K., Sheng, D., 2014. Particle finite element analysis of the granular column collapse problem. Granular Matter, vol. 16, pp.609 – 619

Zhang, X., Krabbenhoft K., Sheng D, Li W., 2015. Numerical simulation of a flow-like landslide using the particle finite element method. Computer Mechnical, vol. 55, pp.167 – 177

Zhang, X., Sheng, D., Sloan, S.W., Bleyer, J., 2017. Lagrangian modelling of large deformation induced by progressive failure of sensitive 25 clays with elastoviscoplasticity. International Journal for Numerical Methods in Engineering, vol. 112, pp. 963 – 989

Zhang, X., Sloan, S.W., Oñate, E., 2018. Dynamic modelling of retrogressive landslides with emphasis on the role of clay sensitivity. International Journal for Numerical and Analytical Methods in Geomechanics, vol. 42, pp. 1806 – 1822

Zhang, X., Oñate, E., Torres, S.A.G., Bleyer, J., Krabbenhoft, K., 2019a. Aunified Lagrangian formulation for solid and fluid dynamics and its possibility for modelling submarine landslides and their consequences. Computer Methods in Applied Mechanics and Engineering, vol. 343, pp. 314 – 338

Zhang, X., Wang, L., Krabbenhoft, K., Tinti, S., 2019b. A case study and implication: particle finite element modelling of the 2010 Saint-Jude sensitive clay landslide. Landslides, vol. 17, pp. 1117–1127. DOI 10.1007/s10346-019-01330-4

Zienkiewicz, O.C., Taylor, R.L., 2000. The finite element method: solid mechanics, vol. 2. Butterworth-Heinemann, Oxford

Zienkiewicz, O.C., Taylor, R.L., Zhu, J.Z., 2005. The finite element method: its basis and fundamentals, Sixth Edition. Butterworth-Heinemann, Spain.

Appendix

Appendix A: Pixel analysis using NDVI

Table A1: The NDVI values for landslide point A.

2004		
0.607084	0.429892	0.129965
0.665306	0.579575	0.307246
0.638259	0.606456	0.522369
		Average=0.49846
2017		
0.47855	-0.144773	-0.164073
0.602333	0.032632	-0.370645
0.454843	0.244538	-0.175402
		Average=0.106444

Table A2: The NDVI values for landslide point B.

2004		
0.396714	0.15952	0.15952
0.189062	0.14824	0.331732
0.491425	0.447955	0.471469
		Average=0.31063
2017		
0.63526	0.294697	-0.022156
-0.185622	-0.349276	-0.513238
-0.084899	-0.182582	-0.463613
		Average=-0.09682

Table A3: The NDVI values for landslide point C.

2004		
0.306811	0.365041	0.380279
0.085461	0.225565	0.315046
0.293693	0.178981	-0.04297
		Average=0.23421
2017		
0.253463	0.246853	0.325311
-0.114384	0.246853	0.47088
-0.477063	-0.333	-0.094156
		Average=0.058306

Table A4: The NDVI values for landslide point D

2004		
0.102404	0.234963	0.068454
0.126203	0.136551	-0.16994
0.152709	-0.07593	-0.13884
		Average=0.04851
2017		
0.313315	-0.284059	-0.576104
-0.066535	-0.48443	-0.580155
-0.367389	-0.570839	-0.566566
		Average=-0.35364

Table A5: The NDVI values for landslide point E

2004		
0.015132	-0.01231	0.236823
0.35142	0.302155	0.166484
0.540969	0.511321	0.434994
		Average=0.283
2017		
-0.46177	-0.333	-0.01923
-0.57526	-0.58115	-0.57948
-0.06795	-0.15258	-0.14477
		Average=-0.32391

Table A6: The NDVI values for landslide point F

2004		
0.676307	0.676307	0.792048
0.623027	0.676307	0.805893
0.4348	0.623027	0.748286
		Average=0.67289
2017		
0.154212	-0.269083	-0.556919
-0.30431	-0.504246	-0.577477
-0.532873	-0.572014	-0.556919
		Average=-0.41329

Table A7: The NDVI values for landslide point G

2004		
-0.02518	0.103114	0.081836
-0.05308	0.103114	0.031275
0.102814	0.1736	-0.0331
		Average=0.05382
2017		
-0.22987	-0.37899	-0.31545
0.006222	-0.11299	-0.24965
0.13944	-0.02216	-0.47423
		Average=-0.18196

Appendix B: Rock Mass Rating Results

Table B1. Rock mass rating resultsing using geological mapping data

Sites	Set	Spacing	Persistence (m)	Aperture (mm)	JRC	Infilling	Weathering	RMR Class
ST1	J1 (108/48)	Close (60-200)	Medium (3-10)	Moderate (2.5-10)	2-4	Soft	Moderate	52 III Fair Rock
	J2 (32/57)	Very close (20-60)	Medium (3-10)	Very tight (<0.1)	4-6	Soft	Moderate	
	J3 (293/40)	Very close (20-60)	High (10-20)	Very tight (<0.1)	8-12	None	slight	
	J4 (213/57)	Moderate (200-600)	Medium (3-10)	Very tight (<0.1)	10-12	None	Slight	
ST2	J1 (248/88)	Very close (20-60)	Medium (3-10)	Partly open (0.25-0.5)	4-6	None	Slight	56 III Fair Rock
	J2 (54/78)	Very close (20-60)	Medium (3-10)	Very tight (<0.1)	2-4	None	Slight	
	J3 (107/15)	Moderate (200-600)	Very High (>20)	Very tight (<0.1)	2-4	None	Slight	
	J4 (192/45)	Moderate (200-600)	High (10-20)	Very tight (<0.1)	8-12	None	Slight	
	J5 (72/60)	Moderate (200-600)	Medium (3-10)	Moderate (2.5-10)	2-4	None	Slight	
	J1 (73/35)	Close (60-200)	Medium (3-10)	Moderate (2.5-10)	8-12	Soft	Moderate	

ST3	J2 (101/17)	Close (60-200)	Very High (>20)	Moderate (2.5-10)	8-12	None	Slight	56 III Fair Rock
	J3 (146/54)	Moderate (200-600)	Medium (3-10)	Very tight (<0.1)	4-6	None	Slight	
	J4 (116/54)	Moderate (200-600)	Medium (3-10)	Very tight (<0.1)	2-4	None	Slight	
	J5 (210/75)	Moderate (200-600)	Medium (3-10)	Very tight (<0.1)	2-4	None	Slight	
	J6 (315/46)	Close (60-200)	Medium (3-10)	Very tight (<0.1)	2-4	None	moderate	
	J7 (250/48)	Very Close (20-60)	High (10-20)	Moderate (2.5-10)	4-6	None	Slight	
	J8 (293/63)	Close (60-200)	Medium (3-10)	Partly open (0.25-0.5)	8-12	None	Slight	
	J9 (356/36)	Moderate (200-600)	Medium (3-10)	Moderate (2.5-10)	2-4	Soft	moderate	
ST4	J1 (270/63)	Close (60-200)	Medium (3-10)	Moderate (2.5-10)	2-4	Soft	Slight	53 III Fair Rock
	J2 (37/65)	Moderate (200-600)	Medium (3-10)	Moderate (2.5-10)	4-6	None	Moderate	
	J3 (153/41)	Moderate (200-600)	Very High (>20)	Moderate (2.5-10)	4-6	None	Moderate	
	J4 (222/76)	Close (60-200)	High (10-20)	Moderate (2.5-10)	4-6	None	Slight	
	J5 (332/58)	Close (60-200)	High (10-20)	Very tight (<0.1)	4-6	None	Slight	
	J1 (243/78)	Moderate (200-600)	High (10-20)	Very tight (<0.1)	2-4	Soft	Slight	

ST5	J2 (79/62)	Very Close (20-60)	Medium (3-10)	Moderate (2.5-10)	2-4	None	Slight	56 III Fair Rock
	J3 (36/54)	Very Close (20-60)	Medium (3-10)	Partly open (0.25-0.5)	8-12	None	Slight	
	J4 (163/55)	Close (60-200)	Medium (3-10)	Moderate (2.5-10)	8-12	None	Slight	
	J5 (302/18)	Close (60-200)	Medium (3-10)	Moderate (2.5-10)	2-4	None	Slight	
ST6	J1 (226/57)	Moderate (200-600)	Medium (3-10)	Very tight (<0.1)	2-4	Soft	Moderate	56 III Fair Rock
	J2 (348/77)	Moderate (200-600)	Medium (3-10)	Very tight (<0.1)	4-6	None	Slight	
	J3 (301/56)	Close (60-200)	Very High (>20)	Very tight (<0.1)	8-12	None	Slight	
	J4 (25/21)	Close (60-200)	Medium (3-10)	Moderate (2.5-10)	4-6	None	Slight	
	J5 (53/68)	Very Close (20-60)	Medium (3-10)	Moderate (2.5-10)	2-4	None	Slight	
	J6 (104/43)	Moderate (200-600)	Medium (3-10)	Partly open (0.25-0.5)	2-4	None	Slight	
	J7 (161/75)	Moderate (200-600)	Medium (3-10)	Moderate (2.5-10)	2-4	None	Moderate	
	J8 (126/67)	Very close (20-60)	Medium (3-10)	Moderate (2.5-10)	4-6	None	Slight	
	J9 (35/71)	Close (60-200)	High (10-20)	Moderate (2.5-10)	8-12	Soft	Slight	

Appendix C: Ethical Clearance

UNISA | university of south africa

UNISA SOE ETHICS REVIEW COMMITTEE

Date: 21/11/2019

Dear Mr Fhatuwani Sengani

Decision: Ethics Approval from 07/10/2019 to 07/10/2024

ERC Reference # : 2019/CSET_SOE/FS/001

Name : Mr Fhatuwani Sengani

Student #:

Staff #: 90430050

Researcher(s): Name: Mr Fhatuwani Sengani
E-mail address: fhatugeorge@gmail.com
Telephone #: +27724430982/0152683036

Supervisor (s): Name: Name: Prof Francois Mulenga
E-mail address: mulengf@unisa.ac.za
Telephone #: 011

Co-Supervisor (s):

Co-Researcher(s): N/A

Working title of research:

Application of particle Finite Element Methods to cases of rockfall and slope stability

Qualification: PhD

Thank you for the application for research ethics clearance by the Unisa SOE Ethics Review Committee for the above mentioned research. Ethics approval is granted for 5 years.

*The **negligible risk application** was **reviewed** by the SOE Ethics Review Committee on 21/11/2019 in compliance with the Unisa Policy on Research Ethics and the Standard Operating Procedure on Research Ethics Risk Assessment. The decision was approved on 21/11/2019.*

The proposed research may now commence with the provisions that:

1. The researcher(s) will ensure that the research project adheres to the values and principles expressed in the UNISA Policy on Research Ethics.
2. Any adverse circumstance arising in the undertaking of the research project that is relevant to the ethicality of the study should be communicated in writing to the SOE Committee.
3. The researcher(s) will conduct the study according to the methods and procedures set out in the approved application.
4. Any changes that can affect the study-related risks for the research participants, particularly in terms of assurances made with regards to the protection of participants' privacy and the confidentiality of the data, should be reported to the Committee in writing, accompanied by a progress report.
5. The researcher will ensure that the research project adheres to any applicable national legislation, professional codes of conduct, institutional guidelines and scientific standards relevant to the specific field of study. Adherence to the following South African legislation is important, if applicable: Protection of Personal Information Act, no 4 of 2013; Children's act no 38 of 2005 and the National Health Act, no 61 of 2003.
6. Only de-identified research data may be used for secondary research purposes in future on condition that the research objectives are similar to those of the original research. Secondary use of identifiable human research data require additional ethics clearance.
7. No field work activities may continue after the expiry date 21/11/2024. Submission of a completed research ethics progress report will constitute an application for renewal of Ethics Research Committee approval.
8. Field work activities may only commence from the date on this ethics certificate.
9. [Permission to conduct research involving UNISA employees, students and data should be obtained from the Research Permissions Subcommittee (RPSC) prior to commencing field work.] AND/OR
10. [Permission to conduct this research should be obtained from the [company, CE organisation, DoE, etc name] prior to commencing field work.]

URERC 25.04.17 - Decision template (V2) - Approve

> Add any other conditions if relevant.
>
> *Note:*
>
> *The reference number* **2019/CSET_SOE/FS/001** *should be clearly indicated on all forms of communication with the intended research participants, as well as with the Committee.*

Yours sincerely,

Signature...................................

Prof E Onyari-Benecha

Chair of SOE ERC

E-mail: onyarek@unisa.ac.za

Tel: (011) 471-3379

Signatures...................................

Prof BB Mamba

Executive Dean : CSET

E-mail: mambabb@unisa.ac.za

Tel: (011) 670-9230

Bikdel
for Director : SOE

Private Bag X5066
Thohoyandou
0950
Limpopo Province
Tel: 015 962 7500
Fax: 015 962 4020

Ref	: 4/3/4/1
Enquiries	: HR OFFICES
Tel	: 015 962 7514
Fax	: 015 962 4020

To	: SENGANI FHATUWANI
From	: THULAMELA MUNICIPALITY
Date	: 02 APRIL 2019

SUBJECT: PERMISSION TO CONDUCT RESEARCH AT THULAMELA MUNICIPALITY

1. The above matter refers.

2. Kindly note that permission to conduct research has been granted.

3. Contact Human Resources Section for more information.

4. Hoping that this will meet your favourable considerations.

MUNICIPAL MANAGER: MALULEKE H.E